INFRARED LASER SPECTROSCOPY OF OPEN-SHELL SPECIES: COLD RADICALS IN SUPERFLUID HELIUM NANODROPLETS

by

TAO LIANG

(Under the Direction of Gary E. Douberly, Jr)

ABSTRACT

In this thesis, infrared laser spectroscopy is employed to probe the structure and dynamics of open-shell molecular complexes in 0.4 K helium droplets. The Λ-doublet splittings of He-solvated OH radical in the ground and first excited vibrational states are determined to be 3.6 and 7.2 times larger than their respective gas phase values, and a model that assumes a realistic parity dependence of the effective moment of inertia reproduces the observed change quantitatively. The HOOO radical is produced via the association reaction between OH and O_2. The ν_1 and $\nu_1+\nu_6$ bands are found for the *trans*-HOOO species, and no evidence for *cis*-HOOO or the weakly bound OH-O_2 is observed. Stark spectroscopy of *trans*-HOOO reveals a large discrepancy between the measured dipole moments and the equilibrium values computed at the CCSD(T) complete basis set limit (CBS) level. When the CCSDT(Q)/CBS equilibrium dipole moments are adjusted for vibrational averaging, excellent agreement with experiment is obtained. The sequential addition of OH and multiple O_2 molecules to helium droplets results in the formation of HO_3-$(O_2)_n$ clusters as large as n=4, and the spectra of these species are probed in the OH stretch region. For n=1, a comparison between the experimental result and *ab initio* calculations indicates a hydrogen-bonded $^{4}A'$ *trans*-HO_3-O_2 structure, consisting of a *trans*-HOOO core. Similarly, Al-$(CO)_n$ clusters ($n \leq 5$) are assembled in helium droplets. The rotationally resolved C-O stretch bands for $^{2}\Pi_{1/2}$ Al-CO and $^{2}B_1$ Al-$(CO)_2$ complexes are observed. A broad band with pressure dependence of two CO molecules is found and tentatively assigned to the weakly bonded Al-CO-(CO) cluster. For the reaction between Al and HCN, a $^{2}A'$ bent-HCNAl species is found near 2690 cm^{-1}. The σ donation and π donation between the Al atom and HCN ligand is investigated via a Natural Bond Orbital (NBO) analysis. These studies expand our understanding of the fundamental behavior of open-shell radical complexes in helium droplets.

INDEX WORDS: Helium Nanodroplet Isolation, Molecular Beam, Cold Molecules, Small Molecules, Infrared Laser Spectroscopy, Rovibrational Spectroscopy, Stark Spectroscopy, Theory and Computation

INFRARED LASER SPECTROSCOPY OF OPEN-SHELL SPECIES: COLD RADICALS IN SUPERFLUID HELIUM NANODROPLETS

by

TAO LIANG

B.S., University of Science and Technology of China, China, 2009

A Thesis Submitted to the Graduate Faculty of The University of Georgia in Partial Fulfillment of the Requirements for the Degree

DOCTOR OF PHILOSOPHY

ATHENS, GEORGIA

2014

INFRARED LASER SPECTROSCOPY OF OPEN-SHELL SPECIES: COLD RADICALS IN SUPERFLUID HELIUM NANODROPLETS

by

TAO LIANG

Major Professor:	Gary E. Douberly, Jr.
Committee:	Michael A. Duncan Wesley D. Allen

Electronic Version Approved:

Maureen Grasso
Dean of the Graduate School
The University of Georgia
May 2014

ACKNOWLEDGEMENTS

Firstly, I would like to express my thankfulness to my advisor Professor Gary E. Douberly for his patience and great enthusiasm in guiding me all the way to the end of my PhD study. It is eventually a mission impossible to finish my PhD without learning from his experimental skill and creative thinking in science. It was an honor to have been his student. I would also like to thank Professor Michael A. Duncan and Professor Wesley D. Allen for being my committee members and willing to help me and prevent me from making scientific mistakes. I want to thank both Dr. Paul Raston and Dr. Christopher Leavitt for being my role models in science and give me tremendous amount of knowledge in the field of physical chemistry. Thanks to all Douberly group members, especially Alex Morrison, Steven Flynn and Chris Moradi for the discussions that stimulate scientific thoughts during the many lunch parties. It would be extremely bored to pursuit science without having so many wonderful mentors and friends.

I want to thank UGA graduate school for giving me the Dissertation Completion Award (2013-2014). I would also like to acknowledge support from the National Science Foundation (CHE-1054742) and the donors of the American Chemical Society Petroleum Research Fund (50223-DNI6).

I would like to thank my wife Tianzhu for coming to the US with me and help me survive my PhD study, during which I am absolutely not able to take care of myself. Without her support, it is not possible to finish this thesis. She is always the best.

TABLE OF CONTENTS

Page

LIST OF TABLES

LIST OF FIGURES

Chapter 1

Introduction

The first spectroscopic study of a molecular species solvated in a helium nanodroplet occurred in 1992 with the study of SF_6. Goyal, Schutt and Scoles captured SF_6 in helium nanodroplets and probed its ν_3 fundamental vibrational transition with a line tunable CO_2 laser, although SF_6 was misassigned to be on the surface of the droplets.[1] Two years later, Fröchtenicht, Toennies and Vilesov reinvestigated the ν_3 band of SF_6 with a continuous-wave (cw) diode laser, and the rotationally resolved spectrum of SF_6 in their experiment firmly supported that SF_6 resides inside the droplets.[2] Shortly thereafter, a measurement was carried out for OCS in both ^{4}He and ^{3}He nanodroplets by Grebenev, Toennies and Vilesov.[3] In their experiment, the OCS IR spectrum is found to contain rotational structure in ^{4}He nanodroplets, while the spectrum of OCS in ^{3}He nanodroplets showed only a single broad peak, which lacked rotational fine structure. This can be explained by the fact that ^{4}He nanodroplets are superfluid at 0.4 K, while ^{3}He nanodroplets are not.[3] In the same paper, they presented a "Microscopic Andronikashvili Experiment" on OCS in ^{4}He/^{3}He-mixed nanodroplets, which revealed that a superfluid environment of ^{4}He can be established with a cluster size as small as 60 ^{4}He atoms,[3] which surrounds OCS and is embedded in the larger ^{3}He droplet. Many other small molecules have been doped into helium nanodroplets in the late 90s and early 2000s,[4-11] providing a considerable amount of insight into the ro-vibrational dynamics of closed-shell molecules in this 0.4 K superfluid environment. Moreover, the dynamics of molecular cluster formation within He droplets have been explored by assembling HCN dimer,[12] HCN-HF,[13] and even larger molecular clusters like $(HCN)_n$ ($n \leq 10$)[14] and H_2O cyclic-hexamer.[15] The study of molecular reaction dynamics in the He droplet environment is less well-developed.

Reactions involving open-shell species play important roles in a broad range of fields, including combustion and atmospheric chemistry.[16-21] While there have been some successful experiments aimed at probing radical reactions inside helium nanodroplets, the knowledge of this class of reactions is still limited compared to the droplet mediated complexation of closed-shell molecules. This dissertation focuses on the investigation of reactions involving open-shell molecular species in the helium nanodroplet environment. The IR spectra of OH, HO_3, HO_3-$(O_2)_n$, Al-$(CO)_n$, and Al-HCN are measured with sufficient resolution to reveal rotational fine structure. The dipole moments of OH and HO_3 are obtained via Stark spectroscopy. High level *ab initio* computations are used throughout to model the structures and the potential energy surfaces of these molecules.

1.1 Reactions of Open-shell Species in Helium Nanodroplets

Open-shell molecules are usually hard to stabilize due to their highly reactive unpaired electrons. Free jet expansion[22-24] and matrix isolation[25-27] are two conventional methods for capturing these radicals, and these two methods have their own advantages and disadvantages. Helium droplets can be thought of as a marriage between free jet expansion and matrix isolation techniques,[28] providing a flexible route to synthesize open-shell species in a cold environment and probe them with high resolution spectroscopy. Helium nanodroplets are able to capture the pre- and post-reactive complexes following the reaction between sequentially captured molecular reactants, as illustrated in Fig. 1.1. The van der Waals complexes of the reactants are often formed in the helium nanodroplets, and the reaction is kinetically arrested due to the system being cooled rapidly to low temperature (0.37 K). The early attempts to characterize reactions of radicals in helium droplets included investigations of metal atom insertion reactions, hydrogen abstraction reactions, and X-H-Y (X and Y = F, Cl, Br or I) type reactions. For systems trapped as pre-reactive complexes, excitation above the reaction barrier via vibrational pumping has been proposed for the study of product branching. A good demonstration of the potential of this approach was an IR-IR double resonance experiment of HCN-HF,[29] where an IR laser was used to transfer the population from the higher energy bent HF-HCN isomer to the lower energy linear HCN-HF isomer.

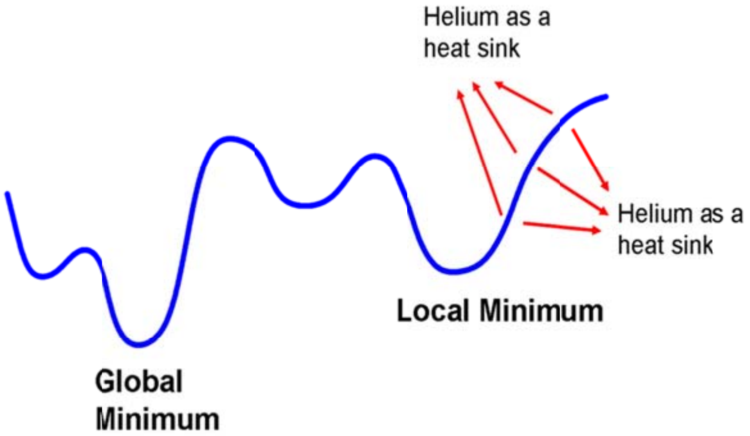

Figure 1.1: Relatively rapid cooling of the condensing molecular system in helium nanodroplets results in kinetic trapping of metastable clusters

The barriers for reactions between closed-shell molecules are usually large so that infrared radiation can not initiate bond-breaking reactions. However, the reactions between radicals and closed-shell molecules can have low enough barriers in the entrance channel such that IR photons would be sufficient to excite the pre-reactive complexes to be above the transition states. The reactions between group 13 metals M (Al, Ga, and In) and HCN have ideal potential energy surfaces, such that IR photoinduced reactions are feasible.[30] Many potential minima for these reaction systems have been predicted by theory.[30, 31] In solid argon matrix isolation studies, MCN was observed, which indirectly supported that HMCN is a potential intermediate that connects M + HCN and MCN + H.[31] Helium nanodroplet isolation spectroscopy is an ideal candidate for finding this intermediate. Using this technique, Merritt, Douberly, Stiles, and Miller searched in the mid-IR from 3180 to 3315 cm^{-1} for the M + HCN reaction products.[30] The measured IR spectra lead to the discovery of the linear nitrogen-bound HCN-Ga and HCN-In complexes as well as the linear hydrogen-bound Al-HCN, Ga-HCN, and In-HCN. The HCN-Al complex was missing in their spectrum, and it was believed to undergo a barrierless reaction that results in a bent-HCNAl structure. Unfortunately, the predicted vibrational frequencies for HMCN, HMNC, and bent-HCNAl are below the range of their laser system and therefore were not available in their experiment. This system is revisited in chapter 8 with a PPLN-OPO laser, which has sufficient coverage to reveal the products of the Al + HCN reaction.

Fundamental insight into the reactions between radical species can be obtained through the study of model systems involving small molecules. One of the simplest model reactions is $F + CH_4 \rightarrow CH_3 + HF$, which has been investigated extensively with both experiments[32] and theory.[33] Merritt, Rudic, and Miller successfully prepared the exit channel complex of this reaction in a helium nanodroplet.[34] Two laser sources, a cw F-center laser system and a PPLN-OPO laser system, were used to study the HF stretches of CH_3-HF and CD_3-HF. The vibrational relaxation time of the HF stretch in CD_3-HF is found to be 6 times larger than that for CH_3-HF, potentially due to the coupling of HF and CH_3 vibrational modes, which is much weaker in the HF and CD_3 case. The dipole moment of CH_3-HF is measured to be 2.4 +/- 0.3 D with Stark spectroscopy. The asymmetric C-H stretch of CH_3-HF was not investigated due to the limited range of their laser system, and this measurement was proposed for future research. The entrance channel complex F + CH_4 is also an important feature on the potential surface, which makes it a candidate for future experimental study as well.

The hydroxyl radical (OH) is an intermediate in both combustion chemistry and atmospheric chemistry. One of the most important reactions involves hydroxyl association with O_2, which leads to the production of HO_2 + $O(^3P)$. An intermediate for this reaction is *trans*-HOOO, which has been studied intensely.[35-50] The bond length has been determined to be 1.684 Å by microwave/millimeter spectroscopy,[50] and the bond energy is measured to be 3.0 kcal mol^{-1}.[45] The theoretical investigation of the HOOO reaction is somewhat less conclusive, due to the unusual long O-O bond length and the presumed multireference character.[48, 49] Helium nanodroplet spectroscopy provides an alternative route to study the OH + O_2 reaction, with a sequential pick-up scheme and continuous cooling during the association reaction. The method is capable of telling whether or not there is a kinetically significant reaction barrier in the entrance channel, which had been predicted by theory. The details of the investigation of OH radical and the OH + O_2 reaction in helium droplets are summarized in chapters 3, 4, 5, and 6.

1.2 Rovibrational Dynamics

In solid rare gas matrixes, the rovibrational motion of molecules is strongly perturbed. This matrix effect often leads to non-negligible discrepancies in the IR spectra of matrix trapped molecules when compared to those measured in the gas phase. The rotational degrees of freedom for molecules are hindered in the solid matrix, and vibrational bands lack rotational structure. Due to the change in the shape of the potential by the surrounding atoms, the vibrational transition is usually shifted in comparison to the gas phase. The magnitude of this shift depends on how strong the interaction is between the doped molecule and the matrix. The situation is different for solvated species in helium nanodroplets. As mentioned above, the IR spectra of SF_6 and OCS in helium nanodroplets are rotationally resolved.[2, 3]

The superfluid nature of helium nanodroplets is supported by the fact that the molecular symmetry of SF_6 and OCS is preserved in helium nanodroplets, as indicated by the high-resolution spectra. Although liquid helium is a poor solvent, the molecules are trapped inside the droplet because helium is still a better solvent than the vacuum. If the intermolecular potential well for helium and the molecule is deeper than that of two helium atoms, the molecule will remain inside the helium nanodroplet to minimize the total free energy of the whole system.[51, 52] This is true for all molecules, the exception being clusters composed of alkali atoms. The laser induced fluorescence (LIF) excitation and dispersed emission spectra of alkali atoms show small solvent shifts (about 10 cm^{-1})

when compared to those in the gas phase, which indicates that the alkali atoms reside on the surface of helium nanodroplets.[53-59] Despite the interior location of most dopants, the interaction between the rotational motion of molecules and the droplet surface excitations results in the rotational relaxation of solvated molecules and the evaporation of helium atoms, and the eventual establishment of thermodynamic equilibrium at about 0.37 K.[8]

The reduction of rotational constants for species in helium nanodroplets is commonly observed. For example, in both the SF_6 and OCS spectra, the rotational constants are reduced by a factor of about 3 when compared to their gas phase values.[2, 3] The change of rotational constants comes from the interaction between molecules and the surrounding helium density, and the effect exhibits certain trends.[60] In general, the reduction factor is about 3 for rotors with rotational constants less than ~1 cm^{-1}. However, for some lighter molecules, such as HF[4] and OH,[61] the rotational constants are close to their gas phase values. The explanation is that the helium density is not able to adiabatically follow the fast motion of light molecules.[3] Although theory[62] has sought to model the properties of molecular clusters solvated in helium nanodroplets, a quantitative theory for modeling the reduction of rotational constants is still not available. Nevertheless, progress is being made on methods that further our understanding of rotationally resolved spectra.

The vibrational motion of molecular dopants is at much higher energy than the rotational motion. For most systems, vibrational relaxation is much faster than the flight time of the helium droplet beam through the apparatus (~3 ms). When the molecule is vibrationally excited, it relaxes to the ground state and the energy is dissipated by the evaporation of helium atoms. It is usually estimated that 5 cm^{-1} is needed to take away one helium atom from the helium droplet.[63] The removal of helium atoms shrinks the cross section of the helium nanodroplet beam, which is critical for the application of electron-impact (EI) mass spectrometry as a detector for IR signal. One of the exceptional cases is the HF monomer, which has a longer vibrational relaxation time than the experimental flight time.[4] Nauta and Miller explained this as, that in order to relax the large vibrational energy of HF via the coupling with the 'bulk' helium excitations, a simultaneous excitation of several hundred phonons/rotons was needed, which was considered a slow process. The vibrational relaxation of polyatomic molecules like HCN[6, 7] happens via a cascading process that quenches the high frequency vibration in small energy steps through the lower energy vibrational modes. This explanation was proved with measurements of Ar-HF and Ne-HF.[64] When the van der Waals complex between a rare gas atom and the HF molecule is formed in helium droplets, two more vibrational modes are added to the system. In the Ar-HF study, a fast vibrational relaxation was observed, while the addition of the Ne atom to HF does not reduce the relaxation time enough to be smaller than the flight time. By switching from Ar atom to Ne atom, the coupling of vibrational modes is fine-tuned, which results in different vibrational relaxation efficiencies.

The vibrational relaxation dynamics of weakly bond complexes in helium nanodroplets has been an active field of research, although the details of this process are still not fully understood. Nauta and Miller found that the free C-H stretch band in HCN dimer contained narrow transitions dominated by inhomogeneous broadening, while the hydrogen bonded C-H stretch band was considerably broader and had an excited state lifetime of only 1/40 of the gas phase value.[12] In a series of IR-IR double resonance experiments on HF-HCN, acetylene-HCN, cyanoacetylene-HCN, and HF-N_2O weakly bond complexes by Douberly and co-workers, vibrational-predissociation-related broadening was observed.[29, 65, 66] It was further noticed that the helium nanodroplets served as a solvent cage that quenched the fragments, and introduced recombination of fragments back to various isomers on the potential energy surfaces. In a recent study of the Al + CO reaction, an (Al-CO)-CO van der Waals complex was tentatively assigned, where the second CO was weakly bound (see chapter 7).[67] In the simulation of the spectrum, a line width of 10 GHz was necessary for a satisfactory fit. This indicates the existence of a fast vibrational relaxation channel. It has been speculated that the isomerization to the strongly bond Al-$(CO)_2$ species following the photoinduced predissociation of (Al-CO)-CO is responsible for such broadening. An IR-IR double resonance experiment will be employed in future work to test this hypothesis.

1.3 *Ab Initio* Methods for Floppy Molecular Clusters

The properties of an equilibrium structure computed with modern *ab initio* methods often provide a good approximation to those measured experimentally. However, this picture fails frequently for floppy molecular clusters, simply because some of the molecules studied are not even approximately static at their equilibrium structures when a measurement is taken. Vibrational averaging is necessary for a better theoretical prediction of molecular properties, especially for molecular clusters with large amplitude vibrational motions. Weakly bound molecular clusters have floppy vibrational modes that are often highly anharmonic and strongly coupled to other vibrational modes. As a result, the harmonic approximation is not capable of predicting properties of these species accurately. An investigation of the full potential energy surface provides the correct solution to this problem. However, this is usually not computationally feasible, given that the number of vibrational modes scales rapidly as the number of atoms increases. On the other hand, not all vibrational modes are large amplitude motions. Therefore one can still achieve good agreement with experiment when restricting the consideration to the modes that have the strongest impact on the vibrationally averaged molecular properties.

Although the dimension is reduced, solving the vibrational Schrödinger equation can still be challenging. Choosing an appropriate coordinate system plays an important role in simplifying the multidimensional vibrational problem. The classical FG method uses normal mode coordinates and develops the vibrational Hamiltonian in a form of harmonic oscillators, while the anharmonic terms are truncated in the serial expansion of the potential operator. The recovery of the anharmonicity for the system is done by including higher order potential terms, which then add to the off diagonal terms in the Hamiltonian matrix. This approach can be used to address molecular systems with small anharmonicity, when cubic and even quartic force constants are included. However, for highly anharmonic systems, it is necessary to include even higher order terms, and the computational cost increases significantly. The common way to get around this problem is to write the Hamiltonian in a set of internal coordinates. The potential energy operator is greatly simplified by this approach, with the cost of increasing the complexity of the kinetic energy operator. Fortunately, Frederick and Woywod successfully derived the full table for the kinetic energy operator in internal bond-angle coordinates.[68] Using their table, the construction of a vibrational Hamiltonian in bond-angle coordinates becomes trivial.

Once the Hamiltonian is established, two main difficulties are computing the matrix elements and diagonalizing a sizable matrix. The discrete variable representation (DVR) method by Colbert and Miller is designed to handle both challenges.[69] Like other DVR methods, the potential energy terms and those that arise from any other local operators are diagonal in the matrix. At the same time, the kinetic energy terms are extremely simple. The DVR-generated Hamiltonian matrix is very sparse, which makes it easy to diagonalize. The spacing of grid points is also flexible, and both evenly spaced and non-evenly spaced grids can be used. For the one dimensional vibrational problem, Colbert and Miller provided the analytical form for the matrix elements when the wave function was expanded in a sinc-DVR basis. The multidimensional version of DVR was also shown to be straightforward. This approach has been applied to the two-dimensional vibrational averaging problem for *trans*-HOOO, which is the subject of chapter 5.

References

[1] Goyal, S., Schutt, D. L., and Scoles, G., *Phys. Rev. Lett.* **69**, 933-936 (1992).

[2] Frochtenicht, R., Toennies, J. P., and Vilesov, A., *Chem. Phys. Lett.* **229**, 1-7 (1994).

[3] Grebenev, S., Toennies, J. P., and Vilesov, A. F., *Science* **279**, 2083-2086 (1998).

[4] Nauta, K., and Miller, R. E., *J. Chem. Phys.* **113**, 9466-9469 (2000).

[5] Nauta, K., and Miller, R. E., *J. Chem. Phys.* **115**, 10254-10260 (2001).

[6] Nauta, K., and Miller, R. E., *Phys. Rev. Lett.* **82**, 4480-4483 (1999).

[7] Callegari, C., Conjusteau, A., Reinhard, I., Lehmann, K. K., and Scoles, G., *J. Chem. Phys.* **113**, 10535-10550 (2000).

[8] Callegari, C., Reinhard, I., Lehmann, K. K., Scoles, G., Nauta, K., and Miller, R. E., *J. Chem. Phys.* **113**, 4636-4646 (2000).

[9] Merritt, J. M., Douberly, G. E., and Miller, R. E., *J. Chem. Phys.* **121**, 1309-1316 (2004).

[10] Nauta, K., and Miller, R. E., *J. Chem. Phys.* **115**, 8384-8392 (2001).

[11] Lindsay, C. M., and Miller, R. E., *J. Chem. Phys.* **122** (2005).

[12] Nauta, K., and Miller, R. E., *J. Chem. Phys.* **111**, 3426-3433 (1999).

[13] Douberly, G. E., and Miller, R. E., *J. Chem. Phys.* **122** (2005).

[14] Nauta, K., and Miller, R. E., *Science* **283**, 1895-1897 (1999).

[15] Nauta, K., and Miller, R. E., *Science* **287**, 293-295 (2000).

[16] Davis, S., Farnik, M., Uy, D., and Nesbitt, D. J., *Chem. Phys. Lett.* **344**, 23-30 (2001).

[17] Chang, B. C., Costen, M. L., Marr, A. J., Ritchie, G., Hall, G. E., and Sears, T. J., *J. Mol. Spectrosc.* **202**, 131-143 (2000).

[18] Cameron, M. R., and Kable, S. H., *Rev. Sci. Instrum.* **67**, 283-287 (1996).

[19] Kohn, D. W., Clauberg, H., and Chen, P., *Rev. Sci. Instrum.* **63**, 4003-4005 (1992).

[20] Morter, C. L., Domingo, C., Farhat, S. K., Cartwright, E., Glass, G. P., and Curl, R. F., *Chem. Phys. Lett.* **195**, 316-321 (1992).

[21] Kobayashi, K., and Sears, T. J., *Can. J. Phys.* **79**, 347-358 (2001).

[22] Lester, M. I., Pond, B. V., Marshall, M. D., Anderson, D. T., Harding, L. B., and Wagner, A. F., *Faraday Discuss.* **118**, 373-385 (2001).

[23] Liu, K., Kolessov, A., Partin, J. W., Bezel, I., and Wittig, C., *Chem. Phys. Lett.* **299**, 374-380 (1999).

[24] Heaven, M. C., *Annu. Rev. Phys. Chem.* **43**, 283-310 (1992).

[25] Engdahl, A., Karlstrom, G., and Nelander, B., *J. Chem. Phys.* **118**, 7797-7802 (2003).

[26] Smith, A. M., Agreiter, J., Hartle, M., Engel, C., and Bondybey, V. E., *Chem. Phys.* **189**, 315-334 (1994).

[27] Hunt, R. D., and Andrews, L., *J. Chem. Phys.* **88**, 3599-3606 (1988).

[28] Callegari, C., Lehmann, K. K., Schmied, R., and Scoles, G., *J. Chem. Phys.* **115**, 10090-10110 (2001).

[29] Douberly, G. E., Merritt, J. M., and Miller, R. E., *Phys. Chem. Chem. Phys.* **7**, 463-468 (2005).

[30] Merritt, J. M., Douberly, G. E., Stiles, P. L., and Miller, R. E., *J. Phys. Chem. A* **111**, 12304-12316 (2007).

[31] Lanzisera, D. V., and Andrews, L., *J. Phys. Chem. A* **101**, 9660-9665 (1997).

[32] Harper, W. W., Nizkorodov, S. A., and Nesbitt, D. J., *J. Chem. Phys.* **113**, 3670-3680 (2000).

[33] Bowman, J. M., *Advances in Molecular Vibrations and Collision Dynamics: Quantum Reactive Scattering* (JA1 Press, Greenwich, CT, 1994).

[34] Merritt, J. M., Rudic, S., and Miller, R. E., *J. Chem. Phys.* **124** (2006).

[35] Suma, K., Sumiyoshi, Y., and Endo, Y., *Science* **308**, 1885-1886 (2005).

[36] Derro, E. L., Murray, C., Sechler, T. D., and Lester, M. I., *J. Phys. Chem. A* **111**, 11592-11601 (2007).

[37] Mansergas, A., Anglada, J. M., Olivella, S., Ruiz-Lopez, M. F., and Martins-Costa, M., *Phys. Chem. Chem. Phys.* **9**, 5865-5873 (2007).

[38] Murray, C., Derro, E. L., Sechler, T. D., and Lester, M. I., *J. Phys. Chem. A* **111**, 4727-4730 (2007).

[39] Braams, B. J., and Yu, H. G., *Phys. Chem. Chem. Phys.* **10**, 3150-3155 (2008).

[40] Derro, E. L., Sechler, T. D., Murray, C., and Lester, M. I., *J. Chem. Phys.* **128**, 244313 (2008).

[41] Varner, M. E., Harding, M. E., Gauss, J., and Stanton, J. F., *Chem. Phys.* **346**, 53-55 (2008).

[42] Murray, C., Derro, E. L., Sechler, T. D., and Lester, M. I., *Acc. Chem. Res.* **42**, 419-427 (2009).

[43] Varner, M. E., Harding, M. E., Vazquez, J., Gauss, J., and Stanton, J. F., *J. Phys. Chem. A* **113**, 11238-11241 (2009).

[44] Anglada, J. M., Olivella, S., and Sole, A., *J. Chem. Theory Comput.* **6**, 2743-2750 (2010).

[45] Le Picard, S. D., Tizniti, M., Canosa, A., Sims, I. R., and Smith, I. W. M., *Science* **328**, 1258-1262 (2010).

[46] Tizniti, M., Le Picard, S. D., Canosa, A., Sims, I. R., and Smith, I. W. M., *Phys. Chem. Chem. Phys.* **12**, 12702-12710 (2010).

[47] Beames, J. M., Lester, M. I., Murray, C., Varner, M. E., and Stanton, J. F., *J. Chem. Phys.* **134**, 044304 (2011).

[48] Varandas, A. J. C., *Phys. Chem. Chem. Phys.* **13**, 15619-15623 (2011).

[49] Varandas, A. J. C., *Phys. Chem. Chem. Phys.* **13**, 9796-9811 (2011).

[50] McCarthy, M. C., Lattanzi, V., Kokkin, D., Martinez, O., and Stanton, J. F., *J. Chem. Phys.* **136**, 034303 (2012).

[51] Lehmann, K. K., and Northby, J. A., *Mol. Phys.* **97**, 639-644 (1999).

[52] Lehmann, K. K., *Mol. Phys.* **97**, 645-666 (1999).

[53] Reho, J., Higgins, J., Callegari, C., Lehmann, K. K., and Scoles, G., *J. Chem. Phys.* **113**, 9686-9693 (2000).

[54] Stienkemeier, F., Higgins, J., Ernst, W. E., and Scoles, G., *Z. Phys. B: Condens. Matter* **98**, 413-416 (1995).

[55] Stienkemeier, F., Higgins, J., Ernst, W. E., and Scoles, G., *Phys. Rev. Lett.* **74**, 3592-3595 (1995).

[56] Stienkemeier, F., Higgins, J., Callegari, C., Kanorsky, S. I., ERnst, W. E., and Scoles, G., *Z. Phys. D: At., Mol. Clusters* **38**, 253-263 (1996).

[57] Reho, J., Callegari, C., Higgins, J., Ernst, W. E., Lehmann, K. K., and Scoles, G., *Faraday Discuss.* **108**, 161-174 (1997).

[58] Stienkemeier, F., Bunermann, O., Mayol, R., Ancilotto, F., Barranco, M., and Pi, M., *Phys. Rev. B* **70**, 214509 (2004).

[59] Bunermann, O., Mudrich, M., Weidemuller, M., and Stienkemeier, F., *J. Chem. Phys.* **121**, 8880-8886 (2004).

[60] Douberly, G. E., Ph.D. dissertation, University of North Carolina, Chapel Hill, NC, 2006.

[61] Raston, P. L., Liang, T., and Douberly, G. E., *J. Phys. Chem. A* **117**, 8103-8110 (2013).

[62] Ing, C., Hinsen, K., Yang, J., Zeng, T., Li, H., and Roy, P. N., *J. Chem. Phys.* **136** (2012).

[63] Brink, D. M., and Stringari, S., *Z. Phys. D: At., Mol. Clusters* **15**, 257-263 (1990).

[64] Nauta, K., and Miller, R. E., *J. Chem. Phys.* **115**, 4508-4514 (2001).

[65] Douberly, G. E., Merritt, J. M., and Miller, R. E., *J. Phys. Chem. A* **111**, 7282-7291 (2007).

[66] Douberly, G. E., and Miller, R. E., *Chem. Phys.* **361**, 118-124 (2009).

[67] Liang, T., Flynn, S. D., Morrison, A. M., and Douberly, G. E., *J. Phys. Chem. A* **115**, 7437-7447 (2011).

[68] Frederick, J. H., and Woywod, C., *J. Chem. Phys.* **111**, 7255-7271 (1999).

[69] Colbert, D. T., and Miller, W. H., *J. Chem. Phys.* **96**, 1982-1991 (1992).

Chapter 2

Experimental Methods

The Helium Nanodroplet Isolation Spectroscopy (HENDI) experimental apparatus was built in our group.[1] This chapter summarizes the production mechanism of helium nanodroplets, the doping process, infrared action spectroscopy of helium solvated species, and the Stark spectroscopy method. The laser enters the instrument via the CaF window from the right side of the mass spectrometry chamber or via the side window on the Stark cell chamber, which results in the counterpropagating configuration or the multipass configuration, respectively.

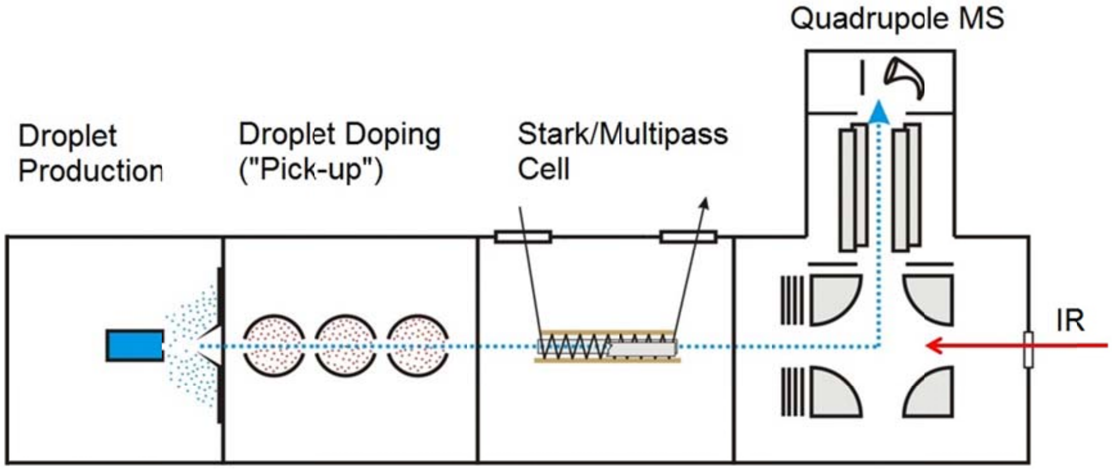

Figure 2.1: The schematic picture of Helium Nanodroplet Isolation Spectroscopy (HENDI) experimental apparatus.

2.1 Production Mechanism of Helium Nanodroplets

Helium nanodroplets were observed for the first time in 1961, when helium gas was expanded through a 4.2 K, 150 micron diameter nozzle.[2, 3] The helium nanodroplets are formed by homogeneous nucleation of helium atoms.[4] In our laboratory, ultra-pure helium gas (99.9995%) is expanded through a 5 μm diameter pinhole nozzle with a backing pressure ranging from 20 to 50 bar, depending on the specific application. The cold head temperature is set to between 13 K and 21 K. The average number of helium atoms per nanodroplet increases when the nozzle temperature is reduced. The higher backing pressure also results in larger helium nanodroplets. The statistics for the size dis-tribution of helium nanodroplets have been studied,[5] which can be described empirically by a log-normal distribution whose mean is determined:

$$P_N(N) = \left(N\sigma\sqrt{2\pi}\right)^{-1} \exp\left[-\frac{(ln\,N - \mu)^2}{2\sigma^2}\right] \qquad (2.1)$$

$$\mu = ln(\bar{N}) - \frac{1}{2} ln\left[\left(\frac{S}{\bar{N}}\right)^2 + 1\right] \qquad (2.2)$$

$$\sigma = \left\{ln\left[\left(\frac{S}{\bar{N}}\right)^2 + 1\right]\right\}^{1/2} \qquad (2.3)$$

Here N is the number of helium atoms in a droplet. μ and σ are the mean and standard deviation of the distribution of $\ln N$. $\bar{N}$ is the mean droplet size, and the associated empirical scaling law is:

$$ln(\bar{N}) = 2.44 + 2.55\,ln(\Gamma) \qquad (2.4)$$

The dimensionless scaling parameter, Γ, is a function of the gas pressure, nozzle temperature, and nozzle diameter. S is the standard deviation of the size distribution which was found to be approximately $0.65\overline{N}$. Fig. 2.2 shows several log-normal size distributions assuming a 50 bar source backing pressure.

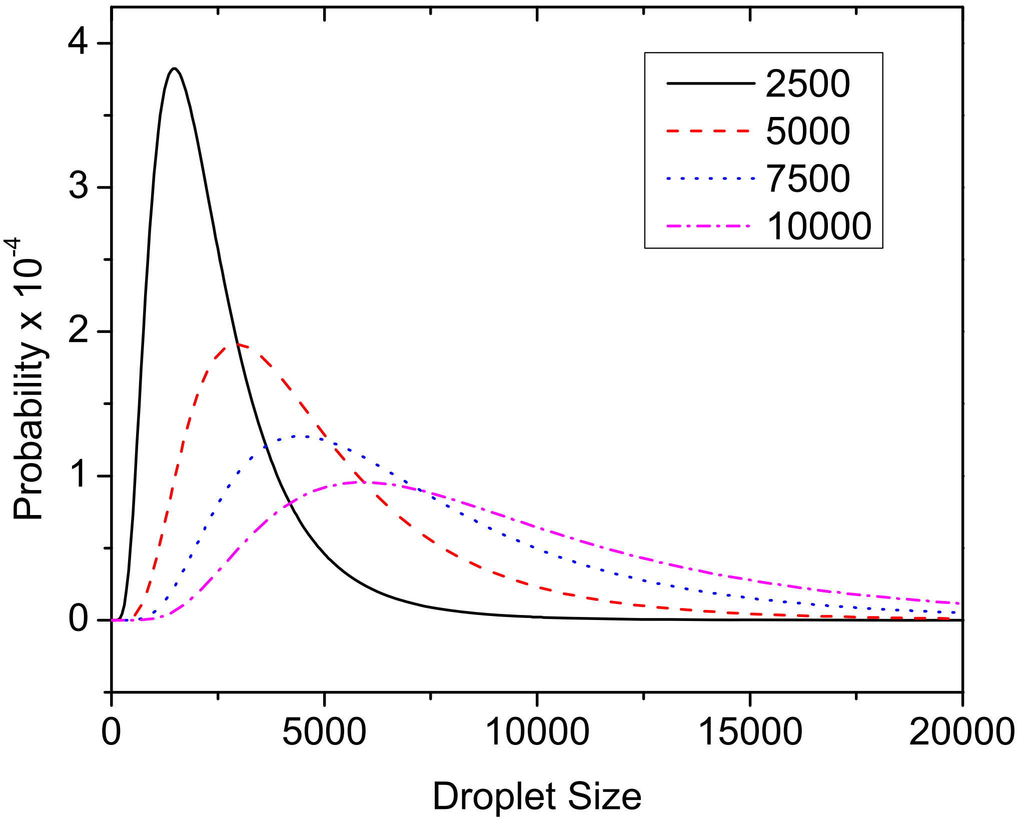

Figure 2.2: Log-normal droplet size distributions for $\overline{N}$ equals 2500, 5000, 7500, and 10000 helium atoms.

After the helium nanodroplets are formed, the beam is skimmed, then travels sequentially through the pick-up chamber and the multipass Stark cell chamber before it finally enters into the electron impact ionization quadrupole mass spectrometer.

2.2 Doping Process

As mentioned above, liquid helium is a poor solvent, but it is still better than the vacuum. This principle allows one to dope the molecules of interest into helium nano-droplets for spectroscopic study.

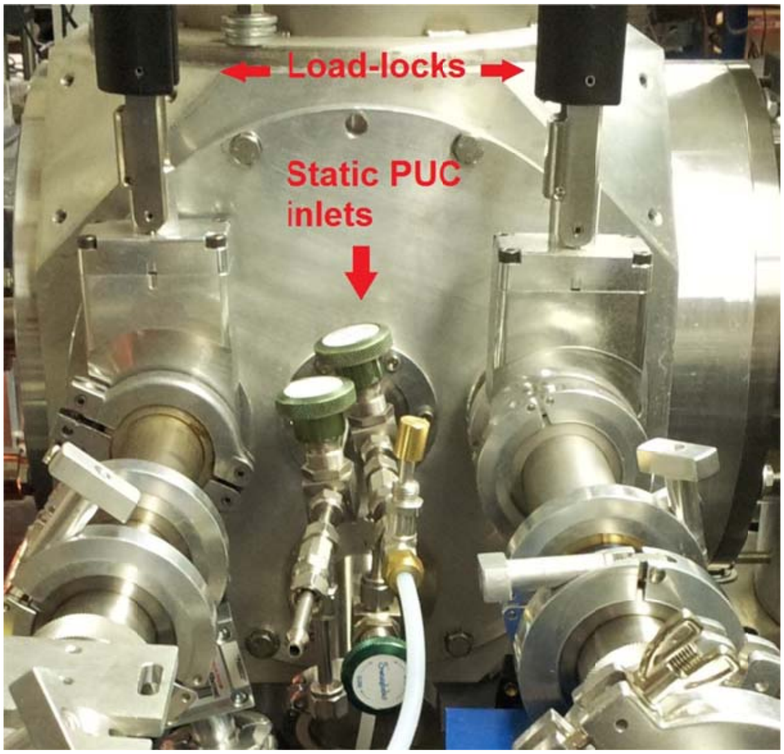

Figure 2.3: The external view of the pick-up chamber.

The pick-up process happens in the pick-up chamber region, where two types of sources are applied, as it is shown in Fig. 2.3. A static pick-up cell is located at the center of the pick-up chamber. Load locks are situated on both sides of the static cell, which allows for the introduction of species produced via pyrolysis or sublimation before or after picking up the gas molecules in the static pick-up cell. The static pick-up cell is basically a differentially pumped tube that allows for the isolation of a local density of external gas controlled by a fine metering needle valve. The helium nanodroplets pass through holes on the wall of the differentially pumped tube. There is also trace amount of gas in the chamber region outside the tube, and the pick-up process can potentially lead to the capture of contaminants, but the vast majority of dopants enter helium nanodroplets via the pick-up cell tube. The other type of design is the load lockable source. This design is mainly for the experiments that require a pyrolysis source for the generation of radicals or a high temperature oven for the vaporization of metal atoms. With the load lock, these sources can be inserted and removed without breaking the pick-up chamber vacuum, which makes it extremely convenient when external diagnosis and repair of a source is necessary.

The energetics associated with the pick-up process have been summarized.[1] The kinetic energy, internal energy and solvation energy of dopants are quickly removed by the quantum evaporation of helium atoms from the surface. As a result, the molecules are quenched into the lowest energy quantum states, which reduces significantly the number of transitions observed in a rovibrational band. The energy removed by helium evaporation is quantified as 5 cm^{-1} per helium atom, [6] and He-solvated systems have been found to be stabilized at about 0.4 K.[7, 8] The doping of multiple molecules is possible under higher pressure conditions. Upon the pick-up of the secondary species, the two fragments quickly find each other and form a van der Waals complex, or possibly a strongly bonded molecule if the reaction is barrierless. The condensation and/or bond energy associated with this process is dissipated by the helium nanodroplets via helium atom evaporation. From the statistical point of view, the pick-up events are independent, and can be described by a Poisson distribution:[9]

$$P(k,N) = \frac{\left(\beta N^{2/3}\right)^k}{k!} \exp\left(-\beta N^{2/3}\right) \qquad (2.5)$$

Here, $\beta N^{2/3}$ is dimensionless, where $\beta = 15.5\eta L$. L is the length of the pick-up region, and η is the gas density. A typical pressure dependence curve measured for the OH + $(O_2)_n$ spectra is shown in Fig. 2.4, where the Poisson statistics apply.

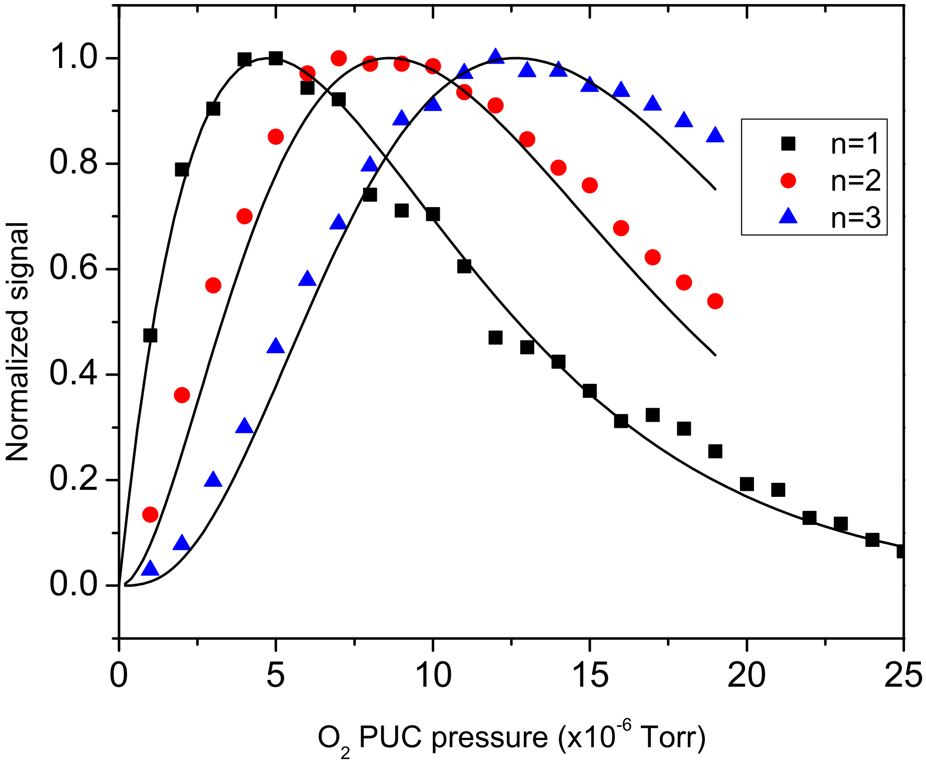

Figure 2.4: Pick-up cell pressure dependence of the OH + $(O_2)_n$ bands. Solid lines are fitted curves based on equation 2.5.

Based on these statistics, the signal dependence as a function of gas pressure can be used to investigate the number of molecules that contribute to the signal. An example of the pressure dependence application can be found in Chapter 6, where HO_3-$(O_2)_n$

clusters are studied.[10] Based on the Poisson statistics, the numbers of O_2 molecules associated with the measured bands are unambiguously assigned.

2.3 Infrared Action Spectroscopy of Helium Solvated Species

The helium droplet is transparent to photons below ~24 eV, and infrared light can therefore pass through the pure helium nanodroplet beam freely. When the helium nanodroplet is doped, the rovibrational motion of the dopant can be excited by the infrared photon. Therefore, IR laser spectroscopy can be used to study the rovibrational motion of helium solvated species, or as an indirect probe of the properties of helium nanodroplets.

Although molecules can be doped into helium nanodroplets, the density of dopants is low. Therefore, direct adsorption methods are not applicable for recording the IR spectrum of helium nanodroplet isolated species. There are two alternative detection schemes. One involves the use of an extremely sensitive thermal detector – a bolometer. The bolometer detects the change in beam flux by measuring the change in the temperature of the bolometer, which is converted to a voltage signal. The other effective detector is a mass spectrometer. The ion signal is reduced when the beam is depleted. Both methods rely on the fact that the relaxation of vibrationally excited molecules lead to the evaporation of helium atoms, which results in the reduction of the cross section of helium nanodroplet beam. In most cases, the relaxation is faster than the flight time of the droplet through the apparatus, although exceptions exist.[11] Both detection schemes have their own advantages. The bolometer is usually more sensitive, and higher signal to noise ratios can be achieved. The mass spectrometer is capable of performing mass-specific measurements, and the spectra can be free of contamination from species that do not contribute a depletion signal in the measured mass channel. In our laboratory, the laser is chopped, and a lock-in amplifier is used to record and average the difference in signal with and without the laser as a function of the laser frequency. Also, the mass spectrometer is the preferred detection method. The mass spectra of the helium droplet beam before/after $^{13}CH_3F$ is doped are shown in Fig. 2.5 as an example. When a high energy (70 eV) electron impacts the helium nanodroplets, a He^+ ion is produced, fragmenting the droplets.[12, 13] For the neat beam, for which the droplet is dopant-free, the positive charge ends up as a He_n^+ cluster, which shows up in m/z=4n mass channels. When there is a dopant inside the helium droplet, the positive charge rapidly finds the dopant and then ionizes it, due to the fact that all molecules have a smaller ionization potential than helium. In the top spectrum of Fig. 2.5, the $^{13}CH_3F$ doped helium droplets are ionized, and $^{13}CH_3F$ fragments into $^{13}CH_3^+$ and CH_2F^+ ions.

There are two detection modes when the mass spectrometer is used as a detector. The first mode is referred to as the "rf-only" mode, in which all masses larger than 6 amu are allowed into the detector. The other mode is the mass-specific mode, which only passes a specific mass to charge channel into the detector. The "rf-only" mode is preferred when the ionization of the dopant leads to fragments spread into many ion channels, and therefore collecting all ion signals helps to increase the signal to noise ratio. For example, in the Al-$(CO)_n$ study, Al has a progression of Al^+-$(He)_n$ ion signals, as shown in Fig. 7.5, and the "rf-only" mode is used. The mass-specific mode is useful when the droplets are contaminated by some other molecules. In the study that involves OH, hydroxyl radical is produced by thermal decomposition of *tert*-butyl hydroperoxide

(TBHP), which also generates a methyl radical and an acetone molecule. A clean OH spectrum can be obtained by collecting the laser-induced depletion signal on mass channel 17, which is mainly from OH radical and free of the other species produced via pyrolysis.

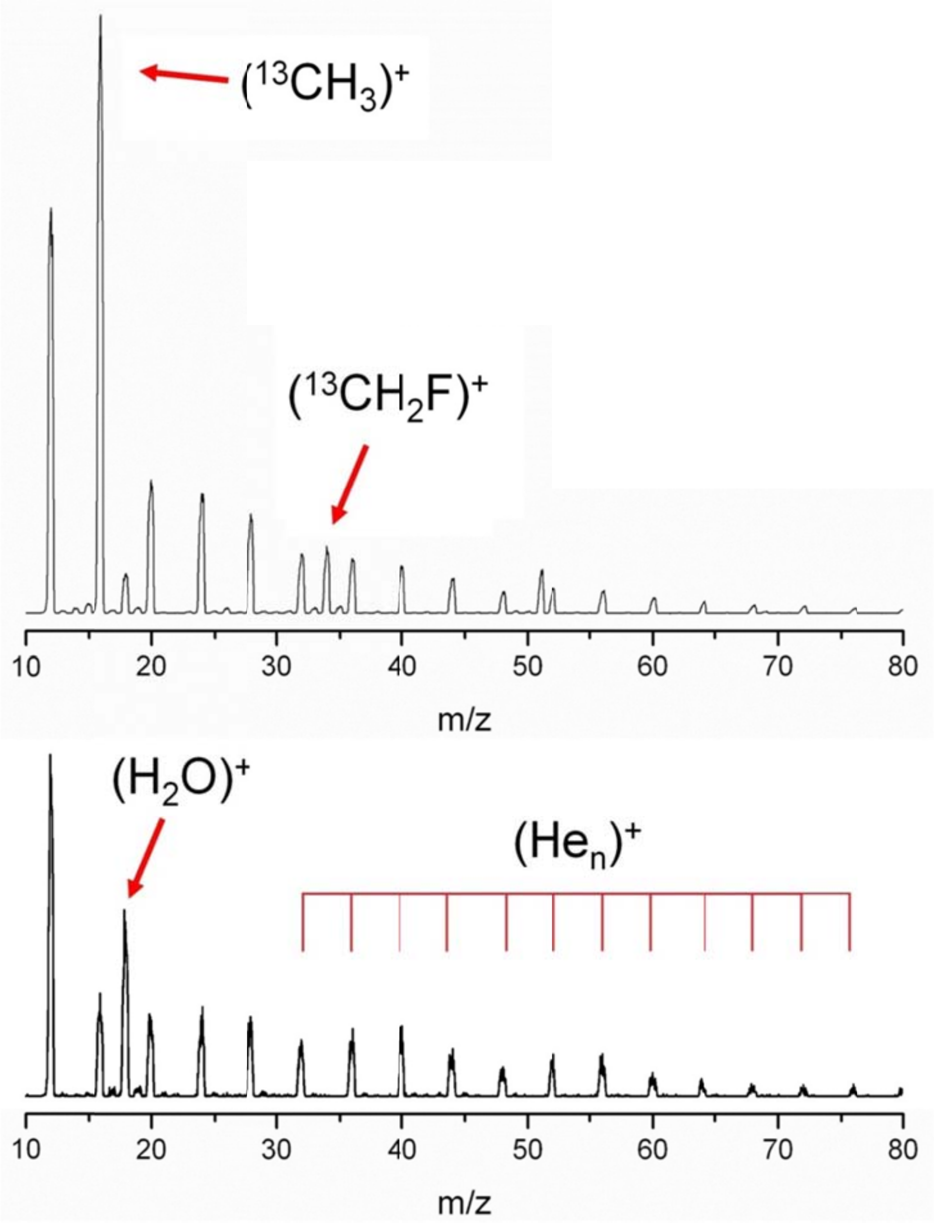

Figure 2.5: Mass spectra of both neat helium droplet beam (bottom) and helium droplet beam with $^{13}CH_3F$ (top).

2.4 Stark Spectroscopy

Between the pick-up chamber and the mass spectrometer chamber, there is a chamber that contains a multipass Stark cell for Stark spectroscopy measurements. The multipass Stark cell is basically two parallel electrodes and two parallel mirrors, as shown in Fig. 2.6. The laser beam is allowed to enter the cell region at a small angle, and intersect the helium droplet beam multiple times (50-100 times can be achieved with good mirror alignment). The signal level is reduced due to less overlap with the helium nanodroplet beam, and only about 1/4 of the signal from the counterpropagating configuration can be recovered. The two polished stainless steel electrodes generate a homogeneous electric field, which is perpendicular to the laser multipass plane. When a molecule having a static electric dipole moment enters the Stark cell, the molecule is aligned along the electric field direction. The laser polarization is set to be either parallel or perpendicular to the electric field direction, which leads to different selection rules ($\Delta M=0$ and $\Delta M=\pm1$, respectively) for the rovibrational transitions of the dopant. From the Stark spectra, the dipole moment can be obtained by spectral fitting incorporating the Stark matrix elements for a semi-rigid rotor in an electric field.

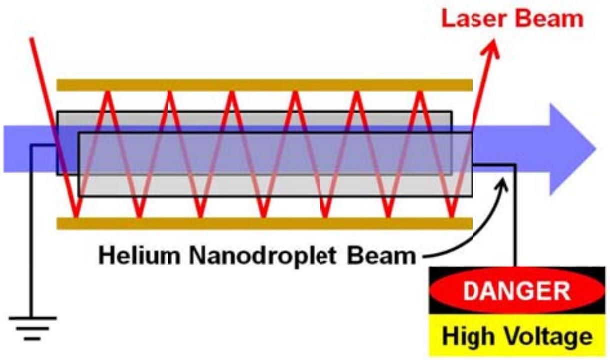

Figure 2.6: The schematic picture of the Stark cell.

References

[1] Douberly, G. E., Ph.D. dissertation, University of North Carolina, Chapel Hill, 2006.

[2] Becker, E. W., Klingelhofer, R., and Lohse, P., *Z. Naturforsch. A Phys. Sci.* **16**, 1259-1259 (1961).

[3] Becker, E. W., *Z. Phys. D: At., Mol. Clusters* **3**, 101-107 (1986).

[4] Northby, J. A., *J. Chem. Phys.* **115**, 10065-10077 (2001).

[5] Knuth, E. L., Schilling, B., and Toennies, J. P., *Proceedings of the 19th International Symposium on Rarefied Gas Dynamics* (Oxford University Press, 1995), pp. 270-276.

[6] Brink, D. M., and Stringari, S., *Z. Phys. D: At., Mol. Clusters* **15**, 257-263 (1990).

[7] Frochtenicht, R., Toennies, J. P., and Vilesov, A., *Chem. Phys. Lett.* **229**, 1-7 (1994).

[8] Grebenev, S., Toennies, J. P., and Vilesov, A. F., *Science* **279**, 2083-2086 (1998).

[9] Choi, M. Y., Douberly, G. E., Falconer, T. M., Lewis, W. K., Lindsay, C. M., Merritt, J. M., Stiles, P. L., and Miller, R. E., *Int. Rev. Phys. Chem.* **25**, 15-75 (2006).

[10] Liang, T., Raston, P. L., and Douberly, G. E., *ChemPhysChem* **14**, 764-770 (2013).

[11] Nauta, K., and Miller, R. E., *J. Chem. Phys.* **113**, 9466-9469 (2000).

[12] Buchenau, H., Toennies, J. P., and Northby, J. A., *J. Chem. Phys.* **95**, 8134-8148 (1991).

[13] Callicoatt, B. E., Mar, D. D., Apkarian, V. A., and Janda, K. C., *J. Chem. Phys.* **105**, 7872-7875 (1996).

Chapter 3

Anomalous Λ-doubling in the Infrared Spectrum of the Hydroxyl Radical in Helium Nanodroplets

The $X^2\Pi_{3/2}$ hydroxyl (OH) radical has been isolated in superfluid ^{4}He nanodroplets and probed with infrared laser depletion spectroscopy. From an analysis of the Stark spectrum of the $Q(3/2)$ transition, the Λ-doublet splittings are determined to be 0.198(3) cm^{-1} and 0.369(2) cm^{-1} in the ground and first excited vibrational states, respectively. These splittings are 3.6 and 7.2 times larger than their respective gas phase values. A factor of 1.6 increase in the $Q(1/2)$ Λ-doublet splitting was previously reported for the helium solvated $X^2\Pi_{1/2}$ NO radical [K. von Haeften, A. Metzelthin, S. Rudolph, V. Staemmler, and M. Havenith, Phys. Rev. Lett. 95, 215301 (2005)]. A simple model is presented that predicts the observed Λ-doublet splittings in helium solvated OH and NO. The model assumes a small parity dependence of the rotor's effective moment of inertia and predicts a factor of 3.6 increase in the OH ground state (J=3/2) Λ-doubling when the B_0^e and B_0^f rotational constants differ by less than one percent.

3.1 Introduction

Helium nanodroplet isolation (HENDI) spectroscopy is becoming a widely adopted technique for the characterization of novel cluster systems.[1-4] When comparisons to gas phase spectra are available, vibrational bands measured with HENDI are shown to have relatively small solvent frequency shifts. The HENDI spectra of previously unobserved species can therefore be directly compared to the predictions of *ab initio* quantum chemistry. Furthermore, vibrational bands in the droplet spectra are often rotationally resolved, and in most cases, the molecular symmetry group of the isolated species is preserved upon helium solvation. Although the helium solvent adds to the rotor's effective moment of inertia, methods now exist that can quantitatively account for the effect of the helium on the rotational constants of the solvated system.[5-12] One interesting helium solvent effect that has yet to be quantitatively accounted for is the increased Λ-doublet splitting observed in the IR spectrum of the $X^2\Pi_{1/2}$ NO radical.[13] We present here an IR laser Stark spectroscopy study of the helium solvated $X^2\Pi_{3/2}$ hydroxyl radical (OH), another open-shell diatomic molecule in which a large increase in Λ-doubling is observed. We present a quantitative single parameter model that predicts the effect of the helium solvent on the Λ-doubling in these diatomic radicals.

In a previous report of the IR spectrum of NO in helium droplets, the Λ-doublet splitting of the $Q(1/2)$ transition was shown to be increased by a factor of 1.55 relative to the gas phase value.[13] This reported 55% change from the gas phase value is indicative of the average increase of the Λ-doublet splitting of the J=1/2 rotational level in the ground and excited vibrational levels, given that the splitting in the $Q(1/2)$ transition corresponds to the sum of the Λ-doubling in v=0 and v=1. The Λ-doubling of the $X^2\Pi_{1/2}$

NO rotational levels originates from $^2\Pi\sim^2\Sigma$ interactions and is approximately equal to the spectroscopic fitting parameter p in the ground J=1/2 level.[14] An expression for p has been derived from perturbation theory,[15] and it is proportional to a $\langle\Sigma|BL_y|\Pi\rangle$ matrix element, which is representative of an L-uncoupling effect that becomes larger with increasing rotational constant and rotational quantum number.[14] Havenith and coworkers suggested an explanation of the effect of the helium droplet on the Λ-doublet splitting in terms of a "confinement of the electronically excited NO states by the surrounding He," and suggested this confinement would increase the magnitude of the above matrix element, although there was no attempt to quantitatively model the observed splitting.[13] The authors noted another possible explanation and suggested that "density fluctuations" in the helium droplet could perturb the rotational symmetry about the NO axis and lead to a further parity splitting of the $X^2\Pi_{1/2}$ ground state. For an isolated $^2\Pi_{1/2}$ diatomic molecule in the J=1/2 rotational level, it is well known that the electron density about the internuclear axis is cylindrically symmetric.[16] There has been no attempt, however, to test whether or not the NO-(He)$_n$ interaction is sufficiently strong to induce an anisotropy in the helium density about the NO axis and a slight alignment of the singly occupied $p\pi$ orbital.

In the present report, we revisit the issue of the effect of the helium droplet on the Λ-doublet splittings in open-shell diatomic molecules. We present a detailed analysis of the Stark spectroscopy of the fundamental vibrational band of the helium solvated hydroxyl radical (OH). This measurement results in accurate values for the J=3/2 Λ-doublet splittings in both the ground and excited vibrational levels. We find that the Λ-doubling of rotational levels in OH is affected to an even larger degree by the droplet than was observed for NO. The singly occupied $p\pi$ orbital of the isolated $X^2\Pi_{3/2}$ OH radical is already partially aligned in the ground state (J=3/2),[16] and we therefore expect some anisotropy in the helium density with respect to the A' and A'' planes of the solvated species. Here the symmetry plane is defined as the plane of the partially localized, singly occupied $p\pi$ orbital. We present a simple model based on a realistic parity dependence of the rotor's effective moment of inertia. The model predicts the observed Λ-doublet splittings in both OH and NO when we assume an approximately 1% difference in the B constant for rotation either in or perpendicular to the plane of the singly occupied $p\pi$ orbital.

3.2 Experimental Methods

Helium droplets are formed by expanding ultra-pure helium gas through a cryogenically cooled 5 μm diameter nozzle into vacuum.[2] The backing pressure and nozzle temperature are 30 bar and 18 K, respectively. Under these conditions, droplets are produced that have an average size of ~2900 atoms (±800 assuming a ±1 μm uncertainty in the nozzle diameter).[17, 18] As the droplets leave the high pressure region of the expansion, they cool by evaporation to 0.38 K.[19] The expansion is skimmed to produce the droplet beam, which passes through a pick-up chamber containing a pyrolysis source for OH radicals. The pyrolysis source has been described elsewhere.[20] The hydroxyl radical is produced from the pyrolysis of *tert*-butyl hydroperoxide,[21] ($(CH_3)_3COOH \rightarrow (CH_3)_3CO + OH \rightarrow (CH_3)_2CO + CH_3 + OH$). The products of this pyrolytic decomposition are picked-up by the helium droplet beam with a maximum single OH doping efficiency of ~12%. The translational and internal OH degrees of freedom are cooled to the droplet temperature on a timescale that is fast in comparison to the measurement timescale. Because of this rapid cooling, only spectroscopic transitions from the ground state ($^2\Pi_{3/2}$, J=3/2) are expected for helium solvated OH.

The doped droplets traverse a multipass/Stark cell prior to entering a quadrupole mass spectrometer where they are ionized by electron impact. The idler output from an optical parametric oscillator (OPO) system (Lockheed-Martin Aculight) is either directed into the multipass cell (for *Q* branch measurements) or down the axis of the droplet beam (for *R* branch measurements). The tuning and calibration of the OPO is given elsewhere.[22] The OPO beam is amplitude modulated at 77 Hz, and the ion signal in mass channel m/z=17 u is demodulated with a lock-in amplifier as the idler wave is tuned through the transitions of OH. Following OH vibrational excitation and subsequent energy transfer to the droplet, a decrease in the droplet size leads to a reduction in the electron impact ionization cross section for OH doped droplets and a depletion of the m/z=17 u ion signal. The ion difference signal is plotted vertically against the idler wavenumber to give the spectra. We note here that the vibrational relaxation timescale for OH may be long in comparison to the droplet flight time through the apparatus, as was observed for HF.[23] It is therefore likely that the depletion signal derives from droplets containing vibrationally excited OH radicals that go on to pick-up an impurity molecule that subsequently interacts with and relaxes the excited OH dopant. A downstream complexation event such as this results in the complete relaxation of the laser-induced OH vibrational energy prior to droplet ionization. The Stark cell consists of two polished stainless steel plates (separated by 3.10±0.03 mm) that are oriented perpendicular to two rectangular, 15 cm long, gold multipass mirrors. The Stark cell is designed such that, in multipass mode, all droplets within the laser interaction region are exposed to a uniform Stark field. The Stark field is calibrated by measuring the known Stark spectrum of helium solvated HCN at a number of field strengths.[24] A Fresnel rhomb is used to orient the laser polarization relative to the external Stark field.

3.3 Experimental Results

The zero-field spectrum of the helium solvated OH radical is shown in Fig. 3.1. The splitting in the *Q*(3/2) transition is the sum of the Λ-doubling of the *J*=3/2 rotational levels in v=0 and v=1. The *R*(3/2) splitting corresponds to the difference in Λ-doubling associated with the v=0, *J*=3/2 and v=1, *J*=5/2 levels. The Λ-doublet splitting of the *Q*(3/2) transition is resolved in the droplet spectrum, while the splitting of the *R*(3/2) transition is washed out by a broadening source most likely associated with rapid rotational relaxation of the *v*=1, *J*=5/2 level, an effect observed previously for the *R*(0) transition of HF.[23] We note, however, that the *R*(3/2) transition is blue shaded, and we discuss the possible implication of this below. The gas phase transitions are shown in Fig. 3.1 by dashed lines.[25] While the centroids of the *Q*(3/2) and *R*(3/2) transitions are not significantly shifted from their gas phase values, the *Q*(3/2) Λ-doublet splitting is increased by a large amount in the droplet spectrum. At zero-field, the two *Q*-branch lines are separated by 0.567 cm^{-1}, which is a factor of 5.30 larger than in the gas phase spectrum. For comparison, as noted above, the Λ-doubling of the NO *Q*(1/2) transition increases by a factor of 1.55 upon helium solvation.[13] A rather weak droplet size dependence of the OH *Q*(3/2) splitting is observed, as shown in Fig. 3.2. The measured splitting systematically increases from 0.564 to ~0.574 cm^{-1} as the average droplet size is varied from approximately 7500 to 1300 He atoms, respectively.

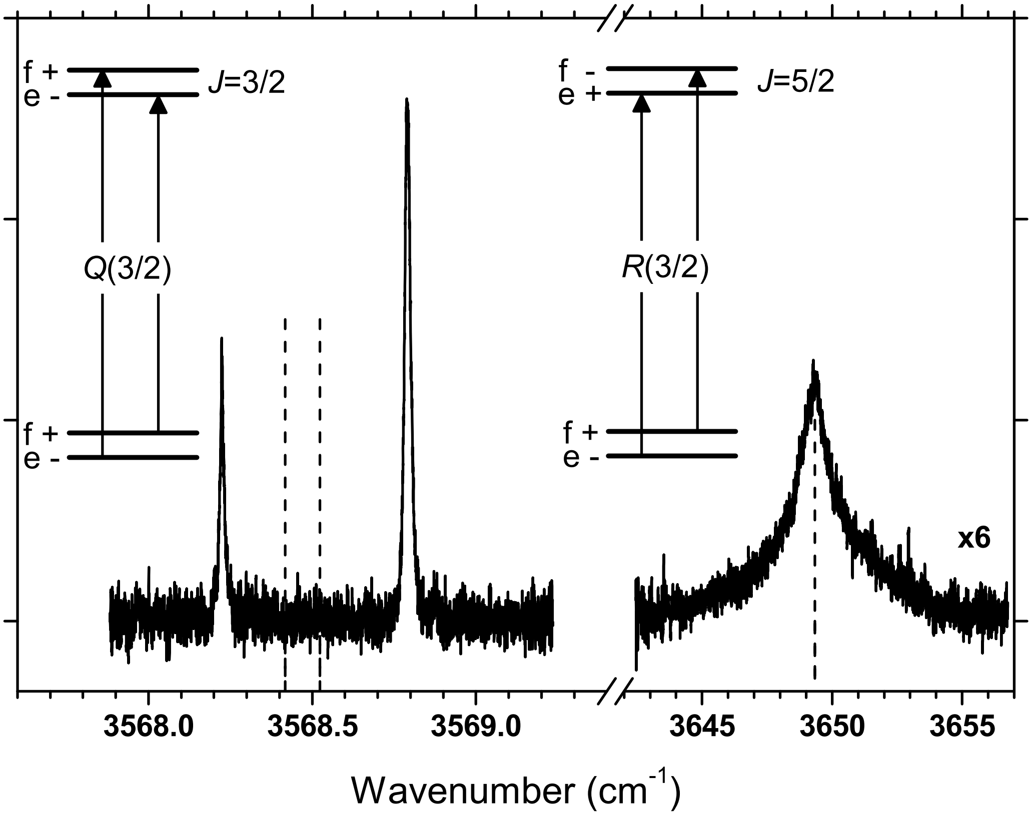

Figure 3.1: Zero-field spectrum of OH in helium nanodroplets. The linewidths of the *Q*(3/2) transitions are ~0.02 cm^{-1}, and the *R*(3/2) transition is broadened with a ~2 cm^{-1} linewidth, which washes out the predicted Λ-doubling. The dashed lines correspond to the gas phase values.[25]

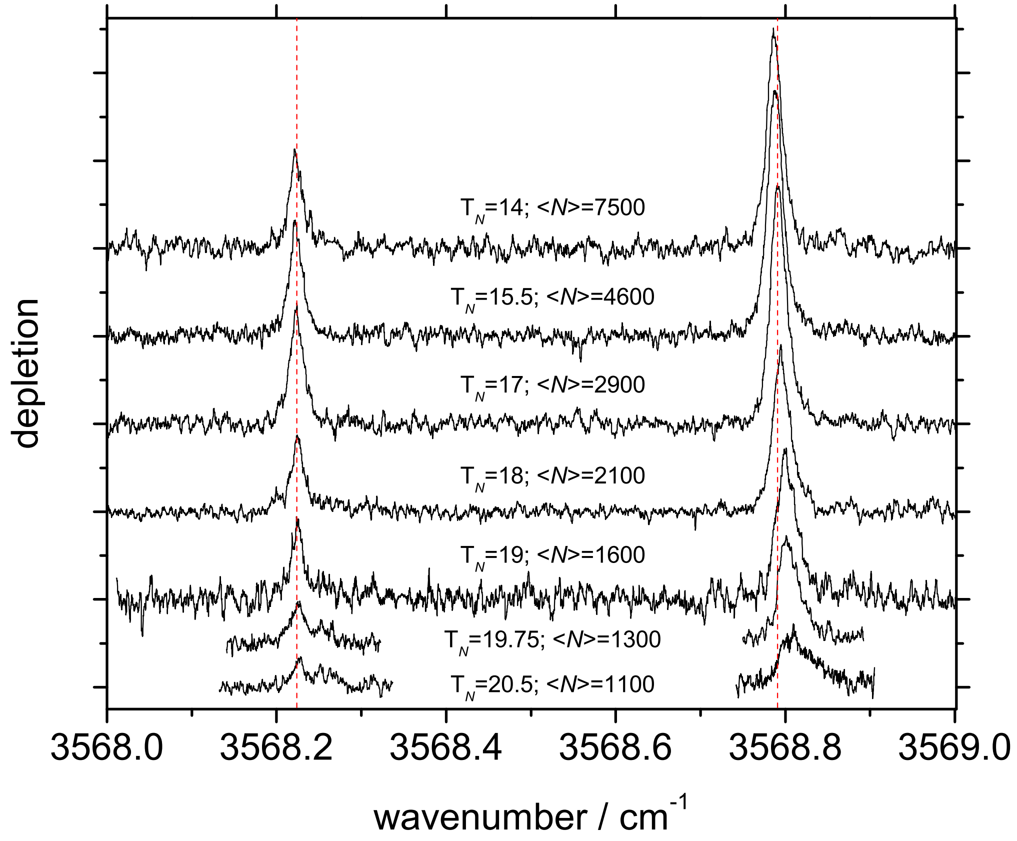

Figure 3.2: Droplet size dependence of the Q(3/2) lines for the hydroxyl radical. The vertical lines are positioned at the wavenumbers corresponding to the peak maxima reported in Table 3.1 (for <N>=2900). T_N is the nozzle temperature in Kelvin (K).

Table 3.1: Line positions and assignments from the zero-field spectra.

	OH	
	Gas Phase[a]	He Droplet
Q(3/2)		
e←*f*	3568.4169	3568.224(1)
f←*e*	3568.5238	3568.791(1)
R(3/2)		
e←*e*	3649.2054	3649.3(2)
f←*f*	3649.3365	-

[a]From Ref. 25.

Although the *Q*(3/2) lines provide only the sum of the Λ-doubling in v=0 and v=1, the *J*=3/2 splitting in each vibrational level can be obtained directly from Stark spectroscopy. Fig. 3.3 shows a series of spectra recorded with increasing electric field strength applied to the laser interaction region. Here the polarization of the laser is aligned such that the laser electric field vector has equal projections onto axes parallel and perpendicular to the static Stark field, resulting in both ΔM=0 and ±1 selection rules. With increasing field strength, the *f*←*e* and *e*←*f* Λ-doublet lines split and diverge, as a result of the partial lifting of the four-fold *M* degeneracy (M = ±3/2, ±1/2) of each $|v=0, J=3/2, M, \Omega=3/2, e/f\rangle$ parity level. Additionally, a new set of peaks grows in near the center of the zero-field transitions. These new peaks derive from the *e*←*e* and *f*←*f* transitions that are forbidden at zero-field. Because the Stark Hamiltonian no longer commutes with the inversion operator (E^*), parity is no longer conserved; hence, these new peaks gain intensity with increasing Stark field due to parity mixing. There are a total of 20 allowed transitions from the four doubly degenerate Stark levels (4 sets of 5 that extrapolate back to single *e*/*f*←*e*/*f* zero-field transitions). At low-field (e.g. 10.32 kV/cm), 14 resolved lines are clearly evident in the Stark spectrum. As the field strength increases, the population in the low-field seeking states is reduced, such that the transitions from these levels gradually decrease in intensity. In order to help assign each observed line, we measured the spectrum of the OH *Q*(3/2) transition at multiple field strengths with the laser polarization aligned either perpendicular or parallel to the Stark field. As an example, the assignments of the 5 transitions that derive from the *f*←*e* zero-field transition are shown in Fig. 3.4 for the 10.32 kV/cm Stark spectrum.

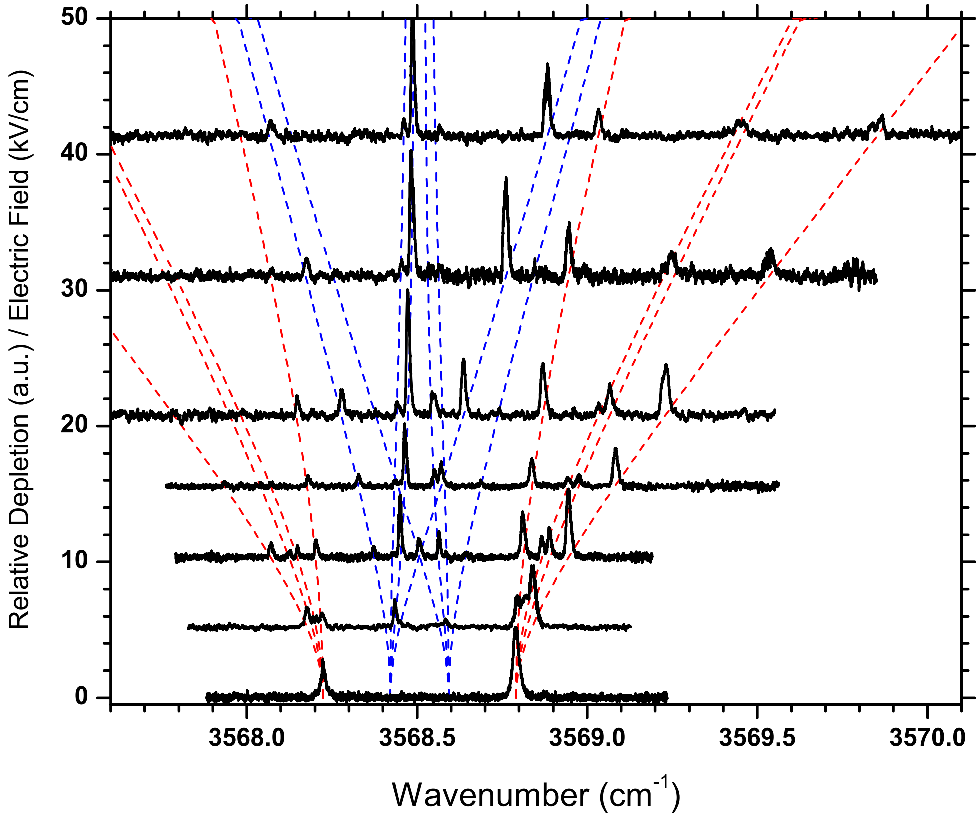

Figure 3.3: Stark spectra of the Q(3/2) transitions of OH in helium nanodroplets. Dashed red (blue) lines correspond to the fitted transition wavenumbers that are allowed (forbidden) at zero field (see text for details). The spectra have been offset such that their baseline value corresponds to the field at which they were measured. The field strengths from bottom to top are 0, 5.16(5), 10.32(10), 15.55(15), 20.74(20), 31.00(30), 41.32(40) kV/cm.

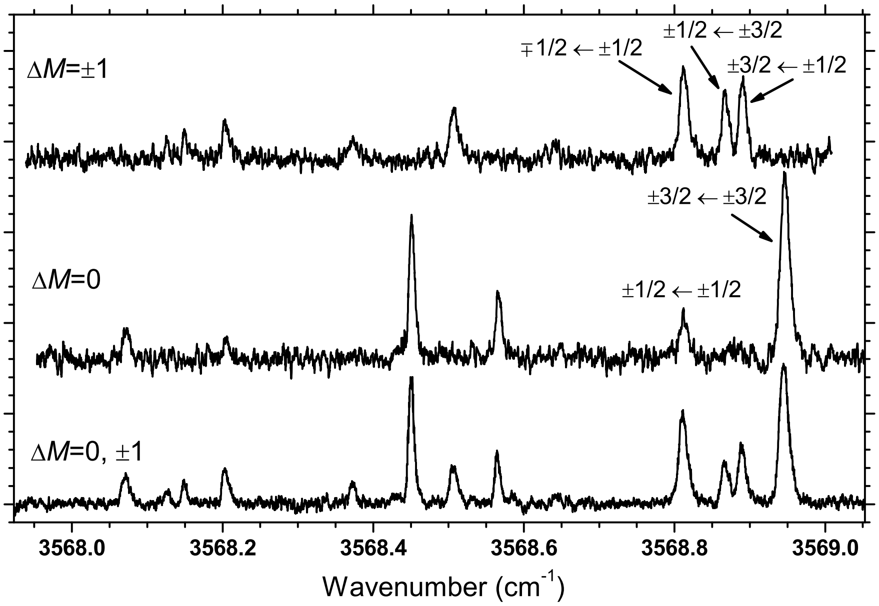

Figure 3.4: Stark spectra of the Q(3/2) transitions of OH at 10.32(10) kV/cm and with polarization configurations either perpendicular (top) or parallel (middle) to the Stark field axis. The bottom spectrum corresponds to a polarization configuration with equal projections of the laser electric field onto the axes parallel and perpendicular to the Stark field axis. The assignments of the five $M'\leftarrow M''$ transitions that extrapolate back to the $f\leftarrow e$ zero-field transition are shown as an example.

The OH radical in the $X^2\Pi_{3/2}$ (J=3/2) state approximately belongs to the Hund's case (a) coupling scheme, for which the orbital angular momentum, ***L***, couples to the molecular axis via electrostatic forces, and the spin angular momentum, ***S***, couples to ***L*** via the spin-orbit interaction.[26] The sum of the projections of ***L*** and ***S*** onto the molecular axis, Λ+Σ, is represented by the nearly good quantum number, Ω. An effective value of Ω can be derived that represents the extent to which the spin angular momentum is uncoupled from the molecular axis with increasing J, resulting in the transition from a case (a) to case (b) coupling scheme. For the J=3/2 level of the $X^2\Pi_{3/2}$ OH radical,

Ω_{eff}=1.47 for both the v=0 and v=1 vibrational states.[27] The effective value of Ω is defined explicitly in terms of the rotational constant, B_v, and the spin orbit coupling constant, A_v, as

$$\Omega_{eff} = \frac{1}{2}\left(a_J\right)^2 + \frac{3}{2}\left(b_J\right)^2, \text{ where } b_J = \left[\frac{X-(Y-2)}{2X}\right]^{1/2}, a_J = 1-\left(b_J\right)^2,$$

$$X = \left[4\left(J+\frac{1}{2}\right)^2 + Y(Y-4)\right]^{1/2} \text{, and} = \frac{A_v}{B_v}.^{28} \tag{3.1}$$

The Hamiltonian for the OH radical in a Stark field is the sum of the Hamiltonians for rotation, spin-orbit coupling and the Stark effect.

$$H = H_{SO} + H_{ROT} + H_{Stark} = A_v\boldsymbol{L}\cdot\boldsymbol{S} + B_v(\boldsymbol{J}-\boldsymbol{L}-\boldsymbol{S})^2 - \boldsymbol{\mu}\cdot\boldsymbol{\epsilon} \tag{3.2}$$

The Stark spectrum is analyzed by finding the eigenvalues of the Hamiltonian matrix in an *e*/*f* symmetrized Hund's case (a) representation, in which

$$|J\Omega M\pm\rangle = \frac{1}{\sqrt{2}}[|J\Omega M\rangle \pm (-1)^{J-\Omega}|J-\Omega M\rangle]. \tag{3.3}$$

Here the + (-) sign corresponds to the *e* (*f*) parity basis state. The analysis is greatly simplified by noting that the separation between J=3/2 and 5/2 levels is sufficiently large (81 cm^{-1}) such that these levels are not significantly mixed by the Stark effect, and hence the matrix elements off-diagonal in J can be neglected. Because the external electric field also does not mix states differing in Ω quantum number, the Stark effect for OH can be approximated as only mixing states of opposite parity within a given J level. Therefore, in our analysis of the Stark splitting of the Q(3/2) transition, each M block of the J=3/2 Hamiltonian matrix is simply a 2x2 matrix with the energies of the zero-field Λ-doublet components on the diagonal. The off-diagonal matrix elements that couple states of opposite parity are derived in Ref. 17. Diagonalization of the 2x2 Stark matrix,

$$\begin{pmatrix} -E_\Lambda/2 & \frac{\mu\epsilon M_J\Omega_{eff}}{J(J+1)} \\ \frac{\mu\epsilon M_J\Omega_{eff}}{J(J+1)} & E_\Lambda/2 \end{pmatrix}, \tag{3.4}$$

results in analytical expressions for the Stark energies,

$$E = \pm\sqrt{\left(\frac{E_\Lambda}{2}\right)^2 + \left(\mu\epsilon\frac{M_J\Omega_{eff}}{J(J+1)}\right)^2}\ , \tag{3.5}$$

where the + (-) sign corresponds to the upper (lower) Λ-doublet component. Here, E_Λ is the zero-field Λ-doublet splitting, μ is the permanent electric dipole moment, ϵ is the strength of the external electric field, and M_J is the projection of the total angular momentum (exclusive of nuclear spin) onto the Stark field axis.[29]

By considering all 20 allowed transitions, we have fit the line positions shown in Fig. 3.3 to the expression, $\nu = \nu_0 + E' - E''$, where ν_0 corresponds to the center wave-number of the zero field *Q*(3/2) peaks (3568.5075 cm^{-1}). In the fit, E_Λ'', E_Λ' and the products $\Omega''_{\text{eff}}\mu''$ and $\Omega'_{\text{eff}}\mu'$ are allowed to float. The fitted constants are compared to the gas phase values in Table 3.2. The fitted line positions as a function of Stark field strength are shown as the dashed lines in Fig. 3.3. The red dashed lines correspond to transitions that converge on either *f*←*e* or *e*←*f* zero-field transitions, and the blue dashed lines converge on the *f*←*f* and *e*←*e* transitions that are forbidden at zero-field. From the fit of the line positions, the Λ-doublet splittings of the *J*=3/2 level in *v*=0 and *v*=1 are determined to be 0.198(3) cm^{-1} and 0.369(2) cm^{-1}, respectively. These splittings are 3.6 and 7.2 times larger than their respective gas phase values. Apparently, there is a rather significant vibrational dependence of the OH Λ-doubling in helium droplets that is not present in the gas phase. From the relative intensities of the *f*←*e* or *e*←*f* zero-field transitions and the Λ-doublet splitting of the *v*=0, *J*=3/2 level, we obtain a temperature equal to 0.30(2) Kelvin.

Table 3.2: Best-fit parameters for the Stark spectra of OH in helium droplets.

	Gas Phase		Helium droplet	
	E_Λ (cm^{-1})[a]	$\Omega_{eff}\mu$[b]	E_Λ (cm^{-1})[c]	$\Omega_{eff}\mu$[d]
v=0	0.0556	2.4326	0.198(3)	2.358(23)
v=1	0.0513	2.4463	0.369(2)	2.363(23)

[a] From Ref. 25.

[b] From Ref. 27.

[c] Reported uncertainties are determined from the propagated errors in the line positions.

[c] Reported uncertainties are dominated by the propagated errors in the field strengths.

Unfortunately, the Stark spectra do not allow for a separation of Ω_{eff} from μ, as only the product $\Omega_{eff}\mu$ is determined. The product $\Omega_{eff}\mu$ is reduced to 97% of its gas phase value in both the ground and excited vibrational states. If we assume that OH has its gas phase values for μ, then a 3% reduction in the Ω_{eff} value implies that the ratio A_v/B_v is reduced to 48% of its gas phase value (see equation 3.1). Assuming the B_v constant of helium solvated OH cannot be greater than its gas phase value, a 3% reduction in Ω_{eff} requires, as a lower limit, a change in the spin-orbit coupling constant from -139 cm^{-1} to -67 cm^{-1}, which, as we discuss below, is inconsistent with the measured spectrum and unphysical. On the other hand, a 3% reduction in μ is reasonable and consistent with what has been found for the polar, linear molecules HCN (2% reduction) and HCCCN (4% reduction) in going from the gas phase to helium droplets.[30]

3.4 Theoretical Methods and Results

The He-HX (X=O, F) potential surfaces ($^2A'$ and $^2A''$ for He-HO and $^1A'$ for He-HF) are computed using UCCSD(T) theory, keeping the OH and HF bond lengths fixed to their equilibrium values at this same level of theory (0.97328 and 0.92096 Å for OH and HF, respectively). Restricted open-shell Hartree-Fock (ROHF) reference wave-functions are used as input to the correlation energy calculations, and core electrons are kept frozen. An aug-cc-pVTZ basis set is used for H, O, and F, while an aug-cc-pVQZ basis is used for He. The potential scan is carried out in R, θ Jacobi coordinates, where R is the distance between the He atom and the HX center of mass. The 180º position corresponds to the He atom being located on the H end of HX. The He atom is scanned from θ = 0 to 180º (10º increments), and R is scanned from 2 to 20 Å (0.05 Å increments from 2-6 Å, 0.5 Å increments from 6-10 Å, and 2.0 Å increments from 10-20 Å). All *ab initio* calculations are performed using the program package CFOUR.[31]

The He-HX potentials are converted to a cylindrical coordinate system with the z-axis defined as the diatomic bond axis. The H atom lies on the negative side of the origin, which is defined as the HX center of mass. The axial and radial coordinates span the ranges -20 to 20 Å and 0 to 20 Å, respectively. These surfaces are shown in in Fig. 3.5. For each of these three potential surfaces, He density calculations are performed using He density functional theory and the Orsay-Trento density functional,[32, 33] according to the procedure outlined in Ref. 34 for a droplet with 500 He atoms. In these calculations, the potentials are treated as fixed external fields for the helium atoms, which is arguably a poor approximation for these light diatomic molecules, in which the helium density cannot adiabatically adjust to the rotational motion of the molecule. Nevertheless, these calculations are sufficient to test our hypothesis that there will be a slight difference in the He density located either in the plane (*A*′) or perpendicular to the plane (*A*″) of the singly occupied *p*π orbital.

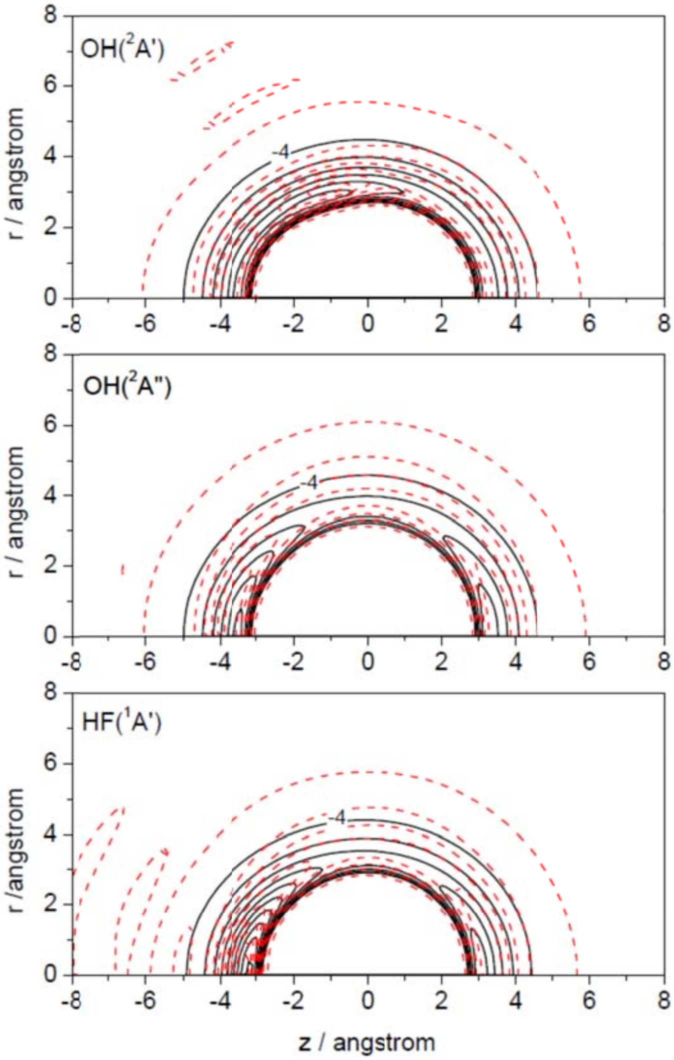

Figure 3.5: He-HX potential energy surfaces and helium density profiles (see text for details). The potential energy is in cm^{-1} and is shown as solid black lines, with increments of 4 cm^{-1}. The helium density profiles are given as dashed red lines with increments of 0.01 atoms/$Å^3$ (range is 0 to 0.1 atoms/$Å^3$).

The minimum energy pathways for rotation of the He atom in the plane of the HX molecules are shown in Fig. 3.6a, and the corresponding He densities are given in Fig. 3.6b. There is a qualitative difference between the A' and A'' He-OH potential surfaces along the minimum energy pathways, with the A' potential being overall more attractive than the A'' potential. This is expected because there is less electron density for the He atoms to be repelled by in the A' plane (singly occupied $p\pi$ orbital), in comparison to the A'' plane (doubly occupied $p\pi$ orbital). At this level of theory, this difference clearly results in an anisotropy in the He density about the axis of the molecule, with more helium residing in the plane of the singly occupied $p\pi$ orbital. The minimum energy pathway for the rotation of a He atom in the plane of the closed-shell HF molecule is qualitatively similar to that for the He-OH A'' potential, although the HF potential is more attractive, especially near the He-HF linear configuration (θ=180º). Moreover, the He density along the minimum energy path is similar for the He-HF and He-OH A'' potentials, except at the H atom end of the molecules, where the He density associated with the HF potential is predicted to be approximately twice as large.

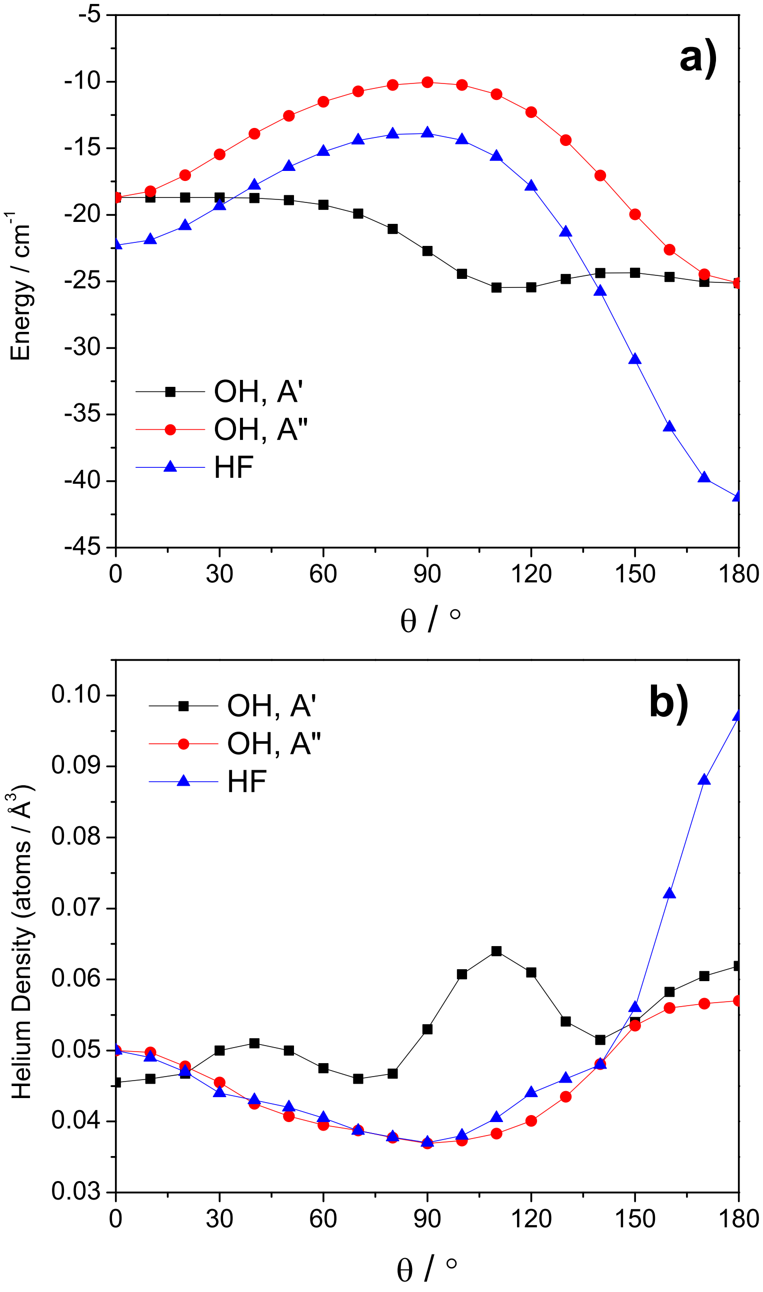

Figure 3.6: a) Minimum energy paths for the He-HX potential surfaces. The energy for the minimum value in *R* (HX center of mass to helium distance) for each value of θ (X-c.o.m.-He angle). b) Helium densities at each point along the He-HX minimum energy pathways as computed with He density functional theory.

3.5 Discussion

The approximate Λ-doubling of the J=3/2 rotational level in a $^2\Pi_{3/2}$ electronic state is known from second-order perturbation theory to be $E_\Lambda \approx 24B_v^3/[A_v(E_\Pi - E_\Sigma)]$.[14] The He droplet effect on the Λ-doubling cannot be rationalized with a simple argument associated with the modification of either B_v, A_v, or (E_Π -E_Σ) upon He solvation. Certainly, the OH rotational constant will not *increase* in He. Furthermore, to approximately reproduce the droplet induced Λ-doublet splitting in OH (v=0, J=3/2), the product $A_v(E_\Pi$ -$E_\Sigma)$ would have to be reduced by a factor of ~4. This seems unreasonable considering that the wavenumber separation between the $^2\Sigma^+$ and $^2\Pi$ states in solid neon (within which OH is free to rotate) is approximately the same as in the gas phase (~100 cm^{-1} redshift).[35] Furthermore, we expect the absolute value of A_v to *increase* in liquid He, analogous to what is observed for the $^2P_{3/2,1/2}$ levels of the Cl atom in solid para-H$_2$.[36] Indeed, the singly occupied $p\pi$ orbital of the isolated $X^2\Pi_{3/2}$ OH radical is partially aligned in the ground state (J=3/2),[16] whereas the electron density about the OH axis is cylindrically symmetric for the J=1/2 rotational level of the $X^2\Pi_{1/2}$ state. We expect that this should lead to a small increase in the solvation energy of the $^2\Pi_{3/2}$ manifold relative to $^2\Pi_{1/2}$, which corresponds to an effective increase in the absolute value of the spin-orbit coupling constant, A_v. A similar argument was used to rationalize the increased spin-orbit splitting of the ^2P level of the Cl atom isolated in solid para-H$_2$.[36]

In our search for an alternative explanation for the origin of the anomalous Λ-doubling, we considered the many previous studies of OH-X, where X is a rare-gas atom (see Ref. 37 and references therein). By means of perturbation theory, Green and Lester identified the major terms responsible for parity splitting (P-type doubling) in such open shell complexes.[38] The dominant perturbation term associated with the OH-Ar complex, for example, is $\hat{V}_{diff} = (A'' - A')/2$. This difference potential couples states that differ by 2λ, which leads to parity splitting of rotational levels in the complex. However, this difference potential operator actually vanishes in helium droplets due to the local two-fold symmetry about the OH molecular axis, an effect discussed extensively for OH-$(Ar)_n$ clusters.[39-41]

We find, however, that the difference in the OH-He A' and A'' potential surfaces can indeed be used to rationalize a model that predicts the helium droplet effect on the Λ-doubling. The basis for this model is the assumption that there exists a parity dependence of the effective moment of inertia of the solvated rotor. Because of the He density anisotropy about the molecular axis, we expect there to be a small difference between the effective rotational constants for rotation either in the plane of the singly occupied *p*π orbital (A', *e* parity levels) or in the plane of the doubly occupied *p*π orbital (A'', *f* parity levels). Indeed, the He density functional calculations predict the local He density near the rotor to be both larger and more anisotropic in the A' plane, in comparison to the A'' plane, suggesting perhaps that the B_v^e rotational constant will be affected by the helium to a larger degree than the B_v^f constant. This is somewhat analogous to the observation that the He contribution to the effective moment of inertia about the *c*-inertial axis in formic acid is 142% larger than it is about the *b*-inertial axis, due to the larger anisotropy of the He density about the *c*-axis.[42] This is true despite the fact that the formic acid *B* and *C* rotational constants in the gas phase are relatively similar. Such an effect for He solvated OH would lead to a parity dependent energy level shift that reveals itself as an increase in the apparent "Λ-doubling" of the rotational levels. We emphasize, however, that the $^2\Pi$

~ $^2\Sigma$ interactions that are responsible for Λ-doubling in the gas phase are not significantly modified by the droplet in this model.

We proceed by finding the eigenvalues of the zero-field $^2\Pi$ ~ $^2\Sigma^+$ interaction matrix represented in an *e*/*f* symmetrized Hund's case (a) basis.[14] The associated Hamiltonian is given in equation 3.2. Here we assume the unique perturber and pure precession approximations,[14] in which the interaction is assumed to involve only the $X^2\Pi$ and $A^2\Sigma^+$ electronic states. Furthermore, the potential curves of all three electronic states are assumed to be equivalent. The matrix elements in this representation and under these approximations are well-known.[14] The parity dependent rotational constant is labeled with an *e*/*f* superscript.

$$\begin{array}{l} X^2\Pi_{1/2} \\ X^2\Pi_{3/2} \\ A^2\Sigma^+{}_{1/2} \end{array} \begin{pmatrix} T_v^\pi - \frac{A_v}{2} + B_v^{e/f}\left(J+\frac{1}{2}\right)^2 & -B_v^{e/f}\left[\left(J-\frac{1}{2}\right)\left(J+\frac{3}{2}\right)\right]^{\frac{1}{2}} & \frac{\sqrt{2}A_v}{2} + \sqrt{2}B_v^{e/f}\left[1 \mp \left(J+\frac{1}{2}\right)\right] \\ - & T_v^\pi + \frac{A_v}{2} + B_v^{e/f}\left[\left(J+\frac{1}{2}\right)^2 - 2\right] & -\sqrt{2}B_v^{e/f}\left[\left(J-\frac{1}{2}\right)\left(J+\frac{3}{2}\right)\right]^{\frac{1}{2}} \\ - & - & T_v^\Sigma + B_v^{e/f}\left[\left(J+\frac{1}{2}\right)^2 \mp \left(J+\frac{1}{2}\right)\right] \end{pmatrix} \tag{3.6}$$

There are two such matrices, and the top (bottom) sign is for the *e* (*f*) parity matrix. The parity independent

$$\left\langle X^2\Pi_{\frac{1}{2}} \middle| H \middle| X^2\Pi_{\frac{3}{2}} \right\rangle \tag{3.7}$$

matrix element is associated with the *S*-uncoupling interaction that mixes the $^2\Pi_{3/2}$ and $^2\Pi_{1/2}$ states. This interaction is responsible for the uncoupling of the spin angular momentum from the molecular axis and a transition from a case (a) to case (b) coupling scheme with increasing *J* quantum number. The parity dependent

$$\left\langle X^2\Pi_{\frac{1}{2}} \middle| H \middle| A^2\Sigma_{\frac{1}{2}} \right\rangle \tag{3.8}$$

matrix element is associated with the *L*-uncoupling interaction that mixes Π and Σ states and leads to the Λ-doubling of the $^2\Pi_{1/2}$ rotational levels. Moreover, this Λ-doubling in the $^2\Pi_{1/2}$ state is transferred to the $^2\Pi_{3/2}$ rotational levels via *S*-uncoupling.

With the gas phase constants, the v=0,1, J=3/2 Λ-doublet splittings are predicted by this model to be 0.0640 and 0.0579 cm^{-1}, which can be compared to the experimental values of 0.0556 and 0.0513 cm^{-1}, respectively. Furthermore, with the gas phase constants, the separation between the Q(3/2) and R(3/2) transitions is predicted to be 80.79 cm^{-1}, which can be compared to the experimental value of 80.80 cm^{-1}. In order to set up the model for the He solvated OH molecule, we must estimate the extent to which the rotational constant is reduced by the helium. In a previous study of HF in He droplets, Nauta and Miller observed a 1.55% reduction of the B_1 constant from the gas phase value.[23] Because the B_1 rotational constants of OH (17.82 cm^{-1}) and HF (19.76 cm^{-1}) are similar in the gas phase,[24] we expect a similar reduction for OH. Furthermore, the A'' He-HO potential surface is similar to the He-HF potential, leading to similar He density profiles along the minimum energy path for rotation. We therefore begin by fixing the ground and excited $B_v^{e/f}$ rotational constants in the model to 18.252 and 17.553 cm^{-1}, respectively, which represent a 1.5% reduction from each constant's gas phase value. As expected, this reduction *decreases* the v=0,1, J=3/2 Λ-doublet splittings to 0.0615 and 0.0556 cm^{-1}, respectively. However, if we further reduce the ground state B_v^e constant from 18.252 to 18.207 cm^{-1}, a 0.25% change, the Λ-doublet splitting in v=0, J=3/2 *increases* to 0.128 cm^{-1}, which is a factor of *two* larger than the predicted gas phase value. Clearly, the Λ-doublet splittings are rather sensitive to even small differences in the *e*/*f* effective rotational constants. To recover the observed factor of 3.6 and 7.2

increases in the *J*=3/2 Λ-doublet splittings, the $B_{0,1}{}^{e}$ constants must differ from the $B_{0,1}{}^{f}$ constants by 0.61 and 1.44% for *v*=0 and *v*=1, respectively.

Fig. 3.7 provides a close look at the dependence of rotational constant for Λ-doublet splitting. The black and red curves in Fig. 3.7 a) is the two lowest e/f eigenvalues with v=0 and *J*=3/2. The blue curve is the difference between the e and f eigenvalues at the same rotational constant. In Fig. 3.7 b), the Λ-doublet splitting is plotted as a function of the percentage difference between $B_0{}^{e}$ and $B_0{}^{f}$, where $B_0{}^{f}$ is assumed to have 0.5% reduction from the gas phase model value. Clearly, the absolute difference in energy between e and f state at various rotational constants are small, and is not sensitive to the small change in rotational constant. However, the difference between the $B_0{}^{e}$ and $B_0{}^{f}$ has a huge effect on the Λ-doublet splitting, as it is shown in Fig. 3.7 b).

An interesting feature of this model is that the "effective" Λ-doubling is somewhat insensitive to the value used to fix the B_{v}^{f} constant. Furthermore, it is not sensitive to the spin-orbit coupling constant, which can be either halved or doubled with little effect on the predicted Λ-doubling. The percent difference between the *e*/*f* parity rotational constants serves essentially as a single fitting parameter. Table 3.3 contains a summary of the constants used in the model and the predicted Λ-doubling, assuming the droplet leads either to a 0.5 or 1.5% reduction in the B_{v}^{f} constant.

Table 3.3: Constants used in the Λ-doubling model.[a]

		B_v^f % reduction						B_v^e % reduction	
OH[b]	Gas Phase[c]	0%	0.5%	1.5%		NO[g]	Gas Phase[h]	0%	26%
B_0^e	18.535	18.535	18.325	18.139		B_0^e	1.696	1.696	1.253[i]
B_0^f	18.535	18.535	18.437	18.252		B_0^f	1.696	1.696	1.245
B_1^e	17.824	17.824	17.486	17.308		E_Λ^{avg} (J=1/2)	0.0117	0.0135	0.0209
B_1^f	17.824	17.824	17.731	17.553		%diff [d]	-	0	0.88
E_Λ'' (J=3/2)	0.0556	0.0640	0.227	0.227					
E_Λ' (J=3/2)	0.0513	0.0579	0.418	0.417					
E_Λ' (J=5/2)	0.187	0.211	1.60	1.60					
%diff (v=0)[d]	-	0	0.61	0.61					
%diff (v=1)[d]	-	0	1.38	1.44					
Δ (A_v gas)[e]	80.80	80.79	79.87	79.12					
Δ (exp)[f]	-139.73	-145	-170	-200					

[a] Units in cm^{-1}.

[b] The unique perturber is the $A\Sigma^+$ state and T_Σ=32684 cm^{-1}.

[c] From Ref. 25.

[d] $\left(1-\left(\frac{B_v^e}{B_v^f}\right)\right)*100$

[e] Center separation between the Q(3/2) and R(3/2) transitions with A_v constant equal to -139.73 cm^{-1} in the model. The experimental He droplet Δ value is 81.1(2) cm^{-1}.

[f] The value of the A_v constant required in the model to reproduce the experimental separation between the Q(3/2) and R(3/2) transitions.

[g] The unique perturber is the $I\Sigma^+$ state and T_Σ=63500 cm^{-1}.

[h] v=0 constants from Ref. 24.

[i] Reported B_1 rotational constant for NO in He droplets from Ref. 13.

Two additional issues that are of interest in the OH droplet spectrum are the blue shading observed in the broadened *R*(3/2) transition and the separation between the *Q*(3/2) and *R*(3/2) transitions. As discussed above, the *R*(3/2) transition should be split by the difference in the Λ-doublet splittings of the v=0, J=3/2 and v=1, J=5/2 levels, which is predicted by the above model to be 1.35 and 1.42 cm^{-1} for either the 0.5% or 1.5% reduction scenarios. Moreover, the weaker transition is predicted to be on the blue side of the pair. Both predictions are consistent with the qualitative feature of the measured *R*(3/2) transition. The predicted separation between the *Q*(3/2) and *R*(3/2) transitions is either 79.87 or 79.12 cm^{-1} (0.5% or 1.5% reduction of B_v^f), which can be compared to the experimental value of 81.1(2) cm^{-1}. Interestingly, within the error of the measurement, which is due to the broadening of the *R*(3/2) transition, the experimental separation is *larger* than the gas phase value (80.80 cm^{-1}). As noted above, with the gas phase constants in the model, the *Q*(3/2) to *R*(3/2) separation is predicted to be 80.79 cm^{-1}, in agreement with the gas phase value. The 81.1(2) cm^{-1} experimental separation can be reproduced by the model if we make the spin-orbit coupling constant more negative, namely to either -170 or -200 cm^{-1} for a 0.5% or 1.5% reduction of B_v^f, respectively. As discussed above, we expect a more negative A_v constant for OH upon helium solvation, and this is apparently predicted by the model. However, more theoretical work will be necessary to determine if it is realistic for the solvation energy of the $^2\Pi_{3/2}$ and $^2\Pi_{1/2}$ electronic states to differ by the predicted 30-50 cm^{-1}.

The model presented here is further validated by its prediction of the average Λ-doubling of the v=0,1, J=1/2 levels of the He solvated $X^2\Pi_{1/2}$ NO radical when we assume a similarly small difference in the B_v^e and B_v^f constants. The reported He droplet value for the NO rotational constant is B_1=1.253 cm^{-1}, and the average Λ-doubling of the J=1/2 levels was observed to increase by a factor of 1.55.[13] We fix B_v^e to 1.253 cm^{-1} and vary the B_v^f constant, which we expect to be the smaller constant, because the He will be more attracted to the NO molecule in the plane of the *unoccupied* $p\pi$ orbital. A factor of 1.55 increase in the J=1/2 Λ-doubling is predicted when B_v^f=1.242 cm^{-1}, which corresponds to a percent difference between the two *e*/*f* parity rotational constants of only 0.88%, similar to the prediction for OH. We note that this small parity dependence of the effective moment of inertia is only possible if there is a reduction in the cylindrical electronic symmetry about the axis of the $X^2\Pi_{1/2}$ NO (J=1/2), as originally suggested by Havenith and co-workers.[13]

3.6 Summary

The hydroxyl (OH) radical has been isolated and characterized in helium nanodroplets. From the Stark spectra of the OH radical, it is determined that the Λ-doublet splitting in the $X^2\Pi_{3/2}$, J=3/2 state in helium nanodroplets is increased by a factor of 3.6 in the v=0 state, and by a factor of 7.2 in the v=1 state, with respect to the gas phase values. Helium density functional calculations are employed to estimate the helium density in the A' and A'' planes of the solvated OH radical. Qualitatively, the helium density is both larger and more anisotropic in the plane of the singly-occupied $p\pi$-orbital (A'), suggesting that rotation in the A' plane may be affected by the helium to a larger degree than rotation in the A'' plane. These results motivate a model that assumes a small parity dependence of the OH effective moment of inertia in helium. This model predicts the observed Λ-doublet splittings if the B_v^e and B_v^f constants differ by 0.6 and

1.4% for v=0 and v=1, respectively. Furthermore, it predicts the average (v=0,1) Λ-doublet splitting previously reported for NO if the B_v^e and B_v^f constants differ by ~0.9%.

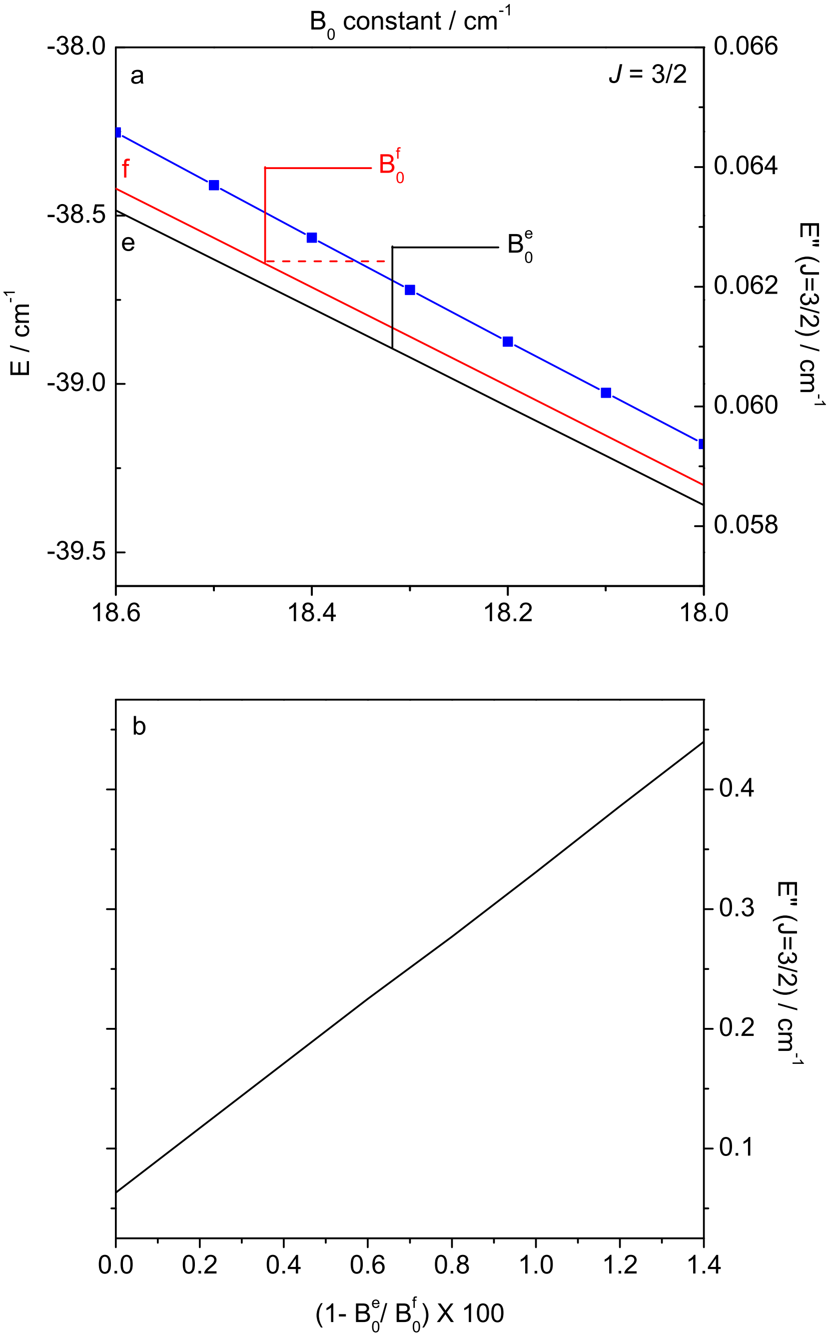

Figure 3.7: a) The lowest e/f eigenvalues with v=0 and J=3/2 as a function of rotational constants. b) Λ-doublet splitting as a function of the percentage difference between B_0^e and B_0^f.

References

[1] Toennies, J. P., and Vilesov, A. F., *Angew. Chem. Int. Edit.* **43**, 2622-2648 (2004).

[2] Choi, M. Y., Douberly, G. E., Falconer, T. M., Lewis, W. K., Lindsay, C. M., Merritt, J. M., Stiles, P. L., and Miller, R. E., *Int. Rev. Phys. Chem.* **25**, 15-75 (2006).

[3] Stienkemeier, F., and Lehmann, K. K., *J. Phys. B* **39**, R127-R166 (2006).

[4] Barranco, M., Guardiola, R., Hernandez, S., Mayol, R., Navarro, J., and Pi, M., *J. Low Temp. Phys.* **142**, 1-81 (2006).

[5] Kwon, Y. K., and Whaley, K. B., *Phys. Rev. Lett.* **83**, 4108-4111 (1999).

[6] Paesani, F., Viel, A., Gianturco, F. A., and Whaley, K. B., *Phys. Rev. Lett.* **90**, 073401 (2003).

[7] Moroni, S., Blinov, N., and Roy, P. N., *J. Chem. Phys.* **121**, 3577-3581 (2004).

[8] Paesani, F., and Whaley, K. B., *J. Chem. Phys.* **121**, 5293-5311 (2004).

[9] Mezzacapo, F., *J. Low Temp. Phys.* **140**, 241-252 (2005).

[10] Moroni, S., and Baroni, S., *Comput. Phys. Commun.* **169**, 404-407 (2005).

[11] Szalewicz, K., *Int. Rev. Phys. Chem.* **27**, 273-316 (2008).

[12] Wang, L., Xie, D., Guo, H., Li, H., Le Roy, R. J., and Roy, P.-N., *J. Mol. Spectrosc.* **267**, 136-143 (2011).

[13] von Haeften, K., Metzelthin, A., Rudolph, S., Staemmler, V., and Havenith, M., *Phys. Rev. Lett.* **95** (2005).

[14] Lefebvre-Brion, H., and Field, R. W., *The Spectra and Dynamics of Diatomic Molecules* (Elsevier Inc., San Diego, CA, 2004).

[15] Dousmanis, G. C., Sanders, T. M., and Townes, C. H., *Phys. Rev.* **100**, 1735-1755 (1955).

[16] Andresen, P., and Rothe, E. W., *J. Chem. Phys.* **82**, 3634-3640 (1985).

[17] Lewerenz, M., Schilling, B., and Toennies, J. P., *Chem. Phys. Lett.* **206**, 381-387 (1993).

[18] Knuth, E., Schilling, B., and Toennies, J. P., *Proceedings of the 19th International Symposium on Rarefied Gas Dynamics* (Oxford University Press, London, 1995).

[19] Hartmann, M., Miller, R. E., Toennies, J. P., and Vilesov, A., *Phys. Rev. Lett.* **75**, 1566-1569 (1995).

[20] Morrison, A. M., Agarwal, J., Schaefer, H. F., and Douberly, G. E., *J. Phys. Chem. A* **116**, 5299-5304 (2012).

[21] Bott, J. F., and Cohen, N., *Int. J. Chem. Kinet.* **21**, 485-498 (1989).

[22] Morrison, A. M., Automation of an Aculight Optical Parametric Oscillator, University of Georgia, 2012.

[23] Nauta, K., and Miller, R. E., *J. Chem. Phys.* **113**, 9466-9469 (2000).

[24] Huber, K. P., and Herzberg, G., *Molecular Spectra and Molecular Spectra* (Van Nostrand Reinhold Co., New York, 1979), Vol. IV. Constants of Diatomic Molecules.

[25] Melen, F., Sauval, A. J., Grevesse, N., Farmer, C. B., Servais, C., Delbouille, L., and Roland, G., *J. Mol. Spectrosc.* **174**, 490-509 (1995).

[26] Brown, M. J., and Carrington, A., *Rotational Spectroscopy of Diatomic Molecules* (Cambridge University Press, 2003).

[27] Peterson, K. I., Fraser, G. T., and Klemperer, W., *Can. J. Phys.* **62**, 1502-1507 (1984).

[28] Zare, R. N., *Angular Momentum* (Wiley, New York, 1988).

[29] Hain, T. D., Weibel, M. A., Backstrand, K. M., and Curtiss, T. J., *J. Phys. Chem. A* **101**, 7674-7683 (1997).

[30] Stiles, P. L., Nauta, K., and Miller, R. E., *Phys. Rev. Lett.* **90** (2003).

[31] CFOUR, Coupled-Cluster techniques for Computational Chemistry, a quantum-chemical program package by J.F. Stanton, J. Gauss, M.E. Harding, P.G. Szalay with contributions from A.A. Auer, R.J. Bartlett, U. Benedikt, C. Berger, D.E. Bernholdt, Y.J. Bomble, L. Cheng, O. Christiansen, M. Heckert, O. Heun, C. Huber, T.-C. Jagau, D. Jonsson, J. Jusélius, K. Klein, W.J. Lauderdale, D.A. Matthews, T. Metzroth, D.P. O'Neill, D.R. Price, E. Prochnow, K. Ruud, F. Schiffmann, W. Schwalbach, S. Stopkowicz, A. Tajti, J. Vázquez, F. Wang, J.D. Watts and the integral packages MOLECULE (J. Almlöf and P.R. Taylor), PROPS (P.R. Taylor), ABACUS (T. Helgaker, H.J. Aa. Jensen, P. Jørgensen, and J. Olsen), and ECP routines by A. V. Mitin and C. van Wüllen. For the current version, see http://www.cfour.de.

[32] Dalfovo, F., Lastri, A., Pricaupenko, L., Stringari, S., and Treiner, J., *Physical Review B* **52**, 1193-1209 (1995).

[33] Casas, M., Dalfovo, F., Lastri, A., Serra, L., and Stringari, S., *Z. PHYS. D ATOM. MOL. CL.* **35**, 67-75 (1995).

[34] Douberly, G. E., Stiles, P. L., Miller, R. E., Schmied, R., and Lehmann, K. K., *J. Phys. Chem. A* **114**, 3391-3402 (2010).

[35] Tinti, D. S., *J. Chem. Phys.* **48**, 1459-1464 (1968).

[36] Raston, P. L., and Anderson, D. T., *J. Chem. Phys.* **126** (2007).

[37] Heaven, M. C., *Int. Rev. Phys. Chem.* **24**, 375-420 (2005).

[38] Green, W. H., and Lester, M. I., *J. Chem. Phys.* **96**, 2573-2584 (1992).

[39] Xu, M. Z., Bacic, Z., and Hutson, J. M., *Faraday Discuss.* **118**, 405-417 (2001).

[40] Xu, M. Z., Bacic, Z., and Hutson, J. M., *J. Chem. Phys.* **117**, 4777-4786 (2002).

[41] Xu, M. Z., Bacic, Z., and Hutson, J. M., *J. Chem. Phys.* **117**, 4787-4799 (2002).

[42] Madeja, F., Markwick, P., Havenith, M., Nauta, K., and Miller, R. E., *J. Chem. Phys.* **116**, 2870-2878 (2002).

Chapter 4

Infrared Spectroscopy of HOOO and DOOO in ^{4}He Nanodroplets

The HOOO hydridotrioxygen radical and its deuterated analog (DOOO) have been isolated in helium nanodroplets following the *in-situ* association reaction between OH and O_2. The infrared spectrum in the 3500-3700 cm^{-1} region reveals bands that are assigned to the ν_1 (OH stretch) fundamental and $\nu_1+\nu_6$ (OH stretch plus torsion) combination band of the *trans*-HOOO isomer. The helium droplet spectrum is assigned on the basis of a detailed comparison to the infrared spectrum of HOOO produced in the gas phase [E. L. Derro, T. D. Sechler, C. Murray, and M. I. Lester, J. Chem. Phys. **128**, 244313 (2008)]. Despite the characteristic low temperature and rapid cooling of helium nanodroplets, there is no evidence for the formation of a weakly bound OH-O_2 van der Waals complex, which implies the absence of a kinetically significant barrier in the entrance channel of the reaction. There is also no spectroscopic evidence for the formation of *cis*-HOOO, which is predicted by theory to be nearly isoenergetic to the *trans* isomer. Under conditions that favor the introduction of multiple O_2 molecules to the droplets, bands associated with larger H/DOOO-$(O_2)_n$ clusters are observed shifted ~1-10 cm^{-1} to the red of the *trans*-H/DOOO ν_1 bands.

4.1 Introduction

Hydridotrioxygen (HOOO) has been the subject of numerous recent experimental and theoretical studies because it has been implicated as both an intermediate in several key atmospheric reactions and as a potential sink for hydroxyl radicals (OH) in the tropopause (see ref. 1 and references therein). The atmospheric abundance of HOOO depends strongly on its binding energy with respect to the OH + O_2 asymptote (D_0),[2] and therefore much of the experimental and theoretical work on this system has focused on an accurate determination of this parameter. An upper limit to the dissociation energy ($D_0 \leq$ 1860cm^{-1}) of HOOO was obtained in a series of seminal studies of its photodissociation dynamics.[3-5] Assuming this experimental upper limit, the fractional abundance of HOOO as a percentage of OH in the troposphere is determined to be ~25%.[2] Several recent theoretical studies of the stability of HOOO, however, predict a dissociation energy in the 350-1050 cm^{-1} range,[6-9] which is well below the current experimental upper limit. Computations employing equation-of-motion coupled-cluster methods predict a D_0 of 860 cm^{-1} along with an exit barrier in the minimum energy dissociation pathway (HOOO → OH + O_2) that lies 700-950 cm^{-1} above the OH + O_2 asymptote.[10] It has been suggested that an exit barrier of this magnitude could potentially result in ~700 cm^{-1} of photo-product translational excitation, which would reduce the experimental D_0 upper limit to ~1150 cm^{-1}.[10]

From measurements of the time-dependent OH concentration in a Laval-type nozzle containing excess O_2, Le Picard and co-workers derive a D_0 value equal to 1030 ± 30 cm^{-1}.[11] When combined with the most recent HOOO partition function,[2] this D_0 value implies that less than 0.1% of atmospheric OH is in the form of HOOO. More recent theoretical studies employing multireference treatments of the dissociation of HOOO predict a *barrierless* pathway with $D_0 \approx 1050$ cm^{-1}.[12, 13] The predicted minimum energy curves for HOOO dissociation in these reports are generally in agreement with both the D_0 value derived from the kinetic measurements and the experimental observation of a strong negative temperature dependence of the OH + O_2 reaction rate over the 55-100 K temperature range.[14]

The structure and potential energy surface of the HOOO system has also been the subject of several experimental and theoretical studies. Depending on the level of theory employed, different isomeric forms of HOOO are predicted as the minimum energy structure. It is now evident that for an accurate description of the potential energy surface associated with this open-shell, weakly bound radical, a proper treatment of both static and dynamical electron correlation effects is required (see for example references 13 and 15 and references therein). The earliest *ab initio* computations predicted a *gauche*-[16] or *perp*-HOOO geometry,[17] while all of the more recent theoretical studies predict either a *cis*-HOOO or *trans*-HOOO planar structure (both $^2A''$) as the global minimum.[6, 7, 12, 13, 15, 18-22] In a quantum dynamics investigation of the rovibrational energies of HO_3, a third, higher energy structural isomer was identified on a DFT potential.[20] This weakly bound, linear, OH-O_2 hydrogen-bonded species is found in the entrance channel to the formation of *cis*-HOOO behind a submerged barrier of ~100 cm^{-1}. In the work of Varner et. al., a van der Waals complex was found in the entrance channel along the minimum energy association pathway leading to the *trans*-HOOO isomer.[10] Furthermore, this complex is predicted to be separated from *trans*-HOOO by an ~900 cm^{-1} barrier located *above* the OH + O_2 asymptote. As noted above, the OH + O_2 → *trans*-HOOO reaction is predicted to be barrierless when multireference methods are employed.[12, 13] In these multireference treatments, however, a shallow local minimum and a submerged barrier does appear in the pathway leading to the *cis* isomer, although with a decreased barrier height when compared to the DFT potential of Braams and Yu.[20]

Using Fourier-transform microwave spectroscopy, Suma *et al.* were the first to provide definitive evidence for the *trans* isomer in the gas phase, which was produced in an electric discharge through a dilute mixture of H_2O and O_2 in an Ar free-jet expansion.[19] Using a similar discharge nozzle, McCarthy and co-workers have measured the rotational spectra of several isotopologues of *trans*-HOOO, providing the effective (r_0) structure for this species.[23] These studies show that *trans*-HOOO is a floppy molecule with a rather long central O-O bond (1.684 Å). In both of these microwave spectroscopy studies, only the *trans* isomer was observed, despite the fact that the *ab initio* computations predict the *cis* isomer to be nearly isoenergetic and separated from the *trans* species by an ~300-600 cm^{-1} torsional isomerization barrier.[2, 20] The absence of the *cis* isomer in these rotational spectra has been suggested to be due to its approximately 10 times smaller dipole moment along the *a*-inertial axis, in comparison to *trans*.[23] Future work in a frequency range that can detect the *b*-type transitions of the *cis* species (μ_b/μ_a =11) will be necessary to determine the relative abundance of this isomeric form of HOOO when produced in these pulsed discharge gas phase environments. The Lester group has reported the infrared (IR) spectra of both the *trans* and *cis*-H/DOOO isomers produced in a free-jet expansion in which OH/D is produced via the photolytic decomposition of nitric acid.[3-5, 24] In these IR spectra, the bands assigned to the *trans* isomer possess rotational fine structure, allowing for definitive, unambiguous assignments. The bands assigned to the *cis* isomer appear as broad features, in which the rotational fine structure is apparently washed out as result of an unidentified homogeneous broadening mechanism. The assignments of these broader features must therefore be considered somewhat less definitive. Nevertheless, there are a number of pieces of corroborating evidence that strongly suggest that the carrier of these broad features is the *cis*-H/DOOO isomer, as discussed in detail by Derro and co-workers.[4]

We report here the IR spectroscopy of the H/DOOO system in low temperature (0.4 K) helium nanodroplets. Helium nanodroplet isolation (HENDI) spectroscopy is a powerful technique for the isolation and characterization of often otherwise difficult to study chemical species, due to the dissipative nature of the droplets and their relatively rapid cooling.[25-27] We have shown recently that helium droplets can be used to spectroscopically probe the outcome of barrierless association reactions occurring within the droplet between sequentially picked-up and cold reactants.[28, 29] For example, the methylperoxy radical was isolated in helium nanodroplets via the *in-situ* association reaction between CH_3 and O_2.[29] On the other hand, if a barrier exists in the entrance channel to an association reaction (greater than ~100 cm^{-1}), the dissipation of the condensation energy has been shown to be sufficiently rapid to kinetically arrest the system in the van der Waals well on the potential.[30] Here, we probe the outcome of the low temperature, helium mediated OH/D + O_2 reaction using IR laser spectroscopy, and discuss the results in terms of their implications for the associated potential energy surface.

4.2 Experimental Methods

The details associated with the HENDI experimental technique have been reviewed,[26, 27, 31] and we focus only on those aspects relevant to the production of H/DOOO and its spectroscopic detection. Helium nanodroplets are formed in a continuous, cryogenic nozzle expansion of helium (99.9995%) through a 5 μm diameter pinhole nozzle. With the nozzle temperatures (15-17 K) and helium stagnation pressures (20 to 30 bar) used here, nanodroplets are generated that contain a few thousand helium atoms on average.[32] The droplet expansion is skimmed before entering a pick-up chamber that contains an effusive pyrolysis source for the production of the OH/D radical and a differentially pumped gas pick-up cell containing a variable pressure of O_2.

The OH/D radicals are produced via the pyrolytical decomposition of either the *tert*-butyl hydroperoxide or *tert*-butyl deuteroperoxide (TBHP and TBDP) precursor molecule. The precursor vapor passes through the heated tip of a quartz tube, and the pressure in the pyrolysis source is controlled with a fine metering valve that separates the heated tip from the precursor reservoir. The out flow of this source crosses perpendicular to the path of the droplet beam. When operating this source near 700 K, each TBHP/TBDP molecule fragments into one methyl radical, one acetone molecule, and one OH/D radical. The precursor density is kept low so as to prevent radical recombination reactions within the source and to optimize for the pick-up of single OH/D radicals. The internal degrees of freedom, along with the translational energy of the hot OH/D radicals are rapidly[33] cooled to 0.4 K upon capture by the droplets.[34] Approximately 300 μs downstream, the droplets pass through a differentially pumped pick-up cell that contains O_2 at a pressure of ~3×10^{-6} Torr. Following O_2 pick-up, the droplets once again rapidly cool to 0.4 K. For the droplets that have picked-up both an OH/D radical and O_2 molecule, the OH/D + O_2 association reaction will proceed on a timescale (< 1 μs) that is less than the flight time through the apparatus (~3 ms).[35] The reaction energy is dissipated via helium atom evaporation at a rate that is estimated to be on the order of 10^{12} K/s, although there is significant uncertainty in this value.[26] Given that each evaporating helium atom carries away ~7 K of internal energy,[36] the pick-up of OH and O_2 and the quenching of the reaction energy results in the evaporation of ~1000 helium atoms, assuming the system evolves barrierlessly to the *trans*-HOOO structure.

The idler output from a continuous wave, IR, optical parametric oscillator (OPO) is aligned to counter-propagate the helium droplet beam. The tuning and calibration of this IR-OPO system is described elsewhere.[37] The vibrational excitation of helium solvated HO_3 followed by vibrational energy relaxation leads to the evaporation of an additional ~700 helium atoms and therefore a laser induced depletion of the droplet beam intensity. This reduction of the average geometric droplet cross section results in a reduction in the ionization cross section as measured by a quadrupole mass spectrometer equipped with an electron impact ionizer. An IR spectrum is obtained as a depletion signal in a specific mass channel by fixing the quadrupole mass spectrometer to a particular mass to charge ratio while scanning the IR-OPO. On the basis of the well-known statistics associated with droplet doping,[38] we estimate that with optimized source conditions approximately 5 percent of all droplets pick up a single OH/D radical *and* a single O_2 molecule. The other 95 percent of the droplet ensemble will either be devoid of dopants or contain other combinations of OH/D, CH_3, $(CH_3)_2CO$, and O_2. Nevertheless, since we are capable of detecting the IR spectrum as ion depletion in selected mass channels, these can be chosen judiciously in order to discriminate against the droplets that do not contain the H/DO_3 reaction products.

4.3 Results

When sequentially adding the OH radicals and O_2 molecules to the droplets, the O_2 pressure in the gas pick-up cell can be kept sufficiently low, so as to prevent the formation of larger HO-$(O_2)_{n>1}$ clusters. The resulting IR spectrum under these conditions is shown as the black trace in Fig. 4.1. This measurement corresponds to the laser induced depletion of the ion signal in mass channel m/z=17 u (OH^+). The appearance of the OH^+ ion is due to the formation of He^+ upon electron impact ionization of a droplet, which goes on to ionize the solvated HO_3 species via the charge transfer reaction, $HO_3 + He^+ \rightarrow He + (HO_3^+)^*$. The subsequent fragmentation of the energized molecular ion, $(HO_3^+)^* \rightarrow He+O_2+OH^+$ and the complete evaporation of the droplet results in the appearance of ion signal in mass channel m/z=17 u.

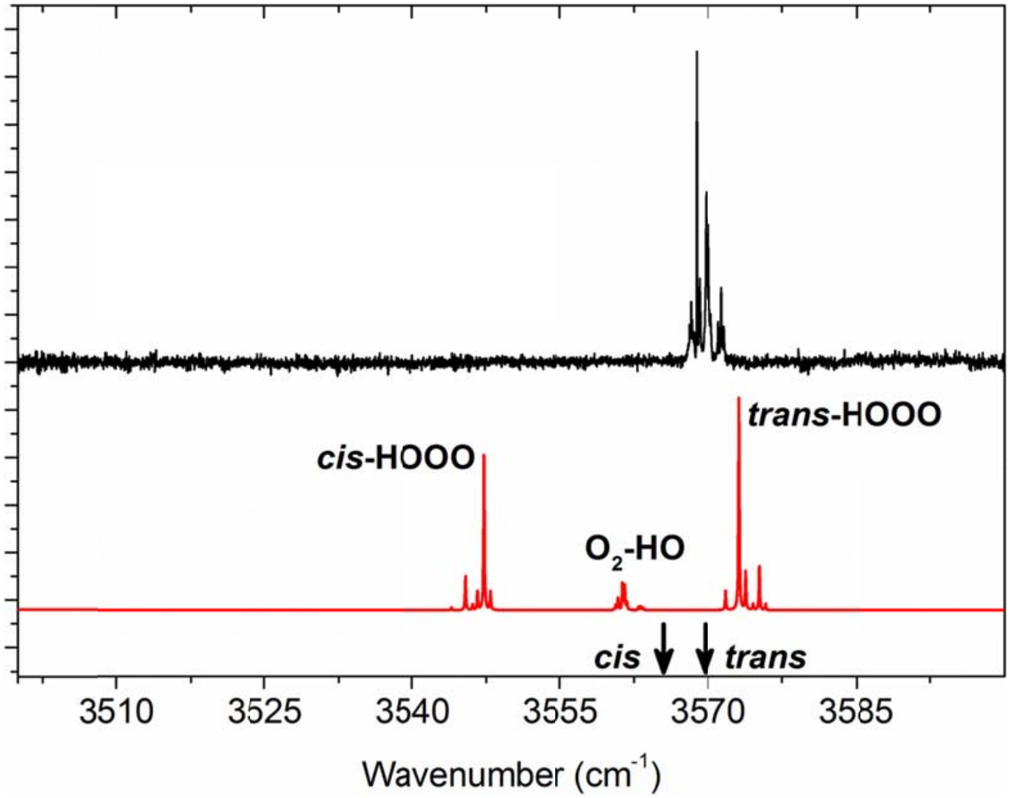

Figure 4.1: Survey scan (top) in the OH stretching region (mass channel m/z=17 u). The O_2 doping cell pressure was kept low, so as to prevent the formation of larger HO_3-$(O_2)_n$ clusters. The simulated spectrum (bottom) shows the predicted band origins and expected rotational fine structure at T=0.4 K for the three computed HO_3 isomers on the basis of CCSD(T)/Def2-TZVP geometry optimizations and anharmonic frequency calculations. The band origins represent the respective *ab initio* anharmonic frequency shifts from the band origin of the hydroxyl radical, which has been shifted to its gas phase value (3568.47 cm^{-1}).[39] The relative intensities of the simulated bands assume an equal abundance for the three isomers. The arrows point at the *cis/trans*-HOOO gas phase band origins.[4]

The gas phase origins reported for *cis* and *trans*-HOOO are indicated with the arrows in Fig. 4.1. The only evident features in our survey spectrum are a group of sharp peaks centered near 3570 cm^{-1}. This group of peaks is near the gas phase band that has been unambiguously assigned to the *trans*-HOOO ν_1 fundamental (OH stretch).[24] The smooth red trace in Fig. 4.1 is a simulation of the predicted ro-vibrational bands of the three possible HO_3 isomers at the droplet temperature. The band origins in the simulations are based on the shifts from the hydroxyl radical OH stretch, which are obtained from VPT2, CCSD(T)/Def2-TZVP anharmonic frequency calculations, using the program CFOUR.[40] From a first inspection of the rotational structure and band position observed in the helium droplet spectrum, it appears that only the *trans*-HOOO isomer is produced in the low temperature OH + O_2 association reaction.

4.3.1 *trans*-H/DOOO

A higher resolution scan of the 3570 cm^{-1} region is shown in Fig. 4.2, which was measured under conditions optimized for the production of HO_3. Analysis of the rotational fine structure corroborates the assignment of this band to the *trans*-HOOO isomer. Our first attempt to simulate the observed spectrum was to simply start with the rotational constants, band origin and orientation of the transition dipole moment reported for the gas phase *trans*-HOOO isomer.[24] The rotational temperature in this initial simulation was set to 0.4 K. From this, it was immediately apparent that the various transitions observed in the helium droplet spectrum were indeed associated with the *a*- and *b*-type components of a mostly *a*-type hybrid band. Because there are relatively few transitions, a complete set of rotational constants cannot be derived from this spectrum. However, the upper state rotational constants and the $(B''+C'')/2$ constant can be estimated from combination differences, assuming a rigid asymmetric top Hamiltonian. The vibrational band origin is then obtained from a least squares fit while keeping the rotational constants fixed. The band origins and rotational constants obtained in this way are reported and compared to the *trans*-HOOO gas phase values in Table 4.1. A similar scan in the OD stretching region under conditions optimized for the production of DO_3 revealed depletion signals with essentially the same pattern. This DO_3 spectrum is shown in Fig. 4.3, and the constants derived from this spectrum are also given in Table 4.1.

Table 4.1: Comparison of gas phase and helium droplet *trans*-HOOO / *trans*-DOOO spectroscopic constants.[a]

Helium	ν_0 [b]	$\Delta\nu_0$ [c]	A' [d]	B' [d]	C' [d]	$(B''+C'')/2$ [d]	Γ
HO_3	3569.455(5)	+0.95	1.800(1)	0.168(1)	0.145(1)	0.175(1)	0.1
DO_3	2635.023(1)	+3.73	1.697(1)	0.167(1)	0.140(2)	0.168(2)	0.06
Gas	ν_0 [e]	$\Delta\nu_0$ [f]	A'' [g]	$(B''+C'')/2$ [g]	$B''-C''$ [g]		
HO_3	3569.30(5)	+0.83	2.3609	0.3125	0.0412		
DO_3	2635.06	+3.52	2.2635	0.2960	0.0384		

[a] Units in cm^{-1}.

[b] Uncertainty is the 1σ error of a least squares fit of the band origin with the rotational constants fixed to the values reported here.

[c] Frequency shift from the $\nu_{OH(D)}$ of the OH(D) radical in helium nanodroplets.

[d] Uncertainty originates from the uncertainty associated with the determination of the line positions used in the combination differences.

[e] Refs. 4, 5

[f] Frequency shift from gas phase OH(D). Refs. 39, 41.

[g] Ref. 19

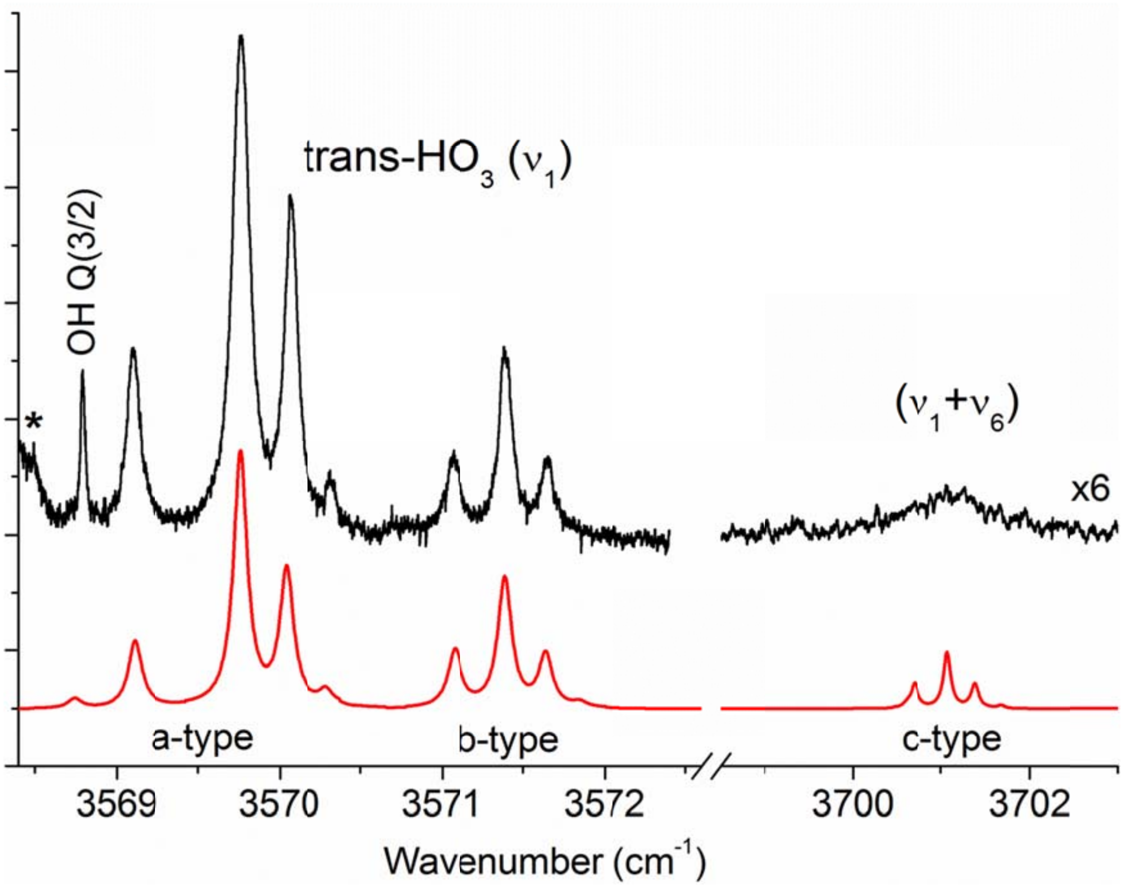

Figure 4.2: Higher resolution spectra in the regions containing the ν_1 (OH stretch) and ν_1+ν_6 (OH stretch plus torsion combination) bands of *trans*-HOOO. The smooth red lines are simulations based on the constants reported in Table 4.1. The sharp peak at 3568.79 cm^{-1} is the e→f component of the Q(3/2) transition of the hydroxyl radical (OH). The asterisk marks the band assigned to HO_5.

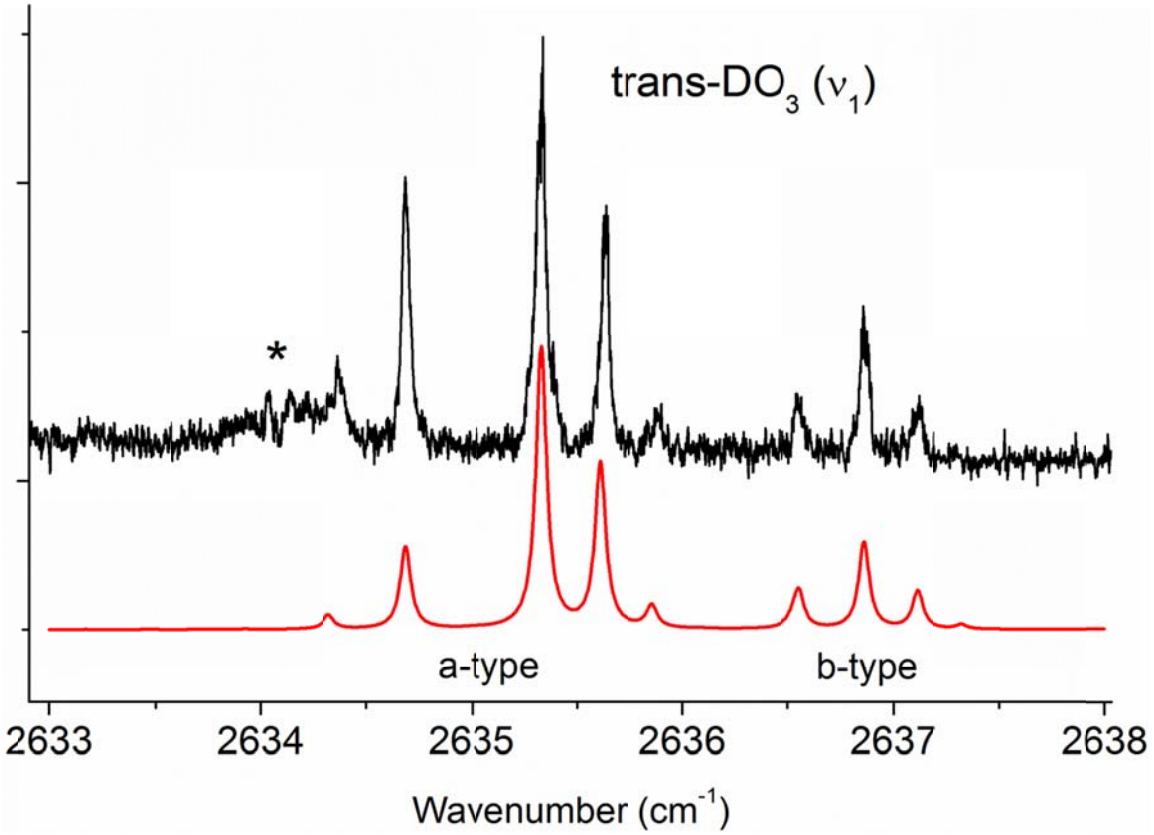

Figure 4.3: The ν_1 (OD stretch) band of *trans*-DOOO. The smooth line (red) is a simulation based on the constants reported in Table 4.1. The asterisk marks the band assigned to DO_5.

The band origin of the spectrum in Fig. 4.2 is shifted 0.16 cm^{-1} to the blue of the gas phase ν_1 band origin of *trans*-HOOO. Similarly, the band origin in Fig. 4.3 is only shifted 0.04 cm^{-1} to the red of the gas phase ν_1 band origin of *trans*-DOOO. These relatively minor frequency shifts are consistent with the helium solvent shifts associated with the spectra of a number of systems having free X-H stretches.[27] The OH stretching fundamentals of the planar ($^2A''$) HOOO isomers are hybrid *a*-/*b*-type bands, and for the *trans* isomer, the *a*-type component has the largest intensity, whereas for the *cis* isomer, the *b*-type component should dominate the spectrum. The *a*-/*b*-type bands in Fig. 4.2

were carefully measured under non-saturating conditions, and from the relative intensities of the two bands, we determine a μ_a:μ_b ratio of 1.9. This can be compared to the μ_a:μ_b =1.4 ratio derived from the gas phase infrared spectrum of the *trans*-HOOO isomer.[4] Along with the band origin, this comparison provides rather definitive support for the assignment of the band observed in the droplet spectrum to *trans*-HOOO. In comparison to the vibrational band origin, the rotational constants for this species are more significantly affected by the helium environment, a solvent effect that is now well-documented for a broad range of molecular systems.[25, 27] The *A* and (*B*+*C*)/2 constants for *trans*-H/DOOO are renormalized to about 77 and 56 percent of their respective gas phase values due to the coupling of helium density to the molecular rotation. This coupling is weaker for the "faster" rotation about the *a*-inertial axis, hence the smaller reduction measured for the *A* rotational constant.[25, 27]

An interesting and striking difference between the spectra measured here for the two isotopologues is the greater line widths observed for *trans*-HOOO, which are about twice as large as those observed in the *trans*-DOOO spectrum. Assuming these line widths derive from homogeneous broadening mechanisms, this may be due to the fact that for *trans*-HOOO there is a higher density of states at the energy of the excited ro-vibrational states, leading to more efficient IVR and/or vibrational predissociation. Perhaps somewhat surprisingly, the line widths of the *trans*-H/DOOO helium droplet spectra are ~2 and ~3 times narrower than the transitions in the gas phase spectra, respectively.

A number of ν_1+ν_n combination bands have been identified in the gas phase for both *cis* and *trans*-HOOO isomers, the strongest of which is the *c*-type ν_1+ν_6 band.[24] This *c*-type combination band, which is associated with the excitation of one quantum of OH stretch and one quantum of torsion, was found to lie 128.7 cm^{-1} to the blue of the *trans*-HOOO ν_1 band origin.[24] On account of its strong intensity, which is ~25% of the ν_1 band intensity,[24] we were able to find depletion signals in the 3700 cm^{-1} region that we assign to this ν_1+ν_6 band. This band is shown in Fig. 4.2 with its intensity expanded by a factor of six. Assuming a *c*-type band with the same rotational constants as those for the ν_1 band, we obtain a ν_1+ν_6 band origin of 3699.10(5). While this band appears as a broad structure-less feature lacking rotational fine structure, it is shifted very little from the gas phase origin (~1.1 cm^{-1} blue shift), which supports its assignment and indicates that the ν_6 torsional mode is very weakly perturbed by the helium droplet environment, similar to what has been observed for other helium solvated molecules with torsional degrees of freedom.[42, 43] Taking into account the solvent frequency shift of the ν_1 band, and assuming no cross-anharmonicity between ν_1 and ν_6 , the ν_6 band is estimated to be blue-shifted from the gas phase value by ~0.9 cm^{-1}. The linewidths of the underlying ν_1+ν_6 transitions are approximately six times broader than the ro-vibrational transitions in the ν_1 band, perhaps on account of a more efficient relaxation of the excited ro-torsional levels to a comparatively higher droplet state density at 130 cm^{-1} than is present below 3 cm^{-1}.[44]

4.3.2 Larger Clusters

With the O_2 pressure kept low and the depletion signal measured in mass channel m/z=17 u, the 3500-3700 cm^{-1} region contains only the *trans*-HOOO bands discussed above, and there are no signatures of the other isomers predicted on the HO_3 potential surface. This is similarly the case for the OD stretch region (see Fig. 4.4). However, with higher O_2 pick-up cell pressures, additional features are observed to the red of the ν_1 *trans*-H/DOOO bands. A survey spectrum recorded with conditions optimized for the formation of larger H/DO_3-$(O_2)_n$ (n=1,2) clusters is shown in Fig. 4.5. These spectra correspond to the depletion of ion signal in either mass channel m/z= 33 (O_2H^+) or 34 u (O_2D^+) for the initial pick-up of OH (top) and OD (bottom), respectively. The doping cell pressure was optimized for the pick-up of approximately two O_2 molecules per droplet. Two broad features are identified in each spectrum, which we assign to clusters containing two or three O_2 molecules, i.e. H/DO_3-$(O_2)_n$ with either n=1 or 2, as indicated in Fig. 4.5. These assignments are confirmed by the pick-up cell pressure dependence of the line intensities (see Fig. 4.6). The spectroscopy and *ab initio* calculations of the possible structures of these larger clusters are discussed in detail elsewhere.[45]

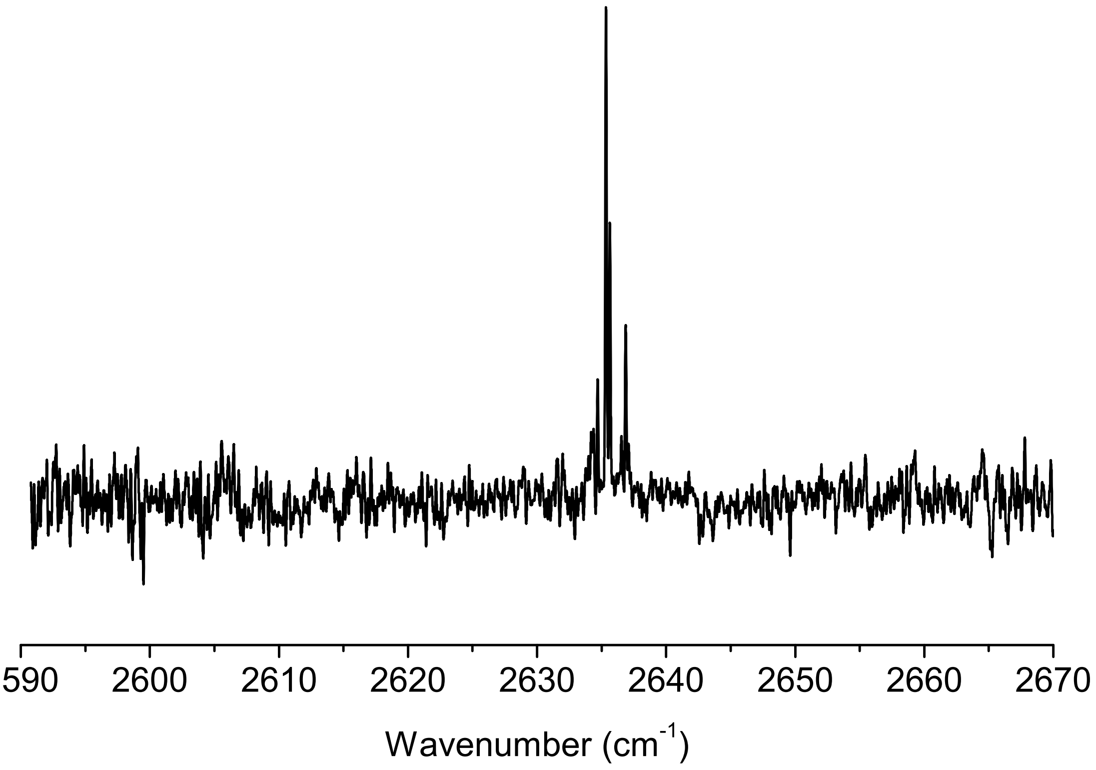

Figure 4.4: Low O_2 pressure survey scan in the OD stretching region in mass channel m/z=34 u. The only band observed under these conditions is the one assigned to the ν_1 OD stretch of *trans*-DOOO (see Figure 4.3).

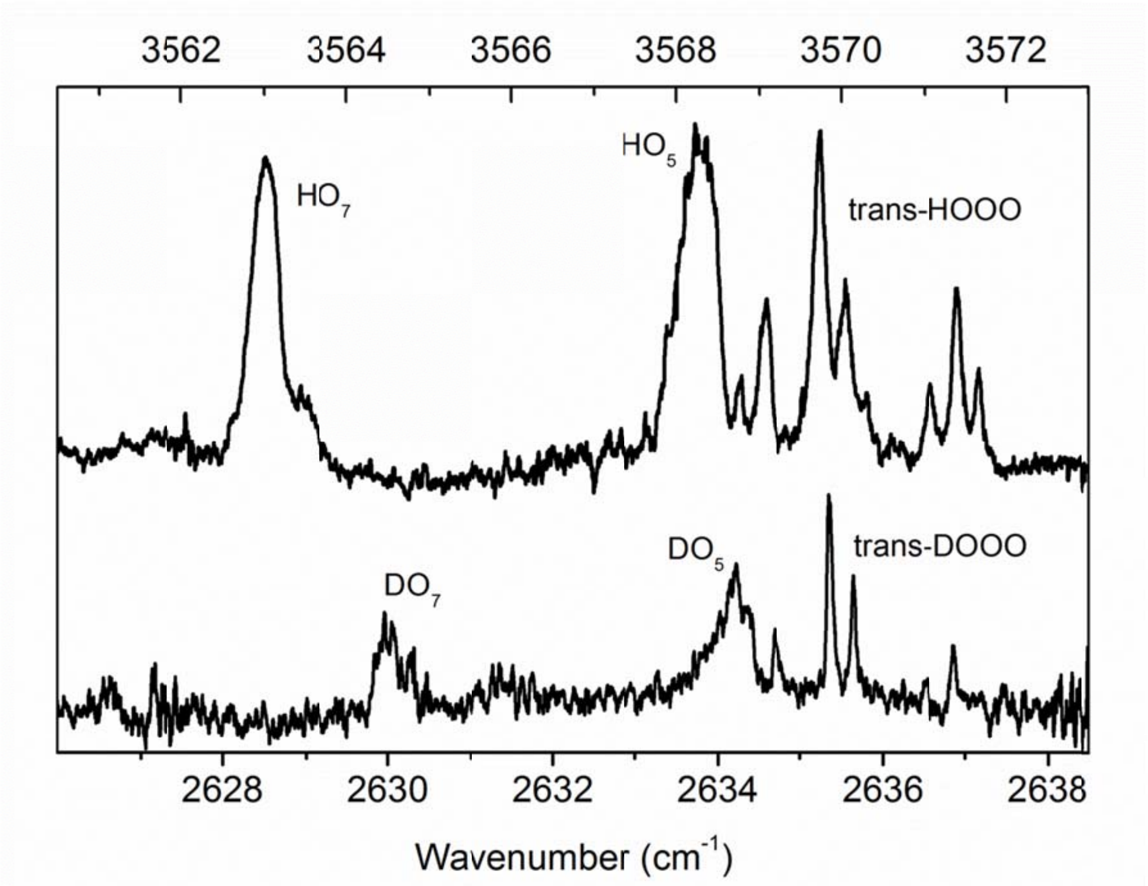

Figure 4.5: Survey spectrum recorded with conditions optimized for the formation of larger HO_3-$(O_2)_n$ (n=1,2) clusters. The spectra correspond to the depletion of ion signal in mass channel m/z= 33 or 34 u for either OH (top) or OD (bottom) initial pick-up, respectively. The doping cell pressure was optimized for the pick-up of approximately two O_2 molecules per droplet.

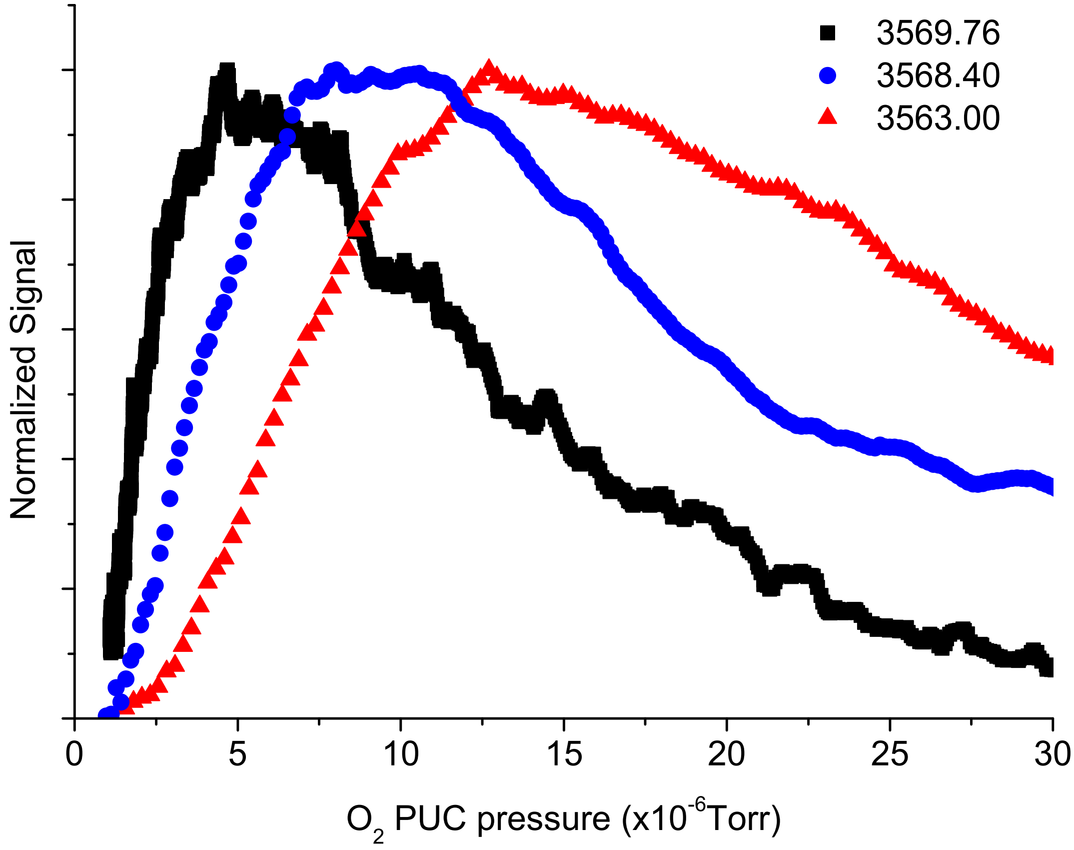

Figure 4.6: Pick-up cell pressure dependence of the OH + $(O_2)_n$ bands at the indicated wavenumbers.

4.4 Discussion and Conclusions

The IR spectrum in the OH stretch region shows that upon sequential pick-up of OH and O_2, the liquid helium mediated OH + O_2 association reaction results in the exclusive formation of *trans*-HOOO. We find no evidence for an entrance channel, van der Waals, OH-O_2 complex stabilized by long-range electrostatic interactions. For the following discussion of this result, it is useful to consider in detail the nature of the association reaction as it occurs within the helium droplet. The temperature of the OH/O_2 vapor is low enough such that the reactants are vibrationally cold upon droplet pick-up.

The ~300 μs flight time between pick-up zones ensures that the OH radical is both rotationally and translationally cold prior to the addition of the O_2 molecule to the droplet. Considering the typical timescale associated with the rotational relaxation of helium solvated molecules,[46] the O_2 rotational energy is likely quenched on a timescale that is faster than or at least competitive with the formation of the HO_3 complex. Therefore, the OH + O_2 association reaction can be viewed as occurring between vibrationally and rotationally cold reactants in their ground ro-vibrational states. Furthermore, it has been demonstrated in multiple reports that the rate of cooling of the vibrational kinetic energy produced as the system condenses in the droplet is often sufficiently fast so as to kinetically trap the system behind small barriers (~100 cm^{-1}) in the entrance channel of the reaction, even if the barrier is submerged below the reactant asymptote.[30, 47]

Since the product of this low temperature association reaction is the *trans*-HOOO isomer, it can be concluded rather definitively that a kinetically significant barrier does not exist in the entrance channel. A barrier above the OH + O_2 asymptote, as predicted by Varner et. al.,[10] would preclude the formation of *trans*-HOOO in the droplets, and this must therefore be ruled out as a possible feature on the HO_3 potential surface. This observation corroborates the explanation of the negative temperature dependence of the kinetics as being due to a barrierless association of OH and O_2,[2, 14] which, as pointed out above, is the same conclusion drawn from multireference treatments of the HOOO dissociation path, in which large, flexible active spaces are employed.[12, 13]

The absence of an entrance barrier to the OH + O_2 association reaction has important implications for the interpretation of the photodissociation measurements of the dissociation energy of HOOO. In particular, a barrierless dissociation suggests that the translational excitation of the OH and O_2 fragments should be minimized upon vibrational predissociation of the complex, as has been observed, for example, in the measurement of the water dimer dissociation energy[48] and in many other studies of the vibrational predissociation dynamics of weakly bound complexes.[49] Therefore, the upper limit measured by Lester et. al. (1860 cm^{-1}),[5] which assumes negligible translational excitation, should be rather close to the actual D_0 value. With this in mind, we view the 830 cm^{-1} discrepancy between this upper limit and the D_0 value derived from the kinetics measurement[11] as an indication that more experimental work is necessary to either refine or affirm the value of this atmospherically relevant parameter. It has been noted that future experiments aimed at measuring the correlated product state distributions using velocity map imaging techniques will provide directly the translational energy release of each fragment and the dissociation energy of HOOO to spectroscopic accuracy.[2]

As discussed above, broad features in the gas phase IR spectra have been tentatively assigned to the *cis*-H/DOOO isomer.[4, 5, 24] We find no evidence for the formation of the *cis* isomer in helium droplets for either isotopologue. This is perhaps surprising, given the semi-empirically determined 340 cm^{-1} torsional isomerization barrier and near degeneracy of the two isomers ($\Delta E = 72$ cm^{-1} between the lowest *cis*/*trans* zero-point levels).[2] Indeed, the non-equilibrium formation of torsional isomers having relatively similar energies has been observed previously in helium droplets.[50] We suggest two possible explanations for the absence of the *cis*-H/DOOO isomer.

One possibility is that the long range OH-O_2 dipole-quadrupole interaction pre-orients the complex as the fragments approach in the droplet, such that the *trans* isomer is formed preferentially. However, this seems unlikely given the randomness of the in-plane angles and relatively weak long range interaction, which is predicted to be on the order of 10 cm^{-1} when the centers of mass are separated by ~5 Å.[13] Instead, it is more likely that the fragment approach geometries are nearly completely randomized, such that the size of the potential basins leading to each isomer determines the relative abundance of the two, suggesting that each should be observed in nearly equal abundance. Nevertheless, the *cis* isomer bands observed in the gas phase are completely absent in the helium droplet spectra. Another possibility is that upon formation and cooling of the *cis* isomer, it is converted to the *trans* isomer *via* a multi-dimensional dynamical tunneling / vibrational energy transfer mechanism that occurs on a timescale that is short in comparison to our measurement timescale. With a 6-dimensional DFT potential, Braams and Yu carried out quantum dynamics calculations that predicted a timescale for this tunneling mechanism on the order of 10 ns,[20] which can be compared to our measurement that occurs ~100-2000 μs after the formation of the HOOO complex. Indeed, one significant difference between the helium droplet spectra and the gas phase IR spectra is the measurement timescale (~20 μs for the gas phase measurement).[4] Nevertheless, the predicted tunneling rate would have to be overestimated by at least a factor of 10^3 to account for the apparent observation of the *cis* isomer in the gas phase IR spectra. A 6D potential in the vicinity of the HOOO complex using an accurate multireference *ab initio* method along with quantum dynamics simulations[51] will be required to accurately assess the tunneling rate, which depends sensitively on the associated barrier heights.

The *cis*-HOOO isomer is indeed elusive, and it is also absent in the FTMW studies. The exceptionally short effective OH bond length derived from the FTMW spectra (0.913 Å)[23] suggests that the HOOO radical may instead be a *single* conformer with a vibrationally averaged non-planar structure. Future theoretical work will be required to confirm this, but it is certainly worthwhile to consider an alternative assignment of the broad features in the gas phase IR spectra that have been tentatively assigned to *cis*-H/DOOO. The broad features in the gas phase spectra of the ν_1 fundamental bands are in the same vicinity as the broad, diffuse features observed in the droplet spectra, which can be unambiguously assigned to HO_3-$(O_2)_n$ clusters.[44] It would therefore be interesting to reinvestigate the gas phase spectra to determine whether or not these broad features could be reassigned to the larger clusters observed here.

References

[1] Murray, C., Derro, E. L., Sechler, T. D., and Lester, M. I., *Acc. Chem. Res.* **42**, 419-427 (2009).

[2] Beames, J. M., Lester, M. I., Murray, C., Varner, M. E., and Stanton, J. F., *J. Chem. Phys.* **134**, 044304 (2011).

[3] Murray, C., Derro, E. L., Sechler, T. D., and Lester, M. I., *J. Phys. Chem. A* **111**, 4727-4730 (2007).

[4] Derro, E. L., Murray, C., Sechler, T. D., and Lester, M. I., *J. Phys. Chem. A* **111**, 11592-11601 (2007).

[5] Derro, E. L., Sechler, T. D., Murray, C., and Lester, M. I., *J. Phys. Chem. A* **112**, 9269-9276 (2008).

[6] Setokuchi, O., Sato, M., and Matuzawa, S., *J. Phys. Chem. A* **104**, 3204-3210 (2000).

[7] Fabian, W. M. F., Kalcher, J., and Janoschek, R., *Theor Chem Acc* **114**, 182-188 (2005).

[8] Mansergas, A., Anglada, J. M., Olivella, S., Ruiz-Lopez, M. F., and Martins-Costa, M., *Phys. Chem. Chem. Phys.* **9**, 5865-5873 (2007).

[9] Denis, P. A., and Ornellas, F. R., *J. Phys. Chem. A* **113**, 499-506 (2009).

[10] Varner, M. E., Harding, M. E., Vazquez, J., Gauss, J., and Stanton, J. F., *J. Phys. Chem. A* **113**, 11238-11241 (2009).

[11] Le Picard, S. D., Tizniti, M., Canosa, A., Sims, I. R., and Smith, I. W. M., *Science* **328**, 1258-1262 (2010).

[12] Anglada, J. M., Olivella, S., and Sole, A., *J. Chem. Theory Comput.* **6**, 2743-2750 (2010).

[13] Varandas, A. J. C., *J. Chem. Theory Comput.* **8**, 428-441 (2012).

[14] Tizniti, M., Le Picard, S. D., Canosa, A., Sims, I. R., and Smith, I. W. M., *Phys. Chem. Chem. Phys.* **12**, 12702-12710 (2010).

[15] Varner, M. E., Harding, M. E., Gauss, J., and Stanton, J. F., *Chem. Phys.* **346**, 53-55 (2008).

[16] Dupuis, M., Fitzgerald, G., Hammond, B., Lester, W. A., and Schaefer, H. F., *J. Chem. Phys.* **84**, 2691-2697 (1986).

[17] Blint, R. J., and Newton, M. D., *J. Chem. Phys.* **59**, 6220-6228 (1973).

[18] Jungkamp, T. P. W., and Seinfeld, J. H., *Chem. Phys. Lett.* **257**, 15-22 (1996).

[19] Suma, K., Sumiyoshi, Y., and Endo, Y., *Science* **308**, 1885-1886 (2005).

[20] Braams, B. J., and Yu, H. G., *Phys. Chem. Chem. Phys.* **10**, 3150-3155 (2008).

[21] Varandas, A. J. C., *Phys. Chem. Chem. Phys.* **13**, 15619-15623 (2011).

[22] Varandas, A. J. C., *Phys. Chem. Chem. Phys.* **13**, 9796-9811 (2011).

[23] McCarthy, M. C., Lattanzi, V., Kokkin, D., Martinez, O., and Stanton, J. F., *J. Chem. Phys.* **136**, 034303 (2012).

[24] Derro, E. L., Sechler, T. D., Murray, C., and Lester, M. I., *J. Chem. Phys.* **128**, 244313 (2008).

[25] Callegari, C., Lehmann, K. K., Schmied, R., and Scoles, G., *J. Chem. Phys.* **115**, 10090-10110 (2001).

[26] Toennies, J. P., and Vilesov, A. F., *Angew. Chem. Int. Ed.* **43**, 2622-2648 (2004).

[27] Choi, M. Y., Douberly, G. E., Falconer, T. M., Lewis, W. K., Lindsay, C. M., Merritt, J. M., Stiles, P. L., and Miller, R. E., *Int. Rev. Phys. Chem.* **25**, 15-75 (2006).

[28] Liang, T., Flynn, S. D., Morrison, A. M., and Douberly, G. E., *J. Phys. Chem. A* **115**, 7437-7447 (2011).

[29] Morrison, A. M., Agarwal, J., Schaefer, H. F., and Douberly, G. E., *J. Phys. Chem. A* **116**, 5299-5304 (2012).

[30] Douberly, G. E., and Miller, R. E., *J. Phys. Chem. B* **107**, 4500-4507 (2003).

[31] Stienkemeier, F., and Lehmann, K. K., *J. Phys. B: At., Mol. Opt. Phys.* **39**, R127-R166 (2006).

[32] Knuth, E., Schilling, B., and Toennies, J. P., *Proceedings of the 19th International Symposium on Rarefied Gas Dynamics* (Oxford University Press, London, 1995), Vol. 19.

[33] Brink, D. M., and Stringari, S., *Z. Phys. D: At., Mol. Clusters* **15**, 257-263 (1990).

[34] Hartmann, M., Miller, R. E., Toennies, J. P., and Vilesov, A., *Phys. Rev. Lett.* **75**, 1566-1569 (1995).

[35] Nauta, K., and Miller, R. E., *J. Chem. Phys.* **115**, 10138-10145 (2001).

[36] Chin, S. A., and Krotscheck, E., *Phys Rev B* **52**, 10405-10428 (1995).

[37] Automation of an Aculight Optical Parametric Oscillator

[38] Lewerenz, M., Schilling, B., and Toennies, J. P., *J. Chem. Phys.* **102**, 8191-8207 (1995).

[39] Melen, F., Sauval, A. J., Grevesse, N., Farmer, C. B., Servais, C., Delbouille, L., and Roland, G., *J. Mol. Spectrosc.* **174**, 490-509 (1995).

[40] CFOUR, Coupled-Cluster techniques for Computational Chemistry, a quantum-chemical program package by J.F. Stanton, J. Gauss, M.E. Harding, P.G. Szalay with contributions from A.A. Auer, R.J. Bartlett, U. Benedikt, C. Berger, D.E. Bernholdt, Y.J. Bomble, L. Cheng, O. Christiansen, M. Heckert, O. Heun, C. Huber, T.-C. Jagau, D. Jonsson, J. Jusélius, K. Klein, W.J. Lauderdale, D.A. Matthews, T. Metzroth, D.P. O'Neill, D.R. Price, E. Prochnow, K. Ruud, F. Schiffmann, W. Schwalbach, S. Stopkowicz, A. Tajti, J. Vázquez, F. Wang, J.D. Watts and the integral packages MOLECULE (J. Almlöf and P.R. Taylor), PROPS (P.R. Taylor), ABACUS (T. Helgaker, H.J. Aa. Jensen, P. Jørgensen, and J. Olsen), and ECP routines by A. V. Mitin and C. van Wüllen. For the current version, see http://www.cfour.de.

[41] Amiot, C., Maillard, J. P., and Chauville, J., *J. Mol. Spectrosc.* **87**, 196-218 (1981).

[42] Hartmann, M., Mielke, F., Toennies, J. P., Vilesov, A. F., and Benedek, G., *Phys. Rev. Lett.* **76**, 4560-4563 (1996).

[43] Raston, P. L., Knapp, C. J., and Jager, W., *Phys. Chem. Chem. Phys.* **13**, 18789-18798 (2011).

[44] Nauta, K., and Miller, R. E., *J. Chem. Phys.* **113**, 10158-10168 (2000).

[45] Liang, T., Raston, P. L., and Douberly, G. E., *ChemPhysChem*, submitted (2012).

[46] Callegari, C., Reinhard, I., Lehmann, K. K., Scoles, G., Nauta, K., and Miller, R. E., *J. Chem. Phys.* **113**, 4636-4646 (2000).

[47] Douberly, G. E., and Miller, R. E., *J. Chem. Phys.* **122**, 024306 (2005).

[48] Rocher-Casterline, B. E., Ch'ng, L. C., Mollner, A. K., and Reisler, H., *J. Chem. Phys.* **134**, 211101 (2011).

[49] Beswick, J. A., and Jortner, J., *Adv. Chem. Phys.* **47**, 363-506 (1981).

[50] Skvortsov, D. S., and Vilesov, A. F., *J. Chem. Phys.* **130**, 151101 (2009).

[51] Dawes R., Personal Communication (2012)

Chapter 5

Dipole Moment of the HOOO Radical: Resolution of a Structural Enigma

A global six-dimensional potential surface for the hydridotrioxygen radical (HOOO) is needed for an accurate assessment of its atmospheric abundance. We report inertial dipole moment components obtained from Stark spectra of the *trans*-HOOO system solvated in superfluid helium, and these are shown to be stringent benchmarks for theoretical computations of the potential surface. Computed dipole moment components at the CCSD(T)/CBS equilibrium geometry disagree qualitatively with the experimental values. The role of large-amplitude motion and vibrational averaging is assessed by computing the ground state wave function on a relaxed, two-dimensional potential surface for the $HO_1O_2O_3$ torsional and O_1O_2 bond-stretching coordinates. The experimental and computed vibrationally averaged dipole moments agree only after shifting the potential along the O_1O_2 bond coordinate, indicating that single-reference CCSD(T)/CBS computations underestimate $r_e(O_1O_2)$ by ≈0.08 Å. In a joint report with our group, Allen and Magers have shown that an optimized *trans*-HOOO geometry at the composite all-electron CCSDT(Q)/CBS level reveals that the inclusion of full triples and a perturbative treatment of quadruple excitations leads to an increase in $r_e(O_1O_2)$ by 0.07 Å. (see Ref. 1)

5.1 Introduction

The abundance of HOOO in the atmosphere and its role as a sink for hydroxyl radicals has been a subject of recent debate.[2-5] The currently accepted experimental value for its dissociation energy (D_0=2.94(7) kcal mol^{-1}) indicates a relatively minor role.[3, 6] Computations of D_0 at high levels of multireference configuration interaction[5, 7] and single-reference coupled cluster theory[8] are generally within 0.5 kcal mol^{-1} of this experimental result, which is derived from the kinetics of OH decay in the presence of excess O_2.[3, 6] However, theoretical predictions of D_0 are complicated by the floppy nature of HOOO, which executes large-amplitude torsional motion on a potential surface that has a low barrier between *cis* and *trans* isomers.[4, 9] Indeed, an accurate theoretical prediction of atmospheric HOOO abundance demands a zero-point energy and partition function derived from a global six-dimensional potential surface. Furthermore, for an accurate global surface, size-extensive multireference methods have been suggested to be essential,[10] as single-reference coupled cluster methods so far appear to be incapable of reproducing the empirically derived equilibrium structure.[9-11] We report here a measurement of the inertial dipole components of *trans*-HOOO, which prove to be stringent benchmarks for computations that include the effects of vibrational averaging. Moreover, in a joint report with Allen and Magers, an equilibrium geometry (Fig. 5.1) computed at the composite, all-electron CCSDT(Q) level is reported that is considerably improved over previous CCSD(T) results and is in very good agreement with the empirical r_e structure and dipole moment (See Ref. 1).

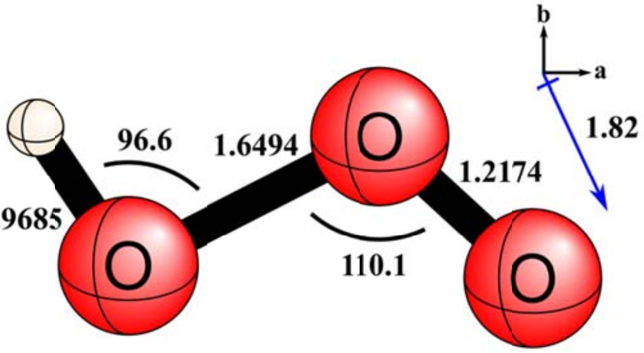

Figure 5.1: Equilibrium *trans*-HOOO structure and dipole moment computed at the composite, all-electron CCSDT(Q)/CBS level of theory (Ref. 1).

5.2 Experimental Section

The HENDI experimental method has been reviewed,[12-14] and the details associated with the spectroscopy of He-solvated H/DOOO are discussed elsewhere.[15, 16] Approximately 10 nm diameter droplets (≈4000 He atoms) were formed in an expansion of He (99.9995%) into vacuum through a 5 μm diameter cryogenic (15-17 K) nozzle. The OH/D radical was produced via the pyrolysis of tert-butyl hydroperoxide.[15, 17] The droplets picked up the OH/D and O_2 reactants sequentially as the droplet beam passed first through the pyrolysis source and then through a gas pick-up cell containing O_2 at $\approx 1\times10^{-6}$ Torr. The combination of OH/D and O_2 in the droplets leads to the barrierless formation of H/DOOO. The doped droplet beam passed through a multipass/Stark cell, consisting of two parallel electrodes situated orthogonal to two gold-coated mirrors. While in the presence of the applied dc electric field, the droplets were irradiated with the idler output from a continuous wave, IR, optical parametric oscillator (OPO).[18] Resonant vibrational excitation leads to a reduction in the geometric cross section of the H/DOOO doped droplets and a concomitant decrease in their electron impact ionization cross section. This allowed for an IR action spectroscopy that was achieved by demodulating the mass spectrometer ion signal (mass channel 33 u; HO_2^+) with a lock-in amplifier as the amplitude modulated OPO idler beam (80 Hz) was tuned continuously with ≈10 MHz resolution.

5.3 Computational Methods

The equilibrium structure of *trans*-$HO_1O_2O_3$ was computed at the CCSD(T)/Def2-TZVPD level of theory using the CFOUR program package.[19] Two-dimensional potential energy and dipole moment surfaces were computed at this same level of theory by varying $r(O_1O_2)$ and $\tau(HO_1O_2O_3)$ while optimizing all other degrees of freedom. These surfaces were fitted to standard functional forms involving a Morse variable in r and a Fourier expansion in τ. The vibrational kinetic energy operator was expressed in internal bond-angle coordinates according to the procedure of Frederick and Woywod,[20] and the two-dimensional Schrödinger equation was solved in a discrete variable representation (sinc-DVR of Colbert and Miller).[21] The resulting fundamental torsional frequency is in good agreement with that derived from one-dimensional models reported here (Table 5.1 and Fig. 5.11) and elsewhere.[4] The ground state wave functions of *trans*-H/DOOO and *cis*-HOOO were used to vibrationally average both μ_a and μ_b dipole components and other geometric parameters for comparison with experimental results (Table 5.2 and Table 5.3). The details associated with the *ab initio* computations, the potential fitting procedure, and the vibrational averaging procedure are available in section 5.6.

Table 5.1: The comparison between experimental and theoretical vibrational frequencies for the torsional modes of HOOO and DOOO.

	ΔE_{theory}				**ΔE_{exp}** [b]
	CCSD(T)/Def2-TZVPD	**Scaled CCSD(T)**	**EOMIP-CCSD*/ANO1** [a]	**Scaled EOMIP-CCSD*** [a]	
v_6 *trans*-HOOO	100	125	109	132	129
$2v_6$ *trans*-HOOO	174	221	183	230	229
v_6 *cis*-HOOO	110	141	129	147	148
v_6 *trans*-DOOO	80	99	86	104	102
v_6 *cis*-DOOO	93	122	113	124	90/103
Torsional barrier	246	344	255	344	-

[a] Ref. 4

[b] Ref. 22

Table 5.2: CCSD(T)/Def2-TZVPD equilibrium, two-dimensional vibrationally averaged, and experimental dipole moment components and geometric parameters for *trans*-HOOO.[a]

trans-HOOO	μ_a/D	μ_b/D	HO_1/Å [b]	O_1O_2/Å	O_2O_3/Å	HO_1O_2/°	$O_1O_2O_3$/°
Experiment r_0	**0.61(2)** [c]	**1.48(2)** [c]	0.913(26) [d]	**1.684(3)** [d]	1.235(4) [d]	92.4(14) [d]	110.7(3) [d]
r_e^{emp} [e]			0.944	**1.660**	1.225	95.3	110.3
r_e [f]	**–0.99**	**1.63**	0.976 (0.976)	**1.611**	1.228	97.2	109.9
$\langle r\rangle$ [g]	**–0.83**	**1.50**	0.976 (0.885)	**1.635**	1.227	96.8	110.2
$\langle r\rangle$ (r_e+0.05 Å) [h]	**–0.62**	**1.50**	0.976 (0.885)	**1.684**	1.220	96.2	110.3
$\langle r\rangle$ (r_e+0.05 Å) scaled [i]	**–0.64**	**1.53**	0.976 (0.901)	**1.681**	1.220	96.2	110.3

[a] *trans*-DOOO and *cis*-HOOO data provided in Table 5.3.

[b] Projection of the HO_1 bond length onto the $O_1O_2O_3$ plane is given in parentheses, which should be compared directly to the result from microwave spectroscopy (0.913(26) Å).

[c] This work. Absolute value.

[d] FTMW, Ref. 11.

[e] CCSD(T)/aug-cc-pVTZ, Ref. 11.

[f] This work.

[g] Vibrationally averaged values without modification.

[h] Vibrationally averaged values after shifting the potential by +0.05 Å ($r(O_1O_2)$ coordinate).

[i] Vibrationally averaged values after shifting the potential by +0.05 Å ($r(O_1O_2)$ coordinate) and scaling the potential to have a torsional barrier height of 344 cm^{-1} (to reproduce the empirical barrier height from Ref. 4).

Table 5.3: This table summarizes both μ_a, μ_b dipole components and geometrical parameters from experimental measurement and various theoretical treatments. The three rows of r_e (1.611 Å), r_e+0.05 Å, and r_e+0.05 Å scaled stands for 2D vibrational averaging from CCSD(T)/Def2-TZVPD result without modification, shifting the wavefunction by +0.05 Å, and shifting the wavefunction by +0.05 Å and scaled the potential to have a torsional barrier height of 344 cm^{-1} (i.e. the empirically determined barrier height from Ref. 4).

		μ_a/Debye	**μ_b/Debye**	**HO_1/Å**	**O_1O_2/Å**	**O_2O_3/Å**	**HO_1O_2/°**	**O_1O_2 O_3/°**
trans-HOOO	*ab initio* Equilibrium	0.99	1.63	0.976	1.611	1.228	97.2	109.9
	Experiment	0.61(2)	1.48(2)	0.913(26)*	1.684(3)*	1.235(4)*	92.4(14)*	110.7(3)*
	r_e (1.611 Å)	0.83	1.50	0.885	1.635	1.227	96.8	110.2
	r_e+0.05 Å	0.62	1.50	0.885	1.685	1.220	96.2	110.3
	r_e+0.05 Å scaled	0.64	1.53	0.901	1.681	1.220	96.2	110.3
cis-HOOO	*ab initio* Equilibrium	0.02	1.05	0.978	1.552	1.248	97.5	112.0
	r_e (1.552 Å)	0.08	0.98	0.902	1.579	1.244	97.3	112.2
	r_e+0.05 Å	0.26	0.98	0.901	1.629	1.235	96.4	112.6
	r_e+0.05 Å scaled	0.26	1.00	0.920	1.624	1.236	96.4	112.5
trans-DOOO	Experiment	0.62(1)	1.52(2)	-	-	-	-	-
	r_e (1.611 Å)	0.85	1.53	0.910	1.635	1.227	96.8	110.1
	r_e+0.05 Å	0.64	1.54	0.91	1.685	1.220	96.2	110.3
	r_e+0.05 Å scaled	0.66	1.56	0.922	1.681	1.220	96.2	110.3

* Ref. 11

5.4 Experimental Results

The HOOO radical was produced from the barrierless association of OH and O_2 within the dissipative environment of a 0.4 K helium nanodroplet.[15] The rotationally resolved spectrum of the OH stretch near 3570 cm^{-1} was measured with several different electric field strengths applied to the laser interaction region. The series of Stark spectra obtained in this way are shown in Fig. 5.2, and the red traces correspond to simulations of an asymmetric top in an electric field parameterized with the constants reported in Table 5.4. The separation between the *a*- and *b*-type spectral features and the structure within each band type are rather sensitive to the magnitudes of the *a*-/*b*- inertial components (μ_a and μ_b) of the permanent electric dipole moment. The uncertainties in the reported dipole components derive largely from those associated with the applied field strengths. When comparisons are available, the dipole moments of molecules in superfluid helium are typically less than 1 percent different from those measured for the isolated gas-phase species.[12] A linear, highly-polar molecule, such as HCCCN or HCN, creates a prolate cavity in the He droplet, and the electrostatic polarization of the liquid leads to a small (2 to 4%) reduction in the measured dipole moment, although these represent the most extreme observed deviations.[23] We estimate that the magnitude of the dipole components measured for the He-solvated HOOO radical will differ from the gas-phase values to a degree that is less than the experimental uncertainty (±0.02 D).[23]

Table 5.4: Constants used in the Stark simulations shown in Fig. 5.2.[a]

Stark Field / kV cm^{-1}	μ_a/D	μ_b/D
HOOO		
40.3(4) $_{//}$	0.60(2)	1.46(2)
31.0(3) $_{//}$	0.61(2)	1.48(2)
15.5(2) $_{//}$	0.60(5)	1.4(1)
31.0(3) $_{\perp}$	0.60(3)	1.50(5)
15.5(2) $_{\perp}$	0.60(5)	1.5(1)
DOOO		
29.8(3) $_{//}$	0.62(1)	1.52(2)
15.0(3) $_{//}$	0.64(2)	1.58(4)

[a] The μ_a and μ_b dipole moment components are adjusted to obtain satisfactory agreement between the simulation and experiment, and uncertainties are estimated. The rotational constants and line widths are kept fixed to the values obtained from the zero-field *trans*-H/DOOO ν_1 band.[15] The band origins, ν_0, in the Stark simulations are 0.005 cm^{-1} less than the previously measured zero-field values.[15] The difference is due to a Doppler shift of the zero-field spectrum, which is measured with the helium droplet and laser beams counter-propagating. The Stark measurements are made in a configuration in which the laser beam is aligned perpendicular to the droplet beam.

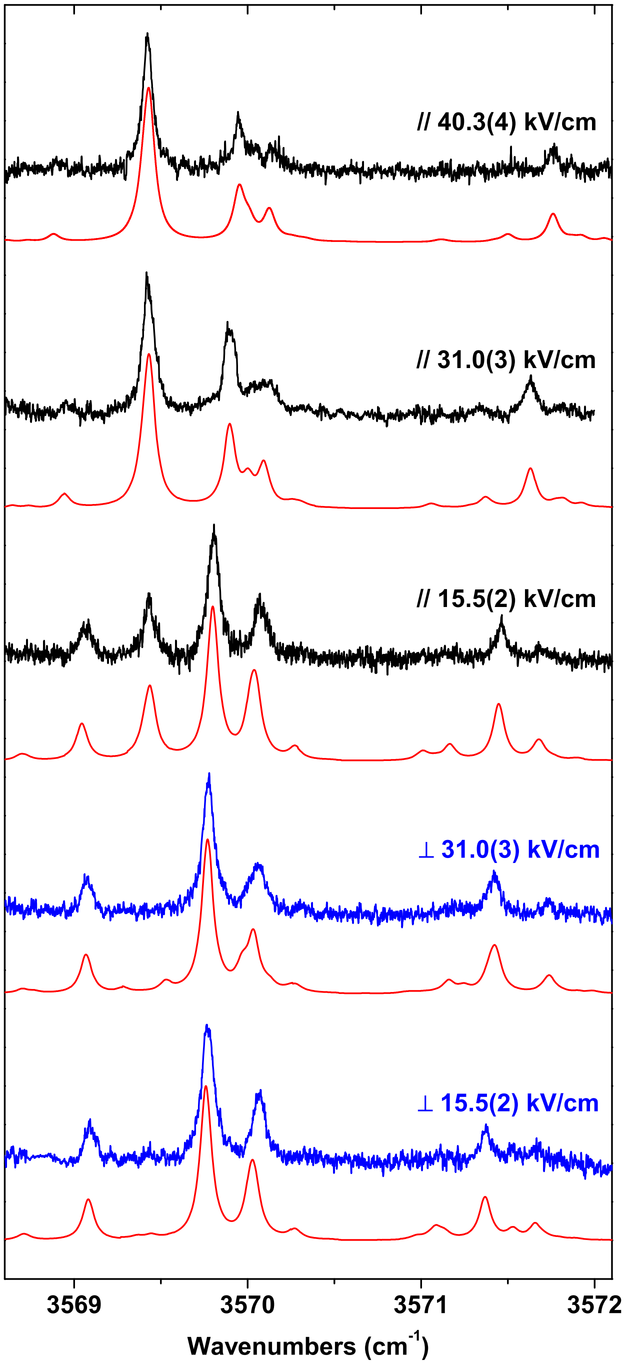

Figure 5.2: Stark spectra and simulations for the OH stretch, ν_1 band of the *trans*-HOOO radical at 40.3(4), 31.0(3), and 15.5(2) kV cm^{-1} electric field strengths. The laser polarization is aligned either parallel (black) or perpendicular (blue) to the Stark field, leading to either ΔM=0 or ΔM=±1 selection rules, respectively (see Fig. 5.3 for *trans*-DOOO Stark spectra).

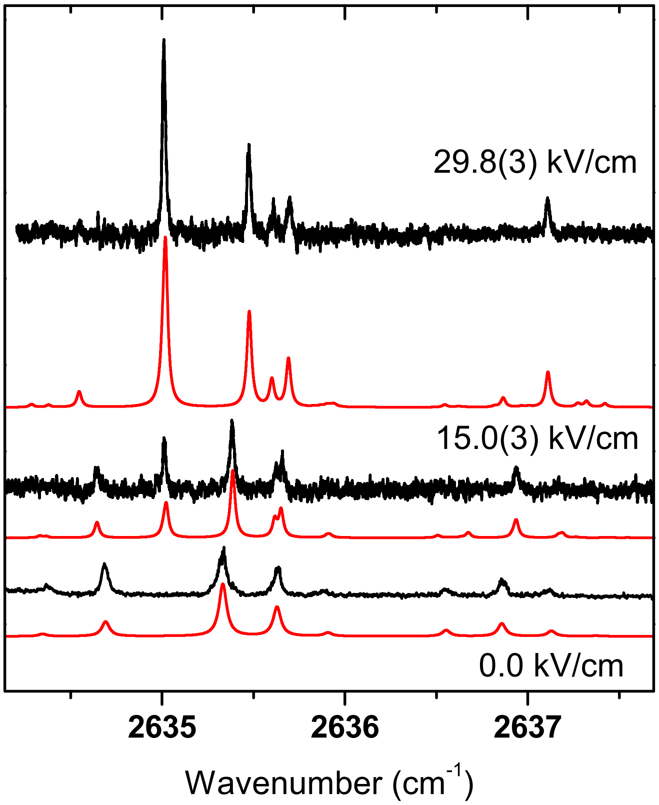

Figure 5.3: Stark spectra and simulations for the OD stretch, ν_1 band of the *trans*-DOOO radical at 29.8(3) and 15.0(3) kV/cm electric field strengths. The laser polarization is aligned parallel to the Stark field. The constants used in the simulations are shown in Table 5.4.

5.5 Discussion and Conclusions

The experiment necessarily reveals the dipole components averaged over the ground vibrational wave function, and a comparison of these ($\langle\mu_a\rangle$ = 0.61(2), $\langle\mu_b\rangle$ = 1.48(2) D) to the equilibrium values computed at the CCSD(T) complete basis set limit (CBS) level ($\mu_a = -1.01$, $\mu_b = 1.63$ D) reveals a large (qualitative) discrepancy (see also

Fig. 5.4). A direct comparison to computed equilibrium values is perhaps not warranted here because of the anharmonic,[4] low frequency (129 cm^{-1})[22] torsional mode present in HOOO. This large-amplitude motion appears to be unaffected by the helium solvent, as the fundamental torsional frequency measured in He droplets is within 1 cm^{-1} of the gas-phase value.[15]

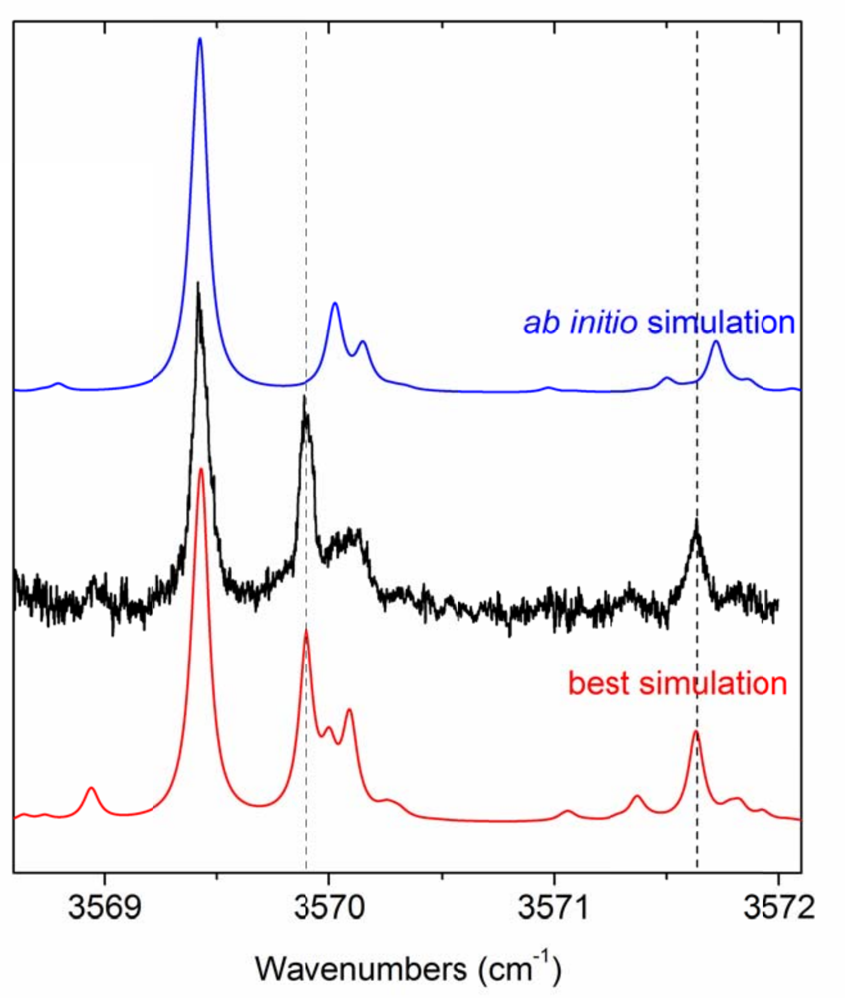

Figure 5.4: Comparison of two 31.0(3) kV/cm parallel polarization Stark simulations to the experimental spectrum. The blue trace is produced with the CCSD(T)/aug-cc-pVQZ equilibrium dipole moment components, and the red trace is produced with the best fit constants given in Table 5.4.

Computations were carried out at the CCSD(T)/Def2-TZVPD[24] level to test the sensitivity of μ_a and μ_b to motion along the $\tau(HO_1O_2O_3)$ torsional and $r(O_1O_2)$ central bond-stretching coordinates. For a *fixed* geometry (r_e at the CCSD(T)/Def2-TZVPD level), we find that the dipole components converge surprisingly quickly with increasing level of theory (Table 5.5), and the difference between the CCSD(T)/Def2-TZVPD level and multireference configuration interaction (MRCI(19,13)/Def2-TZVPD) or higher level single-reference coupled cluster (CCSDT(Q)/CBS) levels is approximately one percent. The dipole components, however, are extremely sensitive to deviations from the equilibrium structure along these degrees of freedom. For example, the magnitude of μ_a changes from 1.15 to 0.67 D as the central O_1O_2 bond is elongated from 1.58 to 1.68 Å (all other coordinates relaxed, Fig. 5.10). Moreover, μ_a changes from −0.99 D at the *trans* equilibrium geometry to −0.12 D at the transition state associated with the torsional interconversion to the *cis* isomer (Fig. 5.11). These computations strongly suggest that it is inappropriate to directly compare the inertial dipole components computed at the equilibrium *trans*-HOOO geometry to those obtained from Stark measurements.

Table 5.5: Inertial dipole moment components at various levels of theory for the CCSD(T)/Def2- TZVPD equilibrium geometry.

	μ_a/D	μ_b/D
B3LYP/Def2-TZVPD	−0.9589	1.6484
MP2/Def2-TZVPD	−1.0278	1.7529
CASSCF(19,13)/Def2-TZVPD	−1.0412	1.6754
MRCI(19,13)/Def2-TZVPD	−1.0127	1.6400
CCSD(T)/CBS [a]	−1.0080	1.6272
CCSDT(Q)/CBS [a]	−0.9991	1.6366
CCSD(T)/Def2-TZVPD	**−0.9917**	**1.6259**

[a] The description of the CBS extrapolation is provided in Ref. 1.

To account for large amplitude motion, we have vibrationally averaged the dipole components computed on a two-dimensional, relaxed potential surface (CCSD(T)/Def2-TZVPD) for the torsional and central bond-stretching coordinates (see section 5.6). These were chosen because the two lowest frequency vibrational modes consist of motion largely along the $\tau(HO_1O_2O_3)$ and $r(O_1O_2)$ coordinates, respectively, and these degrees of freedom have been shown to be significantly coupled (see Ref. 4 and Fig. 5.5). For example, at this level of theory, the O_1O_2 bond length varies from 1.611 to 1.552 Å in going from the *trans* to *cis* configuration. Moreover, test calculations indicate that the dipole components are less sensitive to small deviations about the other four, more rigid degrees of freedom (see Table 5.6 and Fig. 5.6). The two-dimensional potential surface and the four lowest bound state wave functions are shown in Fig. 5.7 and Fig. 5.8. The surfaces for the dipole components and the other geometric parameters are shown in Fig. 5.9, and the ground state wave function is superimposed on each surface. Experimentally, we find evidence for only the *trans* isomer,[15] and, at the droplet temperature, the entire *trans*-HOOO population resides in the vibrational ground state. The vibrational averaging therefore consists of computing the expectation value of each property weighted by the *trans*-(0,0) torsional-vibrational wave function. The results are given in Table 5.2.

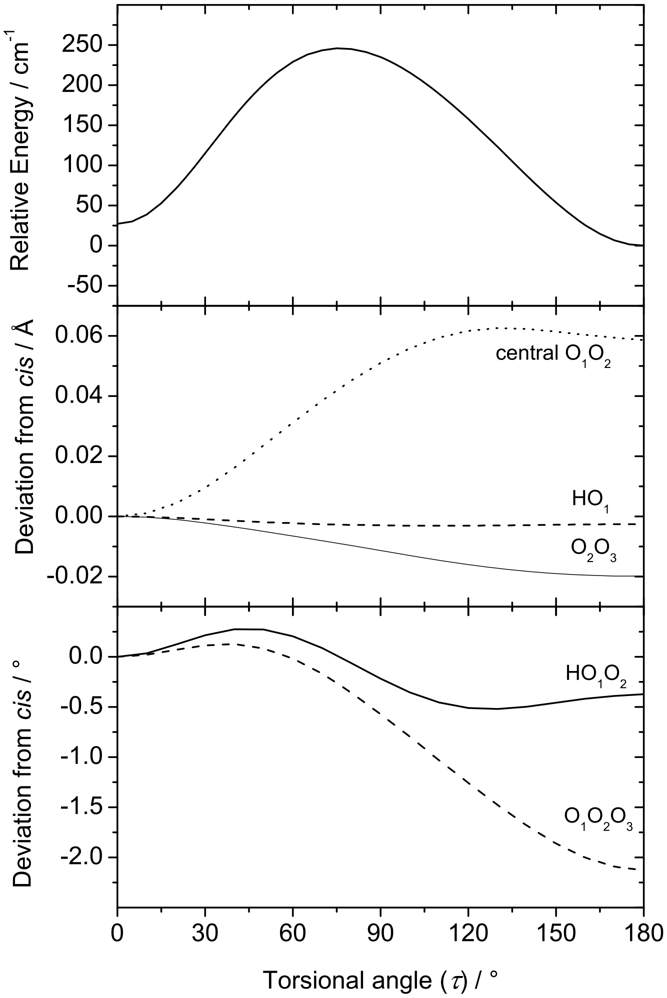

Figure 5.5: Deviation from the *cis* geometry along the torsional degree of freedom, computed at the CCSD(T)/Def2-TZVPD level of theory. Zero degrees is *cis* and 180 degrees is *trans*. From this it is apparent that the OOO bond angle and the central OO bond length are the degrees of freedom that are most strongly couple to the torsional motion. This figure is of the same format as Fig. 5 from Ref. 4, but now at the level of theory employed in this work.

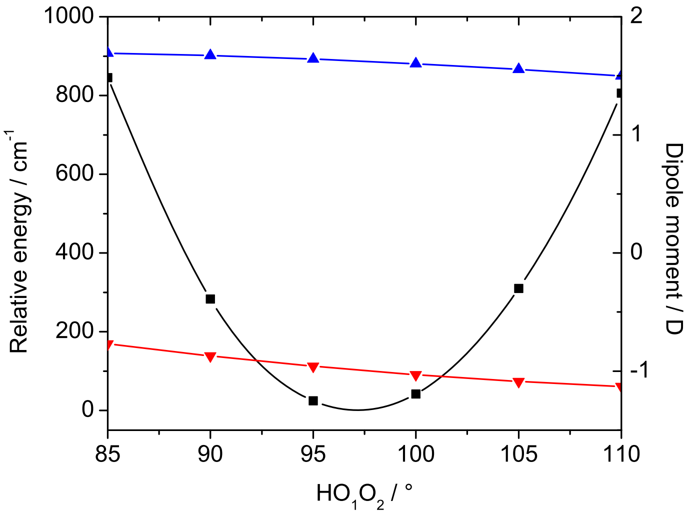

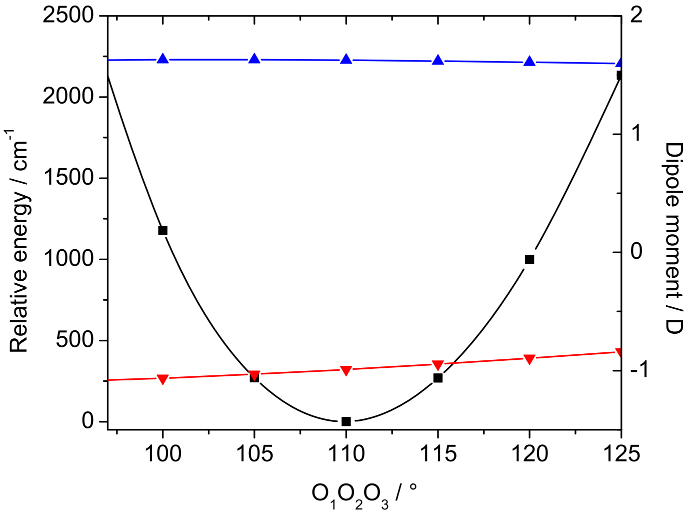

Figure 5.6: Potential scans at the CCSD(T)/Def2-TZVPD level for the HO_1O_2 (top) and $O_1O_2O_3$ (bottom) coordinates (black squares). μ_a and μ_b curves are shown as red or blue triangles, respectively (see Fig. 5.10).

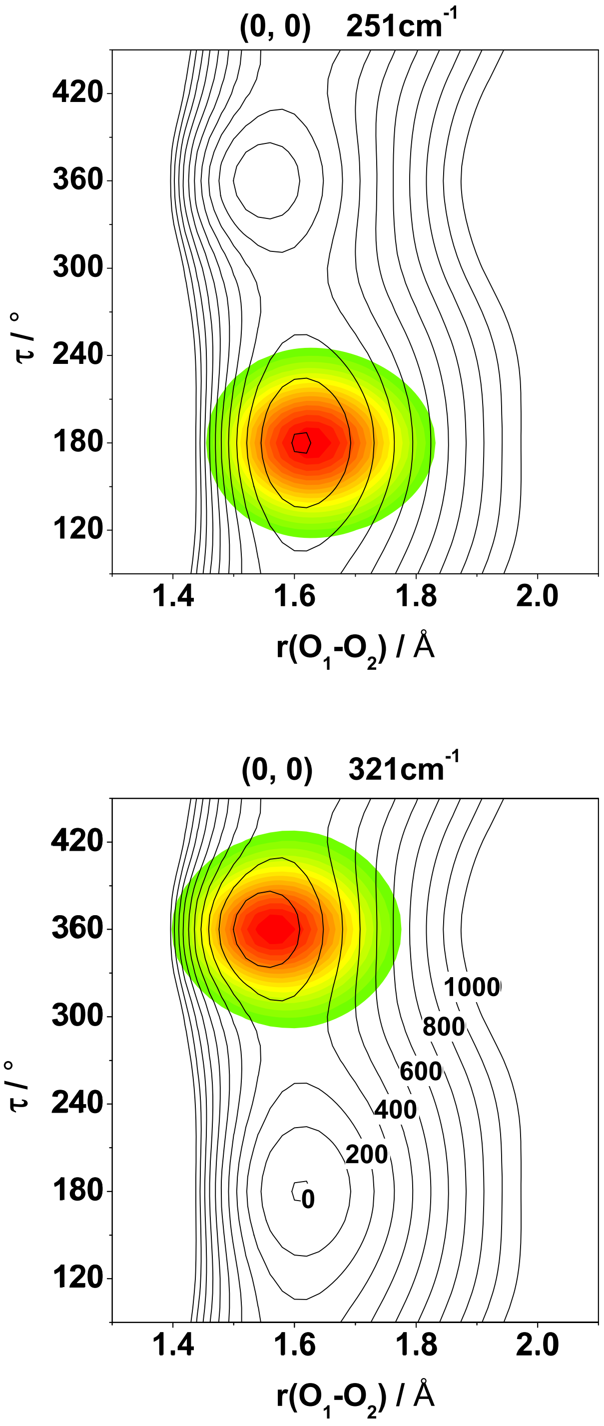

Figure 5.7: The CCSD(T)/Def2-TZVPD potential energy surface and two lowest bound state wave functions of HOOO, with eigenvalues 251 cm^{-1} (*trans*) and 321 cm^{-1} (*cis*). The numbers in parentheses indicate the quantum numbers, (v_r, v_τ). The wave functions associated with other eigenvalues are given in Fig. 5.8.

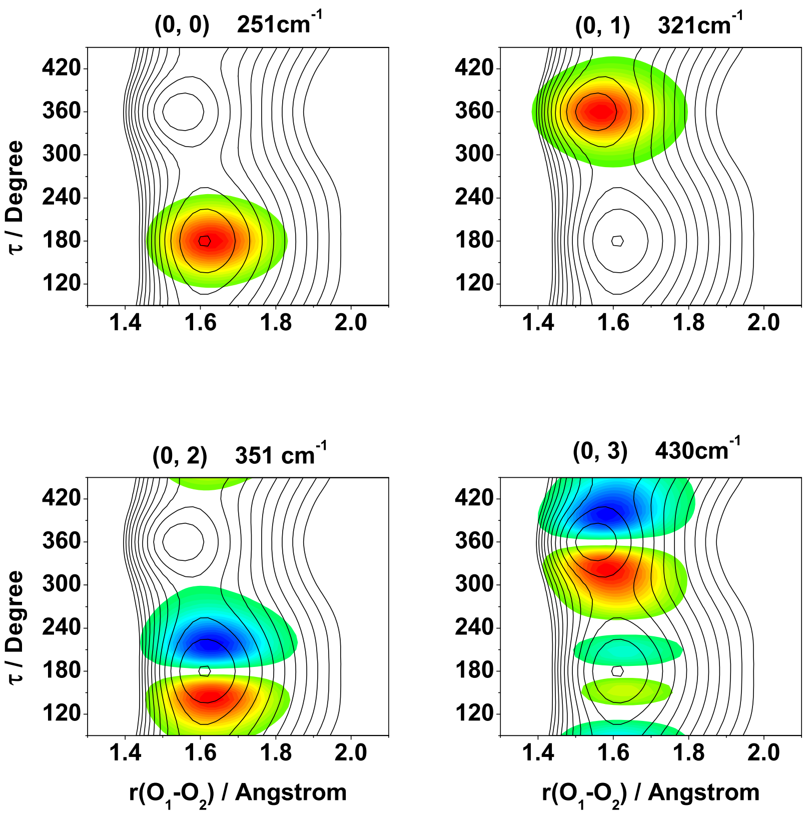

Figure 5.8: The four lowest energy vibrational wavefunctions of HOOO below H-O_1-O_2-O_3 torsional barrier. The numbers in parentheses indicate the quantum numbers of v_r, v_φ. All four wavefunctions shown here have 0 quanta for the O_1-O_2 stretching mode.

Table 5.6: Harmonic frequencies of trans-HOOO at CCSD(T)/cc-pVQZ level of theory.

Frequency(Intensity)	Symmetry
134.0(106)	a"
348.8(78)	a'
588.0(20)	a'
1201.5(110)	a'
1377.7(41)	a'
3762.8(58)	a'

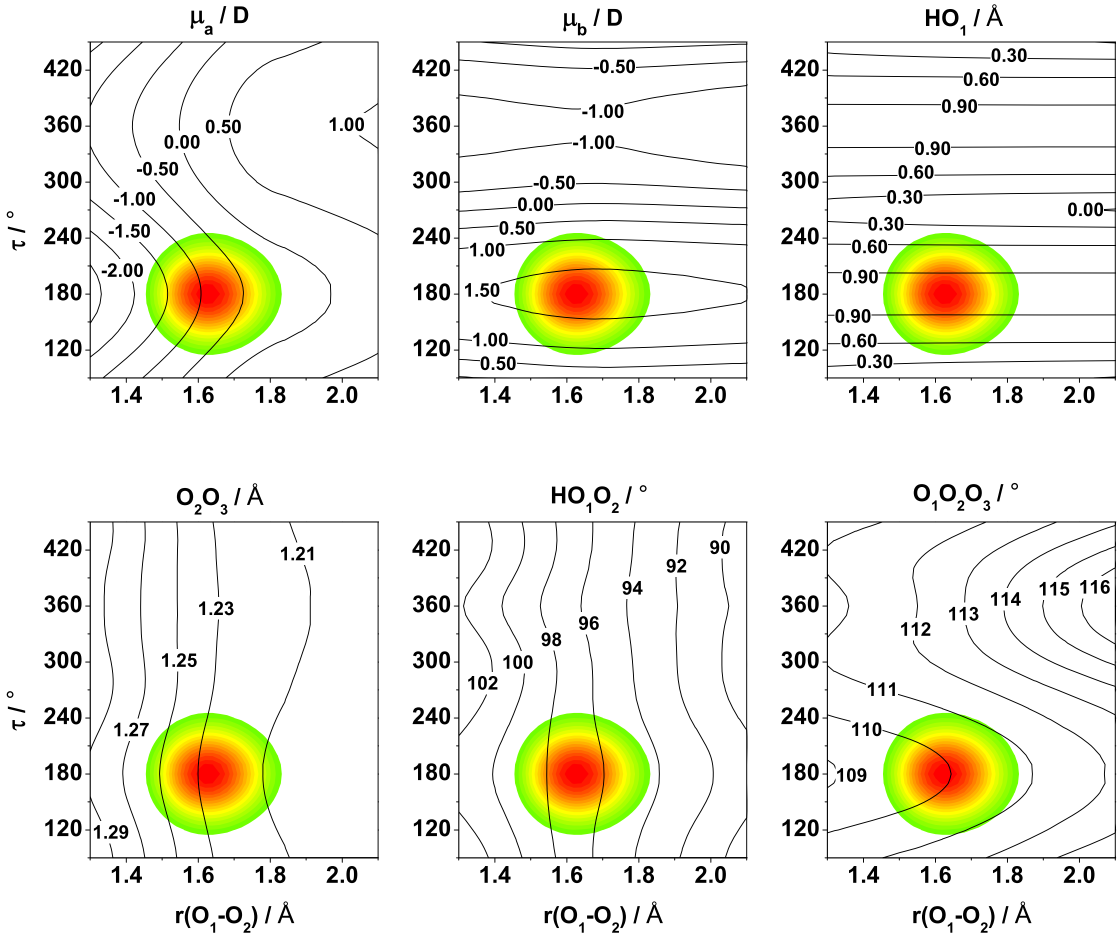

Figure 5.9: The ground state wave function of *trans*-HOOO superimposed on the dipole moment surfaces, μ_a and μ_b, and the surfaces for the HO_1 bond length (projected on the $O_1O_2O_3$ plane), the O_2O_3 bond length, the HO_1O_2 angle, and the $O_1O_2O_3$ angle.

The role of vibrational averaging is to increase the central O_1O_2 bond length by 0.025 Å. For comparison, this is similar to the reported difference between the effective bond length obtained from microwave spectroscopy (r_0 = 1.684 Å) and the "empirical equilibrium" value derived from the observed rotational constants and vibration-rotation constants computed with VPT2 theory (r_e^{emp} = 1.660 Å).[11] A caveat in this comparison is that the perturbation theory upon which both the spectroscopic and theoretical zero-point vibrational energy corrections are based is problematic for large-amplitude motions, as found in HOOO. Two-dimensional vibrational averaging also has the notable effect of reducing the magnitude of μ_a by ≈0.16 D and μ_b by ≈0.13 D, bringing into better agreement the experimental ($\langle\mu_a\rangle$ = 0.61(2), $\langle\mu_b\rangle$ = 1.48(2) D) and CCSD(T)/Def2-TZVPD ($\langle\mu_a\rangle$ = 0.83, $\langle\mu_b\rangle$ = 1.50 D) dipole components, although a significant discrepancy remains for $\langle\mu_a\rangle$. However, at the CCSD(T)/Def2-TZVPD level, $r_e(O_1O_2)$ is apparently underestimated by as much as 0.05 Å, and the equilibrium μ_a value is therefore overestimated. Indeed, upon shifting the $r(O_1O_2)$ coordinate of the potential ($r_e^{\text{shifted}} = r_e^{\text{CCSD(T)}} + 0.05$ Å), such that the vibrationally averaged O_1O_2 distance equals 1.684 Å, the computed and experimental vibrationally averaged dipole moment com-ponents agree quantitatively. We also note that the vibrational averaging scheme employed here can account for the anomalous HO_1 bond length derived from microwave spectroscopy, which necessarily measures its average projection onto the plane of the oxygen atoms (see Table 5.2).

A comparison of the experimental effective and computed equilibrium geometric parameters is shown in Table 5.7. The previously reported multireference results modestly overestimate the central bond length (+0.02 to +0.03 Å). In comparison, the single-reference CCSD(T)/CBS computation considerably underestimates the bond length by 0.08 Å. Allen and Magers have computed a fully optimized *trans*-HOOO geometry at the CCSDT(Q)/CBS level according to the procedure described in Ref. 1. Upon inclusion of full triples and a perturbative treatment of quadruple excitations, the equilibrium O_1O_2 bond length increases to 1.65 Å, only 0.01 Å below the empirical value. The CCSDT(Q)/CBS μ_a and μ_b components at the corresponding equilibrium geometry are

–0.78 and 1.64 D, respectively, which are in excellent agreement with experiment once vibrational averaging is accounted for, as discussed above. Finally, we note that the classical dissociation energy at the CCSDT(Q)/CBS equilibrium geometry ($r_e(O_1O_2) = 1.649$ Å) is 5.79 kcal mol^{-1}. In comparison, the previously reported CCSDT(Q)/CBS value computed at the CCSD(T)/cc-pVQZ equilibrium geometry ($r_e(O_1O_2) = 1.584$ Å) is 5.21 kcal mol^{-1}.[8] Harmonic frequencies computed at the CCSD(T)/cc-pVQZ level allow for an estimate of D_0 (2.84 kcal mol^{-1}) at the CCSDT(Q)/CBS geometry. The combined effect of vibrational anharmonicity, spin-rotation interactions, and spin-orbit interactions on the difference between complex and monomer zero-point energies has recently been estimated by Suma *et al.* with an MRCI+Q force field.[25] Employing their results, we obtain a CCSDT(Q)/CBS D_0 of 3.01 kcal mol^{-1}, which is in excellent agreement with the aforementioned value (2.94(7) kcal mol^{-1}) derived from the supersonic flow experiments.[3]

The CCSD(T)/CBS underestimation of $r_e(O_1O_2)$ is surprising, because it has been demonstrated that HOOO is less of a multireference case than the isoelectronic FOO system,[26] for which CCSD(T) computations reproduce accurately the empirical r_e(FO). The increase in $r_e(O_1O_2)$ by 0.07 Å in going from CCSD(T)/CBS to the composite all-electron CCSDT(Q)/CBS level is indicative of the small binding energy and stretched O_1O_2 bond in HOOO, which make it a prime candidate for the observed unusual sensitivity to level of theory. Apparently, the role of dynamic correlation is substantial, and high-order, single-reference correlation methods *are* capable of generating an accurate description for the HOOO system, at least in the vicinity of the complex. Recent multireference coupled cluster methods[27-30] could provide a proper size-extensive treatment of the full potential energy surface for HO–O_2 dissociation, but this approach does not appear necessary to solve the dipole moment and structural enigma of concern in this report.

Table 5.7: Experimental effective structure, empirical equilibrium structures, and *ab initio* equilibrium structures computed at various levels of theory.

	HO_1/Å	O_1O_2/Å	O_2O_3/Å	HO_1O_2/°	$O_1O_2O_3$/°
trans-HOOO					
r_0[a]	0.913(26)	**1.684(3)**	1.235(4)	92.4(14)	110.7(3)
r_e^{emp} CCSD(T)[b]	0.944	**1.660**	1.225	95.3	110.3
r_e^{emp} MRCI[c]	0.961	**1.665**	1.218	95.2	110.4
MRCI+Q(25,16)/aug-cc-pV5Z[c]	0.968	**1.693**	1.211	96.2	109.6
MRCI(19,13)/cc-pVQZ[d]	0.967	**1.688**	1.215	95.4	110.5
CASPT2(19,15)/aug-cc-pVTZ[e]	0.972	**1.682**	1.221	95.8	110.2
CCSD(T)/CBS[f]	0.969	**1.582**	1.226	97.5	109.7
CCSDT(Q)/CBS[g]	0.9685	**1.6491**	1.2174	96.6	110.1
$OH(^2\Pi)+O_2(^3\Sigma_g^-)$					
Experimental, r_e[h]	0.9697		1.2075		
CCSDT(Q)/CBS[g]	0.9697		1.2069		

[a] FTMW, Ref. 11.

[b] Ref. 11.

[c] Ref. 25.

[d] Ref. 5.

[e] Ref. 7.

[f] Ref. 26. Core electrons were excluded in correlation calculations.

[g] This work.

[h] Ref. 31.

5.6 Vibrational Averaging of *trans*-$HO_1O_2O_3$

All electronic structure and dipole surface calculations for the vibrational averaging are carried out at the CCSD(T)/Def2-TZVPD level of theory using the program CFOUR.[19] The $^2A''$ unrestricted Hartree-Fock (UHF) reference wavefunction is used for the correlation energy computation. All core orbitals are kept frozen in this case.

5.6.1 One-dimensional Vibrational Averaging of O_1-O_2 Bond Stretching

The O_1-O_2 bond length (*r*) of *trans*-$HO_1O_2O_3$ is scanned from 1.52 to 2.00 Å with an increment of 0.02 Å. All other coordinates are allowed to relax while C_S symmetry is conserved. The resulting 1D potential is fit to a Morse potential. Here the reduced mass is approximated using the following equation:

$$\mu_r = \frac{\mu_{OH}\mu_{O_2}}{\mu_{OH} + \mu_{O_2}}$$

This Morse potential problem is solved to get the wavefunction for the v=0 state. The vibrational averaging of the v=0 state for O_1-O_2 stretching mode gives μ_a = 0.9237 Debye and μ_b = 1.6211 Debye.

5.6.2 One-dimensional Vibrational Averaging of H-O_1-O_2-O_3 Torsional Motion

To generate the relaxed potential energy surface for the torsional degree of freedom, the H-O_1-O_2-O_3 torsional angle (τ) is scanned from 0 to 180° with a step size of 5°. These data points will be combined with other terms for the fitting of $V^{eff}(\tau)$, which will be discussed later.

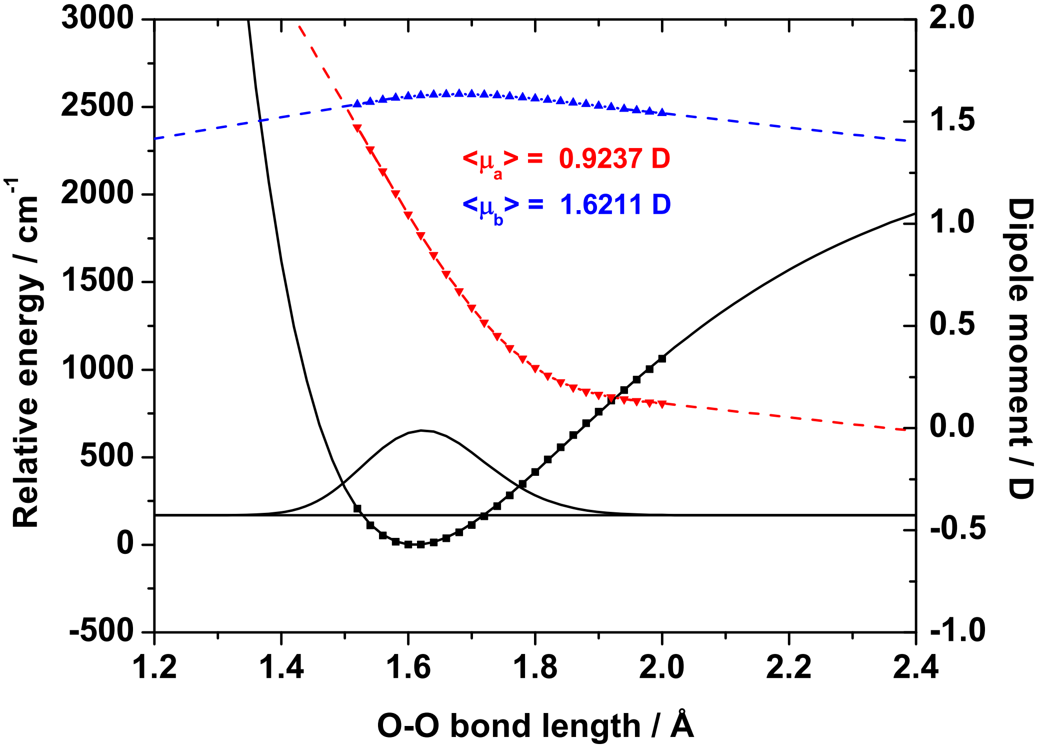

Figure 5.10: One dimensional model Morse potential, ground state wavefunction for O_1-O_2 stretch, and both μ_a and μ_b dipole components of *trans*-HOOO. The squares and down/up triangles are computed *ab initio* points for O_1-O_2 stretch potential and μ_a / μ_b dipole components, respectively. The lines are the fitted Morse function (black) and the interpolate/extrapolate lines of μ_a (red) and μ_b (blue), respectively.

According to the procedure of Laane and co-workers,[32] the one-dimensional internal rotation kinetic energy operator is expressed as:

$$T_\tau = -\frac{d}{d\tau}B\frac{d}{d\tau} - \frac{1}{4}\frac{d}{d\tau}B\frac{d\ln g}{d\tau} + \frac{1}{16}B\left(\frac{d\ln g}{d\tau}\right)^2 \tag{5.1}$$

Here B is the internal rotation constant, and g is the determinant of the G^{-1} matrix.[32]

$$G^{-1} = \begin{bmatrix} I_{11} & -I_{12} & -I_{13} & g_{14} \\ -I_{21} & I_{22} & -I_{23} & g_{24} \\ -I_{31} & -I_{32} & I_{33} & g_{34} \\ g_{41} & g_{42} & g_{43} & g_{44} \end{bmatrix} \tag{5.2}$$

I_{ij} represent the elements of the inertial tensor and the g_{ij} are:

$$g_{44} = \sum_i m_i \left(\frac{\partial \boldsymbol{r_i}}{\partial \tau}\right) \cdot \left(\frac{\partial \boldsymbol{r_j}}{\partial \tau}\right) \qquad (5.3)$$

$$g_{j4} = g_{4j} = \sum_i m_i \left[\boldsymbol{r_i} \times \left(\frac{\partial \boldsymbol{r_i}}{\partial \tau}\right)\right]_{\boldsymbol{j}} \qquad (5.4)$$

The Hamiltonian is:

$$H_\phi = -\frac{d}{d\tau} B \frac{d}{d\tau} - \frac{1}{4}\frac{d}{d\tau} B \frac{d \ln g}{d\tau} + \frac{1}{16} B \left(\frac{d \ln g}{d\tau}\right)^2 + V(\tau) \qquad (5.5)$$

The last three terms in equation (5.5) can be absorbed into an effective potential, $V^{eff}(\tau)$, which is fitted to a simple truncated Fourier expansion:

$$V^{eff}(\tau) = \frac{1}{2}\sum_{n=1}^{7} V_n^{eff}(1 - \cos n\tau) \qquad (5.6)$$

The internal rotation constant B can be computed as a function of τ,[20]

$$B(\tau) = \frac{\hbar^2}{2} g_{\tau\tau} \qquad (5.7)$$

$$\begin{aligned} g_{\tau\tau} = {} & \frac{1}{m_1 r_{12}^2 \sin^2 \theta_{123}} + \frac{1}{m_4 r_{34}^2 \sin^2 \theta_{234}} + \frac{1}{m_2}\left(\lambda_{123}^2 + \frac{\cot^2 \theta_{234}}{r_{23}^2}\right) \\ & + \frac{1}{m_3}\left(\lambda_{432}^2 + \frac{\cot^2 \theta_{123}}{r_{23}^2}\right) \\ & - 2\frac{\cos \tau_{1234}}{r_{23}}\left(\frac{\lambda_{123}}{m_2}\cot \theta_{234} + \frac{\lambda_{432}}{m_3}\cot \theta_{123}\right) \qquad (5.8) \end{aligned}$$

$B(\tau)$ is also fitted to a truncated Fourier expansion:

$$B(\tau) = \sum_{n=0}^{7} B_n \cos n\tau \qquad (5.9)$$

In both $V^{eff}(\tau)$ and $B(\tau)$ expansions, we truncate all n>7 terms. The Hamiltonian becomes:

$$H_{\tau} = -\frac{d}{d\tau}\left(B_0 + \sum_{n=0}^{7} B_n \cos n\tau\right)\frac{d}{d\tau} + \frac{1}{2}\sum_{n=1}^{7} V_n^{eff}(1-\cos n\tau) \qquad (5.10)$$

The general solution of this type of Hamiltonian is given by Laane and co-workers using cos/sin free-rotor basis. All matrix elements were provided in their paper.[32] In this work, we use 100 even and 100 odd functions to solve this one-dimensional Schrödinger equation.

The vibrational averaging of the v=0 state for the $HO_1O_2O_3$ torsional internal rotation mode gives μ_a = 0.9089 Debye and μ_b = 1.5102 Debye for *trans*-HOOO, and μ_a = 0.0031 Debye and μ_b = 0.9757 Debye for *cis*-HOOO.

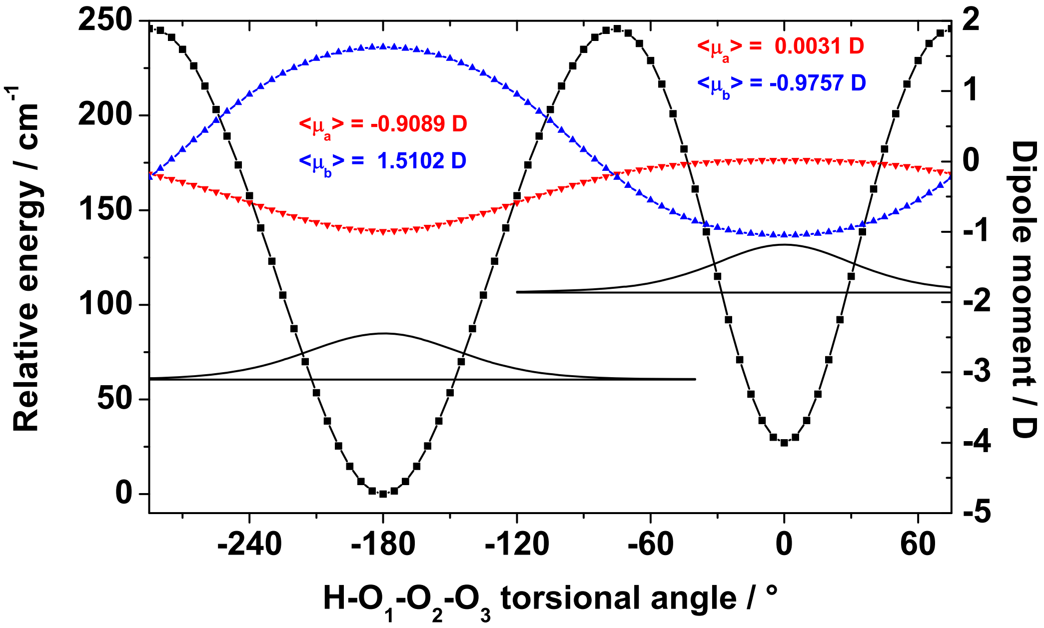

Figure 5.11: The one dimensional torsional model for HOOO. The meaning of squares/trangles and lines are similar to the ones in Fig. 5.10.

5.6.3 Two-dimensional Vibrational Averaging

The terms for the vibrational kinetic energy operator in internal bond-angle coordinates have been tabulated by Frederick and Woywod.[20] For the two-dimensional problem, which considers both bond length r and torsional angle τ, the kinetic energy operator is written as:

$$T_{r,\tau} = -\frac{\hbar^2}{2}\frac{d}{dr}g_{rr}\frac{d}{dr} - \frac{\hbar^2}{2}\frac{d}{d\tau}g_{\tau\tau}\frac{d}{d\tau} - \frac{\hbar^2}{2}\frac{d}{dr}g_{r\tau}\frac{d}{d\tau} - \frac{\hbar^2}{2}\frac{d}{d\tau}g_{\tau r}\frac{d}{dr} + V'(r,\tau) \qquad (5.11)$$

Since $g_{r\tau} = g_{\tau r} = 0$, and $V'(r,\tau) = 0$, the kinetic energy operator is further simplified:

$$T_{r,\tau} = -\frac{\hbar^2}{2}\frac{d}{dr}g_{rr}\frac{d}{dr} - \frac{\hbar^2}{2}\frac{d}{d\tau}g_{\tau\tau}\frac{d}{d\tau} \qquad (5.12)$$

Therefore the Hamiltonian is:

$$H_{r,\tau} = -\frac{\hbar^2}{2}\frac{d}{dr}g_{rr}\frac{d}{dr} - \frac{\hbar^2}{2}\frac{d}{d\tau}g_{\tau\tau}\frac{d}{d\tau} + V(r,\tau) \qquad (5.13)$$

We expand the wave function in the sinc-DVR basis of Colbert and Miller,[21]

$$\langle r,\tau|r_s,\tau_t\rangle = \frac{\sin[\pi(r-r_s)/\Delta r]}{\pi(r-r_s)}\cdot\left(\sum_a \frac{1}{2\pi}e^{ia(\tau+\tau_t)}\right), \quad a = 0, \pm 1, \pm 2, \dots, \pm N_\tau$$

$$r_s = r_a + \frac{r_b - r_a}{N_r}s, \qquad s = 1, \dots, N_r - 1$$

$$\tau_t = a\frac{2\pi}{2N_\tau + 1}, \qquad a = 0, \pm 1, \pm 2, \dots, \pm N_\tau$$

$$\Psi(r,\tau) = \sum_{s,t} C_{s,t}\langle r,\tau|r_s,\tau_t\rangle$$

$$= \sum_{s,t} C_{s,t}\frac{\sin[\pi(r-r_s)/\Delta r]}{\pi(r-r_s)}\cdot\left(\sum_a \frac{1}{2\pi}e^{ia(\tau+\tau_t)}\right) \qquad (5.14)$$

Matrix element: m,n sinc-DVR; p,q free rotor basis set (DVR).

$$\langle mp|H_{r,\tau}|nq\rangle = \left\langle mp\left|-\frac{\hbar^2}{2}\frac{d}{dr}g_{rr}\frac{d}{dr}\right|nq\right\rangle + \left\langle mp\left|-\frac{\hbar^2}{2}\frac{d}{d\tau}g_{\tau\tau}\frac{d}{d\tau}\right|nq\right\rangle$$

$$+ \langle mp|V(r,\tau)|nq\rangle \qquad (5.15)$$

$$\left\langle mp\left|-\frac{\hbar^2}{2}\frac{d}{dr}g_{rr}\frac{d}{dr}\right|nq\right\rangle = -\frac{\hbar^2}{2}g_{rr}\left\langle m\left|\frac{d^2}{dr^2}\right|n\right\rangle\delta_{p,q} \qquad (5.16)$$

$$\left\langle mp\left|-\frac{\hbar^2}{2}\frac{d}{d\tau}g_{\tau\tau}\frac{d}{d\tau}\right|nq\right\rangle = \left\langle mp\left|-\frac{\hbar^2}{4}\left(\frac{d^2}{d\tau^2}g_{\tau\tau} + g_{\tau\tau}\frac{d^2}{d\tau^2} + \frac{d^2 g_{\tau\tau}}{d\tau^2}\right)\right|nq\right\rangle$$

$$= -\frac{\hbar^2}{4}\left(\left\langle p\left|\frac{d^2}{d\tau^2}\right|q\right\rangle\delta_{m,n} * g_{\tau\tau}(r_n,\tau_q) + \left\langle p\left|\frac{d^2}{d\tau^2}\right|q\right\rangle\delta_{m,n} * g_{\tau\tau}(r_m,\tau_p)\right.$$

$$\left. + \frac{d^2 g_{\tau\tau}(r_m,\tau_p)}{d\tau^2}\delta_{m,n}\delta_{p,q}\right) \qquad (5.17)$$

So,

$$\langle mp|H_{r,\tau}|nq\rangle = -\frac{\hbar^2}{2}g_{rr}\left\langle m\left|\frac{d^2}{dr^2}\right|n\right\rangle\delta_{p,q}$$

$$-\frac{\hbar^2}{4}\left(\left\langle p\left|\frac{d^2}{d\tau^2}\right|q\right\rangle\delta_{m,n} * g_{\tau\tau}(r_n,\tau_q) + \left\langle p\left|\frac{d^2}{d\tau^2}\right|q\right\rangle\delta_{m,n} * g_{\tau\tau}(r_m,\tau_p)\right.$$

$$\left. + \frac{d^2 g_{\tau\tau}(r_m,\tau_p)}{d\tau^2}\delta_{m,n}\delta_{p,q}\right) + V(r_m,\tau_p)\delta_{m,n}\delta_{p,q} \qquad (5.18)$$

The matrix elements of $\left\langle m\left|\frac{d^2}{dr^2}\right|n\right\rangle$ and $\left\langle p\left|\frac{d^2}{d\tau^2}\right|q\right\rangle$ are evaluated following Colbert and Miller.[21]

The relaxed two-dimensional potential energy surface regarding both O_1-O_2 bond length (r) and H-O_1-O_2-O_3 torsional angle (τ) are generated at CCSD(T)/Def2-TZVPD level of theory. The data points are chosen that O_1-O_2 bond length varies from 1.52 - 1.84 Å while H-O_1-O_2-O_3 torsional angle ranges from 0 - 180° with step sizes of 0.04 Å and 10°, respectively. The fitting process is summarized here. The parameters of D_e^{π}, α^{π}, and

r_e^{π} are determined from one-dimensional Morse potential fitting when τ is fix at 180° which corresponds to the *trans*-HOOO isomer. The dissociation energy D_e^{π} is used for the rest of our fitting. Two more one-dimensional Morse potential fittings are performed for τ=π/2 and π to get α^0, r_e^0, and $\alpha^{\pi/2}$, $r_e^{\pi/2}$. After that, the functional form below is used to perform the fitting:

$$V_{fit}(r,\tau)=\sum_{n=0}^{7}C_n^0D_e^{\pi}\left(1-e^{-\alpha^0(r-r_e^0)}\right)\times(1-\cos n\tau)$$
$$+\sum_{n=0}^{7}C_n^{\pi/2}D_e^{\pi}\left(1-e^{-\alpha^{\pi/2}\left(r-r_e^{\pi/2}\right)}\right)\times(1-\cos n\tau)$$
$$+\sum_{n=0}^{7}C_n^{\pi}D_e^{\pi}\left(1-e^{-\alpha^{\pi}(r-r_e^{\pi})}\right)\times(1-\cos n\tau) \qquad (5.19)$$

Here the coefficients C_n^0, $C_n^{\pi/2}$, and C_n^{π} are determined using a least-squares fitting scheme. In order to get the vibrational averaged O_1O_2 bond length to match with millimeter/microwave result,[11] shifting the potential is necessary. This is done by adding 0.05 Å to r_e^0, $r_e^{\pi/2}$, and r_e^{π}, respectively.

The surface of $g_{\phi\phi}$ is computed at the *ab initio* grid points using equation 8 shown above as a function of *r* and *τ*. The functional form below is used for fitting:

$$g_{\phi\phi}^{fit}(r,\tau)=\sum_{m=0}^{3}\sum_{n=0}^{7}C_{mn}\frac{1}{r^m}(1-\cos n\tau) \qquad (5.20)$$

After that, the surface of $\frac{d^2g_{\tau\tau}}{d\tau^2}$ is evaluated analytically.

The grids of DVR are evenly spaced. We use 40 and 75 points for radial and angular coordinates with a range of *r* from 1.2 to 3.2 Å and a range of *τ* from 0° to 360°. When we get the wavefunction for ground state of *trans*-HOOO, the vibrational averaging of both μ_a and μ_b dipole components, projection of OH bond length, and other geometrical parameters are evaluated numerically. The numerical grid points for wave-functions are available from the analytical solution, while interpolate/extrapolate procedure is used to generate surface points for the properties that needs to be averaged. The gridding parameters for numerical analysis are 0.02 Å, 5° for r from 1.2 to 2.4 Å and τ from 0 to 360°, respectively.

References

[1] Liang, T., Magers, D. B., Raston, P. L., Allen, W. D., and Douberly, G. E., *J. Phys. Chem. Lett.* **4**, 3584-3589 (2013).

[2] Murray, C., Derro, E. L., Sechler, T. D., and Lester, M. I., *Acc. Chem. Res.* **42**, 419-427 (2009).

[3] Le Picard, S. D., Tizniti, M., Canosa, A., Sims, I. R., and Smith, I. W. M., *Science* **328**, 1258-1262 (2010).

[4] Beames, J. M., Lester, M. I., Murray, C., Varner, M. E., and Stanton, J. F., *J. Chem. Phys.* **134**, 044304 (2011).

[5] Varandas, A. J. C., *Phys. Chem. Chem. Phys.* **13**, 15619-15623 (2011).

[6] Tizniti, M., Le Picard, S. D., Canosa, A., Sims, I. R., and Smith, I. W. M., *Phys. Chem. Chem. Phys.* **12**, 12702-12710 (2010).

[7] Anglada, J. M., Olivella, S., and Sole, A., *J. Chem. Theory Comput.* **6**, 2743-2750 (2010).

[8] Varner, M. E., Harding, M. E., Vazquez, J., Gauss, J., and Stanton, J. F., *J. Phys. Chem. A* **113**, 11238-11241 (2009).

[9] Varandas, A. J. C., *Phys. Chem. Chem. Phys.* **13**, 9796-9811 (2011).

[10] Varandas, A. J. C., *J. Chem. Theory Comput.* **8**, 428-441 (2012).

[11] McCarthy, M. C., Lattanzi, V., Kokkin, D., Martinez, O., and Stanton, J. F., *J. Chem. Phys.* **136**, 034303 (2012).

[12] Choi, M. Y., Douberly, G. E., Falconer, T. M., Lewis, W. K., Lindsay, C. M., Merritt, J. M., Stiles, P. L., and Miller, R. E., *Int. Rev. Phys. Chem.* **25**, 15-75 (2006).

[13] Toennies, J. P., and Vilesov, A. F., *Angew. Chem. Int. Ed.* **43**, 2622-2648 (2004).

[14] Stienkemeier, F., and Lehmann, K. K., *J. Phys. B: At., Mol. Opt. Phys.* **39**, R127-R166 (2006).

[15] Raston, P. L., Liang, T., and Douberly, G. E., *J. Chem. Phys.* **137**, 184302 (2012).

[16] Raston, P. L., Liang, T., and Douberly, G. E., *J. Phys. Chem. A* **117**, 8103-8110 (2013).

[17] Küpper, J., Merritt, J. M., and Miller, R. E., *J. Chem. Phys.* **117**, 647-652 (2002).

[18] Morrison, A. M., Liang, T., and Douberly, G. E., *Rev. Sci. Instrum.* **84**, 013102 (2013).

[19] CFOUR, Coupled-Cluster techniques for Computational Chemistry, a quantum-chemical program package by J.F. Stanton, J. Gauss, M.E. Harding, P.G. Szalay with contributions from A.A. Auer, R.J. Bartlett, U. Benedikt, C. Berger, D.E. Bernholdt, Y.J. Bomble, L. Cheng, O. Christiansen, M. Heckert, O. Heun, C. Huber, T.-C. Jagau, D. Jonsson, J. Jusélius, K. Klein, W.J. Lauderdale, D.A. Matthews, T. Metzroth, D.P. O'Neill, D.R. Price, E. Prochnow, K. Ruud, F. Schiffmann, W. Schwalbach, S. Stopkowicz, A. Tajti, J. Vázquez, F. Wang, J.D. Watts and the integral packages MOLECULE (J. Almlöf and P.R. Taylor), PROPS (P.R. Taylor), ABACUS (T. Helgaker, H.J. Aa. Jensen, P. Jørgensen, and J. Olsen), and ECP routines by A. V. Mitin and C. van Wüllen. For the current version, see http://www.cfour.de.

[20] Frederick, J. H., and Woywod, C., *J. Chem. Phys.* **111**, 7255-7271 (1999).

[21] Colbert, D. T., and Miller, W. H., *J. Chem. Phys.* **96**, 1982-1991 (1992).

[22] Derro, E. L., Sechler, T. D., Murray, C., and Lester, M. I., *J. Chem. Phys.* **128**, 244313 (2008).

[23] Stiles, P. L., Nauta, K., and Miller, R. E., *Phys. Rev. Lett.* **90**, 135301 (2003).

[24] Rappoport, D., and Furche, F., *J. Chem. Phys.* **133**, 134105 (2010).

[25] Suma, K., Sumiyoshi, Y., and Endo, Y., *J. Chem. Phys.* **139**, 094301 (2013).

[26] Varner, M. E., Harding, M. E., Gauss, J., and Stanton, J. F., *Chem. Phys.* **346**, 53-55 (2008).

[27] Evangelista, F. A., Allen, W. D., and Schaefer, H. F., *J. Chem. Phys.* **125**, 154113 (2006).

[28] Evangelista, F. A., Allen, W. D., and Schaefer, H. F., *J. Chem. Phys.* **127**, 024102 (2007).

[29] Evangelista, F. A., Simmonett, A. C., Allen, W. D., Schaefer, H. F., and Gauss, J., *J. Chem. Phys.* **128**, 124104 (2008).

[30] Prochnow, E., Evangelista, F. A., Schaefer, H. F., Allen, W. D., and Gauss, J., *J. Chem. Phys.* **131**, 064109 (2009).

[31] Huber, K. P., and Herzberg, G., *Molecular Spectra and Molecular Structure IV. Constants of Diatomic Molecules* (Van Nostrand Reinhold Co., New York, 1979).

[32] Lewis, J. D., Malloy, T. B., Chao, T. H., and Laane, J., *J. Mol. Struct.* **12**, 427 (1972).

Chapter 6

Helium Nanodroplet Isolation Spectroscopy and *Ab Initio* Calculations of HO_3-$(O_2)_n$ Clusters

HO_3-$(O_2)_n$ clusters are formed via the sequential addition of the hydroxyl radical and O_2 molecules to superfluid helium nanodroplets. Infrared laser spectroscopy in the fundamental OH stretching region reveals the presence of several bands assigned to species as large as n=4. Detailed *ab initio* calculations are carried out for multiple isomers of *cis*- and *trans*-HO_3-O_2, corresponding to either hydrogen or oxygen bonded van der Waals complexes. Comparisons to theory suggest that the structure of the HO_3-O_2 complex formed in helium droplets is a hydrogen-bonded $^4A'$ species consisting of a *trans*-HO_3 core. The computed binding energy of the complex is approximately 240 cm^{-1}. Despite the weak interaction between *trans*-HO_3 and O_2, non-additive red shifts of the OH stretch frequency are observed upon successive solvation by O_2 to form the larger clusters with n>1.

6.1 Introduction

Understanding the interactions between HO_x (OH, HO_2, HO_3) and dioxygen or ozone (O_2, O_3) is of considerable importance owing to the rich chemistry that occurs between these species and the relevance of these reactions to the ozone balance in the earth's atmosphere.[1] For example, the reaction between HO_2 and O_3 to give O_2 and HO_3 is the rate limiting step in the HO_x cycle, which is thought to be responsible for almost half of stratospheric O_3 loss.[2] There is experimental evidence that this reaction proceeds through two competing channels,[3, 4] which correspond to either a hydrogen abstraction from HO_2 by O_3 or an oxygen abstraction from O_3 by HO_2. Using isotopic labeling, Nelson and Zahniser inferred from product branching ratios that the reaction proceeds mainly through H atom abstraction. They also estimated that the barrier height for this channel is ~1 kcal/mol lower than the barrier for O atom abstraction.[5] While this is a difficult reaction to consider theoretically due to the high degree of electron correlation and intrinsic multi-reference character of many of the species involved,[6] the most sophisticated treatment does predict a smaller barrier for H atom abstraction (by ~3 kcal/mol).[7] It was also shown in these computations that a stable minimum exists in the exit channel for the H atom abstraction channel, corresponding to a weakly bound HO_3-O_2 species.[7, 8] We present here a combined experimental and theoretical investigation of this weakly bound exit-channel complex synthesized in helium nanodroplets.

Hydridotrioxygen (HO_3) has been recently investigated by microwave (MW) [9, 10] and infrared (IR) [11-14] spectroscopy in the gas phase and by IR spectroscopy in helium nanodroplets.[15] HO_3 has also been detected by IR spectroscopy in H_2O [16] and in mixed H_2O/O_2 ices.[17] Recent sophisticated theoretical treatments of this species [18-20] predict both *cis* and *trans*-HO_3 isomers to be stable and nearly isoenergetic with the *trans* isomer being more stable by ~70 cm^{-1}.[21] Consistent with this, in the gas phase IR measurements, two bands in the fundamental OH stretch region were observed, and these were assigned to *cis* and *trans*-HO_3 isomers.[14] However, in both the gas phase MW and our helium droplet IR studies, only the *trans* isomer was observed, and the reason for this difference is still an open question. Within a helium droplet, *trans*-HO_3 is produced via the OH + O_2 reaction, as is evident from the ro-vibrational spectrum in the OH stretch region.[15] The timescale associated with the coagulation and cooling of the *trans*-HO_3 species formed in this reaction is on the order of tens of ns, while the timescale between successive O_2 pick-up events is on the order of tens of μs.[22] Therefore, the production of HO_3-O_2 is simply the result of the sequential addition of a second O_2 molecule to a cold *trans*-HO_3 species already residing within the droplet. Once the fragments find each other in the droplet, the vibrational kinetic energy produced as the system evolves towards products is dissipated at a rate that is estimated to be on the order of 10^{12} K/s.[23] This is often sufficiently fast to kinetically trap the system in a configuration separated from other potential energy minima by small barriers.[24] We probe the outcome of this cold collision between the pre-formed *trans*-HO_3 species and O_2 with IR laser spectroscopy in the OH stretching region. Theoretical computations of the possible HO_3-O_2 structures produced within the liquid helium droplets are carried out with specific consideration given to these cluster formation mechanisms, which are operative in this cold, dissipative environment.

6.2 Experimental Methods

The helium nanodroplet isolation method has been recently reviewed,[23-25] and we report here only the experimental details relevant to this work. Helium nanodroplets are generated by expanding into vacuum high purity helium gas (at 30 bar) through a cryogenically cooled (16.0-18.5 K) 5 μm diameter nozzle. As the droplets leave the high pressure region of the expansion, they cool by evaporation to ~0.4 K. The droplet expansion is skimmed into a beam, which passes into a differentially pumped doping chamber containing a pyrolysis source (for the production of OH) and a differentially pumped O_2 doping cell. The hydroxyl radical is generated by the pyrolysis of *tert*-butyl hydroperoxide (TBHP), as described elsewhere.[15] Following the pick-up and solvation of OH, the droplets pass into the O_2 gas cell, which is maintained at a pressure suitable for the pick-up of multiple O_2 molecules. The transit time between the pyrolysis source and this O_2 pick-up cell is ~300 μs. The timescale between successive O_2 pick-up events is estimated to be on the order of 10 μs, while the timescale for cluster coagulation within the droplet occurs within 10-100 ns.[22] The idler beam from a continuous wave IR optical parametric oscillator (OPO) system overlaps the droplet beam in a counter-propagating configuration. When the OPO is tuned into resonance with a transition of an embedded dopant, vibrational energy transfer to the droplet results in the evaporation of several hundred helium atoms from each droplet. This laser-induced size reduction is detected as a reduction in the ionization cross-section of each droplet in an electron bombardment quadrupole mass spectrometer. The OPO beam is chopped, and the ion current in mass channel m/z=49 u (O_3H^+) is processed with a lock-in amplifier as the OPO is tuned through the wavelength range of interest, producing the IR spectrum.

6.3 Computational Methods

To investigate the long range interactions between a pre-formed *trans*-HO_3 and an O_2 molecule within a helium droplet, we carried out scans of the O_2 + *trans*-HO_3 $^4A'$ potential energy surface at the MP2/TZVP level of theory. The *trans*-HO_3 and O_2 geometries were kept fixed in these scans to the values obtained at the same level of theory. Two separate slices of these potential scans are shown in Fig. 6.1. All possible minima found on this MP2 surface were reinvestigated at the CCSD(T)/Def2-TZVP level. Geometry optimizations and harmonic vibrational frequency calculations at this CCSD(T) level reveal only two true minima with no imaginary frequencies. These two minima were re-optimized at the CCSD(T)/Def2-TZVPD level. A similar approach was used to determine geometries, vibrational frequencies and relative energetics of the *cis*-HO_3-O_2 complexes. For the evaluation of the CCSD(T)/Def2-TZVPD dissociation energies of these weakly bound complexes, zero-point vibrational energy (ZPVE) is corrected for with harmonic frequencies obtained at the CCSD(T)/Def2-TZVP level, and basis set superposition error is accounted for via a counterpoise correction.[26] The relative and dissociation energies of these complexes are summarized in Table 6.1. Here we find the *trans*-HO_3 isomer to be lower in energy than the *cis* isomer by ~30 cm^{-1}, which is in relatively good agreement with a recent semi-empirical potential, in which the *trans* isomer is found to lie 70 cm^{-1} below the energy of the *cis* isomer.[21] Complete active space self-consistent field (CASSCF) single point energy calculations are also carried out for each of the minima optimized at the CCSD(T)/Def2-TZVPD level to assess the extent of multi-reference character for these species, as described below. All MP2 and CCSD(T) computations were performed using the program CFOUR.[27] The CASSCF computations are carried out with the program package GAMESS.[28]

Table 6.1: HO_3-$(O_2)_n$ experimental and *ab initio* OH stretching frequencies and relative energetics.

ν_{OH} (cm^{-1})	Helium	CCSD(T)/Def2-TZVP	ΔE (cm^{-1})[a]
trans-HO_3	3569.44	3717	-
trans-HO_3 + O_2	-	-	0
cis-HO_3	-	3669	-
cis-HO_3 + O_2	-	-	27[b]
H-bonded *trans*-HO_3-O_2	3568.3 (-1.14)[c]	3716 (-1)[d]	-237[e]
O-bonded *trans*-HO_3-O_2	-	3713 (-4)[d]	-110[e]
H-bonded *cis*-HO_3-O_2	-	3668	-198[f]
O-bonded *cis*-HO_3-O_2	-	3669	-82[f]
HO_3-$(O_2)_2$	3563.0 (-6.44)[c]	-	-

[a] Computed at the CCSD(T)/Def2-TZVPD level with ZPVE corrections. All species have $^4A'$ electronic symmetry, except for *cis-/trans*-HO_3, which have $^2A''$ electronic symmetry. Relative energies have been counterpoise-corrected, unless otherwise noted.

[b] This value is the difference between the electronic energies for *cis*-HO_3 and *trans*-HO_3.

[c] Frequency shift relative to the band origin of *trans*-HO_3 in helium droplets.

[d] Frequency shift relative to *trans*-HO_3 at this level of theory.

[e] The binding energies of *trans*-HO_3-O_2 are computed relative to *trans*-HO_3 + O_2.

[f] The binding energies of *cis*-HO_3-O_2 are relative to *cis*-HO_3 + O_2, then 27 cm^{-1} is added to account for the energy difference between *trans*-HO_3 and *cis*-HO_3.

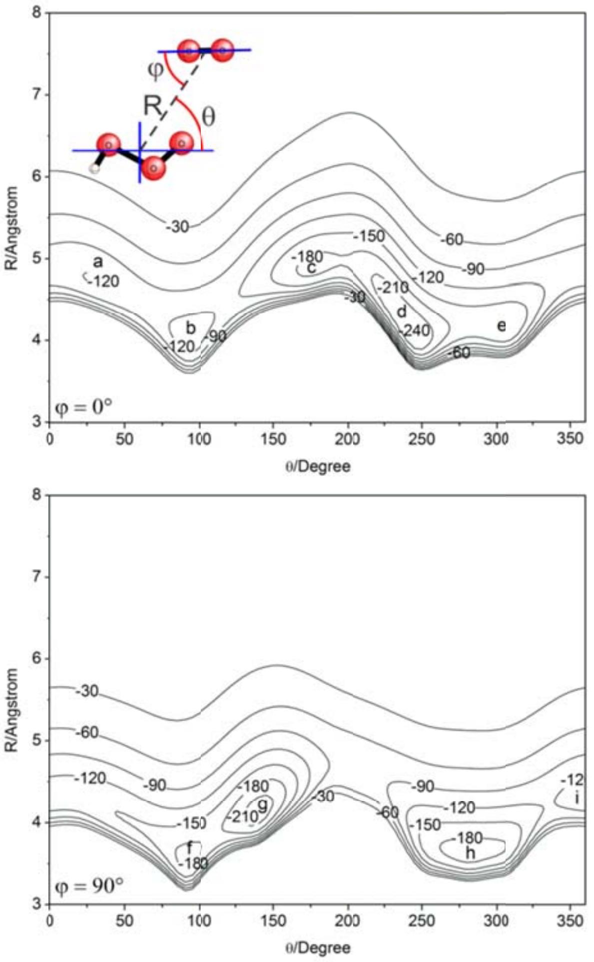

Figure 6.1: Two slices of the MP2/TZVP potential energy surface scan for $^4A'$ (*trans*-HO_3 + O_2) (φ = 0° and 90°). The coordinate system used is shown in the inset. The *trans*-HO_3 and O_2 geometries are fixed to their *ab initio* values at the same level. The energy units are in cm^{-1} and the contour spacing is 30 cm^{-1}.

The structures of the two *trans*-HO_3-O_2 minima are shown in Fig. 6.2, where they are compared to the geometries of isolated *trans*-HO_3 ($^2A''$) and O_2 ($^3\Sigma^-$) at the same level of theory. Similarly the structures of the two minima found having *cis*-HO_3 core structures are shown in Fig. 6.3. Table 6.2 contains the optimized geometric parameters of the *cis*- and *trans*-HO_3 radicals at the CCSD(T)/Def2-TZVPD level, and these are compared to the geometries of these species obtained previously with *ab initio* theory.[21, 29] The geometries of the HO_3 isomers computed here are in good agreement with prior results at the CCSD(T)/CBS level,[29] indicating that CCSD(T)/Def2-TZVPD should be a reasonable level of theory for investigating the larger complexes. As a point of further comparison, the geometries of the *cis*- and *trans*-HO_3-O_2 complexes are also given in Table 6.2. It is interesting to note that the geometry of the *cis*- or *trans*-HO_3 moiety is essentially unchanged upon the formation of the HO_3-O_2 cluster, which is indicative of a relatively weak interaction.

Table 6.2: Comparison of the geometric parameters of HO_3 and HO_3-O_2 isomers computed in this work to those obtained from previous computations of *cis*-/*trans*-HO_3.[a]

	$r(O_2O_3)$ (Å)	$r(O_1O_2)$ (Å)	$\theta(O_1O_2O_3)$ (°)	$r(HO_1)$ (Å)	$\theta(HO_1O_2)$ (°)
trans-HO_3 [b]	1.228	1.611	109.9	0.976	97.2
H-bonded *trans*-HO_3-O_2 [b]	1.229	1.608	109.9	0.976	97.0
O-bonded *trans*-HO_3-O_2 [b]	1.228	1.610	109.9	0.976	97.1
trans-HO_3 EOMIP-CCSD* [c]	1.22	1.62	109.91	0.97	96.74
trans-HO_3 CCSD(T)/CBS [d]	1.226	1.582	109.7	0.969	97.5
cis-HO_3 [b]	1.248	1.552	112.0	0.978	97.5
H-bonded *cis*-HO_3-O_2 [b]	1.249	1.551	112.1	0.979	97.7
O-bonded *cis*-HO_3-O_2 [b]	1.248	1.552	112.0	0.979	97.5
cis-HO_3 EOMIP-CCSD* [c]	1.24	1.57	112.24	0.97	96.98

[a] The numbering of atoms is the same as in ref. 10. $HO_1O_2O_3$.

[b] CCSD(T)/Def2-TZVPD basis set.

[c] Ref. 21, ANO1 basis set.

[d] Ref. 29

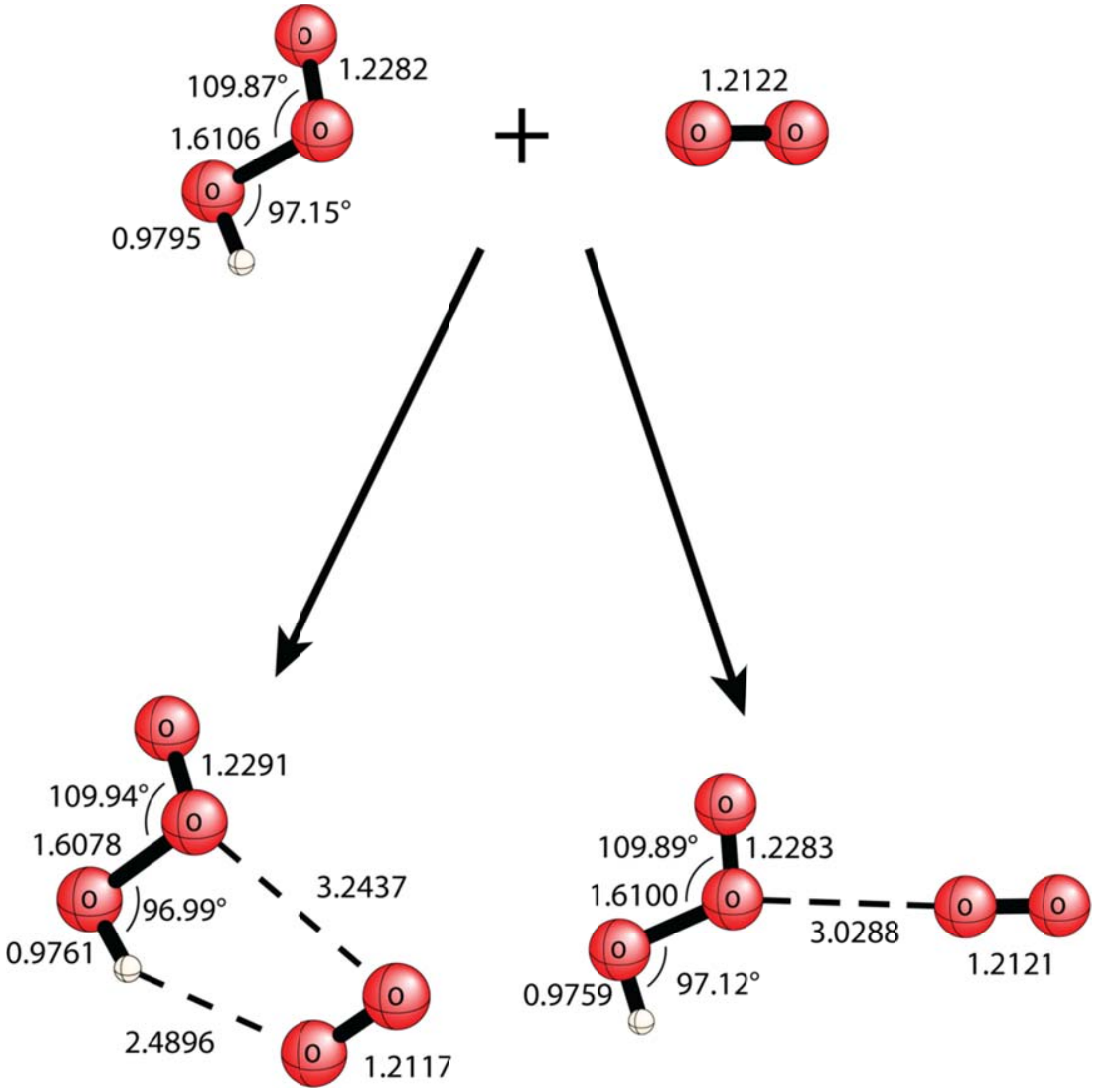

Figure 6.2: Optimized geometries at the CCSD(T)/Def2-TZVPD level for *trans*-HO_3, O_2, and two $^4A'$ *trans*-HO_3-O_2 isomers. The isomer on the left is referred to as the H-bonded *trans*-HO_3-O_2, and the isomer on the right is referred to as the O-bonded *trans*-HO_3-O_2.

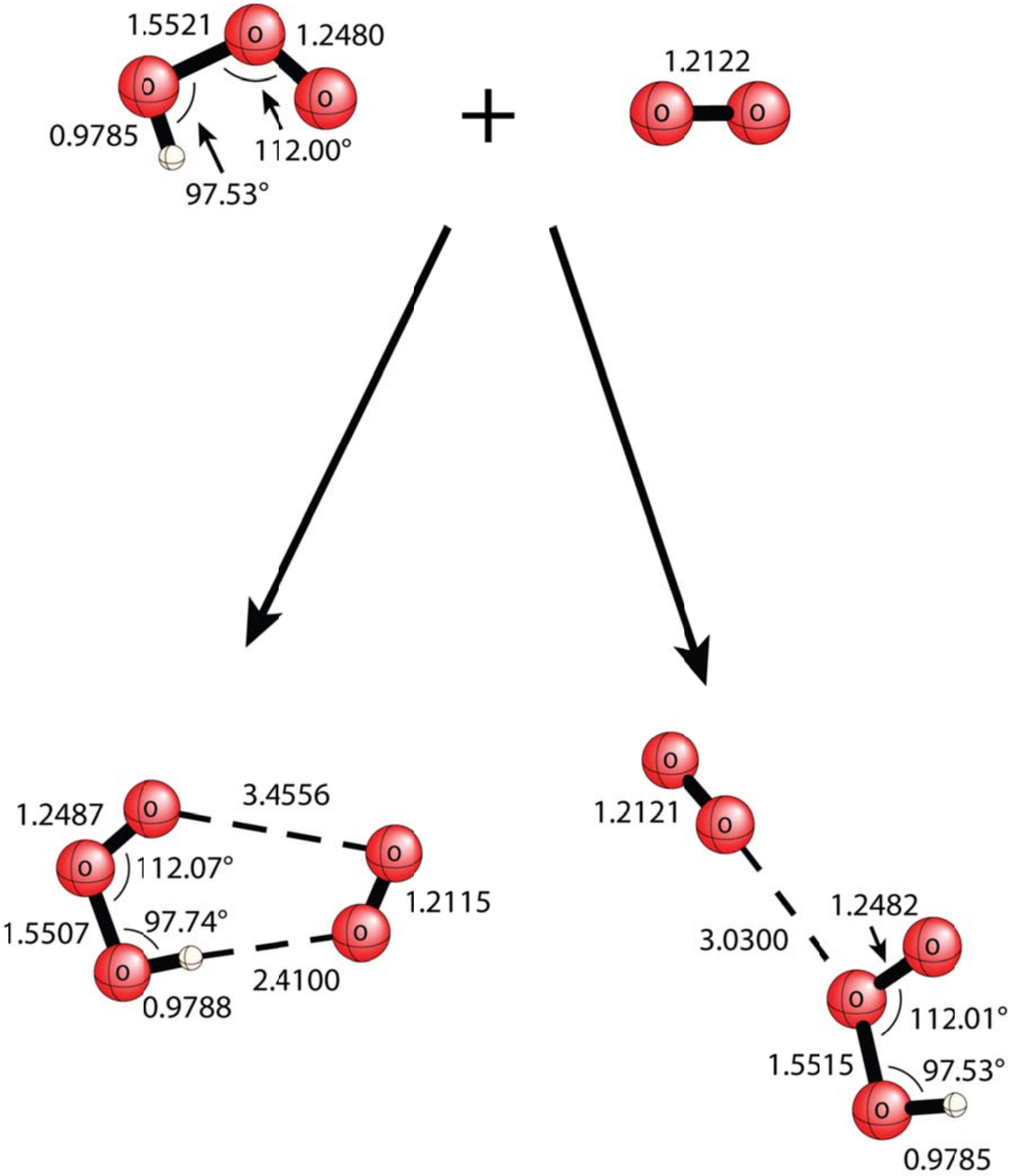

Figure 6.3: Optimized geometries at the CCSD(T)/Def2-TZVPD level for *cis*-HO_3, O_2, and two $^4A'$ *cis*-HO_3-O_2 isomers. The isomer on the left is referred to as the H-bonded *cis*-HO_3-O_2, and the isomer on the right is referred to as the O-bonded *cis*-HO_3-O_2.

6.4 Results and Discussion

In our previous study of the helium droplet mediated OH + O_2 reaction, we briefly noted the presence of weak bands in the OH stretch region shifted to the red of the *trans*-HO_3 band origin (3569.44 cm^{-1}).[15] These bands are only evident under experimental conditions that favor both the production and detection of clusters containing multiple O_2 molecules. For example, the IR depletion signal for *trans*-HO_3 is largest when detected in mass channel m/z=17 u (OH^+). Ionization of the HO_3 doped droplets leads initially to the formation of a He^+ ion, which is followed by the $He^+ + HO_3 \rightarrow He + (O_3H^+)^*$ charge transfer reaction and the fragmentation of the energized O_3H^+ molecular ion to OH^+ and O_2. Detection of the IR depletion spectrum in higher mass channels, such as 33 u (O_2H^+) or 49 u (O_3H^+) leads to an intensity enhancement for the bands observed to the red of *trans*-HO_3, which we assign to clusters containing more than a single O_2 molecule (HO_3-$(O_2)_n$ where n=1-4). The survey spectrum in Fig. 6.4 was recorded in mass channel 49 u and contains the previously discussed rotationally resolved OH stretch band for *trans*-HO_3, along with several features associated with the larger clusters. No other spectral features were found under these conditions in the range 3500-3600 cm^{-1}.

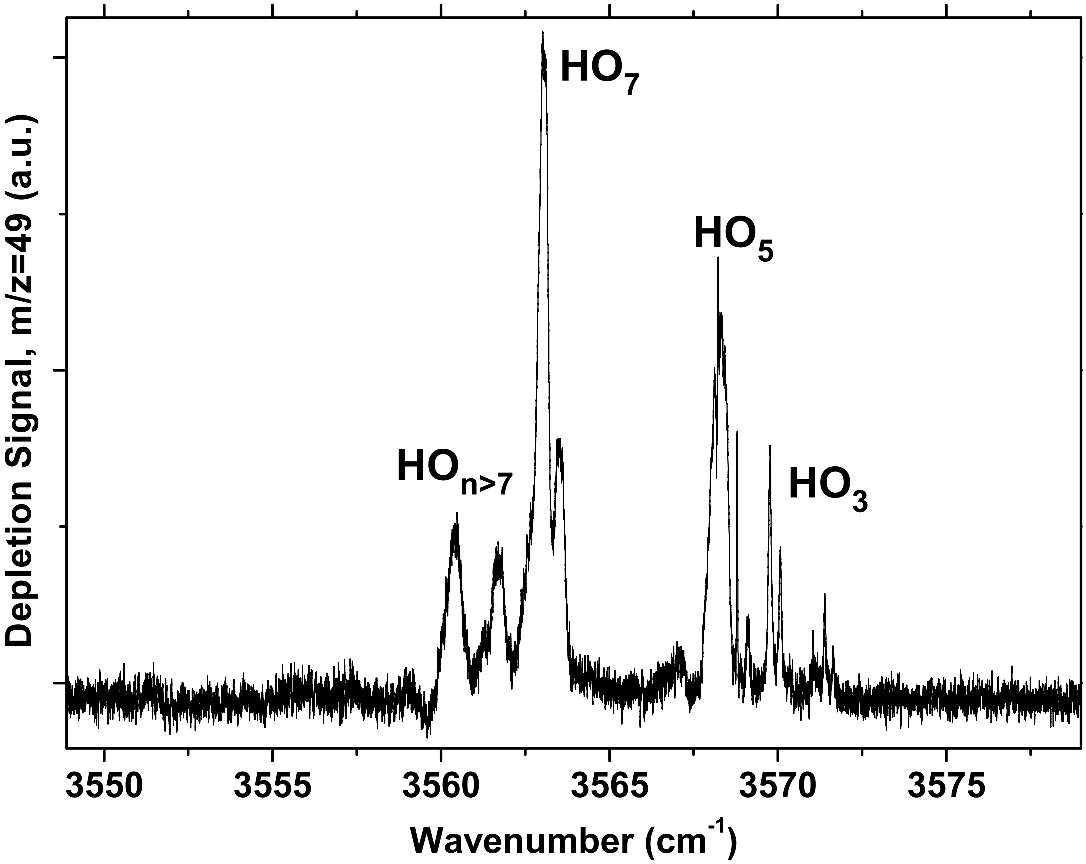

Figure 6.4: OH stretching region measured in mass channel m/z=49 u upon the sequential addition of OH and $(O_2)_n$ to the helium droplets. The nozzle conditions and doping cell pressure were optimized for the pick-up of ~3-4 O_2 molecules per droplet.

The cluster size assignment of the labeled peaks in Fig. 6.4 is based on the O_2 pick-up cell pressure dependence measurements shown in Fig. 6.5. The signal at the maximum of each peak is monitored as the O_2 pressure in the differentially pumped doping chamber is slowly decreased from ~$1x10^{-4}$ to ~$5x10^{-7}$ Torr. The shapes of these pressure dependence curves are consistent with the well-known Poisson statistics associated with helium droplet doping.[23] Indeed the band at 3568.3 cm^{-1} optimizes at about twice the O_2 pick-up pressure that is needed to optimize the HO_3 band. This is consistent with and strongly suggestive of an assignment of the 3568.3 cm^{-1} band to an HO_3-$(O_2)_1$ species. The band origin of this HO_3-$(O_2)_1$ species is shifted to the red of *trans*-HO_3 by 1.14 cm^{-1}. Another intense band is observed at 3563.0 cm^{-1}, which is shifted 6.44 cm^{-1} to the red of *trans*-HO_3. This band has an O_2 pressure dependence consistent with an assignment to an HO_3-$(O_2)_2$ cluster. The features within 3 cm^{-1} of this HO_3-$(O_2)_2$ band optimize at even higher O_2 pressures, with the band centered at 3560.3 cm^{-1} having a pressure dependence consistent with an HO_3-$(O_2)_4$ cluster. Apparently the addition of the first O_2 to *trans*-HO_3 leads to a relatively minor frequency shift of the OH stretch, while the addition of a second O_2 results in a comparatively larger red shift. Further addition of O_2 to the HO_3-$(O_2)_2$ species does not lead to a substantial additional shift of the OH stretch frequency. The experimental band positions and frequency shifts relative to *trans*-HO_3 are given in Table 6.1. We note here that the rotational resolution observed for the OH stretch band of *trans*-HO_3 is lost in going to the larger clusters, which have much smaller computed rotational constants, as shown in Table 6.3.

Table 6.3: Rotational constants and the inertial components of the OH stretch dipole derivative vectors for the two $^4A'$ *trans*-HO_3-O_2 minima optimized at the CCSD(T)/Def2-TZVP level of theory.[a]

trans-HO_3-O_2	*A*	*B*	*C*	$d\mu_a/dQ$	$d\mu_b/dQ$	$d\mu_c/dQ$
H-bonded	0.3236 (0.3139)	0.0627 (0.0659)	0.0525 (0.0545)	-0.228	0.122	0
O-bonded	0.5220 (0.5031)	0.0511 (0.0456)	0.0466 (0.0418)	-0.116	0.202	0

[a] Values in parentheses correspond to geometries optimized at the CCSD(T)/Def2-TZVPD level. The units for the rotational constants are cm^{-1}, and the inertial components of the OH stretch dipole derivative vectors are in atomic units.

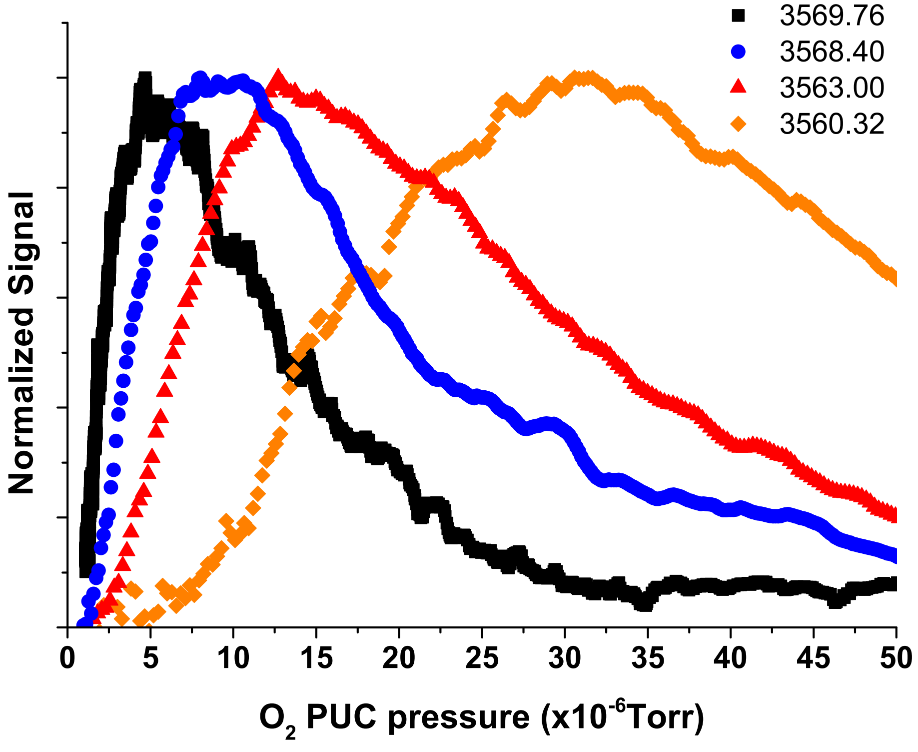

Figure 6.5: Pick-up cell pressure dependence of the depletion signals in mass channel m/z=49 u. The squares, circles, triangles and diamonds correspond to the laser being fixed to 3569.76 (measured in m/z=17 u), 3568.40, 3563.00 and 3560.32 cm^{-1}, respectively.

6.4.1 HO_3-O_2

Here we consider theoretically the structural isomers that may be responsible for the band assigned to HO_3-O_2, assuming it is formed via the addition of an O_2 molecule to a pre-formed planar ($^2A''$) *trans*-HO_3 species. Once again, this assumption is justified by the fact that the timescale for cooling the *trans*-HO_3 species formed via the OH + O_2 reaction is short in comparison to the time it takes for the droplet to pick-up another O_2 molecule, as discussed above. For the interaction between *cis-*/*trans*-HO_3 and O_2, the electronic states can be $^4A'$ and $^2A'$ for in-plane configurations or ^4A and ^2A for out-of-plane configurations. The doublet and quartet states are degenerate at long range. For simplicity we start by considering the long range part of the $^4A'$ surface. The four stationary points found on this surface at the CCSD(T)/TZVP level are verified as true minima with harmonic frequency calculations, as described above. The geometries of the two $^4A'$ *trans*-HO_3-O_2 isomers are shown in Fig. 6.2, and the two $^4A'$ *cis*-HO_3-O_2 isomers are shown in Fig. 6.3. The harmonic frequencies and relative energies for these four minima are given in Table 6.1. We note that every attempt to locate C_1 symmetry minima at this level of theory failed (see Fig. 6.6). The complexation energy of the H-bonded *trans*-HO_3-O_2 isomer is computed at the CCSD(T)/Def2-TZVPD level to be -237 cm^{-1}, which is about 127 cm^{-1} lower in energy than the O-bonded species. A similar magnitude and trend is computed for the complexation energies of the H- and O-bonded *cis*-HO_3-O_2 isomers.

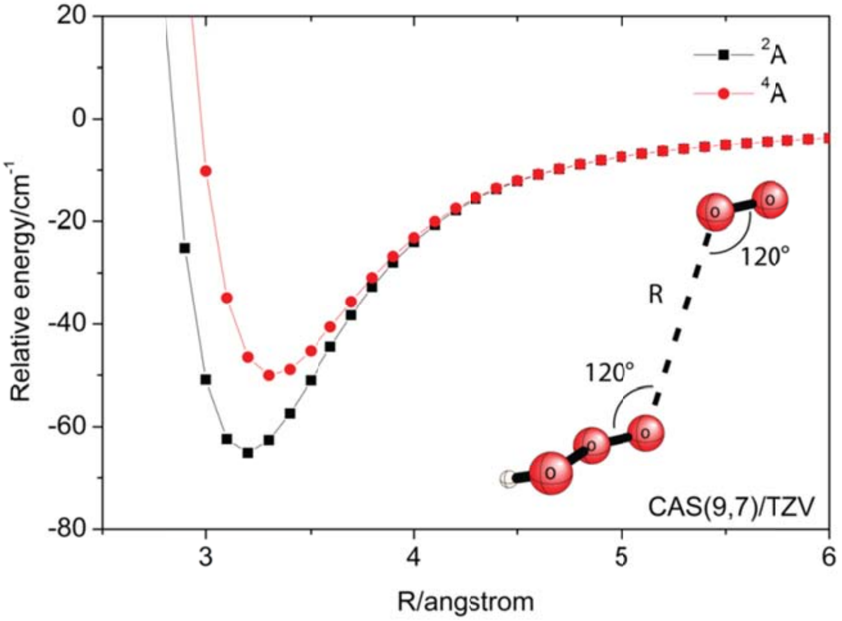

Figure 6.6: The potential scan of C_1 symmetry *trans*-HO_3-O_2. We use geometrical parameters for *trans*-HO_3 and O_2 at the CASSCF(9,7)/TZV level of theory. The HOOO plane is perpendicular to the OOOO plane (O_2 plane). The two OOO angles are fixed at 120°, and we vary the bond distance R to generate the two curves.

The computed frequency shifts of the H-bonded and O-bonded *trans*-HO_3-O_2 isomers from the OH stretch of *trans*-HO_3 are about 1 and 4 cm^{-1} to the red, respectively. The 1.14 cm^{-1} red shift of the experimental HO_3-O_2 band is in rather good (perhaps fortuitous) agreement with the CCSD(T) prediction for the H-bonded *trans*-HO_3-O_2 isomer, especially considering that our theoretical values are obtained with the harmonic approximation. On the basis of the relative energetics of the isomers computed here and the harmonic frequency calculations, we assign the HO_3-O_2 band in the IR spectrum to the H-bonded *trans*-HO_3-O_2 complex. We expect that in the dissipative, low temperature environment of a helium nanodroplet, the thermal energy required to induce rearrangements of the *trans*-HO_3 moiety is unavailable. This expectation seems reasonable and justified, because the binding energy of O_2 to *trans*-HO_3 is less than the torsional interconversion barrier between *cis*- and *trans*-HO_3 isomers (~340 cm^{-1}),[21] and it therefore seems unlikely that the *trans*-HO_3 + O_2 complexation reaction can induce an interconversion of the system to one of the *cis*-HO_3-O_2 isomers. Interestingly, from the pressure dependence measurements, there is only one band that can be assigned to *trans*-HO_3-O_2, despite the prediction of two stable isomers. It is perhaps possible that the evaporative cooling of the helium droplet is not sufficiently fast to kinetically trap the higher energy O-bonded *trans*-HO_3-O_2 cluster as the system condenses, and, instead, the system simply "anneals" to the lower energy configuration. This seems reasonable, given the barrier between O- and H-bonded clusters is estimated to be less than ~50 cm^{-1}, on the basis of the MP2/TZVP potential scan (Fig. 6.1).

HO_n systems present particularly challenging problems for theory, in which it is often desirable to employ high-level multi-reference methods to accurately compute potential energy surfaces.[6, 7, 20, 30, 31] To assess the multi-reference characteristics of the weakly bonded *trans*-HO_3-O_2 clusters, we have carried out CASSCF(15,13)/Def2-TZVPD single point energy calculations, using the $^4A'$ geometries optimized at the CCSD(T)/Def2-TZVPD level of theory. In these calculations, the two largest coefficients in the CI vector for the H-bonded isomer are 0.89 and 0.20, while they are 0.90 and 0.19 for the O-bonded isomer. Moreover, for both isomers, the next 5 largest CI vector coefficients are all near 0.10. This indicates that a multi-reference treatment may be necessary for these complexes. Given this, our assignments based on the single reference CCSD(T) calculations should be viewed as tentative, and we cannot exclude the possibility that other HO_3-O_2 isomers, might contribute to the broad, featureless band observed at 3568.30 cm^{-1}.

As mentioned above, previous CASSCF computations of Viegas and Varandas and Xu and Lin predicted an HO_3-O_2 complex (^{2}A) to be a stable minimum in the exit channel of the $HO_2 + O_3$ hydrogen abstraction reaction (MIN3).[7, 8] The most significant difference between this ^{2}A structure and the ^{4}A′ *trans*-HO_3-O_2 H-bound complex computed here is the HOOO dihedral angle within the HO_3 moiety. Both structures consist of a hydrogen bonded interaction between the HO_3 and O_2 fragments. The associated dihedral angle within the ^{4}A′ structure is 180° (*trans*-HO_3), while the ^{2}A structure is nonplanar with a HOOO dihedral angle of 99.9°. It is interesting to consider whether or not the HO_3-O_2 band in this study is due to this ^{2}A species. Starting from the MIN3 geometry of ref. 7, an optimization using the single-reference CCSD(T)/Def2-TZVP method converges, despite the strong multi-reference character reported for this conformation. These calculations indicate that the ^{2}A UHF reference wavefunction at this configuration is highly spin contaminated by the quartet electronic wavefunction, which results in an $\langle S^2 \rangle$ value equal to 1.82. This value is similar to that reported by Xu and Lin (1.776).[8] Furthermore, the MIN3 stationary point is determined to be a transition state with one imaginary frequency at the level of theory employed here. This is found to be true for both doublet and quartet electronic states. The mode of the imaginary frequency suggests that the ^{4}A MIN3 species is the transition state between the H-bonded *cis*- and *trans*-HO_3-O_2 isomers on the quartet surface.

We computed single point energies at the CCSD(T)/Def2-TZVPD level of theory for both doublet and quartet multiplicities of the MIN3 structure optimized at CCSD(T)/Def2-TZVP. The relative energies of the MIN3 and ^{4}A′ complexes are compared in Table 6.4. At this level, the ^{2}A and ^{4}A states for MIN3 are essentially isoenergetic, lying 211 and 217 cm^{-1} higher in energy than the $^4A'$ H-bonded *trans*-HO_3-O_2 isomer, respectively. Because the interaction between the O_2 and HO_3 fragments is likely similar in both the ^4A MIN3 and $^4A'$ H-bonded *trans*-HO_3-O_2 isomers, it is reasonable that the $^4A'$ complex is lower in energy, due to the fact that *trans*-HO_3 is the global minimum on the HO_3 surface at this level of theory. As discussed above, the ^4A (MIN3) species is the transition state associated with the isomerization of *trans*-HO_3-O_2 to *cis*-HO_3-O_2, and the barrier for this interconversion at this level of theory is found to be 217 cm^{-1}, which is somewhat smaller than the *trans* to *cis* interconversion barrier determined semi-empirically by Stanton and co-workers (340 cm^{-1}).[21] Moreover, the binding energy of the O_2 fragment to *trans*-HO_3 (~237 cm^{-1}) is only 20 cm^{-1} larger than this barrier height, and hence, it seems unlikely that *cis*-HO_3-O_2 complexes can be stabilized in the dissipative droplet environment upon sequential addition of O_2 to *trans*-HO_3. This provides further support to our assignment of the band at 3568.3 cm^{-1} to the OH stretch of the *trans*-HO_3-O_2 complex.

Table 6.4: Relative energies of the HO_3-O_2 isomers.

Relative energy	ΔE (cm^{-1})[a]	$\langle S^2 \rangle$[b]
H-bonded *trans*-HO_3-O_2 $^4A'$	0	3.82
O-bonded *trans*-HO_3-O_2 $^4A'$	153	3.82
H-bonded *cis*-HO_3-O_2 $^4A'$	69	3.83
O-bonded *cis*-HO_3-O_2 $^4A'$	184	3.83
Viegas/Varandas[c] MIN3 ^2A	211	1.82
Viegas/Varandas[c] MIN3 ^4A	217	3.82

[a] Relative electronic energy computed at the CCSD(T)/Def2-TZVPD//CCSD(T)Def2-TZVP level of theory.

[b] Expectation value of the S^2 operator for the UHF reference wavefunction, which is 0.75 (doublet) and 3.75 (quartet) in the absence of spin contamination.

[c] MIN3 geometry from the Supporting Information file of ref. 7, re-optimized at the CCSD(T)/Def2-TZVP level.

6.4.2 Larger Clusters

Fig. 6.7 shows the bands in the region of the larger HO_3-$(O_2)_{n\geq 2}$ clusters. Broad features on either side of the HO_3-$(O_2)_2$ peak grow in intensity with increasing O_2 doping cell pressures, as does a broad peak centered around 3560.3 cm^{-1}. The largest structural change which affects the OH stretching frequency seems to occur in going from *trans*-HO_3-O_2 to HO_3-$(O_2)_2$. Additional O_2 molecules affect the stretching frequency less, and the limiting value of the OH stretch in these cluster systems with increasing *n* is approximately 3560 cm^{-1}. Unfortunately, the *ab initio* search for the structure of HO_3-$(O_2)_2$ has so far been unproductive, and we therefore have no harmonic frequency results to compare to the -6.44 cm^{-1} frequency shift observed for this cluster. Interestingly, the observed sequential shift is highly non-additive. The OH stretch is red-shifted by 5.3 cm^{-1} upon the addition of O_2 to the *trans*-HO_3-O_2 complex, whereas a 1.14 cm^{-1} red shift is observed upon addition of O_2 to *trans*-HO_3. Although we have rather definitive evidence from our pressure dependence curves that this band must be due to a complex with the formula unit HO_7, CCSD(T) calculations of possible structures for this species will have to be left for a future study. Clearly, this non-additivity in the shift provides an important clue as to the carrier of the HO_7 band.

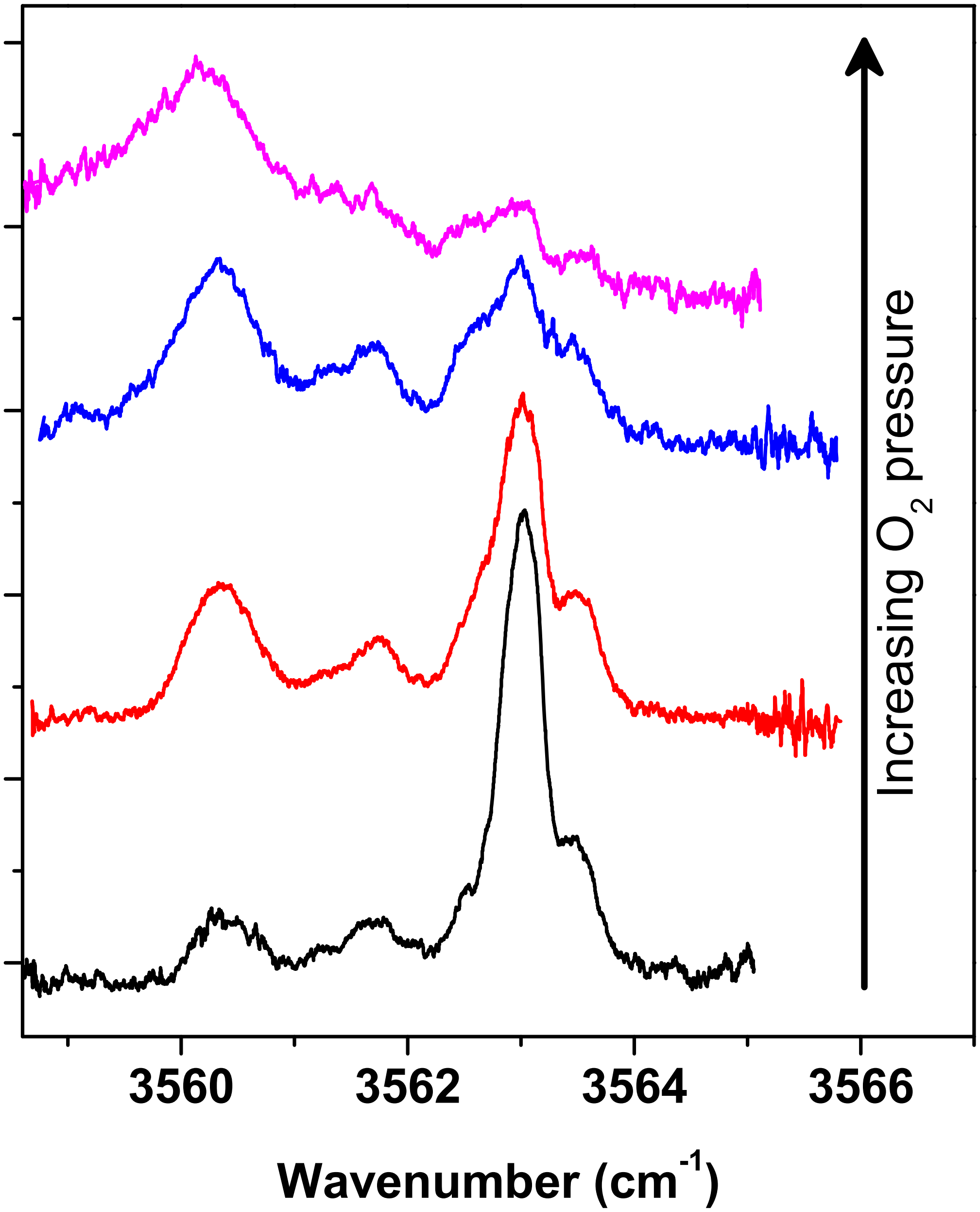

Figure 6.7: Evolution of the spectral signatures of the larger HO_3-$(O_2)_n$ clusters with increasing doping cell pressure. The spectra correspond to depletion signals in mass channel m/z=49 u, and the pick-up cell pressures are 5.0×10^{-6}, 2.0×10^{-5}, 3.0×10^{-5} and 5.0×10^{-5} Torr from bottom to top.

6.5 Conclusions

HO_3-$(O_2)_n$ clusters have been assembled in helium nanodroplets by the sequential addition of the hydroxyl radical and multiple O_2 molecules. Strong vibrational bands in the OH stretch region are observed 1.14 and 6.44 cm^{-1} to the red of the previously determined band origin of the helium solvated *trans*-HO_3 species. On the basis of the signal dependence on O_2 doping cell pressure, and through comparisons to high-level *ab initio* calculations, we assign the 1.14 cm^{-1} red shifted band to an HO_3-O_2 complex, in which the core HO_3 species is in the *trans* configuration. The observed shifts, along with the computations, suggest that the O_2 binds to the hydrogen end of *trans*-HO_3. The band shifted 6.44 cm^{-1} to the red of the *trans*-HO_3 band is assigned to an HO_3-$(O_2)_2$ cluster. With increasing O_2 solvation, the OH stretch bands of these clusters overlap near 3560 cm^{-1}. Broad features centered at this frequency are due to clusters with $n>2$. *Ab initio* calculations at the CCSD(T) level of theory demonstrate that there are *multiple* minima in the exit channel of the $HO_2 + O_3$ hydrogen abstraction reaction, and that the lowest energy of these is most likely the $^4A'$ or $^2A'$ hydrogen-bonded *trans*-HO_3-O_2 complex observed here.

References

[1] Monks, P. S., *Chem. Soc. Rev.* **34**, 376-395 (2005).

[2] Wennberg, P. O., Cohen, R. C., Stimpfle, R. M., Koplow, J. P., Anderson, J. G., Salawitch, R. J., Fahey, D. W., Woodbridge, E. L., Keim, E. R., Gao, R. S., Webster, C. R., May, R. D., Toohey, D. W., Avallone, L. M., Proffitt, M. H., Loewenstein, M., Podolske, J. R., Chan, K. R., and Wofsy, S. C., *Science* **266**, 398-404 (1994).

[3] Sinha, A., Lovejoy, E. R., and Howard, C. J., *J. Chem. Phys.* **87**, 2122-2128 (1987).

[4] Wang, X. Y., Suto, M., and Lee, L. C., *J. Chem. Phys.* **88**, 896-899 (1988).

[5] Nelson, D. D., and Zahniser, M. S., *J. Phys. Chem.* **98**, 2101-2104 (1994).

[6] Varandas, A. J. C., and Viegas, L. P., *Comp. Theor. Chem.* **965**, 291-297 (2011).

[7] Viegas, L. s. P., and Varandas, A. n. J. C., *J. Chem. Theory Comput.* **6**, 412-420 (2010).

[8] Xu, Z. F., and Lin, M. C., *Chem. Phys. Lett.* **440**, 12-18 (2007).

[9] Suma, K., Sumiyoshi, Y., and Endo, Y., *Science* **308**, 1885-1886 (2005).

[10] McCarthy, M. C., Lattanzi, V., Kokkin, D., Martinez, O., and Stanton, J. F., *J. Chem. Phys.* **136**, 034303 (2012).

[11] Murray, C., Derro, E. L., Sechler, T. D., and Lester, M. I., *J. Phys. Chem. A* **111**, 4727-4730 (2007).

[12] Derro, E. L., Murray, C., Sechler, T. D., and Lester, M. I., *J. Phys. Chem. A* **111**, 11592-11601 (2007).

[13] Derro, E. L., Sechler, T. D., Murray, C., and Lester, M. I., *J. Chem. Phys.* **128**, 244313 (2008).

[14] Murray, C., Derro, E. L., Sechler, T. D., and Lester, M. I., *Acc. Chem. Res.* **42**, 419-427 (2009).

[15] Raston, P. L., Liang, T., and Douberly, G. E., *J. Chem. Phys.* **137**, 184302 (2012).

[16] Cooper, P. D., Moore, M. H., and Hudson, R. L., *J. Phys. Chem. A* **110**, 7985-7988 (2006).

[17] Cooper, P. D., Moore, M. H., and Hudson, R. L., *Icarus* **194**, 379-388 (2008).

[18] Varandas, A. J. C., *Phys. Chem. Chem. Phys.* **13**, 15619-15623 (2011).

[19] Varandas, A. J. C., *Phys. Chem. Chem. Phys.* **13**, 9796-9811 (2011).

[20] Varandas, A. J. C., *J. Chem. Theory Comput.* **8**, 428-441 (2012).

[21] Beames, J. M., Lester, M. I., Murray, C., Varner, M. E., and Stanton, J. F., *J. Chem. Phys.* **134**, 044304 (2011).

[22] Lewerenz, M., Schilling, B., and Toennies, J. P., *J. Chem. Phys.* **102**, 8191-8207 (1995).

[23] Toennies, J. P., and Vilesov, A. F., *Angew. Chem. Int. Ed.* **43**, 2622-2648 (2004).

[24] Choi, M. Y., Douberly, G. E., Falconer, T. M., Lewis, W. K., Lindsay, C. M., Merritt, J. M., Stiles, P. L., and Miller, R. E., *Int. Rev. Phys. Chem.* **25**, 15-75 (2006).

[25] Stienkemeier, F., and Lehmann, K. K., *J. Phys. B: At., Mol. Opt. Phys.* **39**, R127-R166 (2006).

[26] Boys, S. F., and Bernardi, F., *Mol. Phys.* **19**, 553-& (1970).

[27] CFOUR, Coupled-Cluster techniques for Computational Chemistry, a quantum-chemical program package by J.F. Stanton, J. Gauss, M.E. Harding, P.G. Szalay with contributions from A.A. Auer, R.J. Bartlett, U. Benedikt, C. Berger, D.E. Bernholdt, Y.J. Bomble, L. Cheng, O. Christiansen, M. Heckert, O. Heun, C. Huber, T.-C. Jagau, D. Jonsson, J. Jusélius, K. Klein, W.J. Lauderdale, D.A. Matthews, T. Metzroth, D.P. O'Neill, D.R. Price, E. Prochnow, K. Ruud, F. Schiffmann, W. Schwalbach, S. Stopkowicz, A. Tajti, J. Vázquez, F. Wang, J.D. Watts and the integral packages MOLECULE (J. Almlöf and P.R. Taylor), PROPS (P.R. Taylor), ABACUS (T. Helgaker, H.J. Aa. Jensen, P. Jørgensen, and J. Olsen), and ECP routines by A. V. Mitin and C. van Wüllen. For the current version, see http://www.cfour.de.

[28] Schmidt, M. W., Baldridge, K. K., Boatz, J. A., Elbert, S. T., Gordon, M. S., Jensen, J. H., Koseki, S., Matsunaga, N., Nguyen, K. A., Su, S. J., Windus, T. L., Dupuis, M., and Montgomery, J. A., *J. Comput. Chem.* **14**, 1347-1363 (1993).

[29] Varner, M. E., Harding, M. E., Gauss, J., and Stanton, J. F., *Chem. Phys.* **346**, 53-55 (2008).

[30] Braams, B. J., and Yu, H. G., *Phys. Chem. Chem. Phys.* **10**, 3150-3155 (2008).

[31] Anglada, J. M., Olivella, S., and Sole, A., *J. Chem. Theory Comput.* **6**, 2743-2750 (2010).

Chapter 7

Quantum Cascade Laser Spectroscopy and Photo-Induced Chemistry of Al-$(CO)_n$ Clusters in Helium Nanodroplets

Helium nanodroplet isolation and a tunable quantum cascade laser are used to probe the fundamental CO stretch bands of Aluminum Carbonyl complexes, Al-$(CO)_n$ ($n \leq 5$). The droplets are doped with single aluminum atoms *via* the resistive heating of an aluminum wetted tantalum wire. The downstream sequential pick-up of CO molecules leads to the rapid formation and cooling of Al-$(CO)_n$ clusters within the droplets. Near 1900 cm^{-1}, rotational fine structure is resolved in bands that are assigned to the CO stretch of a linear $^2\Pi_{1/2}$ Al-CO species and the asymmetric and symmetric CO stretch vibrations of a planar C_{2v} Al-$(CO)_2$ complex in a $^2B_1$ electronic state. Bands corresponding to clusters with $n \geq 3$ lack resolved rotational fine structure; nevertheless, the small frequency shifts from the n=2 bands indicate that these clusters consist of an Al-$(CO)_2$ core with additional CO molecules attached *via* van-der-Waals interactions. A second n=2 band is observed near the CO stretch of Al-CO, indicating a local minimum on the n=2 potential consisting of an “unreacted” Al-CO-(CO) cluster. The linewidth of this band is ~0.3 cm^{-1}, which is about 30 times broader than the transitions within the Al-CO band. The additional broadening is consistent with a homogeneous mechanism corresponding to a rapid vibrational excitation induced reaction within the Al-CO-(CO) cluster to form the covalently bonded Al-$(CO)_2$ complex. *Ab initio* CCSD(T) calculations and Natural Bond Orbital (NBO) analyses are carried out to investigate the nature of the bonding in the n=1,2 complexes. The NBO calculations show that both π-donation (from the occupied aluminum p-orbital into a π* antibonding CO orbital) *and* σ-donation (from CO into the empty aluminum p-orbitals) play a significant role in the bonding, analogous to transition metal carbonyl complexes. The large redshift observed for the CO stretch vibrations is consistent with this bonding analysis.

7.1 Introduction

There is a rich history of Infrared (IR) spectroscopic studies of metal surfaces in which adsorbed molecular chromophores act as probes of surface catalytic activity.[1-3] One practical theoretical approach for modeling these systems includes the first principles treatment of a metal cluster adsorbate complex, which is subsequently embedded in a classically modeled surface.[4-11] Improvements to the accuracy of such methods require spectroscopic studies of isolated metal cluster adsorbate systems, which can provide the important benchmarks necessary for the *ab initio* treatment of the embedded cluster. Gas phase spectroscopy techniques employing either line tunable CO_2 lasers [12-15] or a broadly tunable IR free electron laser [16-23] have been developed in recent years to characterize the adsorbate "probe" molecule and the evolution of its properties with changing size and composition of the underlying metal cluster. Cryogenic matrix isolation experiments have provided an extensive database of IR spectra for single metal atom containing molecular clusters.[24-26] The low temperature of solid rare gas matrices, the broad wavelength coverage available with FTIR, and the ability to compare the spectra of a series of isotopologues allow for structural assignments and the identification of isomers. However, with these techniques, the poor control over the deposition process hinders the production and characterization of small molecules chemisorbed to multi-atom metal clusters.[24]

Recent work in the area of helium nanodroplet isolation (HENDI) has demonstrated the applicability of this methodology as an alternative to traditional matrix isolation and gas phase techniques for the spectroscopic study of metal clusters [27-30] and metal cluster adsorbate systems.[31-36] With HENDI, many of the advantages associated with solid rare gas matrix isolation remain but with the added advantage of drastically reduced matrix effects on the IR spectra and the appearance of rotational fine structure in the measured vibrational bands.[37, 38] The sequential pick-up of metal atoms by helium droplets followed by the introduction of the probe molecule provides the sample production control necessary for a systematic study of the evolution of adsorbate structure with increasing metal cluster size. Furthermore, since helium droplets are formed in a nozzle expansion, standard molecular beam techniques such as IR laser Stark spectroscopy and mass spectrometry can be applied to these systems. Unfortunately, due to the restricted tuning ranges of the available IR lasers,[38] the variety of metal cluster adsorbate systems that has been studied in this way is somewhat limited. Indeed, HENDI so far has not achieved the broad wavelength coverage afforded to FTIR matrix isolation techniques. Nevertheless, the recent appearance of commercially available, narrow linewidth, high power, continuously tunable quantum cascade lasers (QCL)[39, 40] provides a unique opportunity to extend high-resolution infrared measurements of helium nanodroplet isolated species into the important fingerprint region of the mid-IR. Furthermore, these QCL laser systems allow for more relevant probe molecules, such as carbon monoxide,[41] to be applied to the study of the structure and reactivity of small metal clusters. We report here the high resolution rovibrational spectra of Al-$(CO)_n$ complexes formed in helium nanodroplets, which are obtained with a newly available QCL laser system coupled to a HENDI spectrometer.

In general, Al cluster reactions have attracted considerable interest owing to the highly reactive nature of Al and the potential to incorporate these systems into energetic materials.[42, 43] For example, nanoparticles of Al are added to solid rocket propellants to react with the products of combustion, enhancing the exothermicity of the deflagrating fuel.[44, 45] To understand the elementary reactions at play in these systems, it is therefore important to study the outcome of the reactions involving Al atoms and small hydrocarbon molecules, CO, CO_2, H_2O, HCl, and other combustion products. There are several theoretical studies of reactions between Al and small molecules,[46-55] and many of these are shown to be highly exothermic and to have relatively low reaction barriers. This report represents a first step in our effort to characterize the reactivity of small aluminum clusters *via* HENDI IR laser spectroscopy. Complexes of CO with single Al atoms are probed in the CO stretch region, and complementary coupled cluster *ab initio* calculations and natural bond orbital analyses are carried out to provide insights into the associated interactions. The CO stretch vibrations in these clusters provide sensitive signatures of metal-ligand bonding and the extent of charge transfer in these low-valent, main group metal atom complexes.

Aluminum carbonyl complexes were studied with both IR [26, 56-64] and ESR [65, 66] spectroscopy in various solid matrices, and these were some of the first main group metal carbonyls observed. Before these first measurements, it was not generally believed that main group metal carbonyls would be stable, since they lack the d-orbital electrons present in transition metal carbonyls.[56] Nevertheless, strong evidence for the formation of a symmetric C_{2v} Al-$(CO)_2$ molecule was provided by these measurements.[57, 65] Furthermore, upon reducing the CO concentration in the matrix, IR bands associated with an Al-CO binary complex were observed.[58, 59] There have also been several reports of density functional and *ab initio* calculations of the structures and vibrational frequencies of these species,[47, 67-73] which generally agree with the assignments of the matrix isolation spectra and provide fundamental insights into the nature of the bonding in these complexes. Although not as strongly bound as the transition metal carbonyls, a coordinate covalent type interaction between the CO ligand and the Al atom is inferred, and the bond energies are determined to be ~10 kcal/mol.[67] The formation of these species in helium droplets not only provides an opportunity to measure the rotationally resolved spectra of Al-CO and Al-$(CO)_2$, but also allows for the study of larger Al_m-$(CO)_n$ clusters.

7.2 Experimental Methods

Helium nanodroplet isolation is a well-developed technique for trapping molecular species for spectroscopic interrogation, and the experimental details have been recently reviewed.[37, 38, 74] Droplets are formed *via* the continuous expansion of 99.9995% pure helium (30 bar) through a 5 μm diameter pinhole nozzle into vacuum. The nozzle temperature in this experiment was kept at 17 K, resulting in the formation of droplets with an average size of ~5000 helium atoms.[75, 76] The droplet expansion is skimmed and passes into a pick-up chamber containing an aluminum oven source and a differentially pumped gas pick-up cell containing carbon monoxide. Upon pick-up, Al atoms are solvated within the droplet,[77] rather than being attached to the surface. Sequential pick-up of CO molecules results in the formation of helium solvated aluminum-carbonyl complexes. The condensation energy associated with the cluster formation process is removed by helium evaporation,[78] and the temperature of the droplet returns to ~0.37 K.[79] The droplet beam subsequently enters a mass spectrometer chamber where the droplets are electron impact ionized.[80, 81] The resulting ions are detected with a crossed-beam ionizer equipped quadrupole mass spectrometer (Extrel CMS).

Aluminum is vaporized by placing Al shot in a coiled tantalum filament, which is attached to water-cooled copper electrodes. The oven is increased in temperature such that the Al melts and wets the tantalum filament; further increases in temperature result in the evaporation of Al directly from the filament. The droplet beam passes 5 mm from the wetted filament and each droplet picks up a number of Al atoms that depends on the local vapor density.[82] The vapor pressure of Al was initially optimized by observing the appearance of Al^+-$(He)_n$ ions in the mass spectrometer. The CO pick-up cell is located downstream from the Al oven, and the CO pressure was set to ~8×10^{-6} Torr for the initial survey scans. The reported CO pressures are uncorrected readings from an ion gauge attached to the differentially pumped gas cell. Once the Al-CO resonance was found, the

CO pressure was optimized and the Al oven temperature was set such that the signal intensity was about half the optimum value. These conditions ensure that the pick-up of multiple Al atoms by a single droplet occurs with relatively low probability. Only aluminum carbonyl clusters of the form Al-$(CO)_n$ are observed in this study, and a future report will discuss the larger Al_m-$(CO)_n$ species.

An external cavity quantum cascade laser (QCL) (Daylight Solutions) is used to vibrationally excite the helium solvated Al-$(CO)_n$ clusters. The unfocused output from the QCL counter-propagates the droplet beam. Excitation followed by vibrational relaxation results in the evaporation of ~380 helium atoms from each droplet,[38] and the laser induced reduction in the droplet's geometric cross section is observed as a decrease in the total ion signal reaching the mass spectrometer. For the spectroscopy experiments, the quadrupole is operated in an RF-only mode in which all ions greater than m/z=16 are allowed to pass to the detector. The QCL is chopped and the laser induced beam depletion is detected with a lock-in amplifier. This depletion signal is subsequently normalized to the QCL power. The QCL used in this experiment has a tuning range from 1870-1965 cm^{-1} (Fig. 7.1a), a linewidth of ~30 MHz, and an output power of 10-80 mW. The QCL chip is connected to a thermoelectric cooler (TEC) for temperature control. The QCL frequency is tuned by rotating a grating with a stepper motor (0.01 cm^{-1} steps) or by scanning the cavity length continuously (~30 GHz tuning) by applying a 0-100 Volt sine wave ramp to a piezo element. Scans are carried out in a discontinuous fashion as shown in Fig. 7.1b. The QCL is piezo tuned continuously, and at each maximum or minimum in the piezo voltage ramp, the scan is paused and the stepper motor increases the frequency by ~1 cm^{-1}. Absolute frequency calibration is achieved *via* the continuous feedback from a high precision wavemeter (Bristol Instruments 621B-MIR) with an absolute accuracy of ±60 MHz and a repeatability of ±12 MHz. A LabView program automates the tuning, data collection and calibration. Due to imperfections in the anti-reflection coating on the QCL chip, mode-hop free tuning cannot be achieved over the entire QCL gain region. However, we have found that a change in the TEC temperature setting by 3 °C will move the mode hops by as much as 0.5 cm^{-1}; thus, by averaging scans from multiple TEC settings, we can cover the entire tuning range without mode hops.

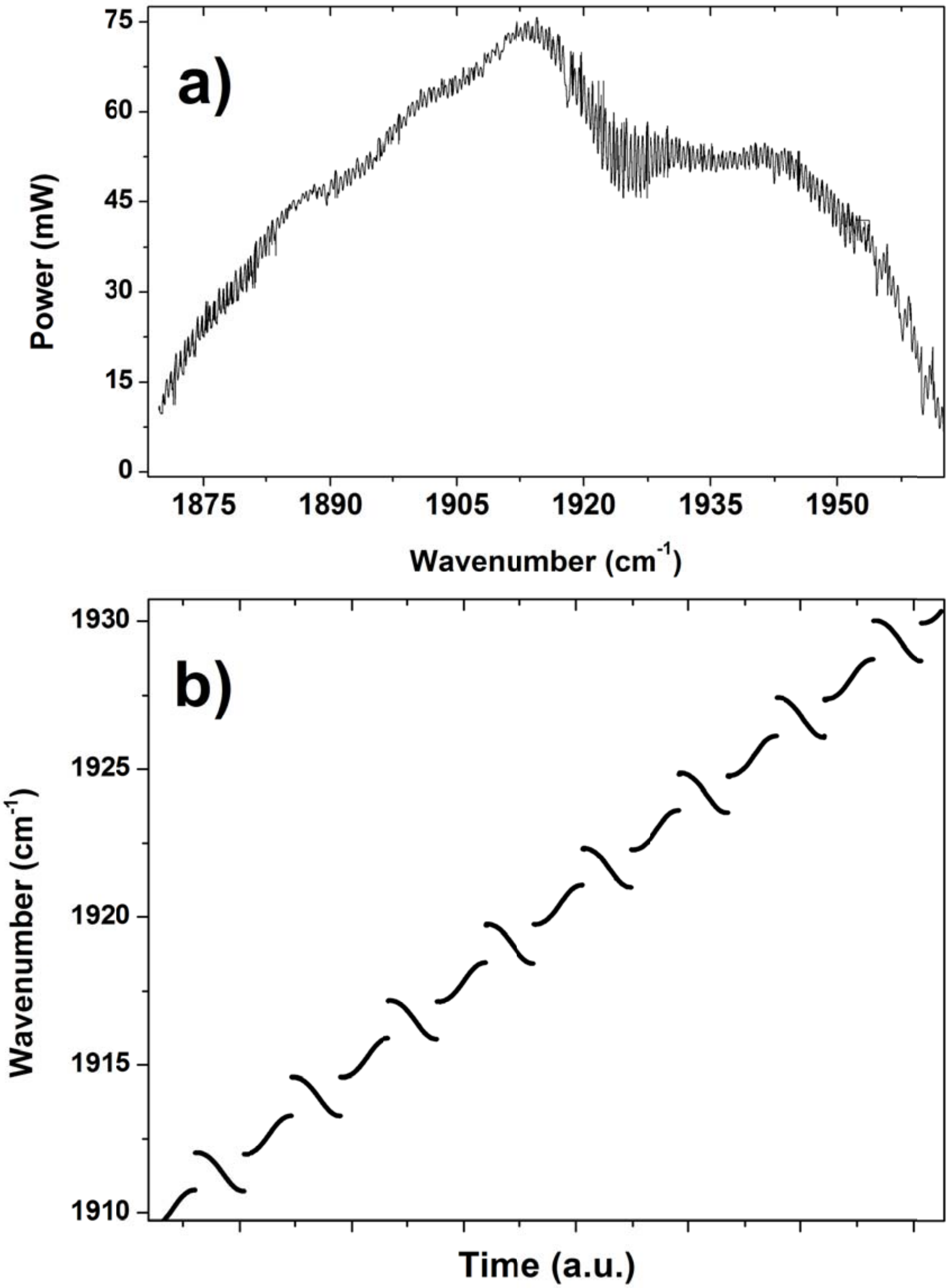

Figure 7.1: a) Output power of the quantum cascade laser system. Oscillations are due to an etalon effect within the QCL external cavity. b) Laser frequency versus time *via* the continuous feedback from a high precision wavemeter, demonstrating the scheme for continuous QCL tuning.

7.3 Theoretical Methods

Geometry optimizations, harmonic frequency calculations, and electron difference density plots of the neutral and cationic aluminum carbonyl clusters are obtained at the CCSD(T) / cc-pVTZ level of theory using the program CFOUR.[83] The geometries are re-optimized at the uB3LYP / cc-pVTZ level of theory in GAMESS,[84] and the uB3LYP density is used for Natural Bond Orbital (NBO)[85] analyses in order to investigate the nature of the bonding in these complexes. The optimized structures for the Al-$(CO)_n$ species considered here are shown in Fig. 7.2.

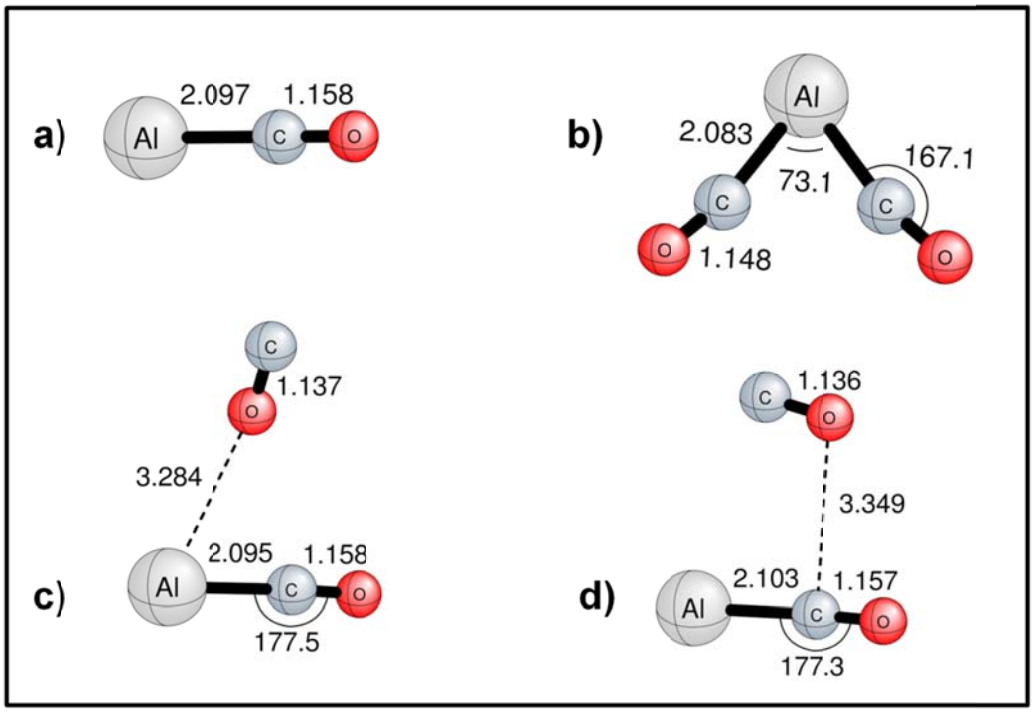

Figure 7.2: Structures of the Al-$(CO)_n$ complexes computed at the CCSD(T)/cc-pVTZ level of theory. Structure a) is the $^2\Pi$ linear complex. Structure d) represents the transition state between structures b) and c) on the Al-$(CO)_2$ potential energy surface.

7.4 Results and Discussion

Several broad bands were previously observed between 1850-2000 cm^{-1} in FTIR matrix isolation experiments of co-deposited Al and CO.[56, 57, 59] In solid Argon, groups of bands near 1870, 1900, and 1990 cm^{-1} were assigned to the CO stretch of Al-CO and the asymmetric and symmetric stretch bands of a C_{2v} Al-$(CO)_2$ species, respectively.[59] The splitting within each set of bands was determined to be due to matrix site effects. After verifying with the mass spectrometer that the droplets were being doped by Al and CO, the QCL was tuned continuously from 1870 to 1965 cm^{-1}, producing the survey spectrum shown in Fig. 7.3. The helium droplet survey spectrum contains bands in two regions centered near 1885 cm^{-1} and 1920 cm^{-1}. These bands are close to those assigned to Al-CO and Al-$(CO)_2$ in solid Argon. No other bands were observed in the tuning range of the QCL.

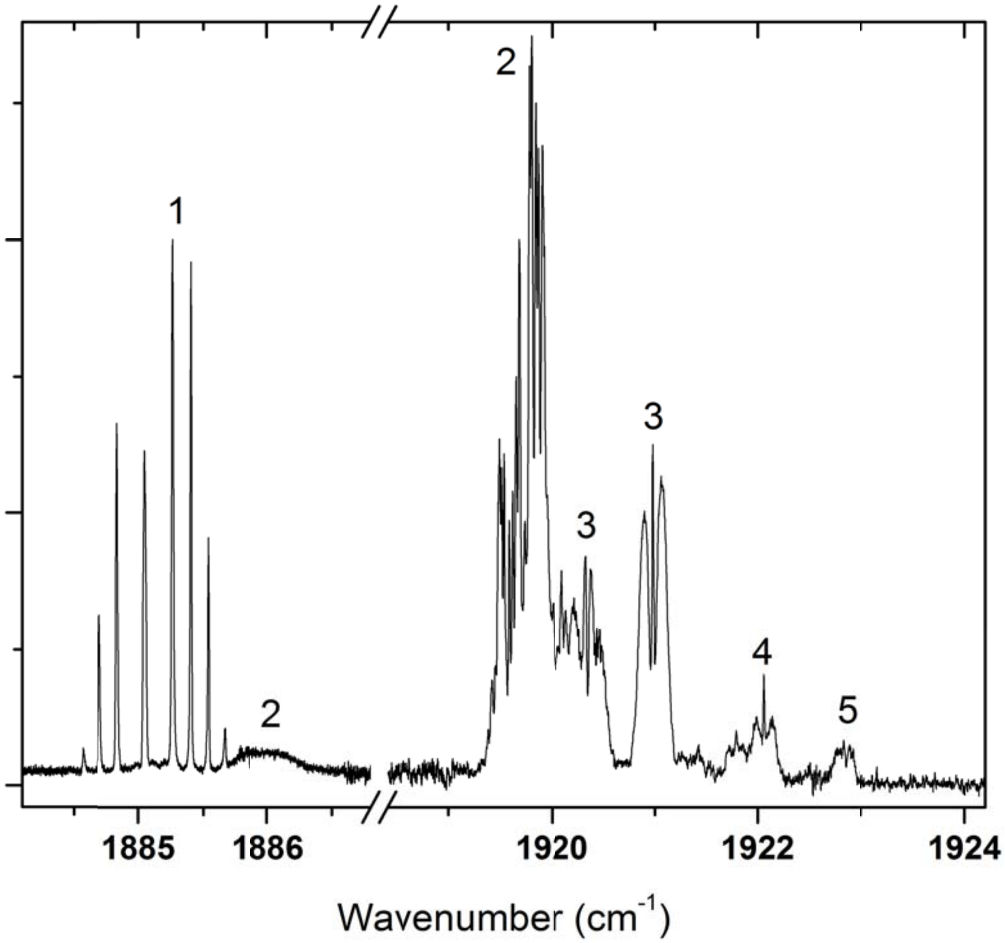

Figure 7.3: Representative regions of the Al-$(CO)_n$ survey spectrum. The QCL was tuned continuously over the entire tuning range. Numbers represent the value of n as determined from the CO pick-up cell pressure dependence curves.

The variation of the signal as a function of CO pick-up cell pressure was determined at various frequencies, as shown in Fig. 7.4. This pick-up cell pressure dependence of the band intensities is used to assign features in the survey spectrum to specific Al-$(CO)_n$ clusters. Approximately 4×10^{-6} Torr is a reasonable pressure for optimizing the pick-up of a single molecule in our differentially pumped gas cell.[38] From this, it is clear that the rotationally resolved band near 1885.0 cm^{-1} is associated with Al-CO, while the bands between 1918 and 1924 cm^{-1} are due to clusters with $n\geq2$. A weak, broader band at 1886 cm^{-1} has the same pressure dependence as the 1919.5 cm^{-1} band and is therefore assigned to an n=2 cluster (red and green pick-up cell pressure curves). The numerical labels in Fig. 7.3 correspond to the Al-$(CO)_n$ assignments based on the CO pressure dependence measurements. To verify the presence of Al in the clusters giving rise to the bands observed here, we fixed the laser on the most intense rovibrational transition in the 1885 cm^{-1} band and measured the optically specific mass spectrum (OSMS).[86] The OSMS shown in Fig. 7.5 is obtained by chopping the fixed frequency laser beam, scanning the quadrupole, and processing the mass spectrometer signal with a lock-in amplifier. As the quadrupole is scanned, a difference spectrum is obtained that corresponds to the difference in the mass spectrum with and without the laser present; that is, a mass spectrum is obtained for only those species being excited by the laser. The OSMS contains an intense peak at m/z=28 due to CO^+ along with two sets of peaks due to $(He)^+_n$ and Al^+-$(He)_n$ ion clusters.

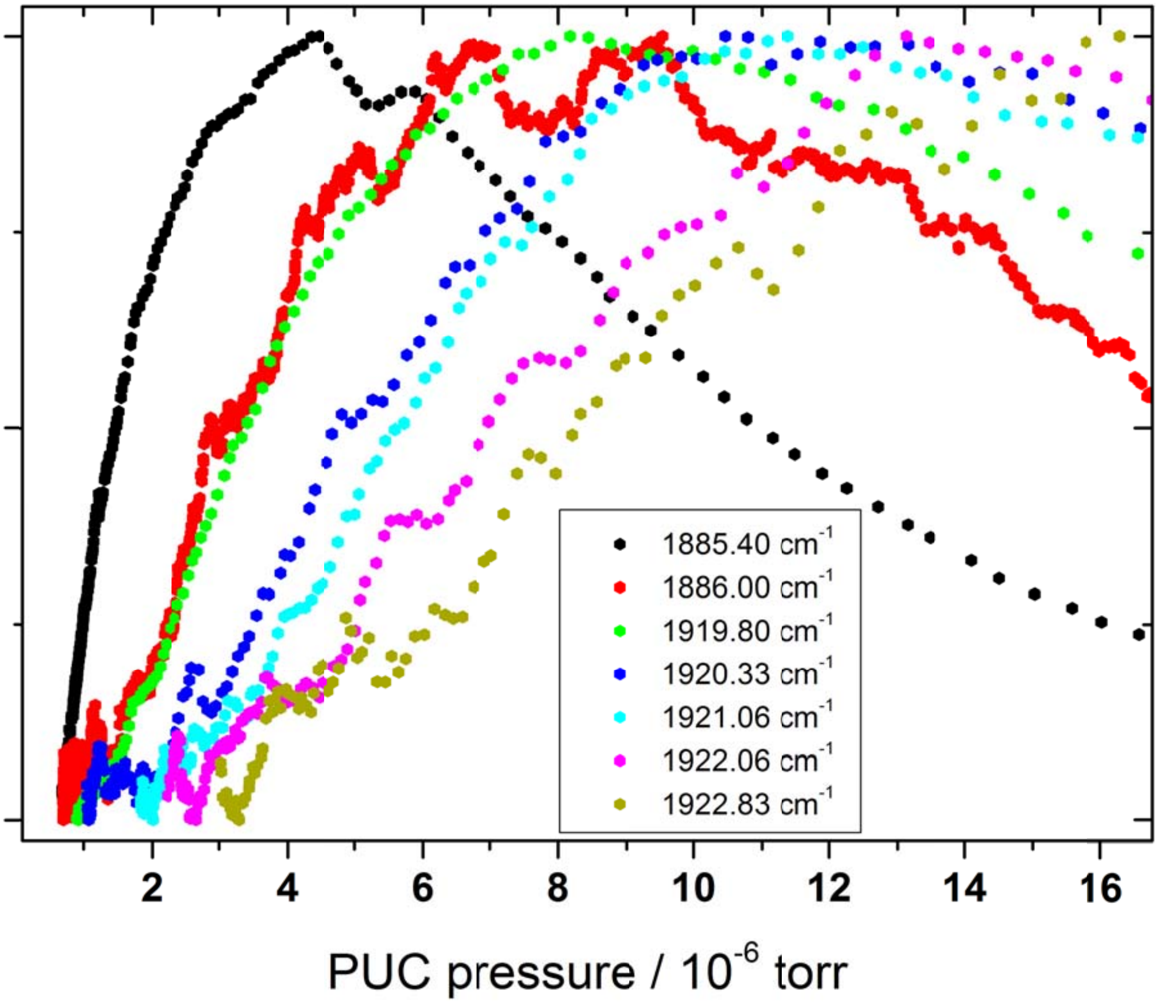

Figure 7.4: Carbon monoxide pressure dependence of the signal intensity at the frequencies indicated in the inset. The leading edges of the pressure dependence curves ($p<\sim 8\times10^{-6}$ Torr) are used to determine the CO composition of the clusters responsible for the observed rovibrational bands.

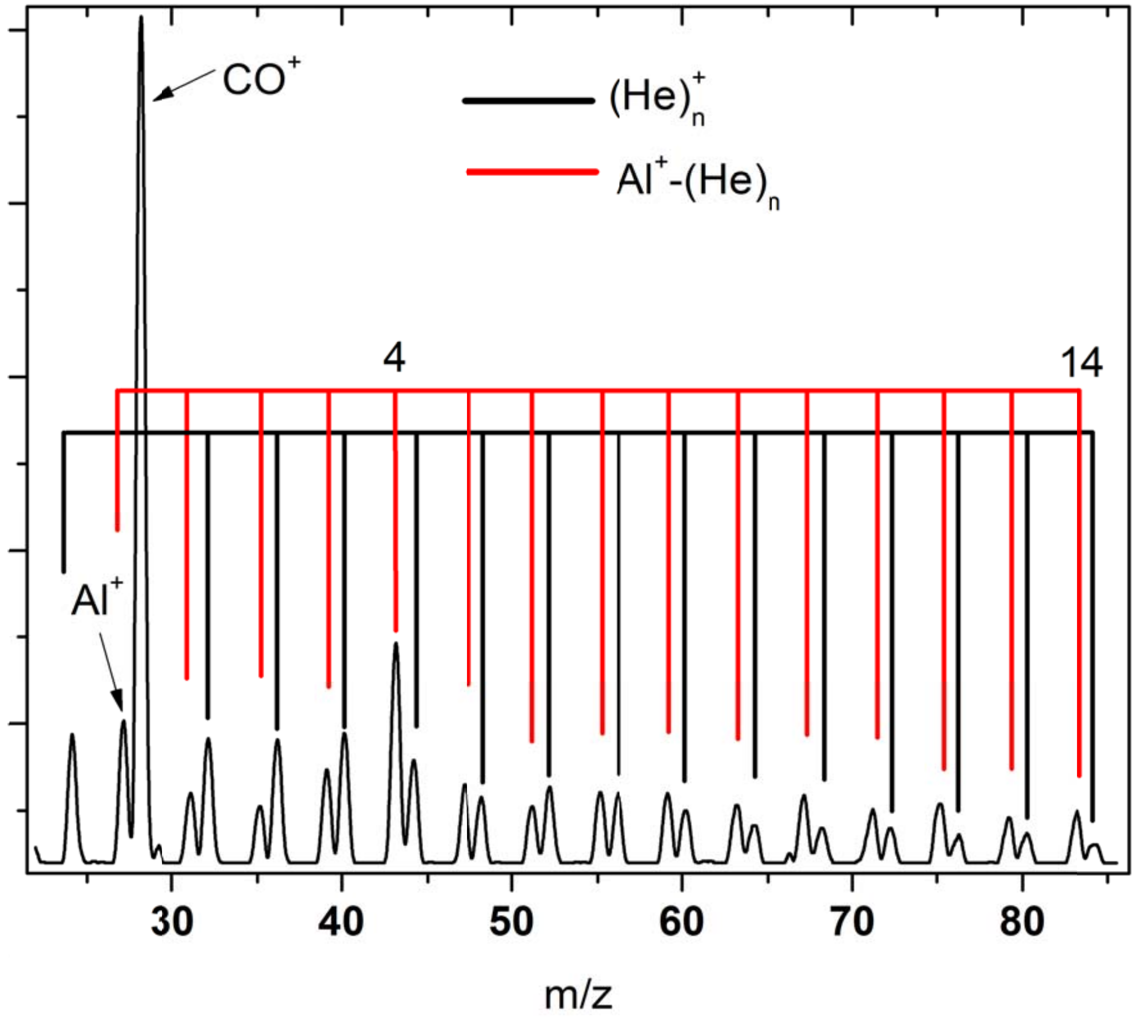

Figure 7.5: Optically specific mass spectrum at 1885.265 cm^{-1}. Along with CO$^+$ (m/z=28), (He)^+_n and Al$^+$-(He)$_n$ progressions are observed, which verifies the presence of Al in the cluster giving rise to the 1885 cm^{-1} band.

7.4.1 $^2\Pi_{1/2}$ Al-CO

The OSMS and the pick-up cell pressure dependence measurements are clearly consistent with an assignment of the feature at 1885 cm^{-1} to an Al-CO band. Fig. 7.6 shows a slower scan through the 1885 cm^{-1} region, revealing well-resolved rotational fine structure (FWHM ≈ 300 MHz). The asymmetric line shapes observed here are often present in the rovibrational spectra of helium solvated molecules,[38] and this inhomogeneous broadening has been attributed to the droplet size distribution [87-89] and other finite size effects associated with the droplets.[90] The smooth red trace below the experimental spectrum is a simulation based on a $^2\Pi_{1/2}$ ground state of Al-CO (ν_1 CO stretch vibration, $\Gamma_{v'}=\Sigma^+$). Indeed, the computed CCSD(T) ground state for Al-CO is $^2\Pi$, and the lowest energy spin-orbit level ($^2\Pi_{1/2}$) is the only one expected to be populated at 0.4 K. The spacing between the $P(3/2)$ and $R(1/2)$ transitions is approximately $6B$, which is consistent with Hund's case (a) spin-orbit coupling; that is, the spin-orbit coupling constant A is much greater than BJ, leading to two well separated $^2\Pi_{1/2}$ and $^2\Pi_{3/2}$ spin components.[91] It is also important to point out that any splitting due to lambda doubling is less than ~300 MHz. This is consistent with a relatively small off-diagonal spin-orbit coupling effect. Apparently, the interaction between the $^2\Pi_{1/2}$ state and $^2\Sigma_{1/2}$ excited states is too small to lead to any parity splitting beyond the inherent inhomogeneous linewidth. The spectrum was fitted assuming a rotational energy level pattern for a Hund's case (a) $^2\Pi$ state in which the spin-orbit coupling constant A is fixed to the Al atomic ($^2P_{3/2}$ – $^2P_{1/2}$) spin-orbit splitting (112 cm^{-1}), and the resulting constants are summarized and compared to the *ab initio* constants in Table 7.1. Any deviation of the B constant from the *ab initio* value is simply interpreted as a change in the effective rotational moment of inertia due to the presence of the helium. The ratio $B''_{\mathrm{CCSD(T)}}:B''_{\mathrm{He}}$ is equal to 2.1, which is consistent with the enhanced moment of inertia observed for other heavy rotors upon solvation in helium, providing further support to our assignment.[38, 74, 92]

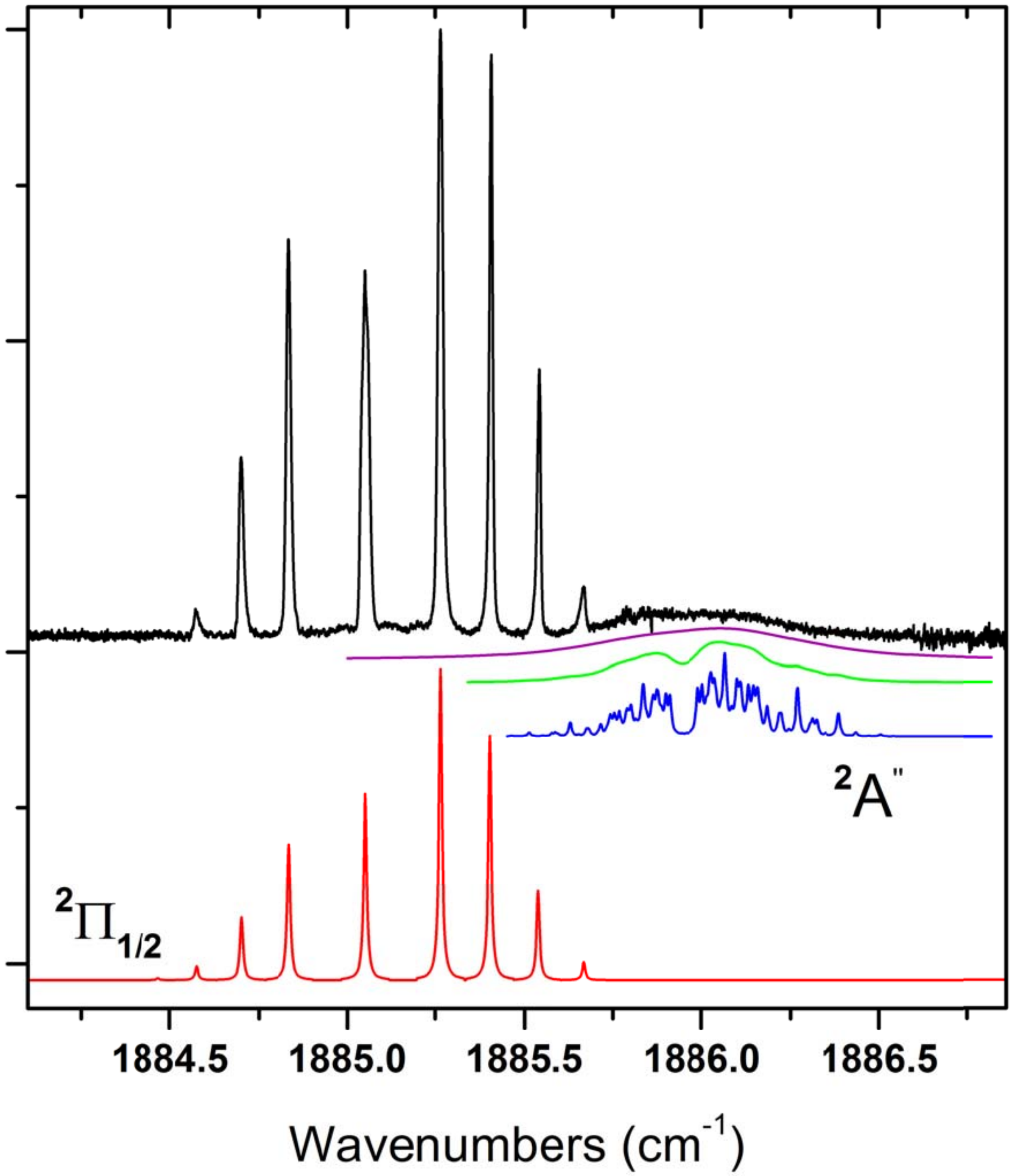

Figure 7.6: Rovibrational spectrum of the $^2\Pi_{1/2}$ Al-CO species (Σ^+, ν_1 CO stretch fundamental). The red curve is the fitted spectrum based on a $^2\Pi_{1/2}$ ground state with Hund's case (a) spin orbit coupling. The blue, green, and purple curves are simulations of the ν_2 CO stretch of a $^2A''$ (Al-CO)-CO complex, assuming 300 MHz, 2 GHz, and 10 GHz linewidths, respectively.

Table 7.1: Constants obtained from the fit of the fundamental (ν_1) and overtone ($2\nu_1$) spectra of $^2\Pi_{1/2}$ Al-CO.[a]

cm^{-1}	B″	B′	D″ ($x10^{-4}$)	D′ ($x10^{-4}$)	ν_0	$\Delta\nu_{CO}$	Γ	$T_{rot}(K)$[d]
ν_1	0.0724(3)[b]	0.0727(1)	1.4(1)	1.22(6)	1885.049(1)	-258	0.01	0.37
$2\nu_1$	0.0724[c]	0.0731(1)	1.4[b]	1.06(3)	3747.536(1)	-	0.01	0.37
CCSD(T)	0.148	-	-	-	1923	-259	-	-

[a] The spin-orbit coupling constant is set to the Al ($^2P_{3/2} - {}^2P_{1/2}$) atomic spin-orbit splitting, 112 cm^{-1}.

[b] Numbers in parenthesis represent 1σ error associated with the fit.

[c] Fixed to the mean values for the ν_1 band.

[d] The rotational temperature was fixed at 0.37 K.

Given the rather large signals associated with the ν_1 CO stretch band, we searched for the $2\nu_1$ band in the 3700-3800 cm^{-1} range using a tunable optical parametric oscillator (OPO) (Lockheed-Martin, Aculight). Fig. 7.7 shows the $2\nu_1$ band centered at 3747.38 cm^{-1}, along with the fitted spectrum. The excited state rotational constants are adjusted in the fit, keeping the ground state constants fixed to the values obtained for the ν_1 band. The resulting constants from the fit are given in Table 7.1. The higher output power of the OPO (~20 times larger than the QCL), the larger degree of droplet evaporation (~750 He atoms),[38] and the intrinsically strong oscillator strength of the fundamental leads to a relatively high signal to noise ratio for the overtone transition observed here. The linewidths and shapes are essentially the same as for the fundamental band, which is consistent with an inhomogeneous broadening mechanism due to the droplets as discussed above.

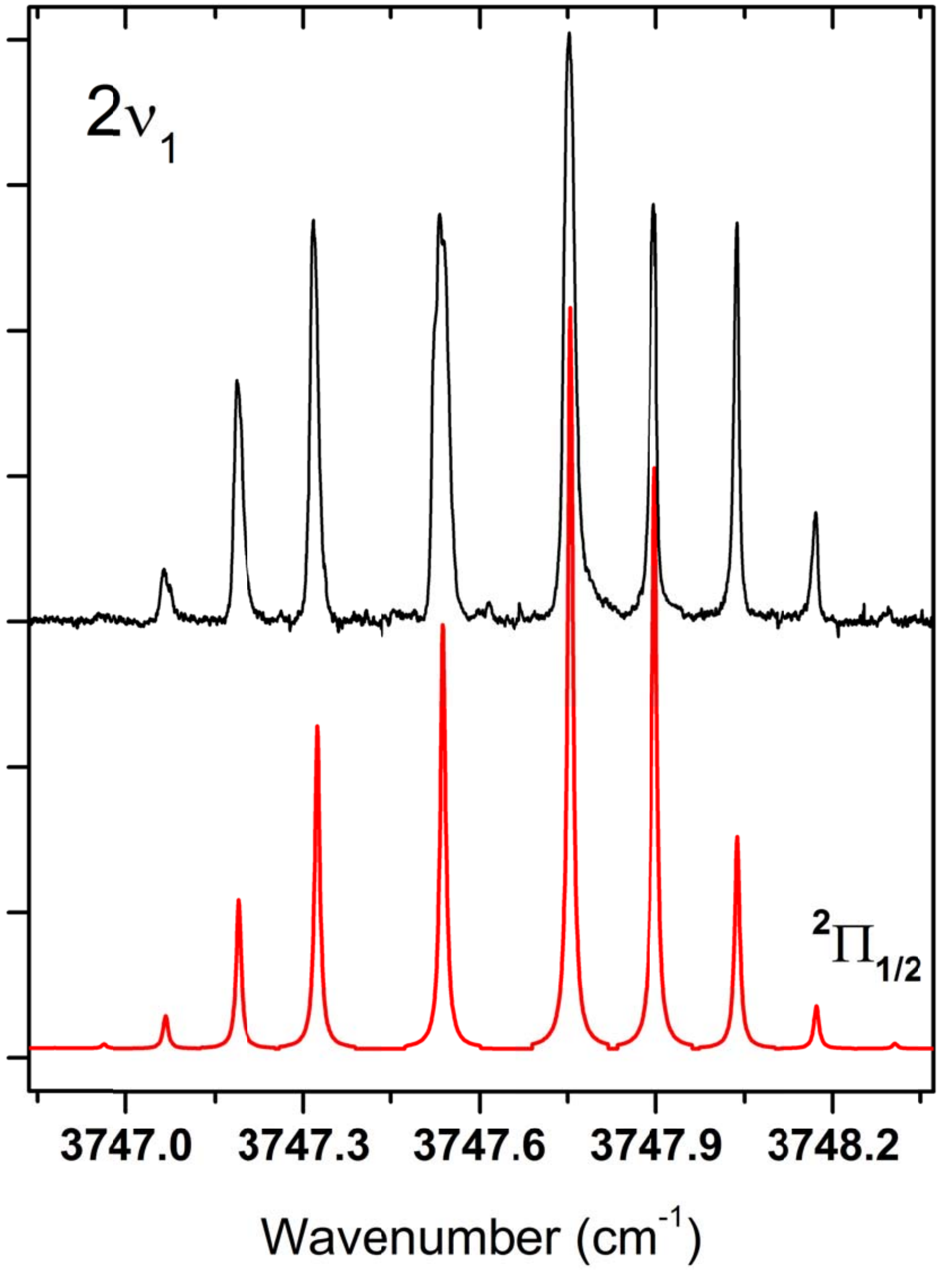

Figure 7.7: Rovibrational spectrum of the $^2\Pi_{1/2}$ Al-CO species (Σ^+, $2\nu_1$ CO stretch overtone). The red curve is the fitted spectrum based on a $^2\Pi_{1/2}$ ground state with Hund's case (a) spin orbit coupling.

7.4.2 $^2B_1$ Al-(CO)$_2$

Turning our attention to the region near 1920 cm^{-1}, an intense band associated with an Al-(CO)$_2$ cluster is observed at 1919.5 cm^{-1}. This band is overlapped by an Al-(CO)$_3$ band at ~1920.3 cm^{-1}. Shifted slightly to the blue are weaker bands associated with clusters having n≥3. The CO pick-up cell pressure was reduced to ~2.0x10^{-6} Torr, decreasing the Al-(CO)$_3$ band intensity significantly such that the rotationally resolved band due to Al-(CO)$_2$ could be measured cleanly. Fig. 7.8 shows the Al-(CO)$_2$ band at this lower pressure condition. On the basis of previous matrix isolation ESR and IR measurements,[56, 57, 59, 65] previous *ab initio* calculations,[67] and our CCSD(T) investigation of the Al-(CO)$_2$ potential energy surface, we began the analysis of the rotational structure assuming a $^2B_1$ electronic ground state of a symmetric C_{2v} Al-(^{12}CO)$_2$ species. The inset of Fig. 7.8 shows the coordinate system used for the simulation. The *z* and *x* axes are defined as the C_2 and out of plane axes, respectively. Hence, the *a*, *b*, and *c* inertial axes lie on the *y*, *z*, and *x* axes, corresponding to a IIr representation for the simulation. The ground state rovibronic symmetries (including nuclear spin: $\Gamma_{nuc}=A_1$) are therefore B_1, A_1, A_2, and B_2 for ee, eo, oe, and oo rotational levels, respectively.[93] Given that ^{12}CO is a composite boson, the Pauli principle requires that $\Gamma_T=A_1$ or A_2, and transitions originating from ee and oo rotational levels are therefore missing. With these symmetry restrictions, we simulated the spectrum for an asymmetric ^{12}CO stretch band (b_2; a-type band; $\Delta K_a=0$, $\Delta K_c=\pm1$), using the PGopher program.[94] In the initial simulation, we used the CCSD(T) rotational constants divided by 3 to account for the added moment of inertia from the helium. The PGopher contour fitting routine was used to refine the values of the rotational constants. The red trace in Fig. 7.8 is the fitted spectrum, which is clearly in excellent agreement with the experiment, providing an unambiguous assignment to the b_2 asymmetric ^{12}CO stretch band of the $^2B_1$ Al-(^{12}CO)$_2$ species. The *ab initio* constants and those obtained from the fit are summarized in Table 7.2. Here, we find that the experimental $(B+C)''/2$ is a factor of 2.9 smaller than the CCSD(T) value, which is again consistent with previous determinations of rotational constant reductions for helium solvated molecules.[38, 74, 92]

Table 7.2: Constants obtained from the PGopher contour fit of the b_2 asymmetric and a_1 symmetric CO stretch spectra of $^2B_1$ Al-(CO)$_2$.

cm^{-1}	$(B+C)''/2$	$(B+C)'/2$	A''	A'	ν_0	$\Delta\nu_{CO}$	Γ	T_{rot} (K)
b_2	0.0272(1)[c]	0.267(1)	0.0680(5)	0.0686(6)	1919.683(1)	-223	0.0191(3)	0.391(3)
CCSD(T)[a]	0.0783	-	0.192	-	1958	-194	-	-
a_1	0.0264(1)	0.0260(1)	0.0656(1)	0.0651(1)	1959.735(1)	-136	0.0274(3)	0.404(2)
CCSD(T)[b]	0.0772	-	0.191	-	1990	-115	-	-

[a] Calculations for Al-(^{12}CO)$_2$

[b] Calculations for Al-(^{13}CO)$_2$

[c] Numbers in parenthesis represent 1σ error associated with the contour fits.

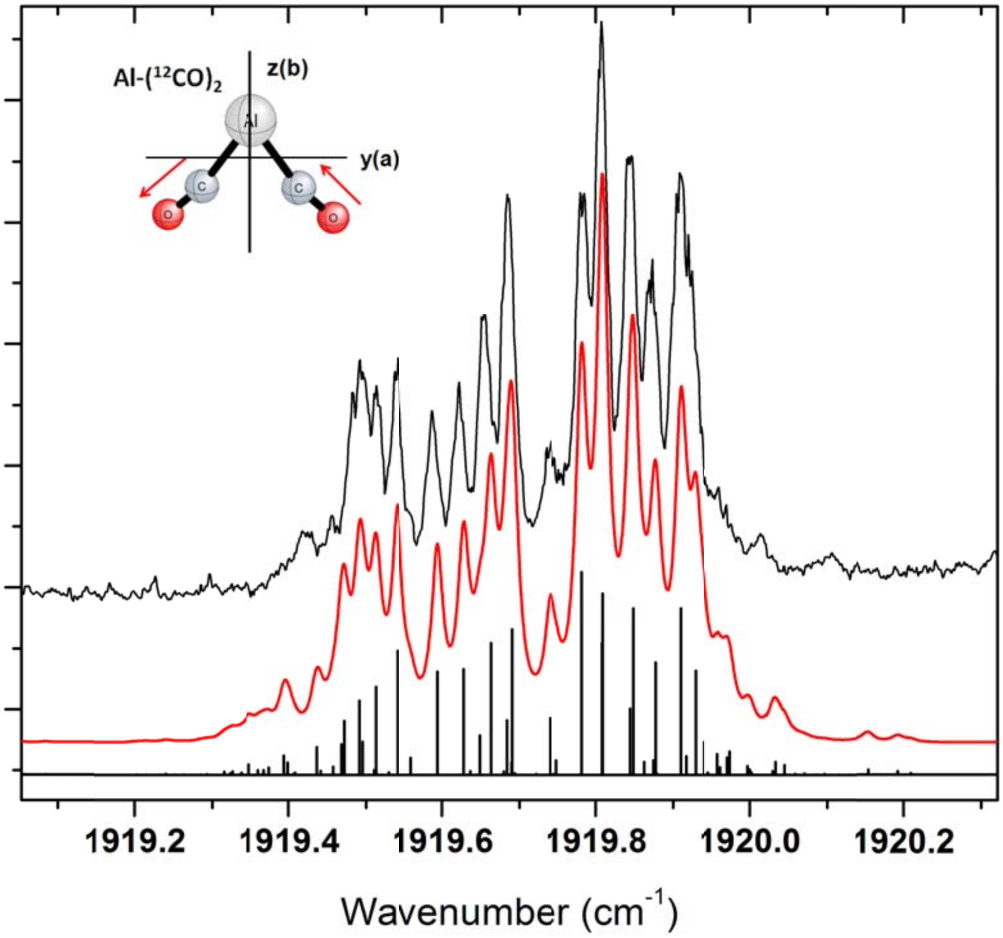

Figure 7.8: Rovibrational spectrum of the $^2B_1$ Al-(^{12}CO)$_2$ species (b_2, asymmetric CO stretch). The inset shows the coordinate system employed in determining the rotational symmetries (IIr representation). The red curve is a simulation based on the symmetry properties and rotational constants discussed in the text.

Our CCSD(T) harmonic frequency calculation for Al-(CO)$_2$ places the symmetric CO stretch band 77 cm^{-1} to the blue of the asymmetric CO stretch band. Unfortunately, this means that the symmetric stretch band is beyond the tuning range of the QCL. However, the red shift associated with ^{13}CO isotopic substitution brings the symmetric stretch band into the QCL tuning range, while also shifting the asymmetric stretch out of the tuning range. Fig. 7.9 shows the experimental and fitted spectrum for the a_1

symmetric ^{13}CO stretch (b-type band; $\Delta K_a = \pm 1$, $\Delta K_c = \pm 1$). The nuclear spin functions now span $3A_1 \oplus B_2$ (^{13}CO is a composite fermion), and the Pauli principle requires that $\Gamma_T = B_1$ or B_2, leading to a 3:1 intensity ratio for transitions originating from ee, oo and eo, oe rotational levels, respectively.[93] Again, the fitted spectrum is in excellent agreement with experiment, and the constants are summarized in Table 7.2.

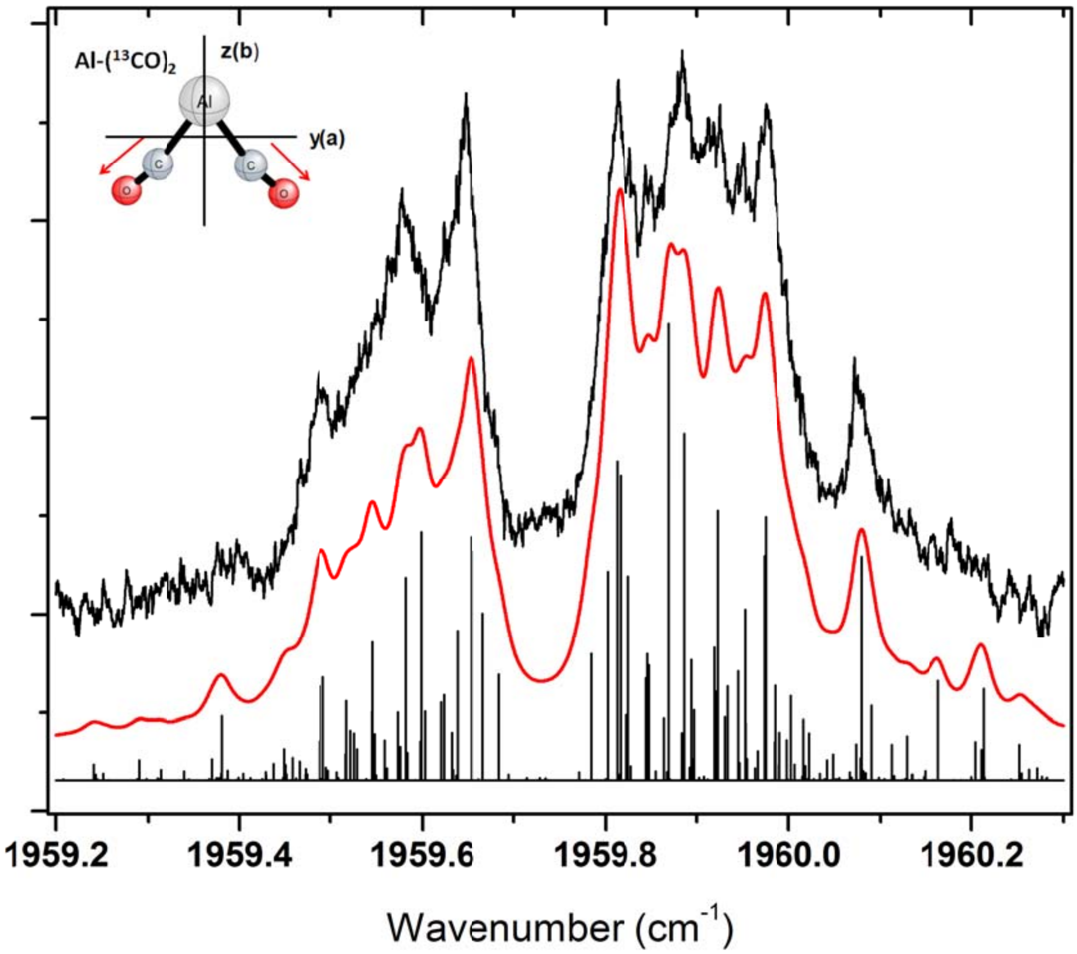

Figure 7.9: Rovibrational spectrum and simulation (red curve) of the $^2B_1$ Al-(^{13}CO)$_2$ species (a_1, symmetric CO stretch).

7.4.3 Al-(CO)$_{n>2}$

The Al-CO ν_1 CO stretch band is red shifted ~258 cm^{-1} from free CO, which indicates a substantial reduction in the CO bond order. This relatively large redshift implies an Al-CO interaction that is stronger than simple physisorption. Indeed, the CCSD(T) (zero-point energy corrected) calculations give an Al-CO bond energy of 2275 cm^{-1} (6.5 kcal/mol) and a CO bond length 0.02 Å longer than for free CO. Apparently, the CO bond order increases upon attachment of the second CO, leading to a shift back to the blue for the Al-(CO)$_2$ bands. Interestingly, all of the bands found in the QCL tuning range associated with clusters larger than n=2 are only slightly blue shifted from the Al-(CO)$_2$ asymmetric stretch band at 1919.5 cm^{-1}. For example, two bands associated with Al-(CO)$_3$ are found at 1920.3 and 1921.1 cm^{-1}, and bands due to Al-(CO)$_4$ and Al-(CO)$_5$ are centered near 1922.1 and 1922.8 cm^{-1}, respectively. Each of these bands consists of unresolved *P*, *Q*, and *R* contours. The relatively small shifts of the n>2 bands from the Al-(CO)$_2$ band suggest that the n>2 clusters consist of a covalently bound Al-(CO)$_2$ core with the additional CO molecules attached *via* van-der-Waals interactions. This is consistent with our CCSD(T) calculations that fail to find an n=3 species in which all three CO molecules are strongly bound. Instead, two minima on the n=3 potential were found that correspond to an Al-(CO)$_2$-CO structure with the third CO molecule bound by only ~250 cm^{-1}. For the n>2 clusters, the Al-(CO)$_2$ core is only weakly perturbed by the "solvent" CO molecules, leading to relatively small frequency shifts of the asymmetric CO stretch of the core species. The CO stretch bands associated with the external CO molecules are predicted to be near the band origin of free CO (2143 cm^{-1}),[95] which is outside the QCL tuning range.

7.4.4 (Al-CO)-CO

A rather weak feature in the survey spectrum near 1886 cm^{-1} has the pick-up cell pressure dependence signature of an Al-(CO)$_2$ species. This band is blue-shifted from the Al-CO ν_1 band origin by only 1.0 cm^{-1}. For the $^2B_1$ Al-(CO)$_2$ complex, the next highest frequency fundamental band below the asymmetric CO stretch is a symmetric C-Al-C stretch, predicted at 500 cm^{-1}. Therefore, it is unlikely that the feature at 1886 cm^{-1} is due to a combination band associated with the C_{2v} n=2 species. Nevertheless, the pick-up cell pressure dependence of the signal is essentially identical for measurements at 1886.00 and 1919.80 cm^{-1}. We therefore searched for other isomers on the n=2 potential surface that could be responsible for this band.

Fig. 7.10 shows schematically the non-relativistic Al-CO+CO potential energy surface, which is zero point energy corrected at the CCSD(T) / cc-pVTZ level of theory. The energies are reported relative to the infinitely separated and relaxed ($^2\Pi$) Al-CO and ($^1\Sigma^+$) CO fragments. We found one locally stable isomer (Fig. 7.2c) that is ~10 kcal/mol higher in energy than the $^2B_1$ Al-(CO)$_2$ global minimum. In this $^2A''$ isomer, the oxygen atom on a weakly bound CO nominally points towards the Al-C bond of an Al-CO moiety, which resembles the $^2\Pi$ Al-CO species. The (Al-CO)-CO $\rightarrow$ Al-CO+CO binding energy is ~400 cm^{-1}, and a small barrier of ~200 cm^{-1} separates this isomer from the global minimum. On the basis of the transition state structure (Fig. 7.2d), it is evident that the reaction path (Al-CO)-CO $\rightarrow$ Al-(CO)$_2$ corresponds simply to the rotation of the weakly bound CO unit; hence, the barrier height is relatively small and on the order of the (Al-CO)-CO binding energy. An extensive scan of the n=2 potential surface failed to find any other locally stable isomers.

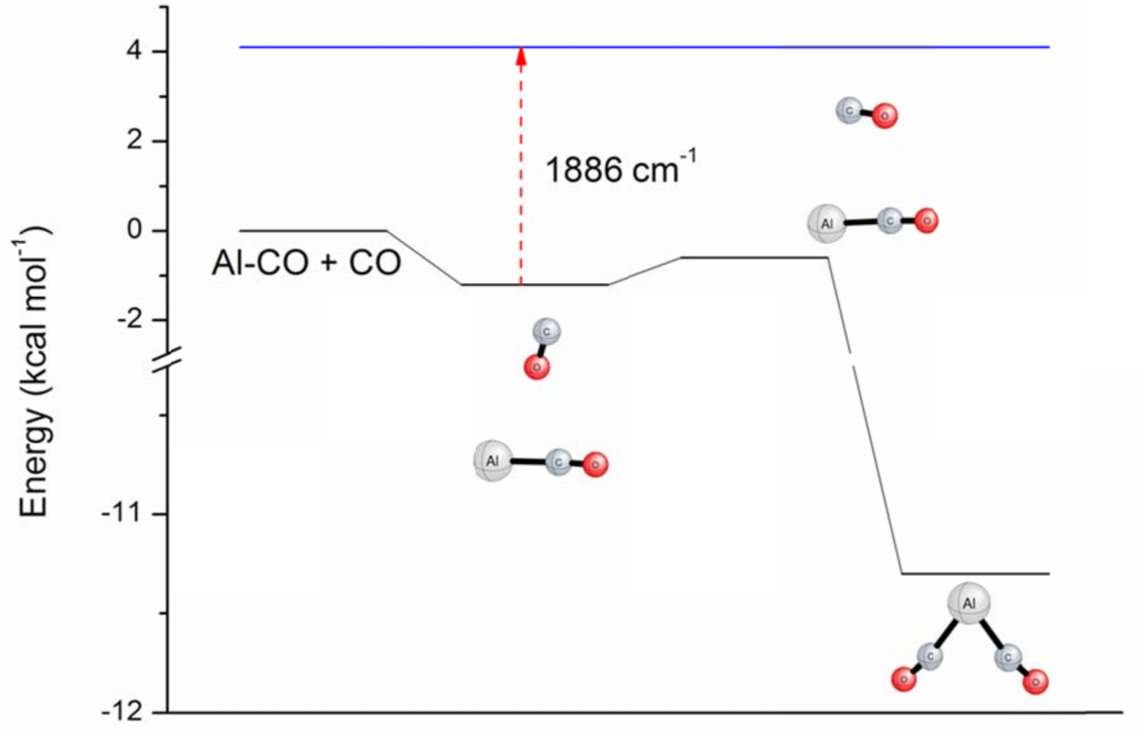

Figure 7.10: Schematic of the Al-CO+CO CCSD(T)/cc-pVTZ non-relativistic potential energy surface. Energies are in kcal/mol and are relative to the infinitely separated $^2\Pi$ Al-CO and $^1\Sigma^+$ CO fragments. The $^2A''$ (Al-CO)-CO complex is bound by ~400 cm^{-1} and is separated from the $^2B_1$ Al-(CO)$_2$ global minimum by an ~200 cm^{-1} barrier. The blue line is representative of the energy associated with ν_2 CO stretch excitation of the (Al-CO)-CO metastable complex.

Given the small shift from the Al-CO band, it is tempting to assign the 1886 cm^{-1} band to the CO stretch of the Al-CO moiety within this weakly bound (Al-CO)-CO cluster. The computed harmonic frequency shift is 13.3 cm^{-1} to the red, which can be compared to the 1 cm^{-1} experimental blueshift. Nevertheless, this may be reasonable agreement given the harmonic approximation employed. Furthermore, the small shifts here are likely representative of the subtle changes in the dipole moment and polarizability of (Al-CO)-CO upon vibrational excitation, which are not taken into account by the *ab initio* frequency calculation. We must also consider the probability for forming the higher energy (Al-CO)-CO species. It is important to point out here the process by which an Al-$(CO)_2$ cluster is formed in a helium droplet. The droplet first picks up an Al atom and then picks up a CO molecule. The Al and CO are attracted to each other, condense within the droplet, and cool to 0.4 K on a timescale that is competitive with the average time it takes to pick-up the second CO molecule.[78, 96] Upon pick-up of the second CO molecule, in addition to the direct formation of the C_{2v} complex, it is reasonable to suspect that some fraction of the n=2 species will be kinetically trapped in the higher energy (Al-CO)-CO configuration. Indeed, non-equilibrium cluster growth in the dissipative helium environment has been demonstrated on multiple occasions.[97-102] When barriers exist between the cluster approach geometry and the global minimum, the dissipation of the condensation energy can be rapid enough to kinetically trap the higher energy cluster configuration. For example, barriers as low as 100 cm^{-1} have been shown to be sufficient to kinetically trap small metastable $(HF)_n$ clusters.[103]

An unambiguous determination of the source of the 1886 cm^{-1} band is unfortunately not possible due to the lack of resolved rotational fine structure. There is a source of broadening that washes out the rotational fine structure, which is in addition to the inhomogeneous broadening sources that limit the linewidths in the ν_1 Al-CO band. We have simulated the Al-CO stretch band of the (Al-CO)-CO isomer using three different linewidths (blue, green and purple traces in Fig. 7.6). The simulation is based on an a′ vibrational band with transition dipole moment components $(\mu_a, \mu_b, \mu_c)=(0.02, 1.01, 0.00)$ and rotational constants equivalent to our *ab initio* values divided by a factor of 3. Assuming the 1886 cm^{-1} band is due to (Al-CO)-CO, a linewidth of at least 2 GHz is required to wash out the rotational fine structure, which is over 6 times broader than the inhomogeneously broadened Al-CO rovibrational transitions. However, for a satisfactory agreement with experiment, the linewidth could be as large as 10 GHz in the simulation. Although we can only speculate as to the source of this additional broadening, one intriguing possibility is a homogeneous mechanism associated with the photo-induced reaction of (Al-CO)-CO to produce the thermodynamically favored Al-$(CO)_2$ species. The blue line in Fig. 7.10 represents schematically the energy associated with the vibrational excitation of (Al-CO)-CO. This energy is above both the dissociation limit to form Al-CO + CO and the reaction barrier to form Al-$(CO)_2$. In principle, the linewidth could be due to the dissociation process rather than a reaction. However, there are many studies of helium solvated clusters that can undergo vibrational predissociation upon single photon excitation, yet they do not have vibrational bands significantly broadened beyond the intrinsic inhomogeneous linewidth.[38, 101, 104-106] One example of this is the $2\nu_1$ band of the Al-CO complex observed in this study. Furthermore, the Q-branch linewidth of the 1921.1 cm^{-1} band associated with Al-$(CO)_2$-CO is only ~300 MHz (Fig. 7.3). For this vibrational transition, the photon energy is again well above the threshold (~250 cm^{-1}) for dissociation of Al-$(CO)_2$-CO to Al-$(CO)_2$ + CO, yet the Q-branch linewidth is no broader than the linewidth observed for the 1919.5 cm^{-1} band associated with the Al-$(CO)_2$ complex, which cannot dissociate upon single photon excitation. The broad linewidth observed for the 1886.0 cm^{-1} band is at least suggestive of the proposed mechanism and would be interesting to investigate further. An IR-IR time-resolved double resonance experiment would be capable of probing the transient population changes associated with the depletion and production of (Al-CO)-CO and Al-$(CO)_2$, respectively.

7.5 *Ab Initio* Calculations

In order to better understand the nature of the bonding in these clusters, we have carried out high level *ab initio* calculations and an NBO analysis of neutral and ionic Al-$(CO)_{1,2}$. Table 7.3 summarizes the geometric parameters and electronic states calculated at the CCSD(T)/cc-pVTZ level, and the incremental Al-CO bond energies are given in Table 7.4. The zero-point corrected bond energy in Al-CO is 6.5 kcal/mol, which, for comparison, is slightly larger than a strong hydrogen bond. Nevertheless, the rather large frequency shift (258 cm^{-1}) suggests that weak electrostatic or van der Waals interactions alone cannot account for the binding in the Al-CO species. Instead, the position of the CO stretch resembles those measured for "classical" transition metal carbonyl compounds in which significant charge transfer occurs between the metal atom and the CO ligands.[24] It is now well known that the interplay between σ- and π-donation can lead to rather dramatic shifts in the CO stretch frequencies of transition metal carbonyls, and the position of the CO stretch bands provides a signature of the charge transfer interactions in these systems.[107-111] Since the CO 5σ molecular orbital (carbon lone pair) is slightly anti-bonding, σ-donation into an empty metal atom d-orbital leads to a small blueshift. For transition metal atom d-orbitals with the appropriate symmetry, donation of electron density into the CO 2π* antibonding orbitals results in a redshift, with a magnitude depending on the extent of charge transfer. Comparing the two effects, π-donation is regarded as having the larger influence on the carbonyl stretch.

Table 7.3: Bond lengths (Angstroms) and angles (Degrees) for Al-CO, Al-$(CO)_2$, Al^+-CO and Al^+-$(CO)_2$ at the CCSD(T)/cc-pVTZ level of theory.

	R_{Al-C}	R_{C-O}[a]	R_{C-C}	R_{O-O}	A_{C-Al-C}	A_{Al-C-O}
AlCO ($^2\Pi$)	2.097	1.158	-	-	-	180.0
$Al(CO)_2$ ($^2B_1$)	2.083	1.148	2.481	4.227	73.1	167.1
$AlCO^+$ ($^1\Sigma^+$)	2.817	1.128	-	-	-	180.0
$Al(CO)_2^+$ ($^1A_1$)	2.793	1.128	3.340	4.846	73.5	174.9

[a] For comparison, the equilibrium bond length of CO is 1.136 Å at this level.

Table 7.4: CCSD(T)/cc-pVTZ dissociation energies (kcal mol^{-1}).

	ΔE_{elec}	ΔZVPE	ΔE_{total}
Al + CO → Al-CO	−7.3	+0.8	−6.5
Al-CO + CO → Al-$(CO)_2$	−13.0	+1.8	−11.2
Al^+ + CO → Al^+-CO	−8.1	+0.7	−7.4
Al^+-CO + CO → Al^+-$(CO)_2$	−7.5	+0.8	−6.7

We have applied two approaches to investigate the degree of charge transfer in Al-CO. Fig. 7.11 shows an electron difference density (EDD) plot, which corresponds to the CCSD(T) electron densities of Al and CO subtracted from the electron density of Al-CO. The plane of the EDD is the same plane as the singly occupied $^2\Pi$ molecular orbital. From the EDD, we can see qualitatively that there is a net reduction of electron density (dashed contours) in the region above and below the Al atom, while there is a net gain (solid contours) above and below the C and O atoms. The EDD plot is already suggestive of a significant π-donation interaction from the singly occupied Al p-orbital into a region that resembles an antibonding CO molecular orbital, which is exactly the type of charge transfer that could lead to the large CO redshift. Natural Bond Orbital analysis is another effective way to investigate semi-quantitatively the relative importance of donor-acceptor interactions of this type.[112] The Al-C and C-O natural bond orders obtained from natural resonance theory [113-115] are given in Table 7.5. The NBO analysis for Al-CO finds an Al-C natural bond orbital with significant occupation (bond order of 0.992) and shows that there is a reduction in the C-O bond order from 3.00 in free CO to 2.55, which is consistent with the observed redshift. Furthermore, the trends in the bond lengths, frequency calculations, and the natural bond orders show that the formation of Al-$(CO)_2$ leads to a CO stretch blueshift relative to Al-CO ($\Delta\nu_{calc}$=35.3 cm^{-1}). For comparison, the experimentally observed blueshift is $\Delta\nu_{exp}$=34.5 cm^{-1}.

Table 7.5: Natural bond orders for Al-CO and Al-$(CO)_2$ from natural resonance theory.

Natural Bond Order[a]	Al-C	C-O
AlCO	0.995	2.551
Al$(CO)_2$	1.272	2.621

[a] NBO analysis is carried out with the uB3LYP/cc-pVTZ density matrix.

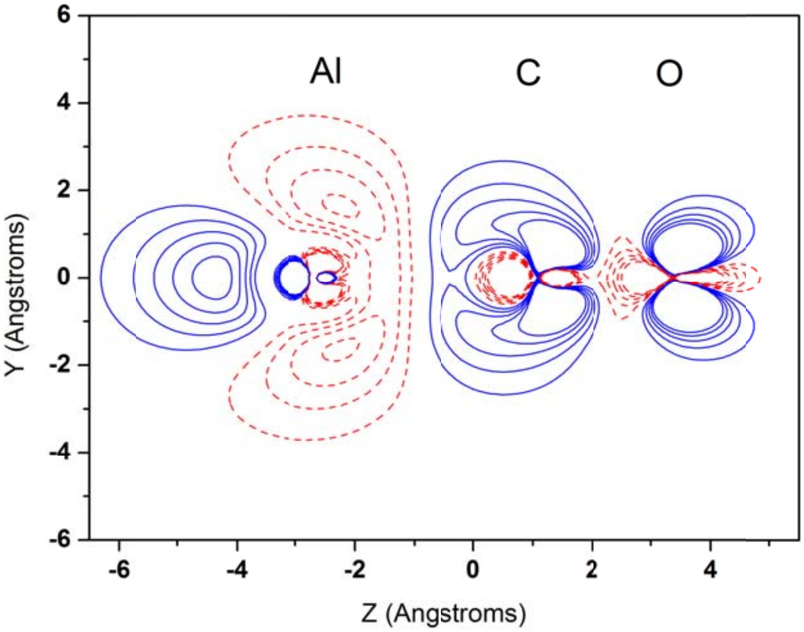

Figure 7.11: Non-relativistic CCSD(T) electron difference density plot for $^2\Pi$ Al-CO. The difference is defined as $^2\Pi$ Al-CO – ($^1\Sigma^+$ CO + ^{2}P Al) in which the singly occupied p-orbital of the isolated Al atom is forced to lie along the y-axis. The plane of the plot corresponds to the plane of the singly occupied $^2\Pi$ HOMO. Contours range from 0.010 to -0.010 e/Å^3 with increments of 0.002. Solid blue contours are associated with regions of electron gain, and dashed red contours are associated with regions of electron loss.

The relative energetic importance of various donor-acceptor interactions between the Al-CO natural bond orbitals can be estimated by a second order perturbation theory analysis of the Fock matrix in the NBO basis.[112] Here we enforce a starting Al-CO Lewis structure in which CO has a triple bond, effectively eliminating the Al-C NBO. The departure from this idealized Lewis structure can then be assessed in terms of the donor-acceptor interactions between NBOs isolated on either the Al or CO. Fig. 7.12a shows the donor-acceptor interactions that give the largest delocalization energies, along with pictures of the NBOs involved. Indeed, these resemble the ligand to metal σ-donation and metal to ligand π-donation charge transfer pathways discussed above. The σ- and π-donation delocalization energies at this level of theory are 83 and 85 kcal/mol, respectively. This shows that both σ- and π-donation are important in the bonding. The combination of the EDD plot and the NBO analysis provides a qualitative picture of the bonding in Al-CO. The lone pair on the carbon atom donates electron density to the two empty Al p-orbitals (p_x, and to a larger degree p_z), and the singly occupied Al p_y-orbital donates electron density to a π* anti-bonding CO orbital. Here the z-axis is defined as the principal axis of Al-CO. The presence of the σ-donated electron density polarizes the Al $3s^2$ electrons such that a build up of electron density occurs on the side of the Al atom opposite the CO ligand. This is clearly observed in the Al-CO EDD plot.

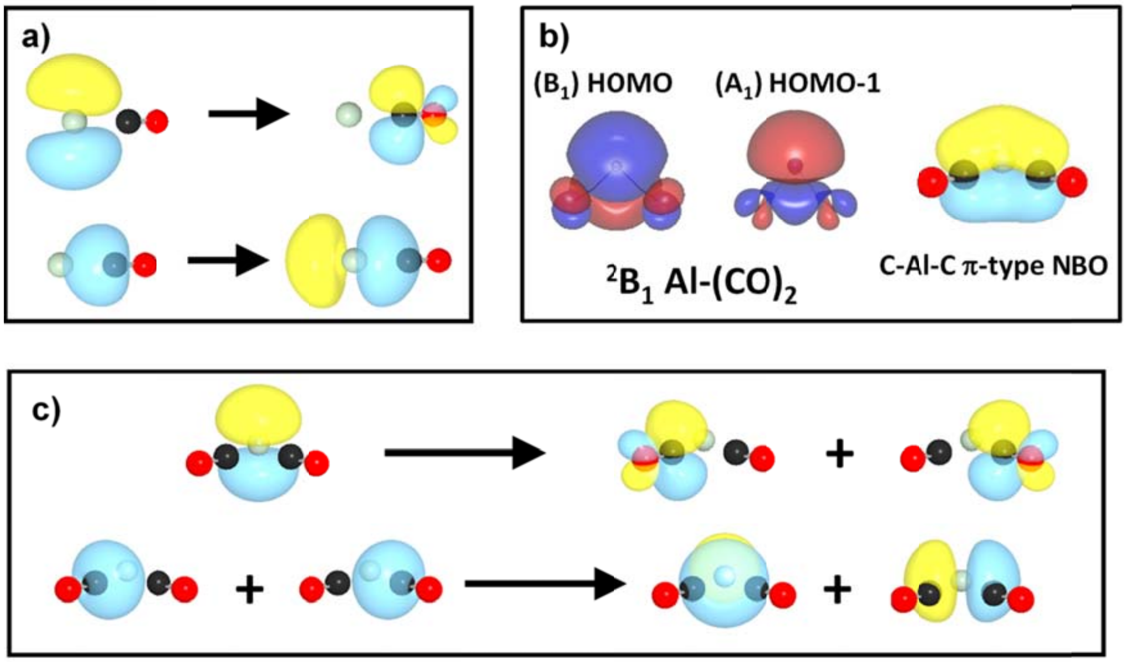

Figure 7.12: a) Natural bond orbitals associated with the most significant donor-acceptor interactions in Al-CO. A zeroth-order Lewis structure is enforced in which there is no Al-C NBO and the CO bond is a triple bond. Substantial stabilization energies are predicted for the interactions shown (see text). b) CCSD(T) HOMO (B_1) and HOMO-1 (A_1) for Al-$(CO)_2$. Also shown is the π-type 3-centered C-Al-C NBO. c) NBOs associated with the most stabilizing donor-acceptor interactions in Al-$(CO)_2$, starting from a zeroth-order Lewis structure with CO triple bonds and without the 3-centered C-Al-C NBO.

It is interesting to compare the bonding in Al-CO and Al^+-CO. In the closed shell ion, the π-donation charge transfer interaction is turned off, and the NBO analysis cannot find an Al-C NBO. Second order perturbation theory gives a CO to Al σ-donation delocalization energy that is ten percent of the magnitude found for Al-CO. Hence, charge transfer does not contribute substantially to the 7.4 kcal/mol Al^+-CO binding energy, and this interaction must be considered purely electrostatic. The CCSD(T) calculations of the ion are consistent with this picture. Upon ionization, the Al-C bond length increases by 0.72 Å, the CO bond length decreases by 0.03 Å, and the CO stretch shifts to the blue by 291 cm^{-1}. At this level of theory, the CO stretch in Al^+-CO is actually 61 cm^{-1} to the blue of free CO. The Al^+-CO ion can therefore be categorized as a "non-classical" metal carbonyl in which the CO stretch undergoes a blueshift.[110, 111, 116] This effect has been discussed by Frenking and coworkers as being due to a metal ion induced polarization of the CO charge density, which leads to a strengthening of the CO bond and a corresponding increase in the CO stretch frequency.[111]

A similar bonding picture is obtained from the CCSD(T) calculations and NBO analysis of Al-$(CO)_2$ and Al^+-$(CO)_2$. For the Al-$(CO)_2$ species, the out-of-plane, singly occupied HOMO is substantially delocalized over both CO ligands. Interestingly, NBO finds a π-type 3-centered C-Al-C bonding orbital that is composed of the out of plane p-orbitals on the Al and C atoms (Fig. 7.12b). This 3-centered interaction is apparently responsible for the tight binding observed in the neutral. For example, ionization removes the 3-centered bonding and the Al-C distances expand from 2.08 to 2.79 Å. Furthermore, the C-C distance increases by 0.86 Å upon ionization. It is also interesting to compare the Al-$(CO)_2 \rightarrow$ Al-CO+CO dissociation energies for the ion and the neutral, which are 6.7 and 11.2 kcal/mol, respectively. Additionally, the energy required to remove the first CO from Al-$(CO)_2$ is nearly twice the dissociation energy of Al-CO. Both of these observations are consistent with a significant 3-centered interaction in the neutral complex. As described above for Al-CO, we performed a second order perturbation theory analysis of Al-$(CO)_2$, starting from a zeroth order Lewis structure with CO triple bonds and no 3-centered bonding. Consistent with the results for Al-CO, significant delocalization energies are obtained for both carbon lone pair σ-donation (122 kcal/mol) and π-donation from the singly occupied Al p-orbital to CO π^* antibonding orbitals (114 kcal/mol), as shown in Fig. 7.12c. Once again, in addition to the loss of the 3-centered π-type interaction, the stabilization energy due to CO σ-donation is reduced by a factor of ten upon ionization. Therefore, as with Al^+-CO, the bonding in the $^1A_1$ Al^+-$(CO)_2$ complex is largely electrostatic. There have been multiple reports of *ab initio* calculations of group 13 metal-carbonyl systems,[47, 67-73] and it has been noted before [69, 70, 117] that the delocalization of metal atom p-electron density into the ligand framework is reminiscent of transition metal carbonyl bonding, which instead involves the metal atom d-orbitals. Our results are in complete agreement with this generally proposed bonding scheme for group 13 metal carbonyls.

A final aspect of the bonding that is worth noting is the computed bond angles in Al-$(CO)_2$ and Al^+-$(CO)_2$. The rather small C-Al-C bond angle (73.1°) and the small deviation from linearity of the Al-C-O units have been noted before.[67, 117] Comparing the ion and the neutral, it is evident that no change in the C-Al-C angle occurs upon ionization. Ionization removes the strong σ and π delocalization, and therefore, the small C-Al-C angle is most likely due to the electrostatic repulsion between the lone pairs on the carbon atoms and the Al $3s^2$ electrons, which can polarize away from the CO ligands, as described above for Al-CO. In contrast, ionization increases the Al-C-O bond angle from 167.1 to 174.9°. This bond angle increase is accompanied by a 0.62 Å increase in the O-O distance, and hence we attribute this small deviation from linearity as being due to lone pair repulsion between oxygen atoms.

7.6 Summary

Aluminum carbonyl clusters, Al-$(CO)_n$, are studied with HENDI IR laser spectroscopy in the CO stretch region, using a tunable, external cavity, quantum cascade laser. For mid-IR measurements, QCLs combine the affordability and narrow linewidth advantages of cw-diode lasers with the broad tunability and high output power advantages of nanosecond pulsed OPOs and free-electron lasers. The recent appearance of these commercially available QCL systems vastly expands the possibilities for high resolution spectroscopic studies of helium nanodroplet isolated molecular systems.

Rotationally resolved CO stretch bands are found near 1885 and 1919 cm^{-1} for the $^2\Pi_{1/2}$ Al-CO and $^2B_1$ Al-$(CO)_2$ complexes, respectively. The 258 and 223 cm^{-1} redshifts of these bands from free CO indicate extensive charge transfer between the Al atom and the CO ligand(s), reminiscent of the interactions responsible for the CO stretch redshifts observed for transition metal carbonyl complexes. NBO calculations indicate that both Al to CO π-donation *and* CO to Al σ-donation are important stabilizing interactions, despite the repulsive interaction between the Al 3s and C lone pair electrons, which results in the polarization of the Al 3s electrons away from the CO ligands. A π-type, 3-centered C-Al-C bond is responsible for the strong binding and short Al-C bond distances of Al-$(CO)_2$, which are substantially elongated upon ionization. Nevertheless, the peculiar C-Al-C bond angle remains near 73° in the ion, despite the absence of the 3-centered bond, indicating that this angle is largely due to Al 3s and C lone pair electron repulsion.

On the basis of the experimental vibrational frequency shifts, we find that clusters containing three or more CO units consist of an Al-$(CO)_2$ core with the additional CO molecules weakly attached with bond energies around ~250 cm^{-1}. Furthermore, we tentatively assign a weak feature in the spectrum to an (Al-CO)-CO metastable species that is over 10 kcal/mol higher in energy than Al-$(CO)_2$. Given the small barrier between (Al-CO)-CO and the globally stable Al-$(CO)_2$ complex, vibrational excitation of the former can in principle lead to reaction. Indeed, a significantly broader linewidth is observed for the band that we assign to (Al-CO)-CO, and it would be of interest to study this species with time-resolved IR-IR double resonance to probe the associated reaction dynamics.

References

[1] Chabal, Y. J., *Surf. Sci. Rep.* **8**, 211-357 (1988).

[2] Chabal, Y. J., Higashi, G. S., Raghavachari, K., and Burrows, V. A., *J. Vac. Sci. Technol., A* **7**, 2104-2109 (1989).

[3] Hollins, P., *Surf. Sci. Rep.* **16**, 51-94 (1992).

[4] Whitten, J. L., and Yang, H., *Surf. Sci. Rep.* **24**, 59-124 (1996).

[5] Radeke, M. R., and Carter, E. A., *Annu. Rev. Phys. Chem.* **48**, 243-270 (1997).

[6] Garcia-Hernandez, M., Lopez, N., Moreira, I. D., Paniagua, J. C., and Illas, F., *Surf. Sci.* **430**, 18-28 (1999).

[7] Govind, N., Wang, Y. A., and Carter, E. A., *J. Chem. Phys.* **110**, 7677-7688 (1999).

[8] Yudanov, I. V., Sahnoun, R., Neyman, K. M., and Rosch, N., *J. Chem. Phys.* **117**, 9887-9896 (2002).

[9] Neurock, M., *J. Catal.* **216**, 73-88 (2003).

[10] Yudanov, I. V., Sahnoun, R., Neyman, K. M., Rosch, N., Hoffmann, J., Schauermann, S., Johanek, V., Unterhalt, H., Rupprechter, G., Libuda, J., and Freund, H. J., *J. Phys. Chem. B* **107**, 255-264 (2003).

[11] Zonnevylle, M. C., Geerlings, J. J. C., and Vansanten, R. A., *J. Catal.* **148**, 417-426 (1994).

[12] Koretsky, G. M., and Knickelbein, M. B., *J. Chem. Phys.* **107**, 10555-10566 (1997).

[13] Knickelbein, M. B., Koretsky, G. M., Jackson, K. A., Pederson, M. R., and Hajnal, Z., *J. Chem. Phys.* **109**, 10692-10700 (1998).

[14] Knickelbein, M. B., and Koretsky, G. M., *J. Phys. Chem. A* **102**, 580-586 (1998).

[15] Knickelbein, M. B., *Annu. Rev. Phys. Chem.* **50**, 79-115 (1999).

[16] Fielicke, A., von Helden, G., Meijer, G., Simard, B., Denommee, S., and Rayner, D. M., *J. Am. Chem. Soc.* **125**, 11184-11185 (2003).

[17] Fielicke, A., von Helden, G., Meijer, G., Pedersen, D. B., Simard, B., and Rayner, D. M., *J. Phys. Chem. B* **108**, 14591-14598 (2004).

[18] Fielicke, A., von Helden, G., Meijer, G., Simard, B., and Rayner, D. M., *Phys. Chem. Chem. Phys.* **7**, 3906-3909 (2005).

[19] Fielicke, A., von Helden, G., Meijer, G., Pedersen, D. B., Simard, B., and Rayner, D. M., *J. Chem. Phys.* **124**, - (2006).

[20] Gruene, P., Fielicke, A., Meijer, G., and Rayner, D. M., *Phys. Chem. Chem. Phys.* **10**, 6144-6149 (2008).

[21] Swart, I., de Groot, F. M. F., Weckhuysen, B. M., Rayner, D. M., Meijer, G., and Fielicke, A., *J. Am. Chem. Soc.* **130**, 2126-+ (2008).

[22] Lyon, J. T., Gruene, P., Fielicke, A., Meijer, G., and Rayner, D. M., *J. Chem. Phys.* **131**, - (2009).

[23] Fielicke, A., Gruene, P., Meijer, G., and Rayner, D. M., *Surf. Sci.* **603**, 1427-1433 (2009).

[24] Zhou, M. F., Andrews, L., and Bauschlicher Jr., C. W., *Chem. Rev.* **101**, 1931-1961 (2001).

[25] Andrews, L., and Citra, A., *Chem. Rev.* **102**, 885-911 (2002).

[26] Himmel, H. M., Downs, A. J., and Greene, T. M., *Chem. Rev.* **102**, 4191-4241 (2002).

[27] Bartelt, A., Close, J. D., Federmann, F., Quaas, N., and Toennies, J. P., *Phys. Rev. Lett.* **77**, 3525-3528 (1996).

[28] Diederich, T., Doppner, T., Braune, J., Tiggesbaumker, J., and Meiwes-Broer, K. H., *Phys. Rev. Lett.* **86**, 4807-4810 (2001).

[29] Tiggesbaumker, J., and Stienkemeier, F., *Phys. Chem. Chem. Phys.* **9**, 4748-4770 (2007).

[30] Stienkemeier, F., and Lehmann, K. K., *J. Phys. B: At., Mol. Opt. Phys.* **39**, R127-R166 (2006).

[31] Nauta, K., Moore, D. T., Stiles, P. L., and Miller, R. E., *Science* **292**, 481-484 (2001).

[32] Stiles, P. L., Moore, D. T., and Miller, R. E., *J. Chem. Phys.* **121**, 3130-3142 (2004).

[33] Stiles, P. L., and Miller, R. E., *J. Phys. Chem. A* **110**, 10225-10235 (2006).

[34] Stiles, P. L., and Miller, R. E., *J. Phys. Chem. A* **110**, 5620-5628 (2006).

[35] Stiles, P. L., and Miller, R. E., *J. Phys. Chem. A* **111**, 7382-7390 (2007).

[36] Douberly, G. E., Stiles, P. L., Miller, R. E., Schmied, R., and Lehmann, K. K., *J. Phys. Chem. A* **114**, 3391-3402 (2010).

[37] Toennies, J. P., and Vilesov, A. F., *Angew. Chem. Int. Ed.* **43**, 2622-2648 (2004).

[38] Choi, M. Y., Douberly, G. E., Falconer, T. M., Lewis, W. K., Lindsay, C. M., Merritt, J. M., Stiles, P. L., and Miller, R. E., *Int. Rev. Phys. Chem.* **25**, 15-75 (2006).

[39] Faist, J., Capasso, F., Sivco, D. L., Sirtori, C., Hutchinson, A. L., and Cho, A. Y., *Science* **264**, 553-556 (1994).

[40] Wysocki, G., Curl, R. F., Tittel, F. K., Maulini, R., Bulliard, J. M., and Faist, J., *Appl. Phys. B* **81**, 769-777 (2005).

[41] Muller, W., and Bagus, P. S., *J. Vac. Sci. Technol., A* **3**, 1623-1626 (1985).

[42] Rossi, C., Esteve, A., and Vashishta, P., *J. Phys. Chem. Solids* **71**, 57-58 (2010).

[43] Yetter, R. A., Risha, G. A., and Son, S. F., *P. Combust. Inst.* **32**, 1819-1838 (2009).

[44] Armstrong, R. W., Baschung, B., Booth, D. W., and Samirant, M., *Nano Lett.* **3**, 253-255 (2003).

[45] Maggi, F., Bandera, A., Galfetti, L., De Luca, L. T., and Jackson, T. L., *Acta Astron.* **66**, 1563-1573 (2010).

[46] Shukla, P. K., and Ray, N. K., *J. Mol. Struct.* **723**, 131-134 (2005).

[47] Cramer, C. J., *J. Mol. Struct.* **81**, 243-262 (1991).

[48] Jursic, B. S., *Chem. Phys.* **237**, 51-58 (1998).

[49] Mele, F., Russo, N., Rubio, J., and Toscano, M., *J. Mol. Struct.* **466**, 77-84 (1999).

[50] Moc, J., *Chem. Phys. Lett.* **429**, 43-48 (2006).

[51] Sakai, S., *J. Phys. Chem.* **96**, 8369-8373 (1992).

[52] Srinivas, R., Sulzle, D., and Schwarz, H., *J. Am. Chem. Soc.* **112**, 8334-8337 (1990).

[53] Swihart, M. T., and Catoire, L., *J. Phys. Chem. A* **105**, 264-273 (2001).

[54] Xie, Y. M., Yates, B. F., and Schaefer, H. F., *J. Am. Chem. Soc.* **112**, 517-523 (1990).

[55] Alvarez-Barcia, S., and Flores, J. R., *Chem. Phys. Lett.* **470**, 196-202 (2009).

[56] Hinchcli, A. J., Ogden, J. S., and Oswald, D. D., *J. Chem. Soc., Chem. Commun.*, 338-339 (1972).

[57] Chenier, J. H. B., Hampson, C. A., Howard, J. A., and Mile, B., *J. Chem. Soc., Chem. Commun.*, 730-732 (1986).

[58] Chertikhin, G. V., Rozhanskii, I. L., Serebrennikov, L. V., and Shevelkov, V. F., *Zh. Fiz. Khim.* **62**, 2256-2259 (1988).

[59] Xu, C., Manceron, L., and Perchard, J. P., *J. Chem. Soc., Faraday Trans.* **89**, 1291-1298 (1993).

[60] Feltrin, A., Guido, M., and Cesaro, S. N., *Vib. Spectrosc* **8**, 175-183 (1995).

[61] Zhang, L. N., Dong, J., Zhou, M. F., and Qin, Q. Z., *J. Chem. Phys.* **113**, 10169-10173 (2000).

[62] Downs, A. J., Himmel, H. J., and Manceron, L., *Polyhedron* **21**, 473-488 (2002).

[63] Himmel, H. J., *Dalton Trans.*, 3639-3649 (2003).

[64] Kong, Q. Y., Chen, M. H., Dong, J., Li, Z. H., Fan, K. N., and Zhou, M. F., *J. Phys. Chem. A* **106**, 11709-11713 (2002).

[65] Kasai, P. H., and Jones, P. M., *J. Am. Chem. Soc.* **106**, 8018-8020 (1984).

[66] Chenier, J. H. B., Hampson, C. A., Howard, J. A., Mile, B., and Sutcliffe, R., *J. Phys. Chem.* **90**, 1524-1528 (1986).

[67] Balaji, V., Sunil, K. K., and Jordan, K. D., *Chem. Phys. Lett.* **136**, 309-313 (1987).

[68] Pullumbi, P., and Bouteiller, Y., *Chem. Phys. Lett.* **234**, 107-112 (1995).

[69] Wesolowski, S. S., Crawford, T. D., Fermann, J. T., and Schaefer, H. F., *J. Chem. Phys.* **104**, 3672-3675 (1996).

[70] Bridgeman, A. J., *J. Chem. Soc., Dalton Trans.*, 1323-1329 (1997).

[71] Jursic, B. S., *Chem. Phys.* **219**, 57-62 (1997).

[72] Wesolowski, S. S., Galbraith, J. M., and Schaefer, H. F., *J. Chem. Phys.* **108**, 9398-9403 (1998).

[73] Bridgeman, A. J., *Inorg. Chim. Acta* **321**, 27-41 (2001).

[74] Callegari, C., Lehmann, K. K., Schmied, R., and Scoles, G., *J. Chem. Phys.* **115**, 10090-10110 (2001).

[75] Lewerenz, M., Schilling, B., and Toennies, J. P., *Chem. Phys. Lett.* **206**, 381-387 (1993).

[76] Knuth, E. L., Schilling, B., and Toennies, J. P., in *International Symposium on Rarefied Gas Dynamics* (Oxford University Press, 1995), pp. 270-276.

[77] Reho, J. H., Merker, U., Radcliff, M. R., Lehmann, K. K., and Scoles, G., *J. Phys. Chem. A* **104**, 3620-3626 (2000).

[78] Brink, D. M., and Stringari, S., *Z. Phys. D: At., Mol. Clusters* **15**, 257 (1990).

[79] Hartmann, M., Miller, R. E., Toennies, J. P., and Vilesov, A., *Phys. Rev. Lett.* **75**, 1566-1569 (1995).

[80] Buchenau, H., Toennies, J. P., and Northby, J. A., *J. Chem. Phys.* **95**, 8134-8148 (1991).

[81] Callicoatt, B. E., Mar, D. D., Apkarian, V. A., and Janda, K. C., *J. Chem. Phys.* **105**, 7872-7875 (1996).

[82] Lewerenz, M., Schilling, B., and Toennies, J. P., *J. Chem. Phys.* **102**, 8191-8207 (1995).

[83] CFOUR, Coupled-Cluster techniques for Computational Chemistry, a quantum-chemical program package by J.F. Stanton, J. Gauss, M.E. Harding, P.G. Szalay with contributions from A.A. Auer, R.J. Bartlett, U. Benedikt, C. Berger, D.E. Bernholdt, Y.J. Bomble, L. Cheng, O. Christiansen, M. Heckert, O. Heun, C. Huber, T.-C. Jagau, D. Jonsson, J. Jusélius, K. Klein, W.J. Lauderdale, D.A. Matthews, T. Metzroth, D.P. O'Neill, D.R. Price, E. Prochnow, K. Ruud, F. Schiffmann, W. Schwalbach, S. Stopkowicz, A. Tajti, J. Vázquez, F. Wang, J.D. Watts and the integral packages MOLECULE (J. Almlöf and P.R. Taylor), PROPS (P.R. Taylor), ABACUS (T. Helgaker, H.J. Aa. Jensen, P. Jørgensen, and J. Olsen), and ECP routines by A. V. Mitin and C. van Wüllen. For the current version, see http://www.cfour.de.

[84] Schmidt, M. W., Baldridge, K. K., Boatz, J. A., Elbert, S. T., Gordon, M. S., Jensen, J. H., Koseki, S., Matsunaga, N., Nguyen, K. A., Su, S. J., Windus, T. L., Dupuis, M., and Montgomery, J. A., *J. Comput. Chem.* **14**, 1347-1363 (1993).

[85] NBO 5.0. E. D. Glendening, J, K. Badenhoop, A. E. Reed, J. E. Carpenter, J. A. Bohmann, C. M. Morales, and F. Weinhold, Theoretical Chemistry Institute, University of Wisconsin, Madison (2001).

[86] Lewis, W. K., Lindsay, C. M., Bemish, R. J., and Miller, R. E., *J. Am. Chem. Soc.* **127**, 7235-7242 (2005).

[87] Merritt, J. M., Douberly, G. E., and Miller, R. E., *J. Chem. Phys.* **121**, 1309-1316 (2004).

[88] Dick, B., and Slenczka, A., *J. Chem. Phys.* **115**, 10206-10213 (2001).

[89] Slenczka, A., Dick, B., Hartmann, M., and Toennies, J. P., *J. Chem. Phys.* **115**, 10199-10205 (2001).

[90] Lehmann, K. K., *Mol. Phys.* **97**, 645-666 (1999).

[91] Herzberg, G., *Molecular Spectra and Molecular Structure* (Krieger Publishing Co., Malabar, FL, 1989), Second Edition edn., Vol. I. Spectra of Diatomic Molecules.

[92] Grebenev, S., Hartmann, M., Havenith, M., Sartakov, B., Toennies, J. P., and Vilesov, A. F., *J. Chem. Phys.* **112**, 4485-4495 (2000).

[93] Bunker, P. R., and Jensen, P., *Fundamentals of Molecular Symmetry* (Institute of Physics Publishing, Philadelphia, 2005), Series in Chemical Physics.

[94] PGOPHER, a Program for Simulating Rotational Structure, C. M. Western, University of Bristol, http://pgopher.chm.bris.ac.uk

[95] Huber, K. P., and Herzberg, G., *Molecular Spectra and Molecular Spectra* (Van Nostrand Reinhold Co., New York, 1979), Vol. IV. Constants of Diatomic Molecules.

[96] Nauta, K., and Miller, R. E., *J. Chem. Phys.* **115**, 10138-10145 (2001).

[97] Higgins, J., Callegari, C., Reho, J., Stienkemeier, F., Ernst, W. E., Lehmann, K. K., Gutowski, M., and Scoles, G., *Science* **273**, 629-631 (1996).

[98] Nauta, K., and Miller, R. E., *Science* **283**, 1895-1897 (1999).

[99] Nauta, K., and Miller, R. E., *Science* **287**, 293-295 (2000).

[100] Choi, M. Y., and Miller, R. E., *Phys. Chem. Chem. Phys.* **7**, 3565-3573 (2005).

[101] Douberly, G. E., and Miller, R. E., *J. Chem. Phys.* **122**, 024306 (2005).

[102] Merritt, J. M., Douberly, G. E., Stiles, P. L., and Miller, R. E., *J. Phys. Chem. A* **111**, 12304-12316 (2007).

[103] Douberly, G. E., and Miller, R. E., *J. Phys. Chem. B* **107**, 4500-4507 (2003).

[104] Nauta, K., and Miller, R. E., *J. Chem. Phys.* **111**, 3426-3433 (1999).

[105] Douberly, G. E., Nauta, K., and Miller, R. E., *Chem. Phys. Lett.* **377**, 384-390 (2003).

[106] Nauta, K., and Miller, R. E., *Chem. Phys. Lett.* **346**, 129-134 (2001).

[107] Cotton, F. A., *Advanced Inorganic Chemistry* (John Wiley and Sons, Inc., New York, 1999), Sixth edn.

[108] Frenking, G., and Frohlich, N., *Chem. Rev.* **100**, 717 (2000).

[109] Bauschlicher Jr., C. W., *J. Chem. Phys.* **84**, 260 (1986).

[110] Aubke, F., and Wang, C., *Coord. Chem. Rev.* **137**, 483 (1994).

[111] Lupinetti, A. J., Fau, S., Frenking, G., and Strauss, S. H., *J. Phys. Chem.* **101**, 9551 (1997).

[112] Reed, A. E., Curtiss, L. A., and Weinhold, F., *Chem. Rev.* **88**, 899-926 (1988).

[113] Glendening, E. D., and Weinhold, F., *J. Comput. Chem.* **19**, 593-609 (1998).

[114] Glendening, E. D., and Weinhold, F., *J. Comput. Chem.* **19**, 610-627 (1998).

[115] Glendening, E. D., Badenhoop, J. K., and Weinhold, F., *J. Comput. Chem.* **19**, 628-646 (1998).

[116] Velasquez, I., J., Njegic, B., Gordon, M. S., and Duncan, M. A., *J. Phys. Chem. A* **112**, 1907-1913 (2008).

[117] Himmel, H. J., Downs, A. J., Green, J. C., and Greene, T. M., *J. Phys. Chem. A* **104**, 3642-3654 (2000).

Chapter 8

On the Al + HCN Reaction in Helium Nanodroplets

The sequential addition of HCN and Al to a helium nanodroplet leads barrierlessly to a bent, planar, $^2A'$, HCNAl species, which is computed to be 20.3 kcal/mol below the separated reactants. A ro-vibrational band near 2690 cm^{-1} is assigned to the ν_1 (a′) CH stretch. A Natural Bond Orbital analysis of this reaction product reveals that both ligand-to-metal σ-donation and metal-to-ligand π-donation are responsible for the strong bonding between HCN and Al. A significant donor-acceptor interaction between the C-N and C-H anti-bonding orbitals is responsible for the bent geometry and the 619 cm^{-1} red shift of the CH stretch band upon complexation.

8.1 Introduction

Helium nanodroplets are increasingly being used as reaction vessels to probe the potential energy surfaces and branching ratios associated with prototypical elementary reactions of importance to areas such as inorganic [1-5], atmospheric and combustion chemistry [6]. The low temperature, dissipative environment of a helium droplet often allows for the kinetic stabilization of either complexes in the entrance channels of the reaction [4, 5] or intermediates along the reaction path [6], even when the reaction barriers are submerged below the energy of the incoming reactants. The sequential “pick-up” technique allows for substantial control over the addition of reactants to the droplets, and the outcome of the reaction between cold reactants can be probed with both laser spectroscopic and mass spectrometric methods [6-8]. In this report, we explore the outcome of the low temperature reaction between an Al atom and HCN. The reaction products are completely cooled to 0.4 K and carried downstream for infrared (IR) laser excitation and mass spectrometric detection, allowing for the characterization of the branching associated with this low temperature reaction.

The first experimental investigation of the reaction between Al atoms and HCN was carried out by Lanzisera and Andrews [9]. They reported IR spectroscopic evidence for the formation of AlCN , AlNC and AlH when Al atoms were co-deposited with HCN into a solid argon matrix. Broad-band UV photolysis was shown to increase both the yield of AlCN and AlNC, which was argued to be due to the initial formation and photolytic decomposition of an [AlHCN] intermediate species. However, there was no direct spectroscopic evidence for the formation of any species containing C-H or N-H bonds in this study. In a previous report by Merritt and co-workers [4], addition and insertion reaction products, along with a hydrogen-bonded Al-HCN complex were predicted with *ab initio* computations, and the CH stretch of the hydrogen-bonded Al-HCN species was found at 3192.07 cm^{-1} upon sequential pick-up of Al and HCN into helium nanodroplets. However, neither the addition nor insertion products were observed experimentally due to the narrow tuning range of the laser used at that time. Here we report a more extensive study of the *ab initio* potential energy surface of the Al + HCN reaction, the nature of the bonding in these prototypical group 13 metal-ligand compounds, and the IR spectroscopy of these species as a probe of the outcome of the reaction.

8.2 Experimental Methods

The helium nanodroplet isolation technique [10-12] and its application for the IR spectroscopy of molecular clusters has recently been reviewed. Helium droplets with mean sizes of approximately 4000 He atoms are formed in a continuous cryogenic nozzle expansion of high purity helium gas (30 bar) into vacuum through a 5 μm diameter nozzle operated at 17 K. The droplet expansion is skimmed, passes into a differentially pumped chamber and over the opening of a Boron-Nitride crucible containing Al shot. The crucible temperature is adjusted to optimize the pick-up of single Al atoms, as described previously [5]. The droplet beam subsequently passes through a differentially pumped gas pick-up cell containing a variable amount of HCN. For the survey spectrum, the HCN pressure in the pick-up cell is set to 5.0×10^{-6} Torr, which is optimum for the pick-up of a single HCN molecule. Nevertheless, at this pick-up pressure, given the statistical nature of the pick-up process, $(HCN)_n$ clusters as large as n=3-4 are evident in the IR spectrum.

The translational and internal degrees of freedom of each picked-up species are cooled to ~0.4 K [13] by the evaporation ~300 He atoms (~5 cm^{-1} is dissipated per helium atom evaporated) [14, 15]. Previous reports have shown that both Al [16] and HCN [17] reside within the droplet upon capture, rather than being expelled to the surface. The mutual attraction between Al and HCN is much stronger than the He-Al and He-HCN interactions. Therefore, the sequential capture of both species leads to the Al + HCN barrierless association reaction. The droplet flight time between the Al atom and HCN sources is approximately 100 μs. The Al atom population is therefore expected to be cooled to the lowest $^2P_{1/2}$ spin-orbit level prior to reaction. The formation and subsequent cooling of the HCN + Al reaction products observed here requires the dissipation of ~20 kcal/mol of thermal energy, which results in the evaporation of ~1400 He atoms. Because an additional ~32 kcal/mol would need to be dissipated upon the formation of an Al-Al bond, clusters with multiple Al atoms cannot be stabilized with the droplet sizes used in this study. These larger $(Al)_n$ -ligand complexes will be the subject of future investigations.

A narrow-linewidth, tunable IR optical parametric oscillator (OPO) (Lockheed-Martin Aculight) is used to probe for the products of the Al + HCN reaction in the 2650 cm^{-1} to 3320 cm^{-1} frequency range. Details associated with the tuning and calibration of this OPO can be found elsewhere [18]. The idler output of the OPO is aligned to counter-propagate the helium droplet beam. Excitation of the dopant followed by vibrational energy transfer to the droplet results in the evaporation of between ~550 to 650 helium atoms. This laser induced droplet size reduction is measured with an electron impact ionization mass spectrometer as a laser induced reduction in the ionization cross section. The output of the OPO is chopped at 80 Hz, and a lock-in amplifier processes the ion signal from the mass spectrometer. An IR spectrum is obtained by monitoring this depletion of ion signal ($m/z > 6$ u) as the OPO is tuned over the frequency range of interest.

8.3 Theoretical Methods

The lowest energy $^2A'$ and $^2A''$ intermolecular potentials for Al + HCN were computed at the MP2/aug-cc-pVTZ level of theory. These surfaces are obtained keeping the HCN geometry fixed to linear with bond lengths obtained at the same level of theory (r_{CH}=1.0646 and r_{CN}=1.1670 Å). Full geometry optimizations without symmetry restrictions are performed to determine the true minima on the potential. Geometries are optimized at the frozen-core CCSD(T)/aug-cc-pVTZ level of theory using ROHF reference wavefunctions. Relative energies of the various species are zero point vibrational energy (ZPVE) corrected with the harmonic approximation at the same level of theory. Basis set superposition error (BSSE) is also accounted for with the following extrapolation formula:

$$E_{\mathrm{HF}}(X) = E_{\mathrm{HF}}^{\infty} + A\exp(-bX) \qquad (8.1)$$

$$\varepsilon_{\mathrm{MP2}}(X) = E_{\mathrm{MP2}}(X) - E_{\mathrm{HF}}(X) = \varepsilon_{\mathrm{MP2}}^{\infty} + \frac{B}{X^3} \qquad (8.2)$$

Here, X is the cardinal number of the aug-cc-pVXZ basis set, where X=3,4,5 or X=4,5 for Hartree-Fock and MP2 computations, respectively. E_{HF}^{∞} and $\varepsilon_{\mathrm{MP2}}^{\infty}$ correspond to the HF energy and MP2 correction at the complete basis set limit (CBS), and our MP2 energy at CBS is:

$$E(\mathrm{MP2/CBS}) = E_{\mathrm{HF}}^{\infty} + \varepsilon_{\mathrm{MP2}}^{\infty}. \qquad (8.3)$$

The final ZPVE and BSSE corrected energies, given in Table 8.1, correspond to:

$$E_{\mathrm{final}} = E\left[\frac{\mathrm{CCSD(T)}}{\mathrm{aug}}\mathrm{ccpVTZ}\right] + E_{\mathrm{ZVPE}} + E\left(\frac{\mathrm{MP2}}{\mathrm{CBS}}\right) - E\left(\frac{\mathrm{MP2}}{\mathrm{aug}}\mathrm{ccpVTZ}\right) \qquad (8.4)$$

Anharmonic corrections to the harmonic frequency calculations are obtained with VPT2 theory [19, 20] and provide fundamental frequencies for HCN, bent HCNAl, cyclic HC(AlN), and the hydrogen bonded Al-HCN complex. Fundamental frequencies are determined at the CCSD(T)/Def2-TZVP level of theory with UHF reference wave-functions. These harmonic and anharmonic frequencies are compared to the experimental band origins in Table 8.2. All of the above *ab initio* calculations are performed using the CFOUR computational package [21]. A Natural Bond Orbital (NBO) [22] analysis of the bent HCNAl isomer was performed at the B3LYP/cc-pVTZ level of theory within the GAMESS computational package [23].

Table 8.1: Relative energies of the CCSD(T) stationary points on the $^2A'$ potential surface.

Species	ΔE (kcal mol^{-1})^a
HCN+Al	0.0
Al-HCN	-2.1
HCNAl	-20.3
HC(AlN)	-19.4
HAlCN	-30.8
HAlNC	-32.1
TS1	-16.5
TS2	-6.5
TS3	7.3
TS4	34.1

^{a}Corrected for ZPVE and BSSE (see text).

Table 8.2: Comparison of *ab initio* frequencies and experimental frequencies for HCN, hydrogen bonded Al-HCN, cyclic HC(AlN), and bent HCNAl.[a]

CCSD(T)/Def2-TZVP	ω_{CH} (cm^{-1})	ν_{CH} (cm^{-1})	I (km/mol)	ν_{exp} (cm^{-1})
HCN ($^1\Sigma^+$)	3430	3296	74	3311.21
Al-HCN ($^2\Sigma^+$)	3361	3225	362	3192.07
HC(AlN) (^{2}A')	3032	2852	21	(2819)[b]
HCNAl (^{2}A')	2910	2726	235	2691.83
HAlCN (^{2}A')	ω_{AlH} 1909	—	—	—
HAlNC (^{2}A')	ω_{AlH} 1885	—	—	—

[a] ν_{CH} and ω_{CH} are the computed fundamental and harmonic CH stretch frequencies, respectively.

[b] The ν_{exp} for cyclic HC(AlN) is obtained by assuming a difference of 33.5 cm^{-1} between *ab initio* ν_{CH} and the actual experimental band origin.

8.4 Results and Discussion

Fig. 8.1 shows a survey spectrum from 2650 to 3320 cm^{-1}, which was obtained with conditions optimized to sequentially add a single Al atom and a single HCN to each helium droplet, on average. Bands above 3200 cm^{-1} and those near 2819 cm^{-1} are due to the CH stretch [24] and the bend plus CN stretch combination bands of (HCN)$_n$ clusters, respectively. In addition to these (HCN)$_n$ cluster bands, new bands are observed at 2692, 2713 and 3192 cm^{-1}. These three features are strongly dependent on the temperature of the Al oven and optimize at approximately 1300 K. The band at 3192 cm^{-1} has been assigned in a previous report to the CH stretch of the $^2\Sigma$, Al-HCN, hydrogen-bonded species [4]. The HCN pick-up cell pressure dependence of the intensities of the lower frequency bands is consistent with an assignment of these bands to complexes containing a single HCN molecule (see Fig. 8.2). The difference in the mass spectra of the beam with and without the laser present reveals the mass channels carrying the depletion signals when the laser is fixed to either 2692 or 2713 cm^{-1} (see Fig. 8.3). These difference mass spectra are identical to the one observed in a previous study of the Al-CO complex [5], except that m/z = 27 (HCN^+) is observed, rather than m/z=28 (CO^+). Both the pick-up cell pressure dependence curves and the difference mass spectra are consistent with the assignment of both the 2692 and 2713 bands to an $(HCN)_1$-Al_1 species. No other strong signals that require both Al and HCN are found in this frequency range. Assuming these two bands correspond to CH stretches, these represent rather dramatic, ~620 cm^{-1}, red shifts of the HCN CH stretch upon complexation with a single Al atom. In order to account for this, the Al + HCN potential surface was explored to identify reaction products that are consistent with this observation.

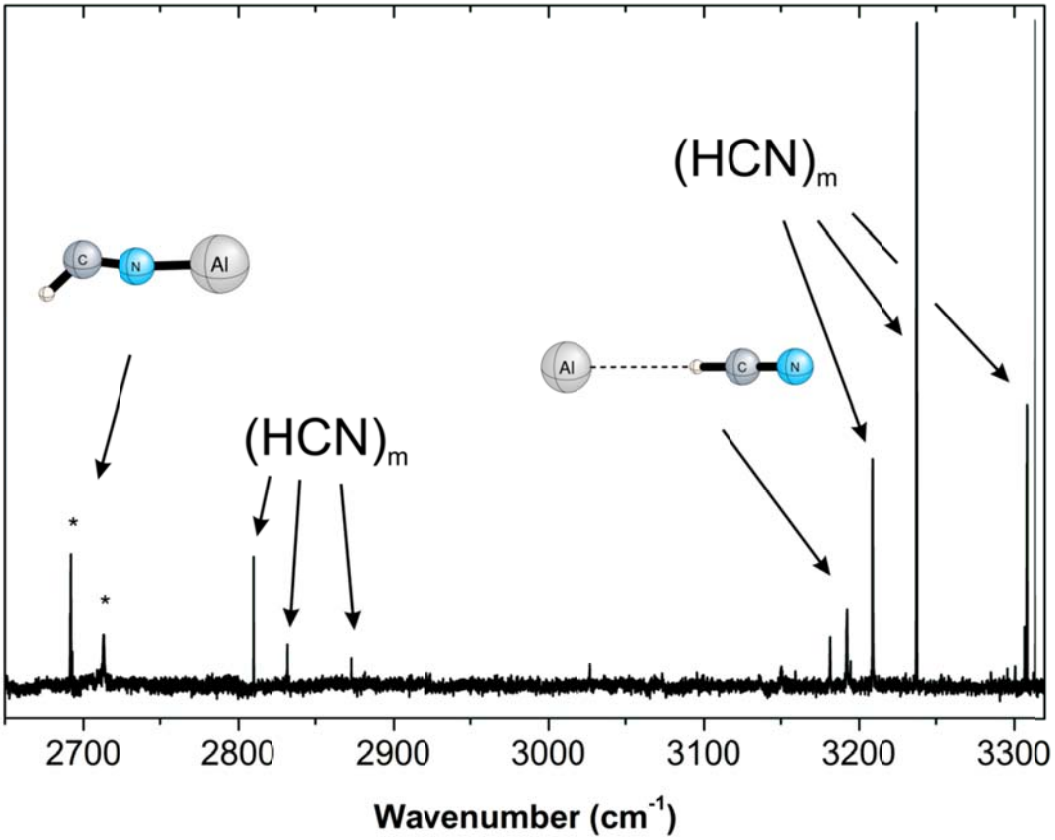

Figure 8.1: Survey spectrum from 2650 to 3320 cm^{-1} obtained as a depletion of the mass spectrometer integrated total ion signal. Previously unassigned bands are marked with asterisks. Bands above 3200 cm^{-1} and those near 2819 cm^{-1} are due to the CH stretch and the bend plus CN stretch combination bands of (HCN)$_n$ clusters, respectively.

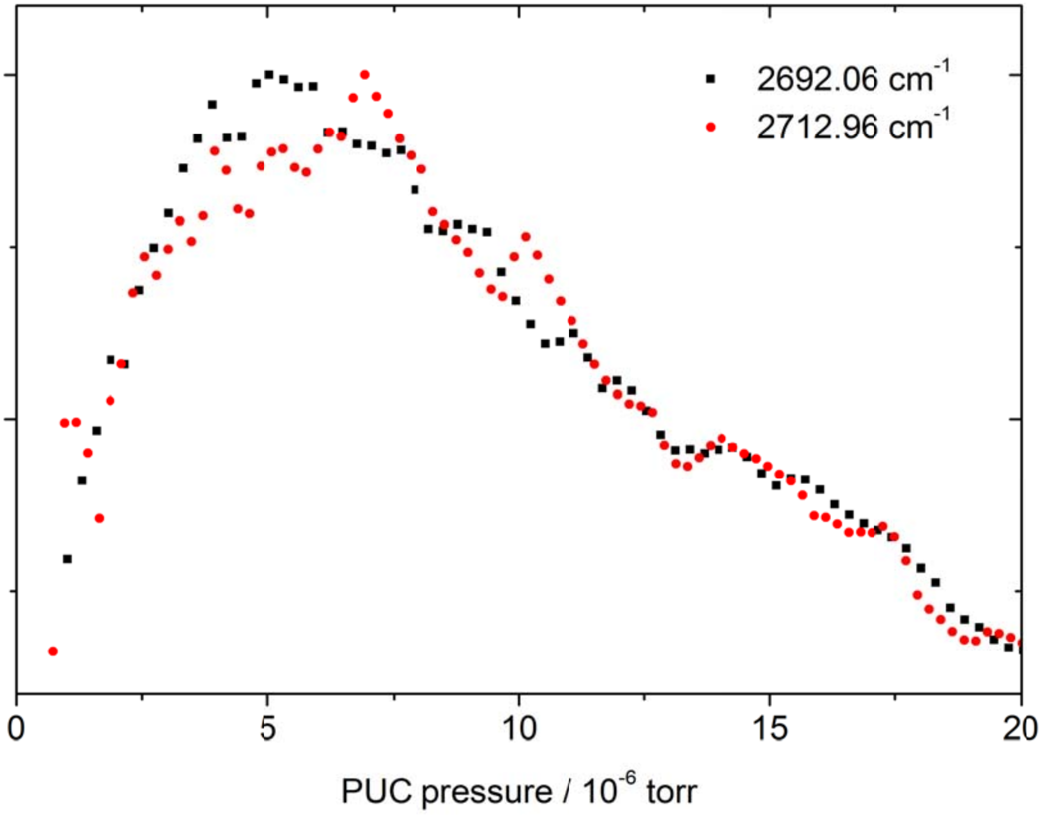

Figure 8.2: HCN pressure dependence of the peak intensity at 2692.06 (black) and 2712.96 cm^{-1} (red).

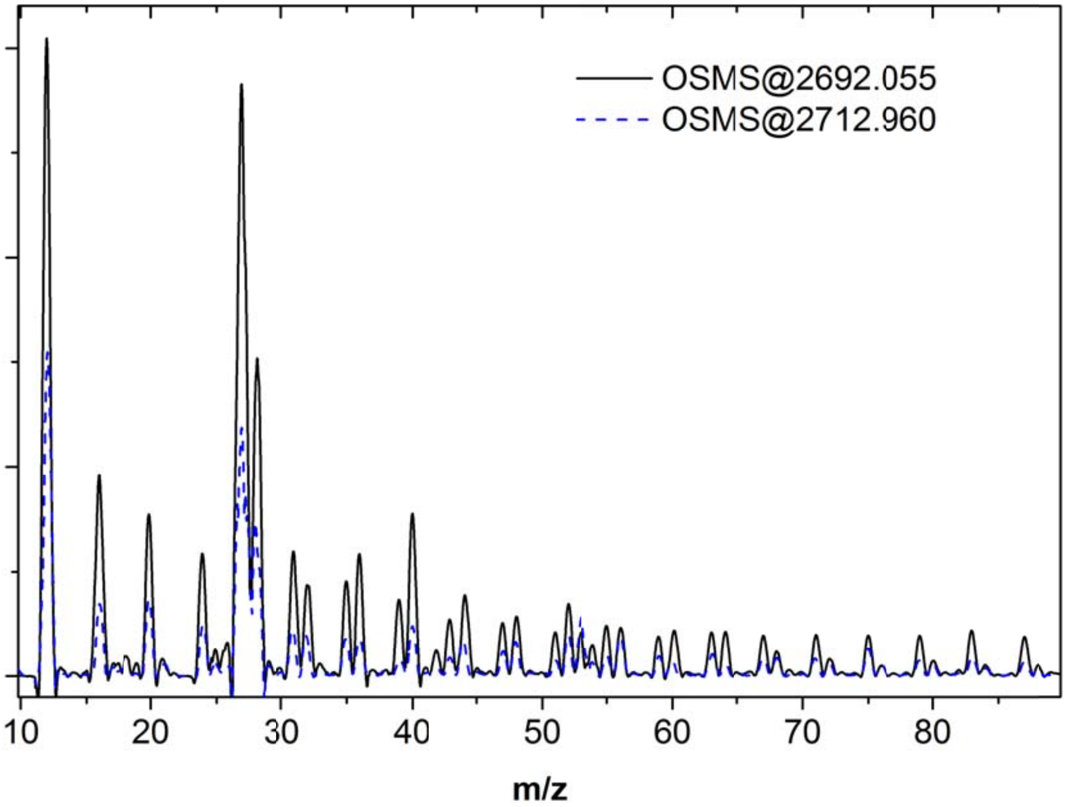

Figure 8.3: Difference mass spectra (laser OFF − laser ON) with the laser fixed to 2692.055 (black) and 2712.960 cm^{-1} (blue).

The lowest energy ^{2}A′ and ^{2}A″, Al + HCN, intermolecular potentials are shown in Fig. 8.4. The Jacobi coordinates, *R* and *θ*, are defined according to the Fig. 8.4 inset where *R* is the distance between the Al atom and the HCN center of mass. The 1A″ surface is overall higher in energy than the 1A′ surface. In the linear HCN-Al configuration ($\theta = 180°$), the 1A′ and 1A″ surfaces become degenerate, and these states in C_s symmetry correlate with the doubly degenerate ${}^2\Pi$ ground state in $C_{\infty v}$ symmetry. In this linear configuration, a third surface, 2A′, correlates with a repulsive ${}^2\Sigma$ excited state where the singly occupied Al *p*-orbital points towards the N atom of HCN. In the Al-HCN configuration ($\theta = 0°$), the lower energy 1A′ state correlates with the ${}^2\Sigma$ ground state, and the 1A″ and 2A′ surfaces become degenerate and correlate with an excited ${}^2\Pi$ state (see bottom panel of Fig. 8.4). The wells on the 1A′ surface indicate three possible minima: ${}^2\Sigma$, hydrogen-bonded, linear Al-HCN; ^{2}A′, T-shaped HCN-Al; and, ${}^2\Pi$, nitrogen-bound, linear HCN-Al. Allowing the geometries to fully relax reveals that the only true minimum on the potential corresponds to the hydrogen-bonded, linear Al-HCN isomer. Harmonic frequency calculations for the nitrogen-bound and T-shaped isomers give one imaginary frequency each, indicating that these species are first order saddle points on the potential. The coordinates of these imaginary frequencies correspond to *a*′ bending modes, indicating that the true minima have A′ electronic symmetry with bent geometries.

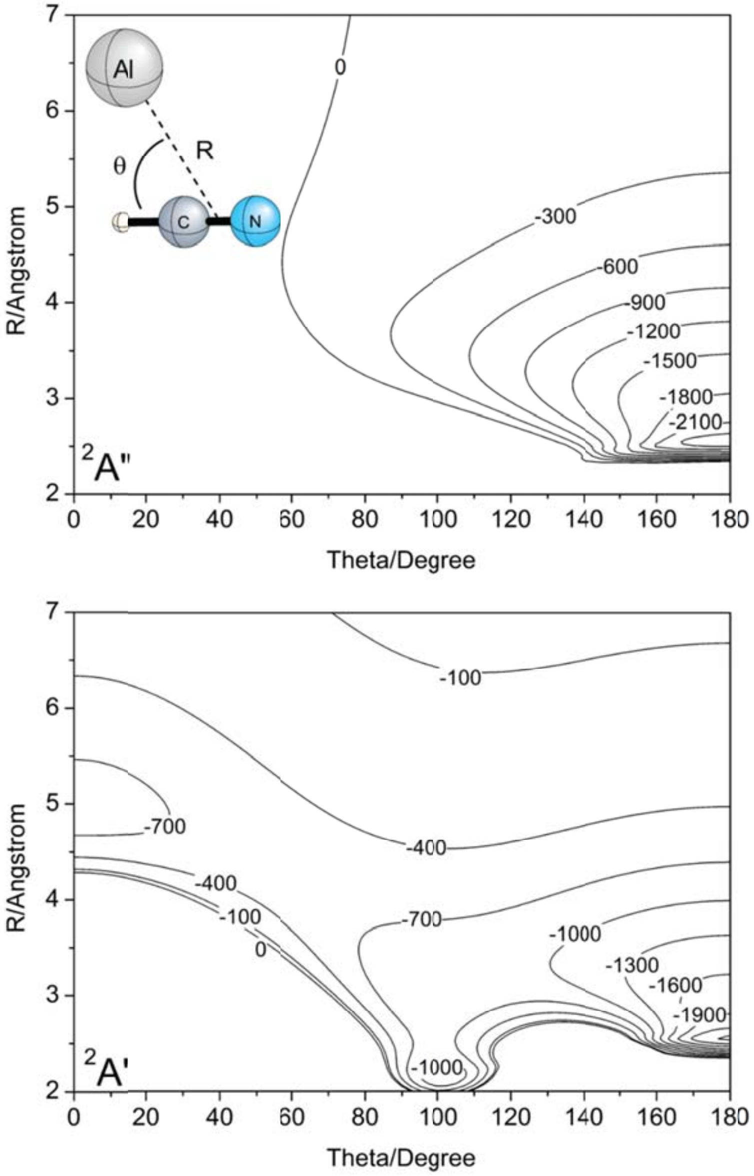

Figure 8.4: Non-relativistic intermolecular Al-HCN potential energy surfaces computed at the MP2/aug-cc-pVTZ level of theory. The HCN is forced to remain linear and the energies represent the lowest energy A′ or A″ electronic energy state at each configuration. Basis set superposition error has been counterpoise corrected. Energies are given in cm^{-1}, and the contour increment is 300 cm^{-1}. The θ = 0° configuration corresponds to the linear Al-HCN geometry. The R coordinate is the distance between the Al atom and the HCN center of mass. The bottom frame shows schematically the relative energy of the three electronic surfaces (1A′, 2A′ and 1A″) of the fully relaxed system as a function of θ.

The fully relaxed potential energy surface at the CCSD(T)/aug-cc-pVTZ level of theory is shown in Fig. 8.5, and the relative energetics of the minima are given in Table 8.1. Three addition products are found, one of which corresponds to the $^2\Sigma^+$, hydrogen-bonded Al-HCN van der Waals complex. The cyclic HC(AlN) and the bent HCNAl additive reaction products are found approximately 20 kcal/mol below the reactants. In both of these $^2A'$ species, the carbon atom is rehybridized such that the HCN bond angle (~130°) deviates significantly from linearity. Insertion products, such as HAlCN and HAlNC, are also found, along with several transition states that connect the various minima. The structural parameters associated with the geometry optimized minima and transition states are given in Fig. 8.6 and Table 8.3).

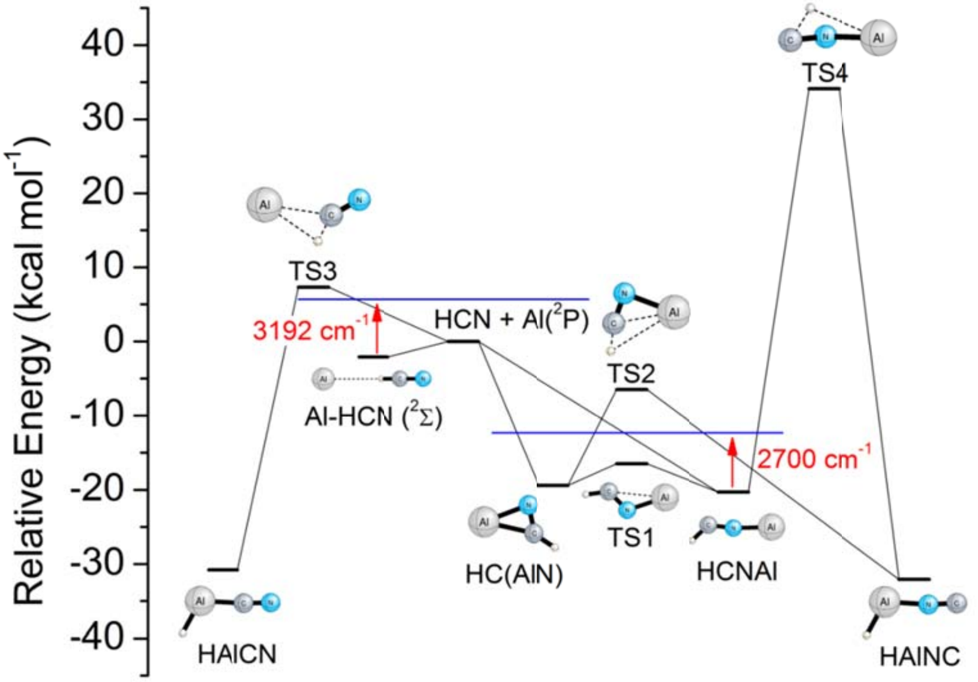

Figure 8.5: Potential energy surface at the CCSD(T)/aug-cc-pVTZ level of theory with ZPVE correction and MP2 basis set extrapolation. The blue lines and red arrows are representative of the CH stretch vibrational excitation energy of the two isomers observed experimentally.

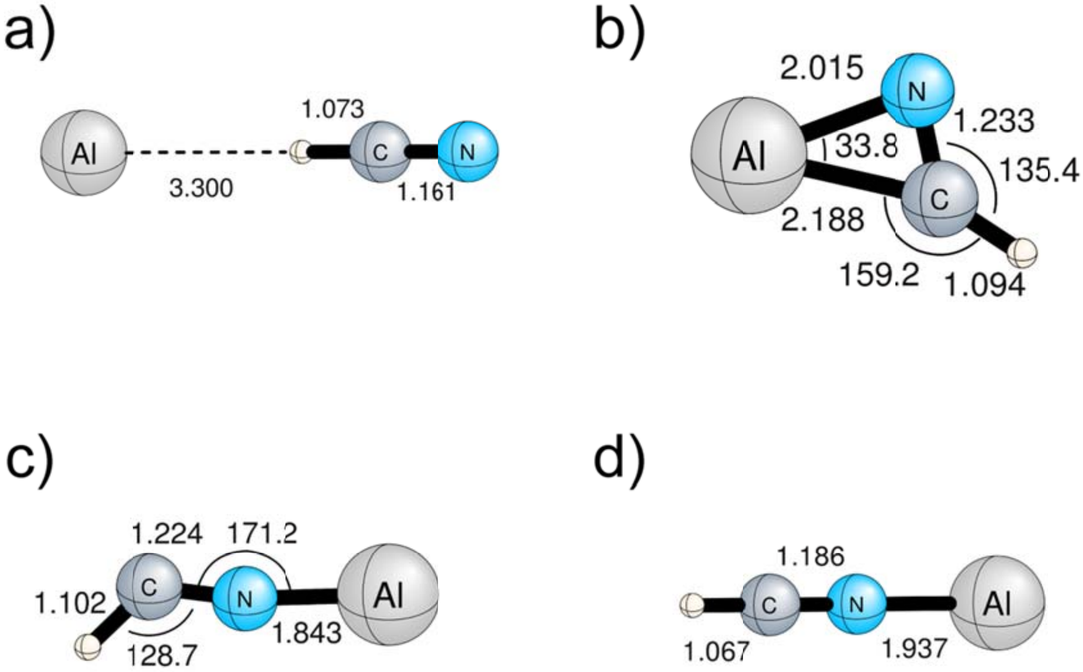

Figure 8.6: Geometries at CCSD(T)/aug-cc-pVTZ level of theory: a) H-bonded Al-HCN, b) Cyclic HC(AlN), c) bent HCNAl, and d) N-bonded HCN-Al (1 imaginary frequency).

Table 8.3: Cartesian Coordinates of Al + HCN minima and transition states at the CCSD(T) / aug-cc-pVTZ level of theory.

H-bonded Al-HCN

	X	*Y*	*Z*
H	0.000000	0.000000	–0.831272
C	0.000000	0.000000	–1.904550
N	0.000000	0.000000	–3.065242
Al	0.000000	0.000000	2.468918

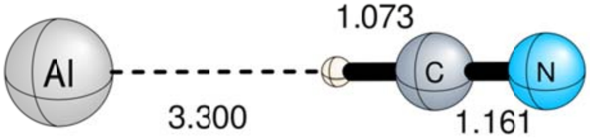

Bent HCNAl

	X	*Y*	*Z*
H	–2.618907	0.663808	0.000000
C	–1.827988	–0.104231	0.000000
N	–0.613390	0.048425	0.000000
Al	1.229159	–0.003570	0.000000

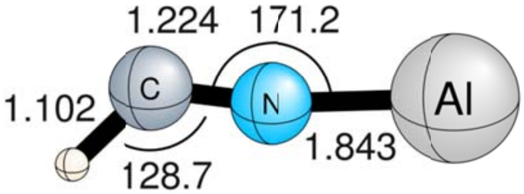

Cyclic HC(AlN)

	X	*Y*	*Z*
H	2.025460	1.150239	0.000000
C	1.114784	0.544156	0.000000
N	0.862659	–0.662732	0.000000
Al	–1.019163	0.058973	0.000000

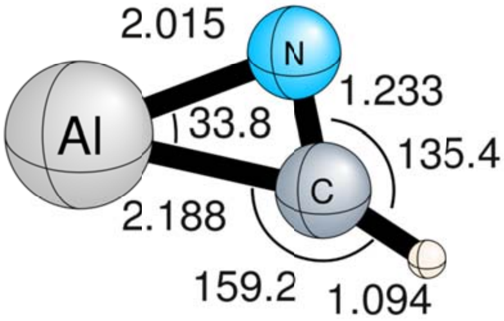

HAlCN

	X	*Y*	*Z*
H	–1.990418	1.330561	0.000000
C	0.725917	0.031071	0.000000
N	1.895701	0.006539	0.000000
Al	–1.232348	–0.066912	0.000000

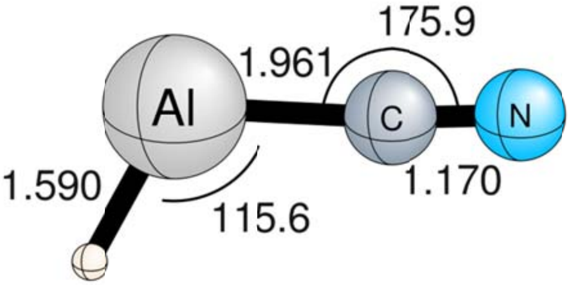

HAlNC

	X	*Y*	*Z*
H	–1.894174	1.325687	0.000000
C	1.883881	–0.006774	0.000000
N	0.698913	0.049445	0.000000
Al	–1.129828	–0.072166	0.000000

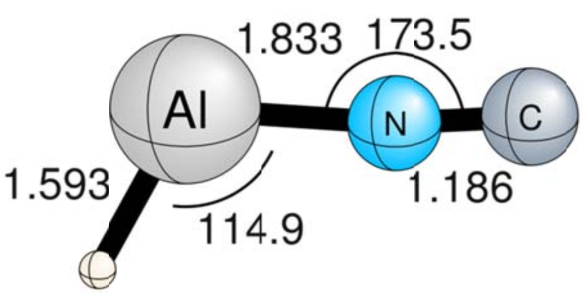

TS1

	X	*Y*	*Z*
H	–2.628984	–0.229735	0.000000
C	–1.532499	–0.375757	0.000000
N	–0.663909	0.513117	0.000000
Al	1.124336	–0.090602	0.000000

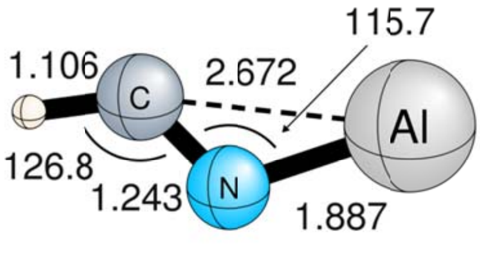

TS2

	X	*Y*	*Z*
H	–1.368702	1.562927	0.000000
C	–1.250798	0.494193	0.000000
N	–0.845728	–0.657746	0.000000
Al	1.046337	0.063191	0.000000

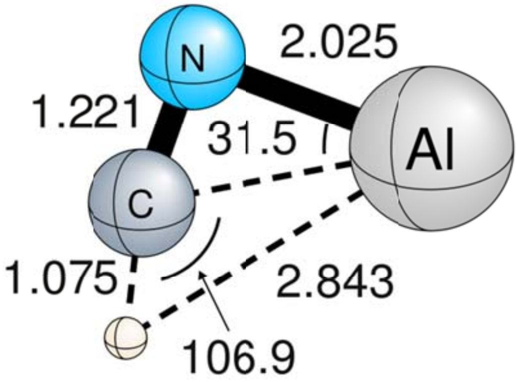

TS3

	X	*Y*	*Z*
H	0.467721	1.311703	0.000000
C	0.968169	0.326594	0.000000
N	1.999419	–0.249976	0.000000
Al	–1.485735	–0.064513	0.000000

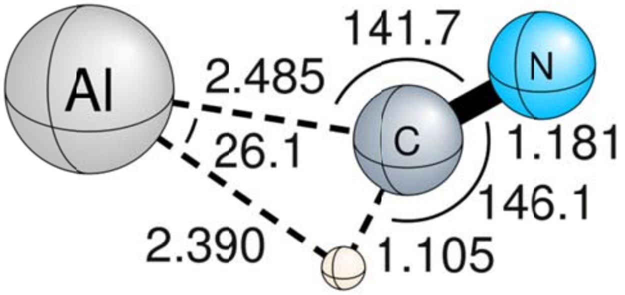

TS4

	X	*Y*	*Z*
H	–1.232130	–1.052347	0.000000
C	–1.941880	0.095428	0.000000
N	–0.676770	–0.037723	0.000000
Al	1.260906	0.016444	0.000000

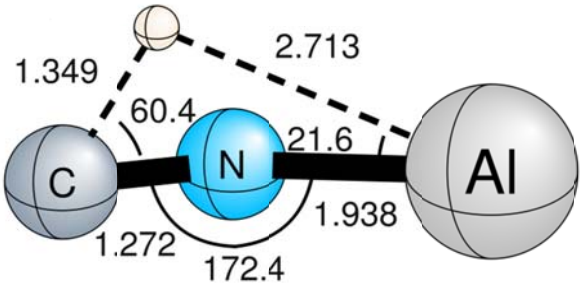

Given that the reaction occurs between sequentially picked up and presumably cold reactants (equilibrated to the droplet temperature), it is not expected that the system can overcome the 7.3 kcal/mol barrier (TS3) leading to the HAlCN insertion product. However, the formation of the cyclic HC(AlN) and bent HCNAl products is predicted to be barrierless in both cases. Furthermore, one of the two transition states (TS2) between HC(AlN) and the HAlNC insertion product lies below the reactants; however, our present laser tuning range prevents us from searching for evidence of the formation of HAlNC. The highest frequency fundamental vibrations predicted for this insertion product are the HAl and CN stretches at 1885 and 2087 cm^{-1}, respectively.

8.4.1 $^2A'$ Bent HCNAl

Given the possibility for the formation of the cyclic HC(AlN) and bent HCNAl products, we computed anharmonic frequencies for these species at the CCSD(T)/Def2-TZVP level of theory, and the results are given in Table 8.2. Bent HCNAl is the only possible structure that accounts for the bands near 2700 cm^{-1}. The large experimental frequency shift of -619.37 cm^{-1} from the HCN band origin (3311.20 cm^{-1}) reasonably matches the *ab initio* VPT2 anharmonic frequency result of -570 cm^{-1}. In comparison, a frequency shift of -444 cm^{-1} is predicted for the cyclic HC(AlN) product. Given the signal dependencies on the experimental conditions discussed above, the anharmonic frequency calculations and the expected outcome of the formation process in helium droplets, it is reasonable to assign the features near 2700 cm^{-1} to the CH stretch band of the bent HCNAl reaction product.

The lowest frequency band observed at 2692 cm^{-1} exhibits partially resolved rotational fine structure, while the peak at 2713 cm^{-1} lacks fine structure. An analysis of this rotational fine structure provides further evidence to support our assignment. The CH stretch band is predicted to be an *a*,*b*-hybrid band of a near-prolate asymmetric top. The computed A'' rotational constant is 27.7 cm^{-1}, which leads to population only in levels with K_a=0. As a result of this, the *a*-type band will resemble a closed-shell linear molecule spectrum with *P* and *R* branches. Furthermore, the *b*-type band should appear to the blue of the *a*-type band by roughly the A' rotational constant. The spectral region containing both the 2692 and 2713 cm^{-1} features is shown in Fig. 8.7 (top panel). The rotational fine structure of the band at 2692 cm^{-1} along with the position of the 2713 cm^{-1}

band is consistent with an assignment of the former to the *a*-type component and the latter to the *b*-type component of the CH stretch band of bent HCNAl.

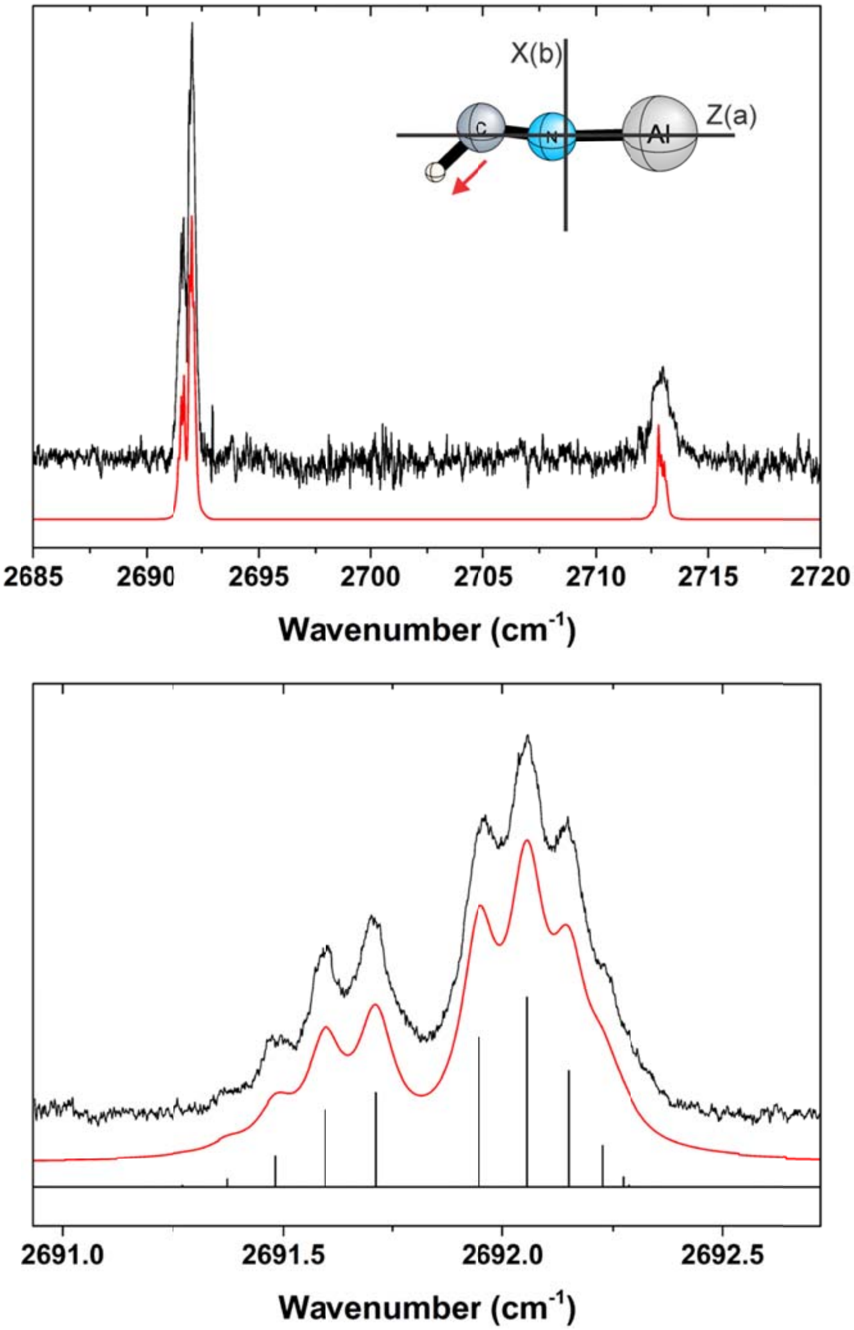

Figure 8.7: Expanded view of the HCNAl ν_{CH} stretch ro-vibrational band near 2700 cm^{-1}. The red smooth curves are simulations based on an *a,b*-hybrid band of a near-prolate asymmetric top. The inset shows the inertial axes of the system.

The rovibrational structure simulation for the bent HCNAl species is performed based on C_S symmetry, $^2A'$ electronic state obtained from the *ab initio* result. The coordinate system used is shown in Fig. 8.7. Here X and Z define the Cs symmetry plane, and Z is mostly along the C-N-Al direction. The a, b, and c inertial axes lie on z, x, and y axes, and an I_r representation is used for our simulation. The CH stretch vibration has A′ symmetry and is an *a*,*b*-hybrid band. The *ab initio* dipole derivative vector has components along both the *a* and *b* inertial axes with $(d\mu_a/dq) = (d\mu_b/dq) * 1.91(2)$. The ground- and excited-state rovibronic symmetries are A′, A″, A′, and A″ for ee, eo, oe, and oo for K_aK_c rotational levels, respectively. Both *a*- and *b*-type bands are simulated with the appropriate selection rules (*a*-type band: $\Delta K_a = 0$, $\Delta K_c = \pm 1$; *b*-type band: $\Delta K_a = \pm 1$, $\Delta K_c = \pm 1$). The rotational constants obtained at the CCSD(T)/aug-cc-pVTZ level of theory were used for initial simulation. The *ab initio* $(B+C)/2$ constant was divided by 3 to account for the effective reduction due to the helium solvent. The A' constant was, however, set to be 21 cm^{-1} in order to fit to the 2713 cm^{-1} band. The rotational temperature and linewidths were set to 0.4 K and 0.1 cm^{-1}, respectively. With these initial settings, the contour fitting routine in PGOPHER was applied to refine the values of the rotational constants.

The fitted spectrum is shown as the red trace in Fig. 8.7, and the associated constants obtained from the fit are given in Table 8.4. The experimental $(B+C)'' / 2$ constant is 3.0 times smaller than the CCSD(T) value, which is completely consistent with the rotational constant reduction factors observed previously for other molecules solvated in helium nanodroplets [11]. This corresponds to a solvent induced increase in the average effective moment of inertia about the *b* and *c* inertial axes of ~191 amu-Å^2. In contrast, the moment of inertia about the *a* axis is increased by only 0.16 amu- $Å^2$, which is a result of the helium not being as capable of following the much "faster" rotational motion about this inertial axis. One other aspect of the fit that is worth mentioning is the difference in the line widths required to satisfactorily simulate the *a*- and *b*-type bands, which have Lorentzian line widths of 0.1 and 1.0 cm^{-1}, respectively. Assuming these linewidths originate from homogeneous broadening mechanisms, a feasible explanation for the additional broadening observed for the *b*-type band is the possibility for nearly resonant rotational energy transfer from the K_a=1 levels accessed in the vibrational excited state to the elementary excitations of the helium droplet. This effect has been observed and discussed for other helium solvated molecular systems [11].

We computed the vibrationally averaged *A* rotational constant for vibrational levels v = 0, 1 and 2, based on the potential energy curve along the C-H stretching normal coordinate at the CCSD(T)/aug-cc-pVTZ level of theory. The potential curve is shown as the black line in Figure S5. The one-dimensional vibrational Schrödinger equation is numerically solved with a fixed reduced mass chosen to fit the v=0→v=1 transition obtained from our spectroscopic measurement. The *A* constant along the normal mode coordinate is also plotted in Fig. 8.10, and it is reduced dramatically as the C-H is elongated beyond its equilibrium value. The vibrationally averaged *A′* constant is 26.3 cm^{-1}, which is reduced by 1.0 cm^{-1} compare to the ground state result of 27.3 cm^{-1}. The *A* constant for ν = 2 is even smaller, with a value of 25.2 cm^{-1}. The vibrationally averaged *A* constants for both the ground and excited vibrational states as functions of the reduced mass are also plotted and shown in Fig. 8.11. Within the range of the reduced mass that would result in an v=0 to v=1 energy spacing that varies between 2450 cm^{-1} to 2950 cm^{-1}, the averaged *A* constants do not change much.

Table 8.4: Contour fitted constants for the HCNAl partially resolved ν_1 band.[a]

(cm^{-1})	ν_0	$\Delta\nu_{CH}$	A′	(B+C)″/2	(B+C)′/2	$D_J(\times10^{-4})$	T_{rot} (K)
Exp	2691.825(1)	-619.38	21.0(1)	0.0594(1)	0.0582(1)	1.6(1)	0.377(1)
CCSD(T)[b]	2726	-570	26.3[c]	0.181			

[a] The numbers in parentheses are the 1σ errors associated with the contour fitting routine in PGOPHER [25]. The *A″* constant is not determined experimentally. A Lorentzian lineshape of 0.1 cm^{-1} is obtained from the contour fit. The reported centrifugal distortion constant is the averaged value for the ground and excited vibrational states. The experimental $(d\mu_a/dq):(d\mu_b/dq)$ ratio is 1.91(2), which can be compared to 5.0 computed at the CCSD(T)/aug-cc-PVTZ level.

[b] The *ab initio* ν_0 is the VPT2 fundamental frequency at the CCSD(T)/Def2-TZVP level of theory, and the ground state rotational constants are from the CCSD(T)/aug-cc-pVTZ level of theory. At this level, A''=27.7 cm^{-1}.

[c] Vibrationally averaged *A′* rotational constant. A description of the method used to determine this constant is given in Fig. 8.10, 11.

8.4.2 ^{2}A′ Cyclic HC(AlN)

The CCSD(T)/Def2-TZVP VPT2 anharmonic frequencies for the CH stretch bands of the linear Al-HCN and bent HCNAl isomers are slightly larger than the experimental results, by 33 cm^{-1} and 34 cm^{-1}, respectively. Assuming a similar difference for cyclic HC(AlN), the CH stretch band should be near 2819 cm^{-1}. However the only bands in this region are due to HCN or HCN clusters, and we find no evidence for HC(AlN), despite the fact that it is nearly isoenergetic with HCNAl. There are two possible explanations for the absence of the cyclic species. The anharmonic frequency calculations predict an IR intensity for the HC(AlN) CH stretch band that is more than a factor of ten times weaker than the CH stretch band of bent HCNAl. Nevertheless, careful scans in this region failed to find any weak bands that relied on the presence of the Al oven source. A second possible explanation is that the abundance of cyclic HC(AlN) may be too low to observe. Indeed, the long range, dipole-quadrupole interaction may result in more trajectories that steer the complex towards either the hydrogen or nitrogen-bonded configurations, in comparison to trajectories that lead to the T-shaped position on the potential. The tendency for the formation of either Al-HCN or HCNAl, as opposed to HC(AlN), seems reasonable upon inspection of the size of the basins around the linear minima on the 1A′ intermolecular potential (Fig. 8.4).

8.4.3 $^2\Pi$ Linear HCN-Al

It is interesting to note that in a previous report by Merritt and co-workers, the nitrogen-bound, linear HCN-Ga and HCN-In complexes were observed in helium droplets in the 3300 cm^{-1} region (CH stretch) upon sequential pick-up of HCN and either Gallium or Indium [4]. The relatively small frequency shift of the CH stretch upon HCN complexation in these systems is indicative of a rather weak interaction. *Ab initio* calculations of these species indicate that they are true minima separated from the lower energy additive HCNM and HC(MN) products by ~2 kcal/mol barriers [4] (see also Fig. 8.8). These entrance channel minima on the HCN + Ga and HCN + In potentials likely appear due to a balance between the electrostatic dipole – quadrupole interaction and the repulsive exchange interaction between the electrons on each fragment. As the intermolecular bond length decreases, charge transfer (orbital mixing) interactions between the metal atom and HCN begin to dominate, leading to additive reaction products that have analogous structures [4] to those computed here for HCN + Al. Apparently, the helium cooling upon cluster formation is sufficiently rapid to trap these systems in the higher energy entrance channel minima. However, in this previous study, there was no evidence for the analogous $^2\Pi$, HCN-Al complex in the free CH stretch region. As noted above, the nitrogen-bound, linear HCN-Al species is not a minimum on the potential surface but is rather a first order saddle point at the CCSD(T) level of theory. A reasonable explanation for the difference between the Al and Ga/In systems is that the repulsive exchange interaction is less significant at long range in the Al case, and a barrier cannot form before orbital mixing begins to dominate the HCN + Al interaction (see Fig. 8.8 for further discussion). Given a favorable approach geometry, we therefore expect that the HCN + Al system will evolve barrierlessly within the helium droplet to either the HC(AlN) or the HCNAl structures. On the basis of the previous spectroscopic analysis [4] and the analysis presented here, it is clear that the system can also become trapped in the linear, hydrogen-bonded Al-HCN configuration.

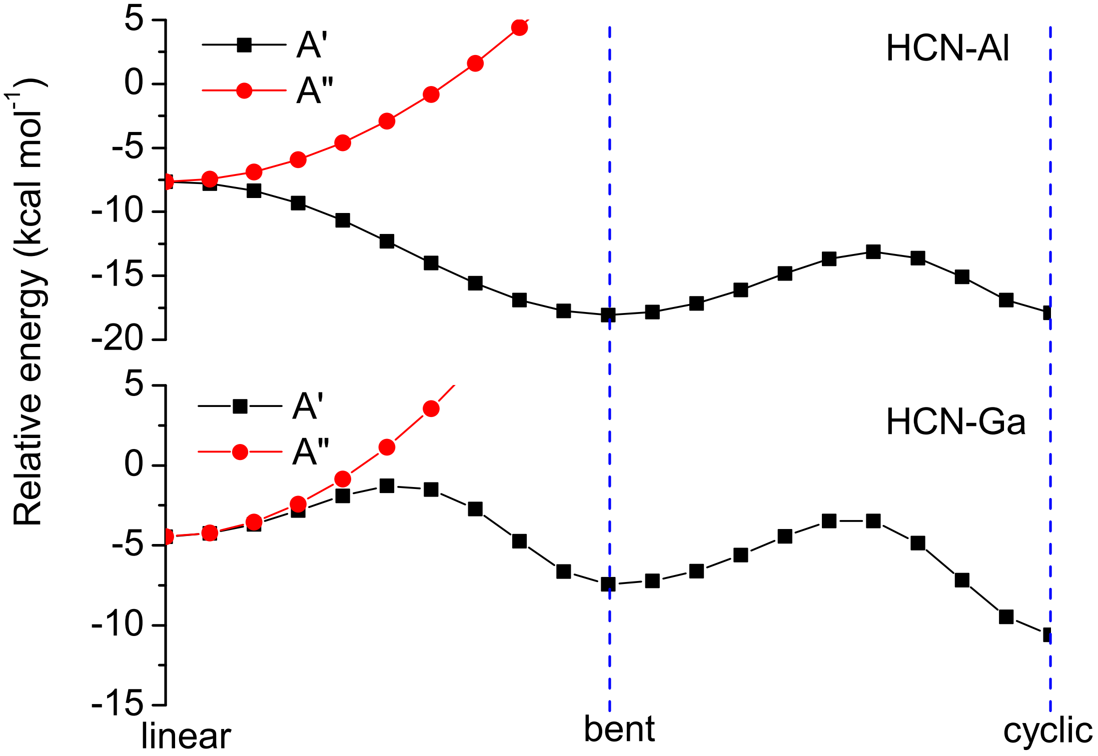

Figure 8.8: The evolution of the A′ and A″ potential curves as the system transforms from the linear configuration to the bent configuration and then to the cyclic configuration. The potentials are computed at the CCSD(T)/Def2-TZVPD level to illustrate that the linear configuration is a true minimum for Ga, but it is a saddle point for Al. In these calculations, the 3d electrons of Ga are not included as part of the frozen core, but are rather included in the valence. Single point energy calculations are carried out at geometries obtained by the interpolation of a consistent set of internal coordinates, starting from the linear HCN-X configuration and moving towards the bent HCNX, and then to cyclic HC(XN) configuration (left to right in the Figure). It is clear that there is no barrier from linear HCN-Al to bent HCNAl on the A′ surface, and there is a submerged barrier from bent HCNAl to cyclic HC(AlN). The A′ surface from HCN-Ga shows submerged barriers from both linear to bent and bent to cyclic. The A″ surface is repulsive for both the Al and Ga cases beyond the linear geometry.

8.4.4 Natural Bond Orbital Analysis for Bent HCNAl

To investigate the nature of the bonding in the bent HCNAl reaction product, we carried out a Natural Bond Orbital (NBO) analysis of this species. From natural resonance theory [26, 27], we find that the C-H, C-N, and Al-N bond orders in HCNAl are 0.971, 2.54 and 0.37, respectively. These can be compared to the C-H and C-N bond orders of HCN, which are 0.989 and 3.01, respectively. The decreased C-H bond order is consistent with the large red shift of the CH stretch upon addition of the Al atom. The relative energetic importance of the donor-acceptor interactions between the natural bond orbitals in HCNAl can be estimated by a second-order perturbation theory analysis of the Fock matrix in the NBO basis [28]. Here we enforce a starting Lewis structure with HCN and Al treated as two separated units, which effectively eliminates the N-Al NBO. This allows us to assess the deviation from this zeroth-order Lewis structure in terms of the donor-acceptor interactions between NBOs isolated on either the HCN or the Al fragments. The three largest donor-acceptor interactions are, *i*) a σ-donation from the N atom lone-pair electrons to an empty, in-plane Al *p*-orbital, *ii*) a π-type back donation of the Al in-plane single *p* electron to an anti-bonding orbital localized on the C-N bond, and *iii*) a donation of electron density from this anti-bonding C-N orbital to an anti-bonding orbital localized on the C-H bond. The NBOs participating in these three donor-acceptor interactions are shown schematically in Fig. 8.9. The delocalization energies associated with these interactions are 56.7, 44.9 and 21.5 kcal mol^{-1}, respectively. This significant degree of delocalization of the Al atom electron density into the HCN moiety results in a rehybridization of the carbon atom and a large red shift of the CH stretching frequency.

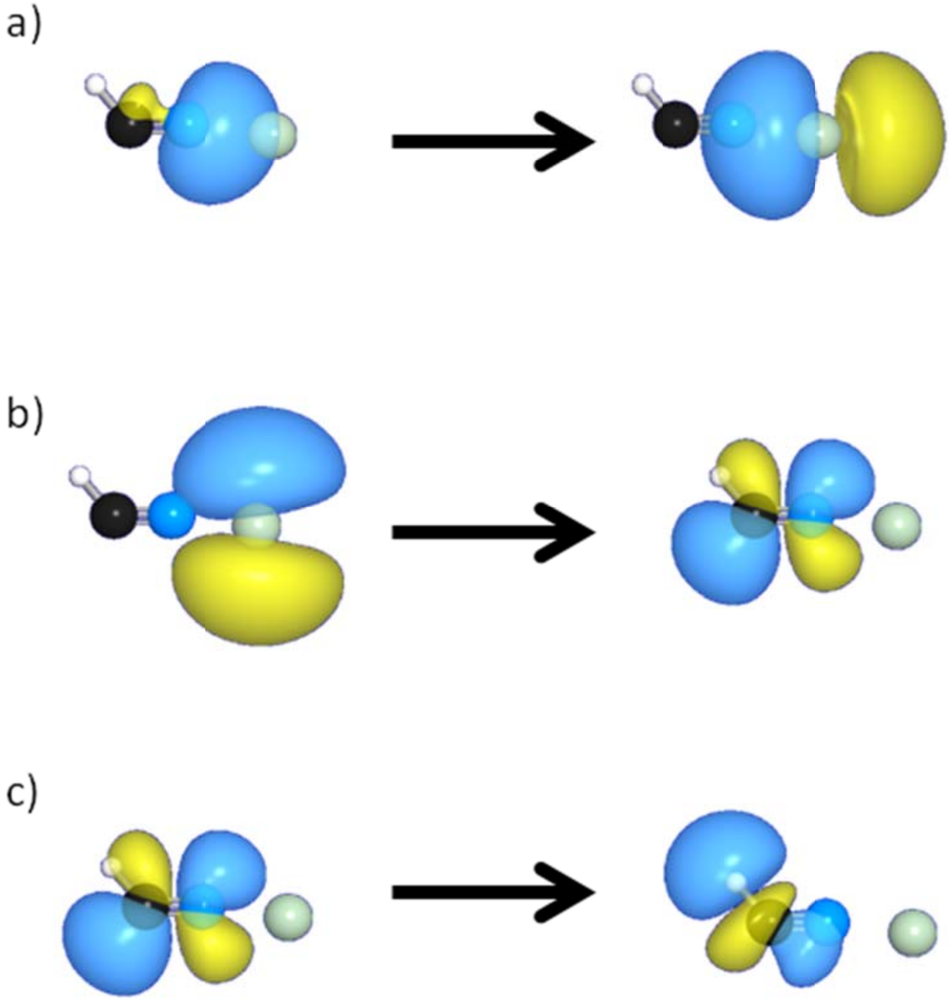

Figure 8.9: The three largest NBO donor-acceptor interactions obtained from 2nd order perturbation theory: a) from lone pair electrons of N to empty *p* orbital of Al; b) from unpaired Al *p* electron to anti-bonding orbital of C-N; c) from anti-bonding orbital of C-N to anti-bonding orbital of C-H.

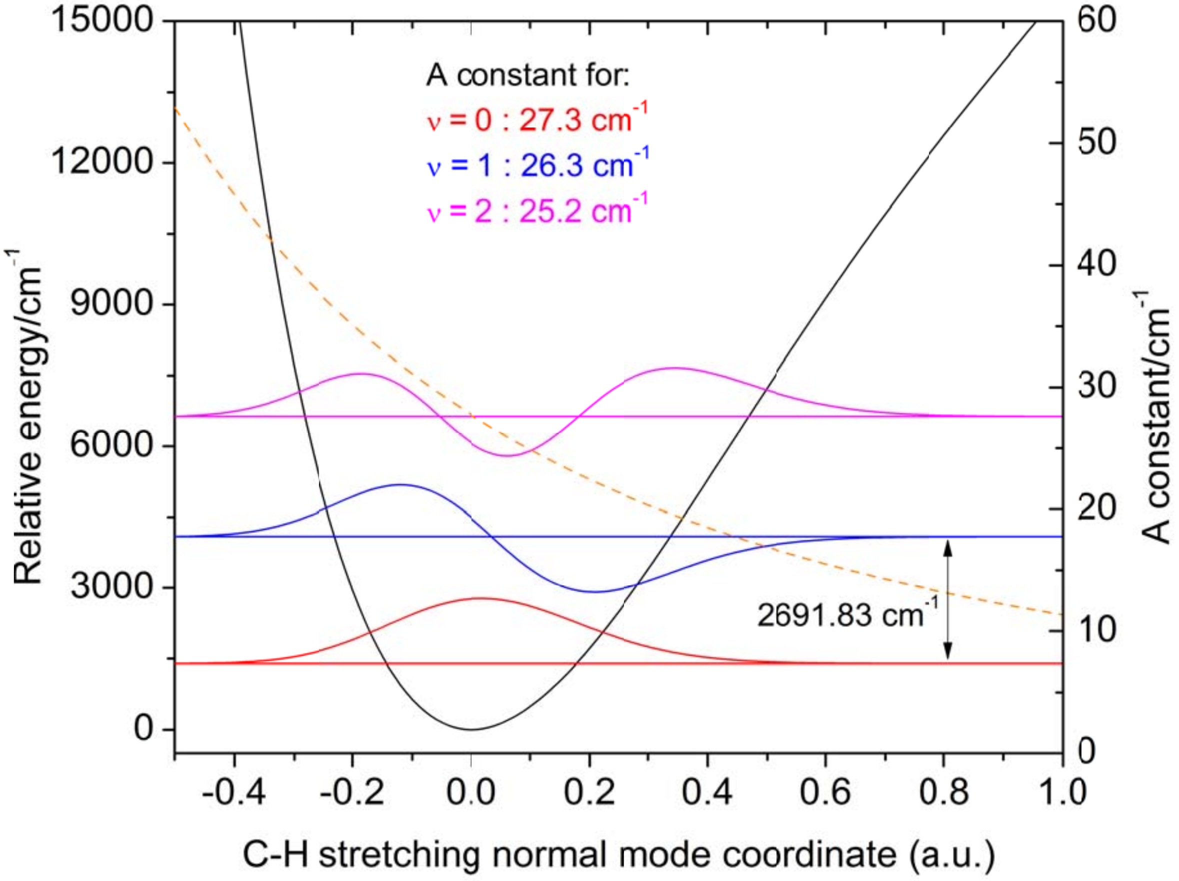

Figure 8.10: Potential energy curve of the C-H stretching normal mode coordinate (black). The orange dashed line is the A'' constant as a function of this coordinate. The red, blue, and pink curves are the energy levels and wave functions for the ground, first excited, and second excited vibrational states, respectively.

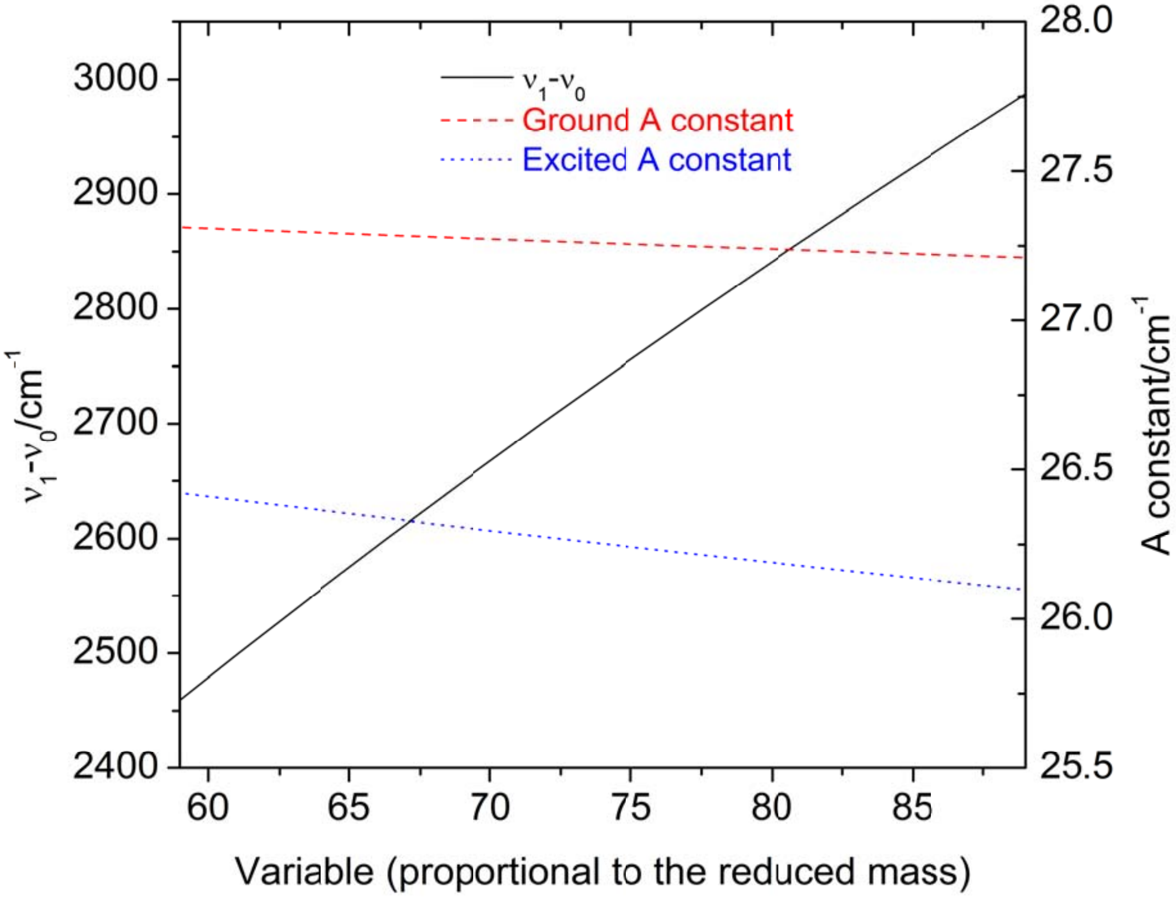

Figure 8.11: Energy spacing of v=0→v=1 and the ground and excited state *A* constants as functions of the reduced mass, showing that these constants are somewhat insensitive to the exact value of the reduced mass used in the numerical solution of the Schrödinger equation.

8.5 Conclusions

The outcome of the Al + HCN reaction between cold fragments in a helium nanodroplet has been probed with IR laser spectroscopy between 2650 and 3320 cm^{-1}. Ro-vibrational bands near 2700 cm^{-1} are assigned to the CH stretch of an additive reaction product, namely the $^2A'$ bent HCNAl species. The assignment is obtained from detailed comparisons to *ab initio* calculations of the various minima on the potential surface, along with VPT2 anharmonic frequency calculations. The CH stretch band of the bent HCNAl has both *a*- and *b*-type components separated by 21 cm^{-1}, which is consistent with the bent geometry and the calculated rotational moment of inertia about the *a* inertial axis. Analysis of the CCSD(T) potential reveals that the $^2\Pi$ HCN-Al complex is a first order transition state and that the formation of the $^2A'$ HCNAl and HC(AlN) additive reactions products proceeds barrierlessly. This is in contrast to the HCN-Ga and HCN-In species, in which a barrier forms in the entrance channel to the reaction, an effect which is likely due to the Ga and In systems exhibiting a comparatively stronger exchange repulsion interaction between the fragments at long-range. Despite the feasibility for the formation of the cyclic HC(AlN) additive product, no evidence for this species is found in the spectrum, indicating that as the system condenses in the helium droplet, the electrostatic interactions that dominate at long-range tend to steer the system towards either the linear, $^2\Sigma^+$ Al-HCN or bent HCNAl configurations. An NBO analysis of the HCNAl species indicates that the single *p* electron on the Al atom is significantly delocalized into anti-bonding molecular orbitals of the HCN fragment. This charge transfer interaction is responsible for the bent geometry and substantial red shift observed for the CH stretch upon complexation.

References

[1] Krasnokutski, S. A., and Huisken, F., *J. Phys. Chem. A* **114**, 13045-13049 (2010).

[2] Krasnokutski, S. A., and Huisken, F., *J. Phys. Chem. A* **114**, 7292-7300 (2010).

[3] Krasnokutski, S. A., and Huisken, F., *J. Phys. Chem. A* **115**, 7120-7126 (2011).

[4] Merritt, J. M., Douberly, G. E., Stiles, P. L., and Miller, R. E., *J. Phys. Chem. A* **111**, 12304-12316 (2007).

[5] Liang, T., Flynn, S. D., Morrison, A. M., and Douberly, G. E., *J. Phys. Chem. A* **115**, 7437-7447 (2011).

[6] Morrison, A. M., Agarwal, J., Schaefer, H. F., and Douberly, G. E., *J. Phys. Chem. A* **116**, 5299-5304 (2012).

[7] Lugovoj, E., Toennies, J. P., and Vilesov, A., *J. Chem. Phys.* **112**, 8217-8220 (2000).

[8] Muller, S., Krapf, S., Koslowski, T., Mudrich, M., and Stienkemeier, F., *Phys. Rev. Lett.* **102**, - (2009).

[9] Lanzisera, D. V., and Andrews, L., *J. Phys. Chem. A* **101**, 9660-9665 (1997).

[10] Toennies, J. P., and Vilesov, A. F., *Angew. Chem. Int. Ed.* **43**, 2622-2648 (2004).

[11] Choi, M. Y., Douberly, G. E., Falconer, T. M., Lewis, W. K., Lindsay, C. M., Merritt, J. M., Stiles, P. L., and Miller, R. E., *Int. Rev. Phys. Chem.* **25**, 15-75 (2006).

[12] Stienkemeier, F., and Lehmann, K. K., *J. Phys. B: At., Mol. Opt. Phys.* **39**, R127-R166 (2006).

[13] Hartmann, M., Miller, R. E., Toennies, J. P., and Vilesov, A., *Phys. Rev. Lett.* **75**, 1566-1569 (1995).

[14] Chin, S. A., and Krotscheck, E., *Phys. Rev. B* **52**, 10405-10428 (1995).

[15] Lehmann, K. K., and Dokter, A. M., *Phys. Rev. Lett.* **92** (2004).

[16] Reho, J. H., Merker, U., Radcliff, M. R., Lehmann, K. K., and Scoles, G., *J. Phys. Chem. A* **104**, 3620-3626 (2000).

[17] Nauta, K., and Miller, R. E., *Phys. Rev. Lett.* **82**, 4480-4483 (1999).

[18] Morrison, A. M., and Douberly, G. E., *Rev. Sci. Instrum.* **83** (2012).

[19] Schneider, W., and Thiel, W., *Chem. Phys. Lett.* **157**, 367-373 (1989).

[20] Stanton, J. F., and Gauss, J., *Int. Rev. Phys. Chem.* **19**, 61-95 (2000).

[21] CFOUR, Coupled-Cluster techniques for Computational Chemistry, a quantum-chemical program package by J.F. Stanton, J. Gauss, M.E. Harding, P.G. Szalay with contributions from A.A. Auer, R.J. Bartlett, U. Benedikt, C. Berger, D.E. Bernholdt, Y.J. Bomble, L. Cheng, O. Christiansen, M. Heckert, O. Heun, C. Huber, T.-C. Jagau, D. Jonsson, J. Jusélius, K. Klein, W.J. Lauderdale, D.A. Matthews, T. Metzroth, D.P. O'Neill, D.R. Price, E. Prochnow, K. Ruud, F. Schiffmann, W. Schwalbach, S. Stopkowicz, A. Tajti, J. Vázquez, F. Wang, J.D. Watts and the integral packages MOLECULE (J. Almlöf and P.R. Taylor), PROPS (P.R. Taylor), ABACUS (T. Helgaker, H.J. Aa. Jensen, P. Jørgensen, and J. Olsen), and ECP routines by A. V. Mitin and C. van Wüllen. For the current version, see http://www.cfour.de.

[22] NBO 5.0. E. D. Glendening, J, K. Badenhoop, A. E. Reed, J. E. Carpenter, J. A. Bohmann, C. M. Morales, and F. Weinhold, Theoretical Chemistry Institute, University of Wisconsin, Madison (2001).

[23] Schmidt, M. W., Baldridge, K. K., Boatz, J. A., Elbert, S. T., Gordon, M. S., Jensen, J. H., Koseki, S., Matsunaga, N., Nguyen, K. A., Su, S. J., Windus, T. L., Dupuis, M., and Montgomery, J. A., *J. Comput. Chem.* **14**, 1347-1363 (1993).

[24] Nauta, K., and Miller, R. E., *Science* **283**, 1895-1897 (1999).

[25] PGOPHER, a Program for Simulating Rotational Structure, C. M. Western, University of Bristol, http://pgopher.chm.bris.ac.uk

[26] Glendening, E. D., and Weinhold, F., *J. Comput. Chem.* **19**, 593-609 (1998).

[27] Glendening, E. D., and Weinhold, F., *J. Comput. Chem.* **19**, 610-627 (1998).

[28] Reed, A. E., Curtiss, L. A., and Weinhold, F., *Chem. Rev.* **88**, 899-926 (1988).

Chapter 9

Conclusions and Outlook

Helium nanodroplet spectroscopy has been shown to be an extremely useful technique to study open-shell radicals. In this thesis, various molecular systems are investigated with this technique.

The hydroxyl (OH) radical has shown anomalous Λ-doubling constants in helium droplets for both the v=0 and v=1 states, being 3.6 and 7.2 times larger with respect to the gas phase values.[1] The helium density distribution is computed based on the He-OH interaction potential in the A′ and A″ planes, and the helium density is found to be larger and more anisotropic for the A′ electronic symmetry configuration. This indicates a larger perturbation on the rotation of OH in the A′ plane, and a model is proposed to predict the Λ-doubling constants. From this model, a good agreement with experimental measurement is obtained when the B_v^e and B_v^f constants are set to differ by 0.6 and 1.4% for v=0 and v=1, respectively. This model is verified by a successful prediction of the Λ-doublet splitting observed for He-solvated NO.[2]

The HOOO molecule is assembled in helium droplets by the sequential pick-up of OH and O_2. The *trans*-HOOO isomer is observed in the OH stretch region with a band origin of 3569.455(5) cm^{-1}, which is about 0.16 cm^{-1} to the blue of the corresponding gas phase result.[3] The *cis*-HOOO species, which was predicted by theory to be nearly isoenergetic to *trans*-HOOO with a torsional barrier of about 340 cm^{-1},[4] is absent in our spectrum. According to the 6D DFT potential by Braams and Yu,[5] the tunneling time is on the order of 10 ns, which is fast if compared with our measurement time of ~100-2000 μs. Therefore the fast tunneling from the *cis*-HOOO to *trans*-HOOO may be responsible for the absence of *cis*-HOOO species in helium droplet. The weakly bound OH-O_2 is not observed in our measurement as well, which indicates a barrierless association reaction from OH + O_2 to HOOO.

The Stark spectra of *trans*-HOOO in helium are measured with both parallel and perpendicular field configurations. Fitting of the Stark spectra reveals the $<\mu_a>$ and $<\mu_b>$ dipole components to be 0.61(2) and 1.48(2) D, in large disagreement with the *ab initio* equilibrium value of 1.01 and 1.63 D at the CCSD(T)/CBS level of theory. Allen and Magers have shown that an optimization at the CCSDT(Q)/CBS level of theory increases the center OO bond length by 0.07 Å, and the equilibrium dipole components are 0.78 and 1.64 D, respectively.[6] By using a two-dimensional vibrational averaging scheme at CCSD(T)/Def2-TZVPD level of theory, the μ_a and μ_a are reduced from their equilibrium values by about 0.16 D and 0.13 D, respectively. When both considerations are combined, a good agreement between experiment and theory is achieved.

When the O_2 pressure is increased, the OH stretching bands of HO_3-$(O_2)_n$ can be observed for up to n=4. The bands are located 1.14 and 6.44 cm^{-1} to the red of the band origin of *trans*-HOOO. Based on *ab initio* frequency computation at CCSD(T) level, the 1.14 cm^{-1} red shifted band is assigned to an H-bonded *trans*-HO_3-O_2. The band appearing at 6.44 cm^{-1} to the red of the *trans*-HOOO is assigned to an HO_3-$(O_2)_2$ cluster. At higher O_2 pressures, the OH stretches for clusters with n>2 grow in around 3560 cm^{-1}.

These bands are broad, and are potentially due to the clusters with a *trans*-HOOO core solvated by 3 or more O_2 molecules.

This thesis covers only a small number of OH containing complexes that haven been recently assembled in helium droplets. Other complexes containing CO, O_3, C_2H_2, and C_2H_4 are currently undergoing investigation and will help to further understand the range of reaction dynamics that are possible in liquid helium. Also, by studying these open-shell clusters, more information about the interaction between helium droplets and the open-shell clusters can be obtained.

The Al-$(CO)_n$ clusters are assembled in helium droplets, and the fundamental CO stretches are probed with a QCL laser. A rotationally resolved band around 1885 cm^{-1} corresponds to the $^2\Pi_{1/2}$ Al-CO, and a band near 1919 cm^{-1} is assigned to the $^2B_1$ Al-$(CO)_2$ cluster. The large frequency shifts of CO stretches of both species are the result of Al to CO π-donation and CO to Al σ-donation, which are revealed by NBO calculations. The NBO calculation also discovers the π-type, 3-centered C-Al-C bond in the Al-$(CO)_2$ cluster. The broad and weak band slightly to the blue of Al-CO band is tentatively assigned to the (Al-CO)-CO weakly bound species. *Ab initio* computations discover that the weakly bound (Al-CO)-CO and the strongly bound Al-$(CO)_2$ are connected by a small barrier of ~200cm^{-1}, with Al-$(CO)_2$ about 10 kcal mol^{-1} below the (Al-CO)-CO. An IR-IR double resonance experiment is proposed in order to support this assignment.

The Al + HCN reaction is investigated in helium nanodroplets. *Ab initio* computations show multiple isomers on the potential energy surface, including H-bonded Al-HCN, bent-HCNAl, cyclic HC(AlN), HAlCN, and HAlNC. Except for the previously found H-bonded Al-HCN,[7] only bent-HCNAl is observed between 2650 and 3320 cm^{-1}. The IR bands near 2700 cm^{-1} are assigned to the CH stretch of the $^{2}A'$ bent-HCNAl species, based on *ab initio* VPT2 anharmonic frequency calculations. In contrast to the linear HCN-Ga and HCN-In molecules,[7] which were found stable by both experiment and theory, the linear HCN-Al species is not found experimentally, and it is also shown by theory to be a transition state. The *ab initio* vibrational frequencies for HAlCN and HAlNC are outside the range of our laser system; therefore, no experimental evidence for these species was found in our spectra. The search should continue, when other laser systems that cover a broader frequency range become available, in order to obtain the IR spectra of these important metal atom insertion products

References

[1] Melen, F., Sauval, A. J., Grevesse, N., Farmer, C. B., Servais, C., Delbouille, L., and Roland, G., *J. Mol. Spectrosc.* **174**, 490-509 (1995).

[2] von Haeften, K., Metzelthin, A., Rudolph, S., Staemmler, V., and Havenith, M., *Phys. Rev. Lett.* **95** (2005).

[3] Derro, E. L., Murray, C., Sechler, T. D., and Lester, M. I., *J. Phys. Chem. A* **111**, 11592-11601 (2007).

[4] Beames, J. M., Lester, M. I., Murray, C., Varner, M. E., and Stanton, J. F., *J. Chem. Phys.* **134**, 044304 (2011).

[5] Braams, B. J., and Yu, H. G., *Phys. Chem. Chem. Phys.* **10**, 3150-3155 (2008).

[6] Liang, T., Magers, D. B., Raston, P. L., Allen, W. D., and Douberly, G. E., *J. Phys. Chem. Lett.* **4**, 3584-3589 (2013).

[7] Merritt, J. M., Douberly, G. E., Stiles, P. L., and Miller, R. E., *J. Phys. Chem. A* **111**, 12304-12316 (2007).